Interaction of antiprotons with nuclear matter within the INCL model

Demid Zharenov

université PARIS-SACLAY

Interaction of antiprotons with nuclear matter within the INCL model

Interaction entre les antiprotons et la matière nucléaire avec le modèle INCL

Thèse de doctorat de l'université Paris-Saclay

École doctorale n° 576, Particules, hadrons, énergie et noyau: instrumentation, imagerie, cosmos et simulation (PHENIICS)
Spécialité de doctorat: Physique nucléaire
Graduate School : Physique
Référent : Faculté des sciences d'Orsay

Thèse préparée dans l'unité de recherche
Département de Physique Nucléaire (Université Paris-Saclay, CEA),
sous la direction de **Jean-Christophe DAVID**, Ingénieur-chercheur au CEA

Thèse soutenue à Paris-Saclay, le 8 décembre 2023, par

Demid ZHARENOV

Composition du jury

Membres du jury avec voix délibérative

Béatrice RAMSTEIN Directrice de recherche, Université Paris-Saclay	Présidente
Alexandre OBERTELLI Professeur, Technischen Universität Darmstadt	Rapporteur & Examinateur
Josef POCHODZALLA Professeur, Johannes Gutenberg University Mainz	Rapporteur & Examinateur
Alberto RIBON Ingénieur-chercheur, CERN	Examinateur
Davide MANCUSI Ingénieur-chercheur, CEA, Université Paris-Saclay	Examinateur

THESE DE DOCTORAT
NNT : 2023UPASP180

université PARIS-SACLAY

ÉCOLE DOCTORALE
Particules, hadrons, énergie et noyau : instrumentation, imagerie, cosmos et simulation (PHENIICS)

Title: Interaction of antiprotons with nuclear matter within the INCL model.
Keywords: Antiproton, INCL, nucleus

Abstract:

In the wake of renewed experimental interest in antiproton physics and related research, there has emerged a necessity for robust modeling tools to simulate antiproton-nucleus interactions across a broad energy spectrum. This work aims to fill this gap by extending the existing INCL (Intra-Nuclear Cascade Liège) model with the capability to set an antiproton projectile and integrating this model into the GEANT4 particle transport code. Antiprotons, as investigative probes, provide a broad spectrum of opportunities for high-precision experiments in nuclear physics. They allow for the generation of exotic antibaryons and facilitate the study of their subsequent interaction with nuclear matter and atomic shells. Additionally, they shed light on the structure and properties of unstable nuclei.

This research is based on extensive data compiled from past antiproton experiments conducted at CERN, Fermilab, and KEK. This historical dataset serves as both the source for extracting input parameters for the model and as a benchmark for validating our results. In doing so, this thesis meets the growing demand for accurate simulation tools essential for the new era of precision measurements in nuclear and particle physics.

One of the unique advantages of using antiprotons is their ability to facilitate the study of nuclear surfaces and halos through "at-rest" annihilations with various nuclei. We model such annihilations in INCL by implementing a distinct initialization procedure. This scenario is extensively compared with "in-flight" interactions to understand the interplay between the two and the influence of scenario choice on the resulting output.

université PARIS-SACLAY

ÉCOLE DOCTORALE
Particules, hadrons, énergie et noyau : instrumentation, imagerie, cosmos et simulation (PHENIICS)

Titre: Interaction entre les antiprotons et la matière nucléaire avec le modèle INCL
Mots clés: Antiproton, INCL, noyau

Résumé:

Dans le sillage du regain d'intérêt expérimental pour la physique de l'antiproton et des recherches associées, il est apparu nécessaire de disposer d'outils de modélisation robustes pour simuler les interactions antiproton-noyau dans un large spectre d'énergie. Ce travail vise à étendre le modèle INCL++ (Intra-Nuclear Cascade Liège) existant en incluant les antiprotons comme projectiles possibles et d'intégrer ce modèle dans le code de transport de particules GEANT4. Les antiprotons, en tant que sondes d'investigation, offrent un large éventail de possibilités pour des expériences de haute précision en physique nucléaire. Ils permettent de générer des antibaryons exotiques et facilitent l'étude de leur interaction ultérieure avec la matière nucléaire et les enveloppes électroniques. L'un des avantages de l'utilisation des antiprotons est la possibilité d'étudier les distributions densité nucléaire grâce à des annihilations "au repos" avec divers noyaux.

Ce travail est basé sur de nombreuses données compilées à partir d'expériences antérieures sur les antiprotons menées au CERN, au Fermilab et au KEK. Ces ensembles de données historiques servent à la fois de source pour l'extraction des paramètres d'entrée du modèle et de référence pour la validation de nos résultats. Ce faisant, cette thèse répond à la demande croissante d'outils de simulation précis, essentiels pour la nouvelle ère de mesures de précision en physique nucléaire et en physique des particules.

Le premier chapitre est introductif et donne un aperçu des progrès scientifiques dans le domaine des antiprotons. Le deuxième chapitre présente un bref historique et une description du modèle INCL avec ses hypothèses de base et le déroulement de la méthode. Le troisième chapitre est une compilation des données existantes issues de recherches antérieures. Enfin, les quatrième et cinquième chapitres examinent les scénarios d'annihilation "au repos" et "en vol" tout en comparant les résultats de notre modèle avec les codes existants et les données expérimentales.

Acknowledgments

Writing this thesis was not at all an easy journey for me, and I am utterly thankful to all the people who helped me along my way, whether this help was related to scientific or technical nuances or to administrative and moral support, which is also extremely important. It might be challenging to mention everyone to whom it may concern, but I will try to do so here.

First of all, I want to thank my supervisor, Jean-Christophe David, whose advice, understanding, wisdom, and patience have been invaluable throughout this journey. Another reason for my gratitude is the fact that my thesis topic was so well-defined and realistic in terms of what I had to accomplish. I am saying this because I know PhD students who have suffered from an ill-defined topic imposed by a supervisor. In my case, the topic was excellent from both fundamental and technical points of view, and I truly believe this work will be a useful contribution to the scientific community, this credence played a role in keeping me motivated throughout my PhD studies. As a physicist, I don't really believe in luck, but still intuitively consider myself a lucky person, and having such a great supervisor is another gift of fortune. His guidance has been instrumental in shaping my research and refining my ideas and I am truly grateful for his dedication and expertise, which have undoubtedly enriched my academic experience.

I am profoundly grateful to my thesis reviewers, Alexandre Obertelli and Josef Pochodzalla for their insightful comments, valuable suggestions, and rigorous examination of my work. I would also like to thank the jury members, Béatrice Ramstein, Alberto Ribon and Davide Mancusi for agreeing to be on the jury and for their comments and thoughtful questions during my defense.

There are also several individuals who have devoted their precious time to me and my questions: Alain Letouneau, Anna Ershova, Eric Dumonteil, Jason Hirtz, Jaume Carbonell, Joseph Cugnon, Pierre Herran, Slawomir Wycech, Sylvie Leray, Thomas Materna, and Valerie Lapoux. I explicitly appreciate having had the opportunity to know these people. It is hard for me to assign preference to any of them, so I have intentionally ordered their names alphabetically.

Finally, I would like to extend my gratitude to all whose names may not be mentioned but who have played a big or small role in completing this thesis. Your contributions, whether through discussions, feedback, or support in various forms, have been invaluable, and I am sincerely thankful. Your unwavering support, encouragement, and belief in my abilities have been pivotal in my academic growth and the successful completion of this milestone. Thank you all for being an integral part of this journey and for the memories, some of which I have accurately written in my secret diary to remind myself of these good years when I will get old and forgetful. Thank you!

Résumé étendu

De nos jours, les physiciens nucléaires et les physiciens des particules s'appuient fortement sur des simulations afin de tester les prédictions théoriques et de rechercher des anomalies expérimentales. Des outils de simulation de particules tels que Geant4 sont utilisés pour modéliser la réponse des détecteurs de particules à diverses particules dont l'énergie cinétique varie de quelques keV à plusieurs TeV. Les mécanismes d'interaction des diverses particules avec les enveloppes atomiques et la matière nucléaire sont radicalement différents et dépendent de l'énergie et du type de la particule. Pour certaines particules, comme par exemple l'antiproton, il y avait un manque d'instruments de simulation pour modéliser l'interaction antiproton-noyau aux énergies incidentes faibles et moyennes (jusqu'au GeV). La cascade intra-nucléaire est une approche de modélisation phénoménologique de l'interaction particule-noyau qui a démontré son applicabilité pour la gamme d'énergie susmentionnée, où les modèles de cordes de quarks et de gluons (QGS) ne sont pas encore adaptés. Dans cette thèse, le modèle *Intra-Nuclear Cascade of Liège* (INCL) est utilisé afin d'inclure le projectile antiproton comme une option qui devrait permettre aux physiciens de modéliser les interactions antiproton avec la matière nucléaire de manière plus précise. La nécessité d'un outil de modélisation de l'interaction antiproton-noyau est due au récent regain d'intérêt expérimental pour l'antiproton en tant que sonde dans les expériences de haute précision en physique nucléaire. Les antiprotons permettent de produire des antibaryons exotiques et facilitent l'étude de leur interaction ultérieure avec la matière nucléaire et les enveloppes atomiques. En outre, ils permettent de mieux comprendre la structure et les propriétés des noyaux instables et de la périphérie nucléaire.

La particularité de l'interaction antiproton-noyau est qu'à faible énergie, elle peut passer par le mécanisme de capture par l'enveloppe atomique, lorsque l'antiproton se comporte comme un électron lourd capturé sur l'orbite d'un atome. C'est la raison exacte pour laquelle l'antiproton peut être sensible à la périphérie nucléaire - l'antiproton à faible énergie fusionne avec le noyau en descendant des orbitales à nombre quantique principal élevé de sa couche électronique au lieu d'une collision directe particule-noyau. Dans ce cas, il descend en cascade vers des orbites plus basses en raison de sa masse élevée et finit par s'annihiler à la périphérie du noyau, ce qui est différent de l'interaction en vol à des énergies plus élevées. L'existence d'un tel scénario rend la mise en œuvre de l'antiproton beaucoup plus compliquée, c'est pourquoi cette thèse comporte deux chapitres distincts qui examinent à la fois les scénarios au repos (capture) et en vol. L'interaction entre les deux scénarios est également prise en compte en raison de la gamme d'énergie intermédiaire où les deux scénarios sont possibles.

Après une brève introduction, le chapitre 2 de cette thèse est consacré à la description du rôle actuel de l'antiproton en physique des particules et en physique nucléaire, ainsi qu'à son potentiel pour la recherche fondamentale et la technologie appliquée. Le modèle INCL étant phénoménologique, il a besoin d'informations d'entrée telles que les sections efficaces exclusives pour fonctionner. Le chapitre 3 décrit la quintessence des expériences passées sur les antiprotons, à la recherche de données précieuses sur lesquelles notre modèle phénoménologique sera basé et dont les résultats seront vérifiés par la suite. Une description d'INCL est donnée dans le chapitre 4, avec l'accent mis sur les initialisations de la particule incidente et du noyau, les caractéristiques générales de la cascade et, enfin, un mot sur la désexcitation finale du noyau résiduel issu de la cascade. Les chapitres 5 et 6 sont consacrés à l'implantation dans le code de l'antiproton au repos et en vol et fournissent une évaluation des résultats de l'interaction antiproton-noyau dans la nouvelle version de l'INCL par rapport aux données expérimentales. La conclusion et les perspectives forment le dernier chapitre.

Contents

1 Introduction

In 1931 [Dir31], British physicist Paul Dirac proposed an equation that combined quantum mechanics and special relativity. This equation, known as the Dirac equation, suggested that every particle has an antiparticle - a counterpart with the same mass but opposite charge. This was a novel concept at the time and was met with considerable skepticism.

Two years later, in 1933 [And33], American physicist Carl Anderson did a publication studying cosmic rays using a cloud chamber. He noticed a particle that behaved like an electron but curved in the opposite direction in a magnetic field, indicating it had a positive charge. After eliminating other possibilities, Anderson concluded that this particle was the positron, the antiparticle of the electron, providing experimental evidence for Dirac's prediction.

Detecting an antiproton through cosmic rays, however, was a more daunting task than discovering the positron due to its higher stopping power and lower abundance. According to a brilliant historical investigation of Kevin Orrman Rossiter [Orr21]: *there was a contest between the serendipitous observations of cosmic-ray events and the deliberate observation possible with the new accelerator-based experiments.* Observation of cosmic-ray events using ground-and balloon-based cloud-chambers and emulsion stacks have resulted in at most three tenuous sightings of annihilation events that could be associated with the annihilation of any antiproton. One such claim was based around the cloud chamber image (Fig. 1.1), it was made by Herbert S. Bridge and colleagues from the Massachusetts Institute of Technology in 1954 [Bri+54]. Still, that was not yet clear for the community as in the case of positron, meanwhile a new accelerator called Bevatron (Billions of eV Synchrotron) has begun its operation.

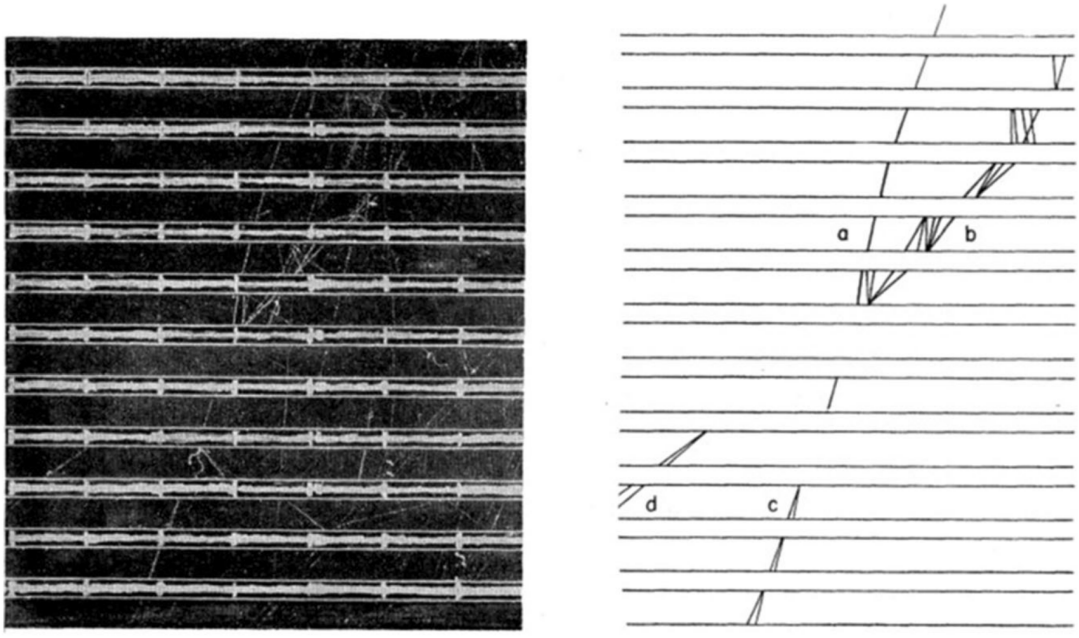

(a) Original photograph of the chamber **(b)** Sketch of the event

Figure 1.1: Photograph and schematic diagram of the annihilation of a heavy charged particle in a multiplate cloud chamber, line marked with "a" is the incident particle. Taken from.[Orr21]

Discovering the antiproton was not a major focus of the particle physics community, even for the group at Berkeley. Even as late as December 1954, there was so little interest in the antiproton that

at the American Physical Society (APS) meeting in Berkeley no one presented a paper speculating on its discovery, in fact the hot subjects at the time were the strange particles. The concept of the antiproton was an artifact of prewar, 1930s nuclear physics - the neutron, positron, and muon were all discovered, and the neutrino and antiproton predicted, in the 1930s, the pion and strange particles were observed in the late 1940s. The antiproton was not part of the contemporary excitement in new strange particles. It was, however, almost a imperative necessity to demonstrate its existence. In retrospect, the discovery of the antiproton may seem almost inevitable, given the beam energy of the Bevatron; nevertheless, considering the current state of the art equipment and knowledge, it was not at all straightforward.

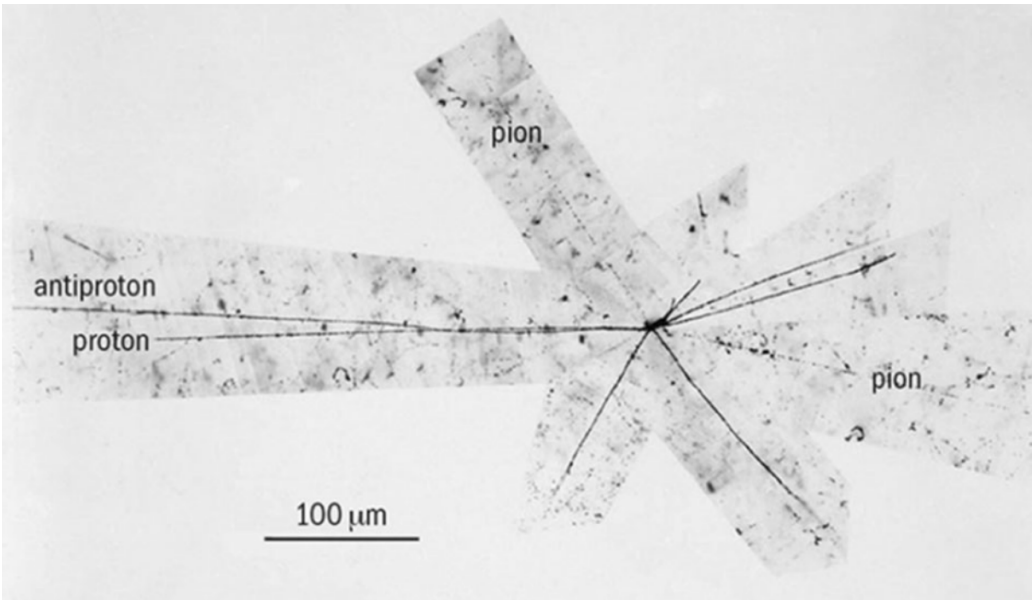

Figure 1.2: One of the first annihilations of an antiproton observed at the Bevatron with a photographic emulsion. The antiproton enters from the left. The fat tracks are from slow protons or nuclear fragments, the faint tracks from fast pions.[Orr21]

One of the main difficulties of the experiment was to select the few antiprotons from a "huge" pion (π-) background. The simple time-of-flight method was not enough due to the copious pions which could have faked the antiproton by passing with a right delay. This is where the ingenuity of Owen Chamberlain and Emilio Segrè was really useful, as they came up with an idea of simultaneous measurement of the momentum and velocity of antiprotons with their certain distinction from other particles. for this they have built a sophisticated Cherenkov detector consisting principally of a guard counter and a velocity-selective counter working in anti-coincidence. Since the momentum is accurately known from the magnet arrangement, and since each time measurement determines the velocity of the particle in question, rough mass measurement became possible. By October 1955 Chamberlain's team were able to clearly demonstrate that there were negative particles of protonic mass and there was a threshold to produce these particles at about 4 GeV of incident beam kinetic energy, so the next step was to observe the annihilation according to the predictions, which was accomplished later by the Chamberlain group using good old emulsions in order to "see" the annihilation with their own eyes(Fig. 1.2). The antineutron was discovered in proton–antiproton collisions at the Bevatron by the team of Bruce Cork, Glen Lambertson, Oreste Piccioni, and William Wenzel in 1956[Cor+56], one year after the antiproton.

Since that time, the mere existence of antimatter has set countless minds ablaze. The fervent frenzy surrounding this enigmatic substance stems from a couple of paramount factors that captivate the imagination:

1. It is stable.
2. It is the densiest form of energy.
3. (as long as you have some matter nearby).

Antimatter received repeated mentions in sci-fi culture, here are just some most iconic of them.

- *Star Trek* (1966-present): One of the most popular uses of antimatter in science fiction is in the *Star Trek* franchise, where it's used as a power source for starships' warp drives. Antimatter and matter are combined in a controlled reaction to generate the immense energy necessary for faster-than-light travel.
- *Tau Zero* (1970): This hard science fiction novel by Poul Anderson uses a Bussard ramjet, a theoretical method of spacecraft propulsion, which uses a magnetic field to collect interstellar hydrogen, which is then collided with onboard antihydrogen to produce thrust.
- *Angels & Demons* (2000): This novel by Dan Brown, later adapted into a film, features a canister of antimatter as a central plot device. It's used as a potential bomb that could devastate Vatican City.
- *Cosmonaut Keep* (2000): In this novel by Ken MacLeod, part of the Engines of Light series, one of the main characters is an antimatter-based artificial intelligence.
- *Anathem* (2008): In this novel by Neal Stephenson, antimatter is used in weaponry, capable of causing immense destruction.

Science fiction literature, with its imaginative narratives and futuristic extrapolations, stands as a profound testament to its capacity to illuminate the uncharted realms of tomorrow. Nowadays we may only encounter antimatter in the cosmic void or costly and huge human build facilities, and can hardly accumulate a bunch of antihydrogen atoms, but if the human civilization will choose to proceed along the Kardashev scale (see Fig. 1.3) this might change. One of the famous futurologists Dr. Michio Kaku, whose books have actually done the job of convincing myself into doing physics, believes that humans need to increase their energy consumption by 3% per year, thereby reaching type I in 100-200 years[Kak07]. At the type I level our civilization would have four times more energy than now (now we have about 4×10^{12} watts) and the antiparticles might be already adopted as a common instrument in some hospitals and laboratories. At type II humanity might adopt antimatter as a way to store energy and accelerate spaceships. Perhaps we should stop here as my mind struggles to speculate about the type III level and beyond, as we will be already heating our food not with microwaves, but rather with antiprotons just because it tastes better.

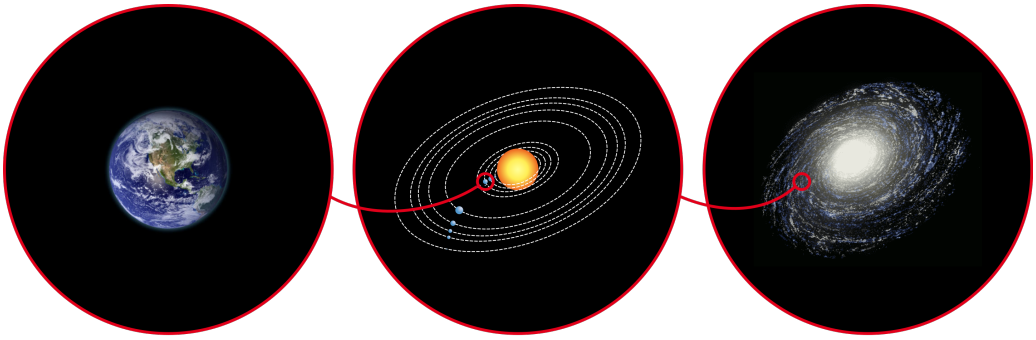

Figure 1.3: Energy consumption in three types of civilization as defined by Carl Sagan's extended Kardashev scale[Sag80]. Type I consumption corresponds to the total amount of power our planet gets from the Sun, type II to the power of the whole Sun, type III to the power of the galaxy.

Prior to considering the implementation of antiprotons in our kitchens and cars, it is essential to have a better understanding of them, particularly their interactions with nuclear matter. This is the focus of my PhD work. In particular, my mission is to assemble a tool which would allow to simulate the repercussions of antiproton-nucleus collisions. Building such tool from zero would be an uphill battle, but fortunately the INCL++: Intra-Nuclear Cascade Liege model already existed at the time and was taken as the starting point to develop. INCL at the beginning was already able to simulate particle-nucleus interactions for a broad range of targets and projectiles and was accessible via GEANT4 physics lists. Now it is possible to claim that INCL includes antiproton as projectile as well and thus GEANT4 simulation framework is now able to simulate the physics of antiprotons.

The general context of the topic will be given in the next chapter. It aims to shed some light on the actual situation in antiproton physics with its current and potential applications and existing simulation methods. Chapter 3 is devoted to INCL model, its main physics ingredients and assumptions used in this model. In chapter 4 I will summarize the existing experiments with antiprotons and all the experimental data we used as inputs for our phenomenological model together with the data used for model validation. Chapters 5 and 6 describe the two different antiproton interaction scenarios at rest and in-flight which apparently exist at low and high incident energy respectively.

References

[And33] Carl D. Anderson. "The Positive Electron". In: *Phys. Rev.* 43 (6 Mar. 1933), pp. 491–494. doi: 10.1103/PhysRev.43.491.

[Bri+54] H. S. Bridge et al. "Possible Example of the Annihilation of a Heavy Particle". In: *Phys. Rev.* 95 (4 Aug. 1954), pp. 1101–1103. doi: 10.1103/PhysRev.95.1101.

[Cor+56] Bruce Cork et al. "Antineutrons Produced from Antiprotons in Charge-Exchange Collisions". In: *Phys. Rev.* 104 (4 Nov. 1956), pp. 1193–1197. doi: 10.1103/PhysRev.104.1193.

[Dir31] Paul Adrien Maurice Dirac. "Quantised Singularities in the Electromagnetic Field". In: *Proceedings of the Royal Society of London A* 133 (1931), pp. 60–72. doi: 10.1098/rspa.1931.0130.

[Kak07] Michio Kaku. *The Physics of Extraterrestrial Civilizations*. Official Website of Dr Michio Kaku, 2007.

[Orr21] Kevin Orrman-Rossiter. "Observation and Annihilation: The Discovery of the Antiproton". In: *Physics in Perspective* 23.1 (Mar. 2021), pp. 3–24. issn: 1422-6960. doi: 10.1007/s00016-021-00271-7.

[Sag80] Carl Sagan. *Cosmos*. English. First. New York: Random House, 1980, pp. xvi, 365. isbn: 978-0-345-53943-4.

2 | Basic Concepts and applications

Such a general chapter is always necessary before the onset of countless plots and figures to inspire some interest both in the author and the reader. There was a lot of effort invested in studying the properties of antiproton and its interaction with matter in the past, which serves us today as a valuable source of information for our phenomenological model, so the summary of the past research will be offset to a separate chapter 4 (page 39). This one however is devoted to motivation, as the model we build could be already used to verify our current understanding of the underlying physics and nowadays almost any experiment requires a thorough simulation prior to budget allocation. Hereafter we will discuss some of the ongoing and oncoming human activity related to antiproton, while mentioning modern antiproton sources, experiments and the potential of this particle to be applied in scientific research and other areas.

2.1 Experimental state-of-the-art

This part contains an overview of antiproton factories and experiments. Most antiproton facilities have been shut down, but the one at CERN is still operating and have received upgrades for efficient antiproton deceleration after production and provides a place for multiple experiments. Currently, the low energy antiproton research is of higher popularity, which may be understood as antiprotons has unique properties in its interaction with matter at low energies (see section 2.2). Fortunately, another facility is under construction at GSI, which will allow experiments with high energy antiprotons beam.

2.1.1 Antiproton sources

As it was mentioned in the introduction, antiprotons exist in nature and can be found in cosmic rays. The spectra of various galactic cosmic ray particles is depicted in Fig 2.1. The main contribution of antiprotons is a result of high-energy particle collisions with subsequent production of a nucleon-antinucleon pair (e.g. $N+N- > N+N+N+\bar{N}$). This process is also used in laboratories to generate antiproton beams using accelerators like it was done in Bevatron. The modern sources apply the same principles and the difference is essentially in higher flux, higher energies and lower beam emittances, thanks to the multiple advancements in accelerator and storage ring technology. Hereafter we will only discuss the currently operating source which is at CERN, past experiments had similar principle of antiproton generation, while future experiments would be considered in chapters 5 (page 89) and 6.

2.1.1.1 CERN AD

CERN has a rich history of dealing with antiproton beams, in particular CERN Low Energy Antiproton Ring (LEAR) was the world's first source of low energy antiprotons whose infrastructure was adopted and upgraded for Antiproton Decelerator (AD) storage ring (Fig. 2.2). Antiprotons are created by impinging a proton beam from the Proton Synchrotron on the iridium target. 10^{13} protons of 26 GeV/c collide with iridium nuclei to produce $0.5 \cdot 10^7$ antiprotons of 3.5 GeV/c. A magnetic bi-conical aluminum horn-type lens collects the antiprotons emerging from the target. Then the antiprotons are separated from protons with a magnetic bi-conical aluminum horn-type lens and injected into the AD. AD's oval-shaped perimeter has four straight sections where the deceleration and cooling systems are placed. There are several dipole and quadrupole magnets in these sections to avoid

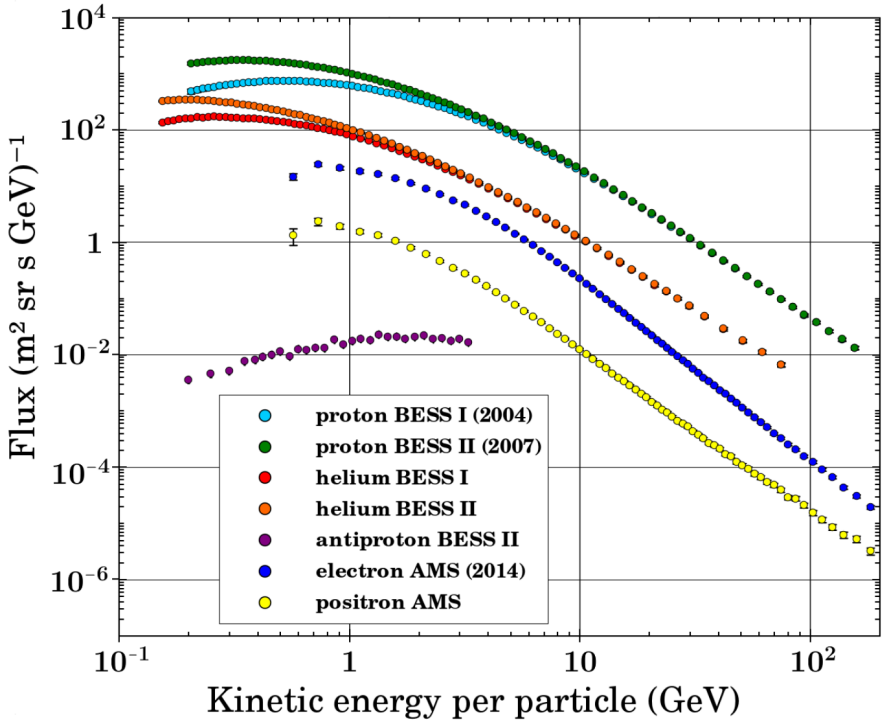

Figure 2.1: Galactic cosmic ray spectra taken from [Hir19]. Data for protons, alphas, antiprotons were measured by the the BESS-Polar collaboration [Abe+16; Abe+12] and data for electrons and positrons were measured by the the AMS collaboration [Agu+14].

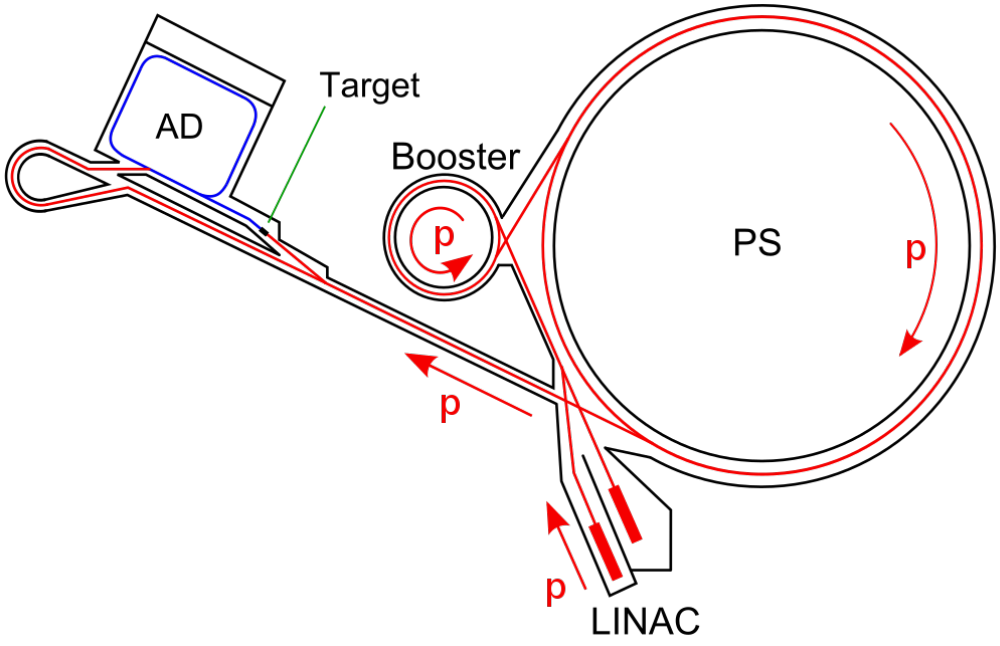

Figure 2.2: Antiproton Decelerator, antiproton track is in blue.

beam dispersion. Stochastic cooling and electron cooling stages are used inside the AD to decrease the energy of beams and limit the antiproton beam from any significant distortions. Stochastic cooling is applied for antiprotons at 3.5 GeV/c and then at 2 GeV/c, followed by electron cooling at 0.3 GeV/c and at 0.1 GeV/c. The final output beam has a momentum of 0.1 GeV/c (kinetic energy of 5.3 MeV).

At 5.3 MeV antiprotons still have velocity about 10% of the speed of light, while many experiments require lower energies. For that the series of degrader foils is used to decelerate the beam down to 3-5 keV before feeding them to various experiments. This degradation results in a loss of about 99.9% of the precious antiprotons. In order to reduce the losses, an additional deceleration stage was constructed: ELENA.

2.1.1.2 CERN ELENA

Extra Low ENergy Antiproton ring (ELENA) is a 30 m hexagonal storage ring designed to further decelerate the antiproton beam coming from the AD to an energy of 100 keV. The ELENA ring with its efficient beam cooling and deceleration method is meant to increase the effective number of antiprotons that could be made available to the antimatter experiments by substituting a part of degrader foils with RF-cavities and electron cooling. In addition to the increased number of antiprotons, ELENA is able to deliver beams almost simultaneously to all four experiments resulting in an essential gain in total beam time for each experiment.

2.1.1.3 FAIR

Facility for Antiproton and Ion Research (FAIR) will be based upon an expansion of the GSI Helmholtz Centre for Heavy Ion Research. A proton beam will be provided by the existing GSI facility and will be further accelerated by FAIR's SIS100 ring accelerator up to 30 GeV. By the beam hitting the antiproton production target, antiprotons with a momentum of around 3 GeV/c will be produced and can be collected and pre-cooled in the Collector Ring. Afterwards the antiprotons will be injected into the High Energy Storage Ring. This race track shaped storage ring will host the $\bar{p}ANDA$ experiment - the one to carry out research with antiprotons. The antiprotons can be cooled using stochastic and later also electron cooling and afterwards slowed down or further accelerated to momenta from p = 1.5 GeV/c up to p = 15 GeV/c[Gia15].

2.1.2 Ongoing experiments at CERN AD

In this section we will briefly mention the experiments currently running at the CERN AD facility. Past experiments and the data recorded will be summarized in Chapter 4 (page 39), as this data would serve both to obtain necessary input ingredients for our model and to validate the model by comparing its output with the experimental results. The planned experiments and those in preparation would be addressed in Chapters 5 (page 49) and 6 (page 95) for low- and high-energy beams correspondingly. This organisation follows from the context of INCL potential application to model some of these experiments.

2.1.2.1 AEgIS

The Antimatter Experiment: Gravity, Interferometry, Spectroscopy (AEgIS) experiment is designed with the primary objective of testing the weak equivalence principle for antimatter. By propelling an antihydrogen beam through a Moiré deflectometer, it aims to measure the gravitational interaction between matter and antimatter with high precision. The test uses a gratings-based interferometry approach which uniquely distinguishes it from other antimatter experiments. This comprehensive examination seeks to provide insights into one of the fundamental questions in modern physics: does antimatter fall upwards or downwards in a gravitational field?

2.1.2.2 ALPHA

Antihydrogen Laser Physics Apparatus (ALPHA), the ALPHA experiment focuses on the study and analysis of the properties of antihydrogen. Its ultimate goal is to conduct a precise comparison of hydrogen and antihydrogen, testing the fundamental symmetries between matter and antimatter. In a

landmark achievement, the ALPHA experiment successfully trapped and measured the spectral characteristics of antihydrogen atoms, thereby paving the way for high-precision tests of antimatter in the future. These tests could potentially provide invaluable insights into the asymmetry between matter and antimatter in the universe.

2.1.2.3 ATRAP

The Antihydrogen Trap (ATRAP) experiment seeks to delve into the fundamental mysteries of the universe through the precise comparison of hydrogen and its antimatter counterpart, antihydrogen. Utilizing state-of-the-art techniques for trapping and cooling antiprotons and positrons, the team is able to form antihydrogen atoms and study their properties. ATRAP has been instrumental in determining the charge neutrality of antihydrogen and has also conducted the first ever measurement of the antiproton's magnetic moment. By providing comprehensive data on the properties of antimatter, the ATRAP experiment contributes significantly to our understanding of the physical universe.

2.1.2.4 BASE

The Baryon Antibaryon Symmetry Experiment (BASE) experiment is designed to scrutinize the fundamental symmetries between baryons and antibaryons by comparing the properties of protons and antiprotons with unprecedented precision. It employs an advanced Penning trap system to make highly precise measurements of the antiproton's magnetic moment and charge-to-mass ratio. The results from the BASE experiment have set new benchmarks for precision in the field, contributing significantly to our understanding of antimatter and providing vital tests of the fundamental principles of the Standard Model of particle physics.

2.1.2.5 GBAR

Gravitational Behaviour of Antimatter at Rest (GBAR) experiment [CER] first combines the antiprotons with two antielectrons to form antihydrogen ions with a positive charge. Although more difficult to produce than the simpler antiatoms, the antimatter ions can be more easily manipulated. Using laser-cooling techniques, these ions are brought to microkelvin temperatures before they are stripped of the additional antielectron, transforming them into antihydrogen atoms. These antihydrogen atoms are then allowed to fall from a height of 20 centimetres, and their annihilation at the end of the fall is recorded.

By measuring the acceleration of antihydrogen under gravity and comparing it with the acceleration of regular hydrogen, we can look for differences in the behaviour of matter and antimatter. In particular, the scientists are testing the Equivalence Principle put forth by Albert Einstein, which states that the trajectory of a particle is independent of its composition and internal structure when it is only submitted to gravitational forces. Observing a difference in the way hydrogen and antihydrogen fall under gravity would demonstrate that this principle is in fact wrong.

2.2 Antiproton as a probe in nuclear research

Almost all kind of particles have been historically used to study nuclear structure and forces. Electron beam can provide us the charge density distribution of a nucleus, for example, while photons may be used to study its excitation modes and nucleon separation energies. Hadronic beams of high energies were also applied as probes to study nuclear reactions which involve strong nuclear forces. Although studying spatial structure of a nucleus with such beams is not straightforward, as their selectivity towards any specific part of a nucleus reduces with increasing incident energy, while higher energies are required to penetrate the Coulomb barrier. Antiprotons on the other hand, when interact at low energy, are able to sense the outer region of a nucleus, which makes them a unique instrument for discovering the nuclear structural properties (e.g. PUMA experiment, which is described later in this chapter).

It is worth to describe some peculiarities of antiproton-nucleus interaction at low energy, as this process is particularly sensitive to the nuclear surface. Antiprotonic atoms formed after low energy (eV to keV range) $\bar{p}$ is captured into atomic state instead of an electron, which is emitted. The capture

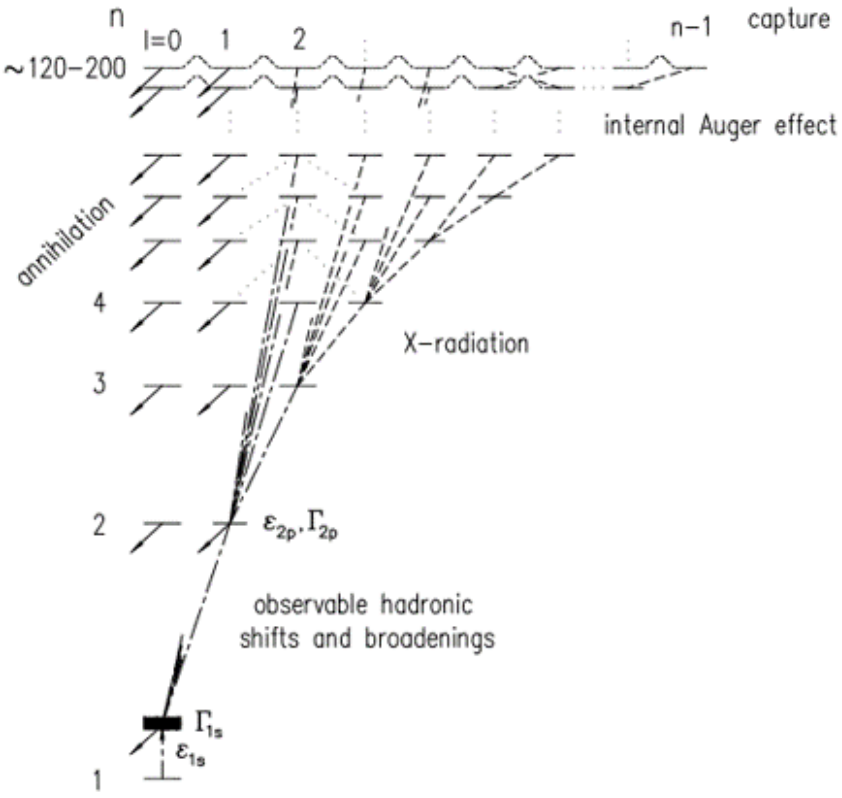

Figure 2.3: De-excitation cascade in antiprotonic atom.

process is governed by atomic and molecular properties of the target media and is not well understood in detail. However, in naive picture it is assumed that the $\bar{p}$ is captured into an orbit whose radius is close to that of the electronic 1s state. This corresponds to an initial state with the principal quantum number i[Pot84]:

$$x_p^i = \sqrt{\frac{m_{\bar{p}}}{m_e}} n_e^{1s} \approx 43. \tag{2.1}$$

The angular momentum sublevels are populated with an exponential distribution similar to that of the Rydberg atoms. From the Rydberg state the $\bar{p}$ cascades down to lower levels dissipating energy in form of Auger electrons at higher levels and gamma-ray emission at the latest transitions (see Fig.2.3). The probabilities of these transitions are:

$$W_{gamma} = \frac{4\alpha}{3\hbar} \frac{(\Delta E)^3}{(\hbar c)^2} |\langle \psi_f | r | \psi_i \rangle|^2, \tag{2.2}$$

$$W_{Auger} = \frac{2\pi}{\hbar} |\langle \psi_f \phi_f | \frac{1}{r} | \psi_i \phi_i \rangle|^2, \tag{2.3}$$

to give the total width: $\Gamma_{tot} = \Gamma_{Auger} + \Gamma_{gamma} + \Gamma_{strong}$, where the strong interaction component needs to be determined experimentally, while the Auger and gamma-ray transitions may be calculated to a desired accuracy.

Γ_{strong} increases rapidly at latest transitions up to a point, when antiproton is absorbed by the nucleus. Studying the widths and shifts of the latest gamma-ray transitions in the $\bar{p}$ cascade has been used to infer nuclear structure information[Pot84; Sch+98; Har+99; Har+01].

Another approach is to study the annihilation by analysing yields of residual nuclei which are determined with residual nuclei gamma-ray spectroscopy and subsequent radiochemical methods after exposure[Lub+98; Wyc+96; Har+01; Trz+01] and the direct detection of particles produced with annihilation[Bug+73; WL76; WP23]. Nuclear residues will be considered more in detail in chapter 5 (page 49).

Furthermore, it is possible to study superficial properties of nuclei not only via at rest $\bar{p}$ annihilations, but also at higher energy, which is just above the threshold of certain production channels.

One of the recently developed methods[Chr+22] proposes to measure the difference of neutron skin thickness of two isotopes of the same element by exploring the relative probabilities of $\Lambda\bar{\Lambda}$ and $\Sigma^-\bar{\Lambda}$ hyperon-antihyperon pair production (see Fig.2.4).

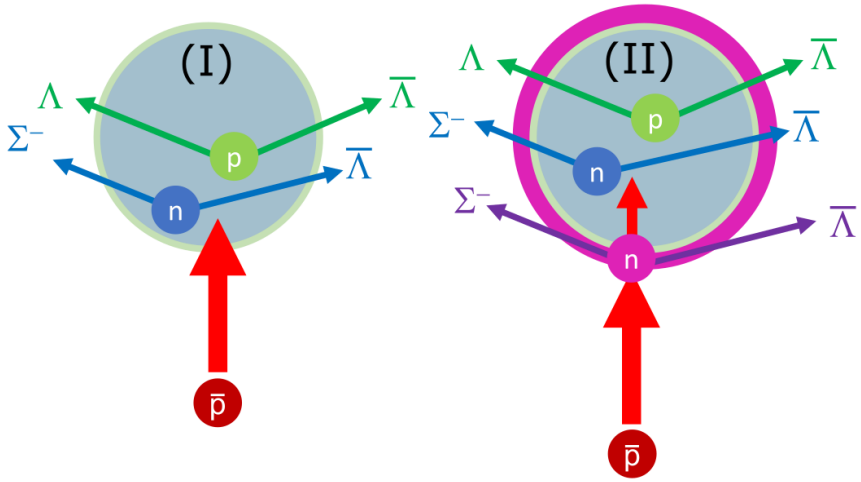

Figure 2.4: $\Lambda\bar{\Lambda}$ and $\Sigma^-\bar{\Lambda}$ pair production in antiproton–nucleus interactions, I and II denote two isotopes, where the heavier one (II) has additional neutron thickness. Taken from [Chr+22].

2.3 Cosmological concern

Hereafter, the relation of antiprotons to the problem of dark matter is discussed. Dark matter is believed to account for approximately 84% of the matter in the universe, but it has not yet been directly detected and its exact nature remains unknown. Present observations indicate that dark matter is inconsistent with any standard model particle, and only interacts with standard model particles very weakly. Determining the fundamental properties of dark matter remains a major goal in physics and astronomy.

Many hypothetical dark matter particles can annihilate or decay into Standard Model particles. Dark matter may then be observed indirectly through the detection of these particles, in excess of their conventional backgrounds. Cosmic-ray antimatter provides one of the cleanest channels of indirect dark matter detection since their natural astrophysical fluxes are low in comparison to other cosmic ray components.

Antibaryons are produced via secondary interactions of high-energy cosmic ray components, which in turn are produced and accelerated via several astrophysical phenomena. One of high-energy particle sources is the Fermi acceleration in supernova shockwaves, while the other is the active galactic nuclei (AGNs) black holes. These primary high-energy particles interact with the interstellar matter and produce secondary components, including anti-particles such as the antiproton, and most cross-sections of such reactions are well-known, thus the amount of antiparticles must correspond to the amount of the primary cosmic rays. New sources like dark matter are supposed to produce particles and antiparticles in equal amount, which would modify the antiproton flux, and antiproton-to-proton flux ratio.

Another interesting possibility is to measure the antideuteron flux. Unlike antiprotons, which can be produced in abundance by cosmic rays interacting with interstellar gas, antideuterons are expected to be much rarer in the cosmic ray spectrum. This is because producing an antideuteron requires not only the production of an antiproton and antineutron, but also their binding together, which requires specific energy conditions.

However, some theories predict that collisions or annihilations of dark matter particles could produce antideuterons. Given the rarity of other sources of antideuterons, these particles could serve as a relatively clear signal of dark matter, with less "background noise" to interfere with the detection. In particular, the General AntiParticle Spectrometer (GAPS) aims to study dark matter through sensitive observations of cosmic-ray antiprotons, antideuterons, and antihelium.

2.4 Related technology

As a stable particle, antiproton allows its accumulation and manipulation more than any other exotic particle. This possibility lead to several applications, which can be seen in Fig. 2.5. There was even a commercial attempts to apply antiprotons by the company called Hbar Technologies, LLC[Jac02]. While they have never conducted any operations it would be nice to mention such an enterprise as a trace of past optimism in the field. Apparently, all of the most realistic commercial applications are in the field of medicine[Bit+14], but at the moment $\bar{p}$ have only been used in research.

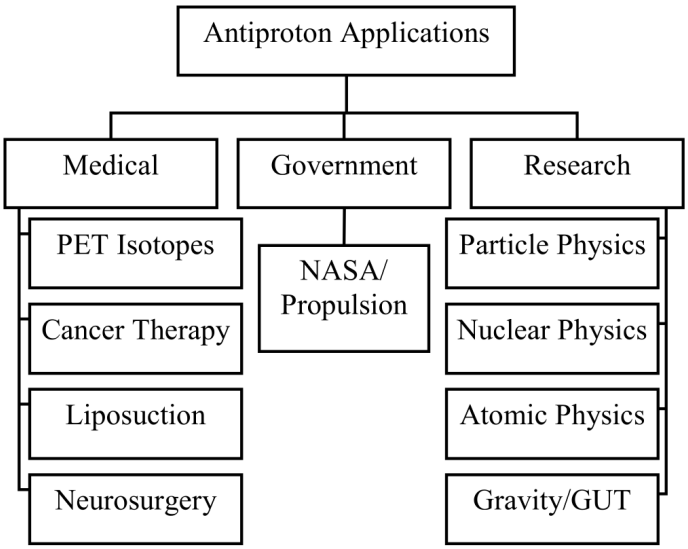

Figure 2.5: Diagram of the various categories of antiproton applications. The strongest commercial possibilities are in the field of medicine [Jac02].

2.4.1 Proton-Antiproton colliders

Antiprotons have played their instrumental role in high-energy hadron colliders. Early collider configurations had two separate storage rings for contra rotating proton beams, these rings were intersecting in several locations (Fig. 2.6). As the storage rings were increasing in size and cost, it was decided for subsequent hadron collider projects to switch to proton-antiproton configuration like Tevatron and Super Proton–Antiproton Synchrotron (SPS). Such configuration allowed the use of same set of dipole magnets (and their cryogenic subsystems) for both contra-rotationaly traveling beams and thus significantly reduce the cost. Later, with the invention of LHC double dipole magnet physicists would continue the high-energy conquest with proton-proton colliders. For the moment of writing there is currently only one operating facility (CERN) which is still providing antiproton beam for experiments.

2.4.2 Cancer therapy

Antiprotons have been considered for cancer therapy first in the 1980's. This is based on the fact that antiprotons will penetrate a target similar to protons, but will at the end of their range annihilate. In this annihilation process twice the mass energy of a proton will be released. Much of this energy will leave the target in the form of minimum ionizing particles (ions and high energy photons) but a small, but clinically significant, portion of the energy will be deposited locally through short range secondaries and recoil ions. The Antiproton Cell Experiment (ACE) was a research project conducted at CERN and showed that for an identical energy deposition at the skin level the energy deposited in the Bragg peak of antiprotons is twice the value obtained for protons (see Fig.2.7). But in addition to this doubling effect it is expected that the additional energy deposited locally by the annihilation event will exhibit a higher biological efficiency – essentially it is as if there is a microscopic heavy ion accelerator being implanted in the tumour cell [SWH11; Cyb+11].

Figure 2.6: Intersecting Storage Rings (ISR) at CERN. The world's first hadron collider. source: https://cds.cern.ch/record/2379471.

2.4.3 Driver for inertial confinement fusion

Antiprotons have been proposed as the ignition energy source for inertial confinement fusion (ICF) for energy and space propulsion applications[POT04]. In contrast to the large mass, complexity and recirculating power of conventional drivers for ICF, antiproton annihilation offers a specific energy of 90 $MJ \cdot \mu g^{-1}$ and thus a unique form of energy packaging and delivery. The energy content of 1 μg of delivered antiprotons (plus an equal mass of normal matter) is equivalent to one hundred full power shots from the National Ignition Facility (NIF), a laser-driven facility presently under construction and designed to achieve ICF ignition and thermonuclear energy gain. Thus, in principle, antiproton drivers could provide a profound mass reduction for advanced space propulsion by ICF. For example, a few moles of onboard, stored antiprotons together with the appropriate antiproton storage, handling and low energy injection system, could comprise the complete driver system for an ICF-powered spacecraft delivering a 100 tonne payload to Mars. Of course, from the viewpoint of $\bar{p}$ production today, this is an enormous amount.

2.4.4 Portable antiproton traps

Many of the experiments mentioned in this chapter are using electromagnetic fields to trap, store and cool antiprotons, but such traps could also be designed to be portable. These devices would also enable some new applications, as it would be possible to carry the antiprotons away from the production facility.

2.4.4.1 NASA HiPAT

The High Performance Antiproton Trap (HiPAT) project was initiated by NASA's Marshall Space Flight Center driven by the necessity for new high energy density propulsion systems to enable future aggressive deep space missions. The matter-antimatter reaction, representing the densest form of energy storage known to modern physics, provides a promising solution. The HiPAT system aimed to maintain 10^{12} particles for up to 18 days, using the antiproton's significant annihilation energy. This

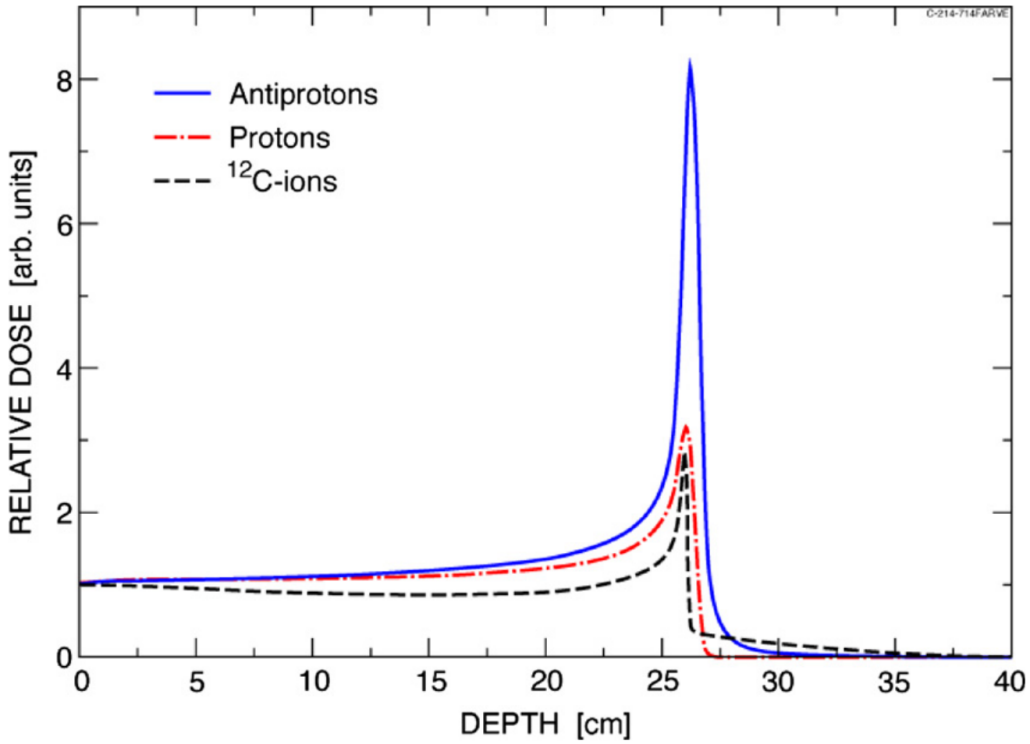

Figure 2.7: The dose deposited by antiprotons, protons and carbon ions, normalized at the surface of the target which is water. SHIELD-HIT calculations [Knu+08].

project not only targeted propulsion systems for space exploration but also had potential commercial applications such as the production of medical radioisotopes and tumor diagnosis and treatment.

HiPAT has been designed around a portable architecture since the production and utilization sites will in most cases not coincide. The trap was built and tested with positive hydrogen ions to evaluate the device's capacity to hold charged particles, with the ions produced either through an electron gun method or an external ion source. Unfortunately, since these tests the project was not developed any further and has never been tested with antiprotons [Mar+02].

2.4.4.2 PUMA

As it was mentioned earlier in this chapter, antiproton serves a good probe to investigate the nuclear structure of matter. It would be of particular interest to study the structure of unstable nuclei, even beyond the dripline of proton/neutron stability region. While these nuclei are unstable, it is possible to accumulate them in a storage ring and use trapped antiprotons as a target [Aum+22]. The experiment employs a portable trap for antiprotons that will be filled with $\bar{p}$ at ELENA and later be transported to the ISOLDE facility, where they will be used to study short-lived radioactive isotopes stored in the ring.

antiProton Unstable Matter Annihilation (PUMA) experiment is expected to begin operation in 2023 with the first $10^9\bar{p}$ accumulation and perform reference measurements on site with stable nuclei. Benchmarks of the antiproton transportation and the half-life of the antiproton plasma would be one of the first aims for measurement. This experiment would be addressed more in detail in the section of Future experiments of chapter 6.

References

[Abe+12] K. Abe et al. "Measurement of the Cosmic-Ray Antiproton Spectrum at Solar Minimum with a Long-Duration Balloon Flight over Antarctica". In: *Phys. Rev. Lett.* 108 (5 Jan. 2012), p. 051102. doi: 10.1103/PhysRevLett.108.051102.

[Abe+16] K. Abe et al. “MEASUREMENTS OF COSMIC-RAY PROTON AND HELIUM SPECTRA FROM THE BESS-POLAR LONG-DURATION BALLOON FLIGHTS OVER ANTARCTICA”. In: *The Astrophysical Journal* 822.2 (May 2016), p. 65. doi: 10.3847/0004-637X/822/2/65.

[Agu+14] M. Aguilar et al. “Electron and Positron Fluxes in Primary Cosmic Rays Measured with the Alpha Magnetic Spectrometer on the International Space Station”. In: *Phys. Rev. Lett.* 113 (12 Sept. 2014), p. 121102. doi: 10.1103/PhysRevLett.113.121102.

[Aum+22] T. Aumann et al. “PUMA, antiProton unstable matter annihilation”. In: *The European Physical Journal A* 58.5 (2022), p. 88. issn: 1434-601X. doi: 10.1140/epja/s10050-022-00713-x.

[Bit+14] Martin-Immanuel Bittner et al. “A systematic review of antiproton radiotherapy”. In: *Frontiers in Physics* 1 (2014). issn: 2296-424X. doi: 10.3389/fphy.2013.00037.

[Bug+73] W. M. Bugg et al. “Evidence for a Neutron Halo in Heavy Nuclei from Antiproton Absorption”. In: *Phys. Rev. Lett.* 31 (7 Aug. 1973), pp. 475–478. doi: 10.1103/PhysRevLett.31.475.

[CER] CERN. *GBAR Experiment*. Accessed: October 11, 2023. url: https://home.cern/science/experiments/gbar.

[Chr+22] Christiansen, Martin et al. “Exploring the neutron skin by hyperon-antihyperon production in antiproton-nucleus interactions”. In: *EPJ Web Conf.* 271 (2022), p. 02011. doi: 10.1051/epjconf/202227102011.

[Cyb+11] T. Cybulski et al. “Development of Imaging Techniques for Medical Accelerators in the QUASAR Group”. In: *Conf. Proc. C* 110328 (2011). Ed. by Todd Satogata and Kevin Brown, pp. 2160–2162.

[Gia15] Boca Gianluigi. “The experiment PANDA: physics with antiprotons at FAIR”. In: *EPJ Web of Conferences* 95 (May 2015). doi: 10.1051/epjconf/20159501001.

[Har+01] F. J. Hartmann et al. “Study of the nuclear periphery with Antiprotons”. In: *Acta Physica Hungarica* 13.1 (Mar. 2001), pp. 51–60. issn: 1588-2675. doi: 10.1556/APH.13.2001.1-3.7.

[Har+99] F.J. Hartmann et al. “Antiprotonic atoms as a tool to study the nuclear periphery”. In: *Nuclear Physics A* 655.1 (1999). Proceedings of the Fifth Biennial Conference on Low-Energy Antiproton Physics, pp. c289–c294. issn: 0375-9474. doi: https://doi.org/10.1016/S0375-9474(99)00215-8.

[Hir19] Jason Hirtz. “Nuclear reaction codes development for the particles and nuclei production in meteoroids and planetary atmospheres”. Inaugural dissertation (https://boris.unibe.ch/147129/1/Hirtz Jason Defence.pdf). Bern, Switzerland: Faculty of Science, 2019.

[Jac02] G. Jackson. “Commercial production and use of antiprotons”. In: *8th European Particle Accelerator Conference (EPAC 2002)*. June 2002, pp. 119–123.

[Knu+08] Helge V. Knudsen et al. “Antiproton therapy”. In: *Nuclear Instruments and Methods in Physics Research Section B: Beam Interactions with Materials and Atoms* 266.3 (2008). Low Energy Positron and Positronium Physics, pp. 530–534. issn: 0168-583X. doi: https://doi.org/10.1016/j.nimb.2007.12.035.

[Lub+98] P. Lubinski et al. “Composition of the nuclear periphery from antiproton absorption”. In: *Phys. Rev. C* 57 (6 June 1998), pp. 2962–2973. doi: 10.1103/PhysRevC.57.2962.

[Mar+02] James Martin et al. “Ion storage tests with the high performance antiproton trap (HiPAT)”. In: *AIP Conference Proceedings* 608.1 (Jan. 2002), pp. 793–800. issn: 0094-243X. doi: 10.1063/1.1449804.

[POT04] L. Perkins, Charles Orth, and Max Tabak. “On the utility of antiprotons as drivers for inertial confinement fusion”. In: *Nuclear Fusion* 44 (Sept. 2004), p. 1097. doi: 10.1088/0029-5515/44/10/004.

[Pot84] H. Poth. “Physics with Antiprotonic Atoms”. In: *Physics at LEAR with Low-Energy Cooled Antiprotons*. Ed. by Ugo Gastaldi and Robert Klapisch. Boston, MA: Springer New York, 1984, pp. 567–588. isbn: 978-1-4684-8727-5. doi: 10.1007/978-1-4684-8727-5_54.

[Sch+98] R. Schmidt et al. “Nucleon density of ^{172}Yb and ^{176}Yb at the nuclear periphery determined with antiprotonic x rays”. In: *Phys. Rev. C* 58 (6 Dec. 1998), pp. 3195–3204. doi: 10.1103/PhysRevC.58.3195.

[SWH11] Stefan Sellner, Carsten P. Welsch, and Michael Holzscheiter. “Real-time imaging of antiprotons stopping in biological targets – Novel uses of solid state detectors”. In: *Radiation Measurements* 46.12 (2011). Proceedings of the 16th Solid State Dosimetry Conference , September 19-24 , Sydney , Australia, pp. 1770–1772. issn: 1350-4487. doi: https://doi.org/10.1016/j.radmeas.2011.05.052.

[Trz+01] Agnieszka Trzcinska et al. “Information on antiprotonic atoms and the nuclear periphery from the PS209 experiment”. In: *Nuclear Physics A* 692 (Mar. 2001), pp. 176c–181c. doi: 10.1016/S0375-9474(01)01176-9.

[WL76] M. Wade and V. G. Lind. “Ratio of antiproton annihilations on neutrons and protons in carbon for low-energy and stopped antiprotons”. In: *Phys. Rev. D* 14 (5 Sept. 1976), pp. 1182–1187. doi: 10.1103/PhysRevD.14.1182.

[WP23] S. Wycech and K. Piscichia. “Pionization: A method to study the nuclear surface”. In: *Phys. Rev. C* 108 (1 July 2023), p. 014313. doi: 10.1103/PhysRevC.108.014313.

[Wyc+96] S. Wycech et al. “Antiprotonic studies of nuclear neutron halos”. In: *Phys. Rev. C* 54 (4 Oct. 1996), pp. 1832–1842. doi: 10.1103/PhysRevC.54.1832.

3 Experimental data compilation

Significant strides have been undertaken in the domain of antiproton research since to its momentous discovery in 1955. These efforts have yielded a profusion of empirical information pivotal to the construction and validation of our model. In the early experiments performed at Berkeley, BNL, CERN or KEK, antiprotons were used just after being produced, in the form of secondary beams with low intensity, ill-defined energy, and a large contamination by negatively charged mesons. Few decades later new devices were elaborated to provide antiproton beams with high purity, intensity and momentum resolution, at CERN and at Fermilab. Within this chapter, we will expound upon the most relevant experiments and their findings, which have served as either input parameters for the INCL or as the datasets we use to test it.

3.1 Early experiments

During the 1960s, two significant experiments were conducted: one at Brookhaven National Laboratory by Columbia University and another at CERN in collaboration with the Collège de France. We will focus on the CERN experiment as it was very similar to the BNL one. The CERN bubble chamber, constructed at Saclay, featured an illuminated volume of 80 cm $\times$ 30 cm $\times$ 30 cm. Antiprotons from LEAR beam with momentum 700 MeV/c were moderated in a Cu degrader. The chamber, placed in a 2.1 T magnetic field, ensured a baseline momentum resolution with a mean track length of about 16 cm. Three stereoscopic images per expansion allowed 3D track reconstruction.

Analyzing the films and reconstructing the events was an intricate process. Four spatial coordinates per track were precisely determined from the films to an accuracy of 80 micrometers. From these, the momenta of charged particles were deduced. For example, the momentum resolution for 928 MeV/c pions resulting from the $\bar{p}p \to \pi^+\pi^-$ reaction was estimated to be around 25 MeV/c.

A total of 1.6×10^6 events were documented at CERN and 7.5×10^5 at BNL. Due to limited scanning capabilities, subsets of the data were analyzed: approximately $80,000$ events at CERN and $45,000$ at BNL. References for the Brookhaven experiments include [Bal+65c; Bal+65d; Bar+65c; Bal+65a; Bal+65b; Bar+65a; Bal+66; Bar+65b; Bal+67; Cha+63b; Arm+64a; Arm+65c] , while CERN's publications range from [Cha+63a; Arm+64b; Bos64; Bet+65; Arm+65b; Arm+65a; dAn+65; Ndi65; Con+67; Ast+67; Bai+67; Fos+68b; Fos+68a; Jam+68; Fow+68; Ast+69; Biz+69; Biz+70; Agu+69; Dia+70] for H_2-filled chambers and [Bet+66; Bet+67; Bet+69a; Bet+69b; Biz68; Biz+74c; Biz+74b; Biz+74a; Ann+68; Biz+70] for D_2-filled chambers.

Additionaly, in the 1970s, experiments at BNL studied gamma-rays from antiproton annihilation. Antiprotons were stopped in liquid H_2 or D_2 targets, with photons detected using Cu(Pb) layers and scintillation counters. Some experiments employed a NaI detector for enhanced precision. The Rome–Syracuse collaboration's data using the D_2-filled BNL bubble chamber were also analyzed.

3.2 KEK

The KEK experiment was conceived to probe narrow spectral lines in the momentum distributions of π^0 and η mesons emerging from $\bar{p}p$ annihilation. Originally, the goal was to discover narrow multiquark or quasi-nuclear bound states. In subsequent phases, annihilation rates into two distinct mesons were ascertained using both H_2[Chi+88] and D_2[Chi+00] targets.

The experimental setup is depicted in Fig.3.1. Antiprotons with momentum 580 MeV/c, originating from the KEK 12 GeV proton synchrotron, underwent degradation in a graphite slab and were halted in

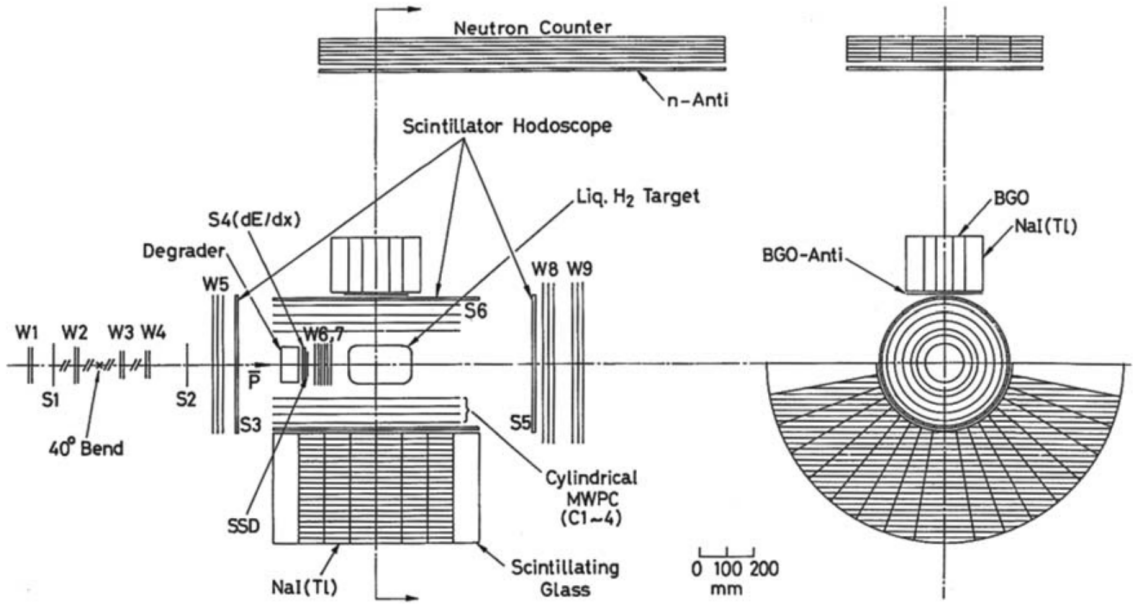

Figure 3.1: Side and end view of the KEK detector[Chi+86].

a liquid H_2 target measuring 14 cm in diameter and 23 cm in length. The $\bar{p}$ beam underwent a double-stage mass separation, achieving a contamination ratio of $e\mu\pi/\bar{p} = 8$. The typical stopping intensity was 270 $\bar{p}$/synchrotron pulse. Charged particles arising from $\bar{p}p$ annihilation were detected using scintillation counter hodoscopes and were tracked using cylindrical and planar multiwire proportional chambers, which covered a total of $93\% \times 4\pi$ sr. Photons were detected using a calorimeter made up of 96 NaI(Tl) crystals, which were enveloped by 48 scintillating glass modules, forming a semi-cylindrical shape. The geometrical acceptance for π^0 rose from 10.5% at a π^0 energy of 500 MeV to 14.5% at 900 MeV. The overall energy resolution at FWHM for photons is approximately $\Delta E_g/E_g = 6.2\%/(E_g \text{ in GeV})^{-1/4}$ for energies exceeding 80 MeV.

Events were logged when the apparatus indicated an incident slow antiproton on the liquid H_2 target and either one or two photons were detected in the NaI instrument. A rapid cluster counting mechanism differentiated the multiplicities of charged from neutral clusters. If these aligned with predetermined criteria, the event was logged. In a few of the subsequent experiments, an added minor BGO detector (covering $1.3\% \times 4\pi$ sr.) encased by NaI modules was employed. In this setup, no cluster counting mechanism was operational, and the energy resolution (FWHM) was approximated as $\Delta E_g/E_g = 6.8\%/(E_g \text{ in GeV})^{1/4}$. Owing to the NaI photon spectrometer's sub-2π acceptance, for two-body branching ratio analyses, detecting both mesons becomes unfeasible. Here, the presence and mass of the second meson are inferred from the inclusive energy spectrum logged for an individual π^0 or η.

3.3 LEAR

The Low Energy Antiproton Ring (LEAR) decelerated and stored antiprotons for experiments, it was built in 1982 and operated until 1996. This facility served for multiple antiproton experiments and its results are crucial for this work. Here is the list of experiments ever conducted within the facility:

1. PS170 Precision measurements of the proton electromagnetic form factors in the time-like region($p\bar{p} \to e^+e^-$)
2. PS171 (ASTERIX) Study of proton-antiproton interactions at rest in a hydrogen gas target at LEAR
3. PS173 Measurement of antiproton-proton cross sections at low antiproton momenta
4. PS177 Study of the fission decay of heavy hypernuclei
5. PS179 Study of the interaction of low-energy antiprotons with ^{2}H, ^{3}He, ^{4}He, Ne-Nuclei with a streamer chamber

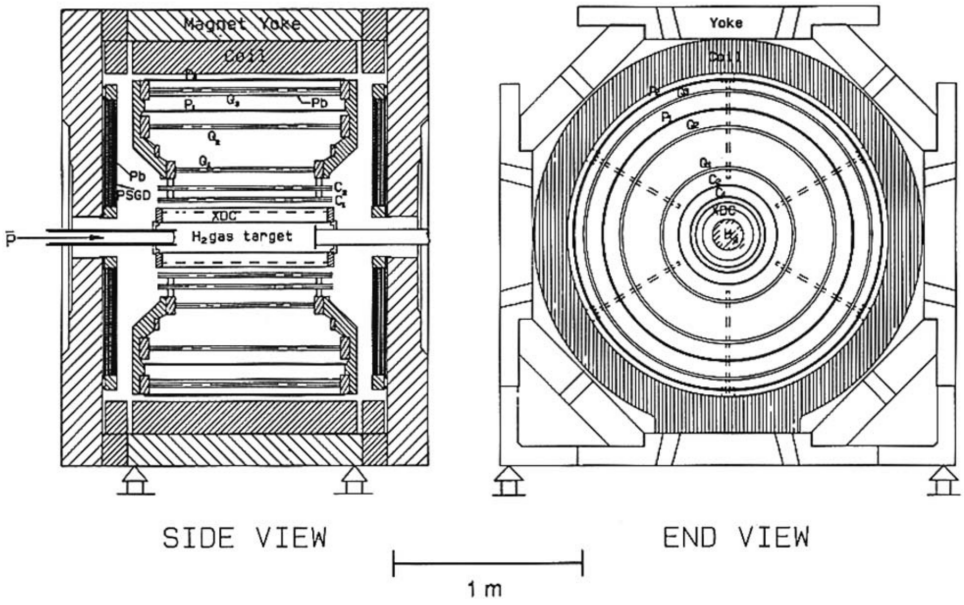

Figure 3.2: Side and front view of the Asterix detector[Ahm+90].

6. PS182 Investigations on baryonium and other rare $p\bar{p}$ annihilation modes using high-resolution π^0 spectrometers
7. PS183 Search for bound $N\bar{N}$ states using a precision γ and charged pion spectrometer at LEAR
8. PS184 Study of antiproton-nucleus interaction with the high resolution SPESII magnetic spectrometer
9. PS186 Nuclear excitations by antiprotons and antiprotonic atoms
10. PS187 A high statistics study of antiproton interactions with nuclei
11. PS197 (CRYSTAL BARREL) Meson spectroscopy at LEAR with a 4π detector
12. PS201 (OBELIX) Study of $p\bar{p}$ and $p\bar{n}$ annihilations at LEAR with a large acceptance and high resolution detector
13. PS202 (JETSET) Physics at LEAR with an internal gas jet target and an advanced general purpose detector
14. PS203 Antiproton induced fission and fragmentation
15. PS208 Decay of hot nuclei at low spins produced by antiproton-annihilation in heavy nuclei

The results from ASTERIX, CRYSTAL BARREL and OBELIX were most fruitful providing data for more than 350 journal publications.

3.3.1 PS 171: the Asterix experiment

In liquid H_2 or D_2, annihilation takes place at rest, initiated by the capture of an antiproton by either a hydrogen or deuterium atom. When the protonium atom collides with H_2 molecules, transitions from high orbital angular momentum states are triggered through Stark mixing (detailed description of Stark mixing in annihilation dynamics is given here[KBR05]). This Stark mixing is swift enough to predominantly ensure capture from S-wave orbitals. In gaseous H_2, the collision frequency is diminished, leading to a significant contribution from P-wave annihilation. Notably, at extremely low target pressures, the P-wave contribution is dominant. As another approach, pure samples of P-wave annihilation can also be explored by detecting X-rays emitted in the atomic cascade of the $\bar{p}p$ system, predominantly feeding the $2P$ level.

The ASTERIX experiment aimed to investigate $\bar{p}p$ annihilation from P-wave orbitals by stopping antiprotons in H_2 gas at ambient temperature and pressure, while observing the concurrent X-ray spectrum. The main components of the detector, depicted in Fig.3.2, include:

1. A gas target measuring 45 cm in length and 14 cm in diameter, containing the full $\bar{p}$ stopping distance for antiproton beams at 105 MeV/c.

2. An X-ray drift chamber that surrounded the target was also used to enhance the tracking ability and for particle identification via $\frac{dE}{dx}$. The energy resolution of this detector for 8 keV X-rays was approximately 20%. Pions and kaons could be differentiated up to 400 MeV/c. A 6 μm aluminised mylar foil ensured gas tightness and efficient X-ray transmission, even at low energies.

3. Charged particles were tracked using seven multi-wire proportional chambers, sometimes with cathode readout for spatial resolution. The momentum resolution for $\bar{p}p \to \pi^+\pi^-$ events at 928 MeV/c was about 3%.

4. A one-radiation-length lead foil positioned in front of the outer chambers enabled the reconstruction of photon impact points.

5. Two end-cap detectors, equipped with three wire planes and cathode readouts on both sides, provided a wide solid-angle coverage. A lead foil was mounted behind the initial chamber. These end-cap detectors were utilized to identify γ photons but not for charged track reconstruction.

6. The entire assembly was placed within a uniform magnetic field of 0.8 T.

Given the detector's resolution, minimal background was observed for fully-constrained final states and up to 14% for final states with a solitary missing π^0.

The primary datasets collected with the Asterix detector included 1.38×10^6 events with two elongated tracks (passing at least the first five chambers) without any X-ray triggers, 2.13×10^6 events with two such tracks and an X-ray trigger, and 1.89×10^6 events with four elongated tracks along with the X-ray trigger. The criterion for "long-track" ensured the particles reached the furthest chambers, ensuring the best momentum resolution. The X-ray enhancing trigger operated with a 25% efficiency; a quarter of the triggered events—after all considerations—identified a low-energy X-ray. The X-ray data sample had a contamination from Bremsstrahlung X-rays of approximately 15%.

A comprehensive description of the detector can be found in [Ahm+90]. The published physics results are available in [Dah+82; Ahm+85c; Ahm+84a; Ahm+84b; Ahm+85a; Ahm+85b; Tru+85; Kle+86; Mar+86; Dos+88b; Duc+89b; Zie+88; Dos+88a; May+89; Duc+89a].

3.3.2 PS 201: the Obelix experiment

OBELIX observed annihilations of $\bar{p}$ and $\bar{n}$ on H_2, D_2, and other denser gas targets both at rest and low energies. Beams of $\bar{p}$ sourced from the LEAR's slow extraction and $\bar{n}$ beams generated via charge exchange in a liquid H_2 target located upstream of the detector are employed. The experimental apparatus comprises the following specialized subdetectors [Aff+93; Ada+92] (see Fig. 3.3):

1. **Spiral Projection Chamber (SPC)**: Serving as an imaging vertex detector, the SPC is equipped with a 3D readout for charged tracks and X-ray detection. It played a pivotal role in capturing data with a substantial P-wave annihilation fraction and facilitated the measurement of angular correlations between X-rays of the $\bar{p}p$ atomic cascade and annihilation by-products.

2. **Time-of-Flight (TOF) System**: Comprising two coaxial barrels of plastic scintillators with 30 and 84 slabs situated 18 cm and 136 cm away from the beam axis respectively. The system achieves a time resolution of 800 ps FWHM.

3. **Jet Drift Chamber (JDC)**: Dedicated for tracking and particle identification, it employs dE/dx measurements using 3280 wires coupled with flash-analog-to-digital readout. The chamber is bisected into two half-cylinders, each measuring 160 cm in diameter and 140 cm in length. The intrinsic spatial resolution stands at $\sigma_z = 12$ mm and $\sigma_{r\phi} = 200$ μm. Monoenergetic pions (at 928 MeV/c) from the $\bar{p}p \to \pi^+\pi^-$ reaction are discerned with a momentum resolution of 3.5%.

4. **High-Angular-Resolution Gamma Detector (HARGD)**: As documented in [Aff+93], this calorimeter is segmented into four modules. Each module incorporates layers of 3×4 m^2 lead converter

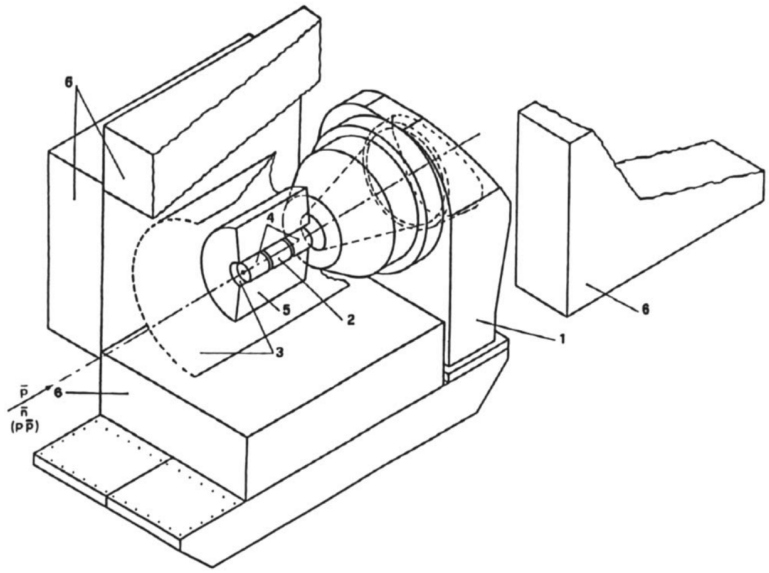

Figure 3.3: Schematic view of the Obelix experiment set-up. The numbers indicate the main components of the apparatus: the open axial field magnet (1), the SPC (2, 4), the TOF (3), the JDC (5), the HARGD (6).

foils paired with planes of limited streamer tubes functioning as the active elements. Twenty converter layers, each 3 mm in thickness, were integrated, resulting in total depth approaching 10 radiation lengths. Owing to its excellent spatial precision, good energy resolution is realized during the reconstruction of final states. For instance, π^0 is restructured with a mass resolution of $\sigma_{\pi^0} = 10$ MeV and an efficiency varying between 15-25% based on momentum.

The detector system allowed a variety of targets to be used: a liquid H_2 target, a gaseous H_2 target at room temperature and pressure, also a target at low pressures (down to 30 mbar). The wide range of target densities could be used to study in detail the influence of the atomic cascade on the annihilation process. The H_2 could also be replaced by D_2. A further special feature of the detector was the possibility to study antineutron interactions. The $\bar{n}$ beam was produced by charge exchange in a liquid H_2 target (positioned 2 m upstream of the centre of the main detector). The intensity of the collimated beam was about 40 $\bar{n}/10^6\bar{p}$ of which about 30% interact in the central target. The $\bar{n}$ beam intensity was monitored by a downstream $\bar{n}$ detector.

3.3.3 PS 197: the Crystal Barrel experiment

The primary aim of the Crystal Barrel experiment was to investigate meson spectroscopy. This included the search for glueballs (gg) and hybrid (g$\bar{q}q$) mesons originating from $\bar{p}p$ and $\bar{p}d$ annihilation when stationary and in motion. Additionally, it focused on understanding the dynamics of $\bar{p}p$ and $\bar{p}d$ annihilation and delving into radiative and uncommon meson decays. An essential characteristic of this experiment was its efficient photon detection across a significant solid angle combined with excellent energy resolution. Some of the outcomes of the physics experiments are documented in [Ani+94; Hei+94; Koc+87; Ams+89; Ake+91; Ams+92c; Ams+92a; Ams+92d; Ams+92b; Ams+93; Aug+93].

A visual representation of the Crystal Barrel spectrometer is depicted in Fig.3.4. A comprehensive overview of the equipment, utilized for initial data collection from 1989 onwards, is provided in [Ake+92]. To analyze annihilation in a static state, an antiproton beam of 200 MeV/c, sourced from LEAR, was halted in a 4 cm long liquid hydrogen target positioned at the detector's core. The entire apparatus was positioned inside a 1.5 T solenoidal magnet, aligned with the incoming antiproton beam. Encircling the target were a set of multiwire proportional chambers (PWCs) and a cylindrical jet drift chamber (JDC). The JDC was segmented into 30 sectors, with each holding 23 sense wires positioned radially between 63 mm and 239 mm. The transverse plane resolution related to the beam axis was $\sigma = 125\mu m$. The wire's coordinate was ascertained by charge segregation, achieving a resolution of $\sigma = 8mm$. This resulted in a pion momentum resolution of $\sigma_p = 2\%$ at 200 MeV/c, escalating to 7% at 1 GeV/c for those tracks spanning all JDC layers. Ionization sampling also allowed the JDC to distinguish π/K under 500 MeV/c.

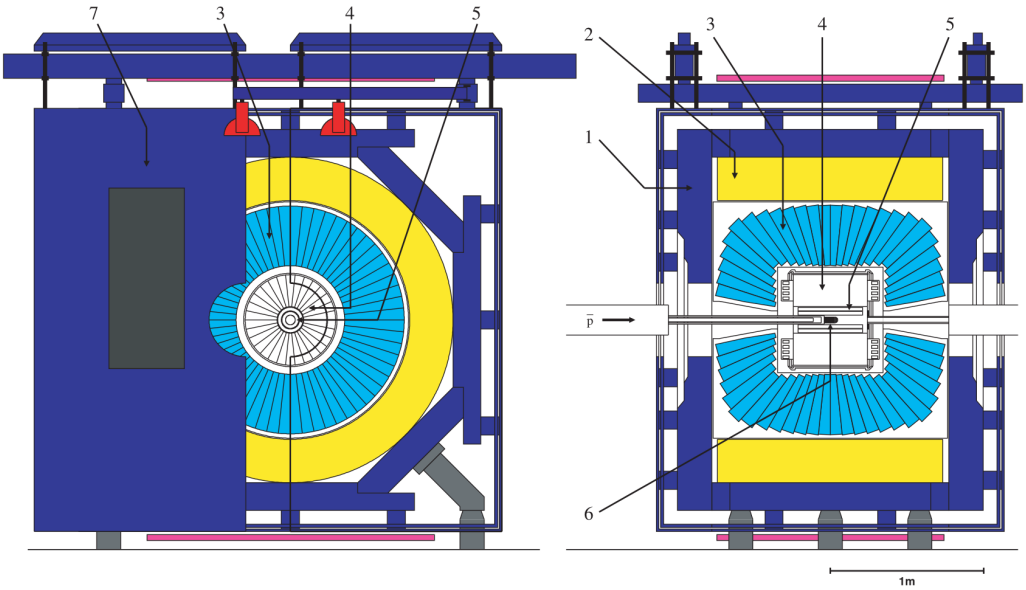

Figure 3.4: Overall layout of the crystal barrel detector showing (1) magnet yoke, (2) magnet coils, (3) CsI barrel, (4) jet drift chamber, (5) proportional chamber, (6) liquid hydrogen target, (7) one half of endplate. Left—longitudinal cross section; Right—transverse view.

The JDC was ensconced by a barrel-style calorimeter comprising 1380 CsI(Tl) crystals configured in a directed geometry. The calorimeter spanned polar angles from 12° to 168° and had full azimuthal coverage. The overall detection acceptance for showers was $0.95 \times 4\pi sr$. Common photon energy resolutions for energy E (in GeV) were $\Delta E/E = 2.5\%/E^{1/4}$, and $\sigma_{\phi,\beta} = 1.2°$ in both polar and azimuthal directions. The mass resolution was $\delta = 10MeV$ for π^0 and 17 MeV for $\eta \rightarrow 2\gamma$. In 1995, the PWCs were substituted with a microstrip vertex detector (SVTX), composed of 15 single-sided silicon devices, each embedded with 128 strips spaced at 50 μm and running in parallel to the beam's direction. An expansive depiction of the detector can be found in [Dos+98]. This apparatus not only enhanced the identification of secondary vertices but also elevated the resolution for vertex in r, ϕ and boosted momentum accuracy with a resolution $\Delta p/p$ for charged trajectories of 3.4% at 0.8 GeV/c and 4.2% at 1.0 GeV/c.

For investigations into annihilation in hydrogen gas, the liquid target was swapped with a 12 cm Mylar vessel with walls measuring 230 μm and an entry window of 195 μm. It housed hydrogen gas at ambient temperature and pressurized at 12 bar. The incoming 105 MeV/c antiproton beam was counted using a 55 μm thick Si detector.

A particular feature of the detector system was a multi-level trigger on charged and neutral multiplicities and on invariant mass combinations of the neutral secondary particles. This design allowed the suppression of well-known channels and enhancement of rare channels of interest. The PWC/SVTX and JDC's internal layers determined the charged multiplicity of the final state. Events with long tracks could be selected to give optimum momentum resolution by counting the charged multiplicity in the outer layers of the JDC. An embedded processor determined cluster multiplicity in the CsI barrel. Concurrently, a software trigger, integrated with the calorimeter's read-out system, enabled a trigger based on the total energy deposited in the barrel or the π^0 or η multiplicity. Typical beam intensities were $10^4 \bar{p}/s$ at 200 MeV/c for stopping in liquid H_2 or 105 MeV/c in a 12 bar gas target. For studies examining in-flight interactions, greater intensities between 10^5 and $10^6 \bar{p}/s$ were necessary with beam momentum ranges of 600-1940 MeV/c.

A concise summary of the data garnered by the experiment, both at rest and in motion, for liquid H_2, liquid D_2, and gaseous H_2 targets is presented by Amsler, detailed in [Ams98]. Typical data sets contain between 10^6 and 2×10^7 events.

3.4 Experimental data compilation

The experiments mentioned in this chapter frequently used hydrogen or deuterium targets to infer the properties of $\bar{p}p$ and $\bar{p}n$ binary interactions. These represent the annihilation final states and fre-

quencies for stopped antiprotons, as well as elementary (binary) cross-sections at higher energies. We utilized this information as inputs for INCL. Another category of experiments employed larger nuclei as targets. Data from these experiments, specifically the spectra of emitted particles, multiplicities, and yields of residual nuclei, will serve to verify our model. Subsequent sections provide an overview of the data used for validation in chapters 5 and 6.

3.4.1 Residual nuclei measurements

Table 3.1: Available data sources on residual nuclei yields

Target	Reference	Beam ($\mathrm{MeV/c}$), (MeV)	Data type
^{nat}Cu	[Jas+93]	105, 6	Cumulative and Independent yields
^{197}Au	[Lub+02]	200, 21	Cumulative and Independent yields
^{nat}Ba	[Egi+90]	200, 21	Measured and Fitted yields
^{92}Mo	[Mos+89]	200, 21	Measured and Fitted yields
^{95}Mo	[Mos+89]	200, 21	Measured and Fitted yields
^{98}Mo	[Mos+89]	200, 21	Measured and Fitted yields
^{165}Ho	[Mos+89]	200, 21	Measured and Fitted yields
^{238}U	[Mac+92]	200, 21	Measured and Fitted yields

The data on residual nuclei yields measured after the target irradiated with a low-energy antiproton beam is summarized in table 3.1. These targets were irradiated at LEAR, but the subsequent study of the residual isotopes' γ-ray spectra was done in different places always with some delay. γ-ray lines were identified by their energies, half-lives, and intensity ratios. These spectra were taken for certain time period ranging from days to weeks in the publications mentioned in the table 3.1, while the overall amount of stopped antiprotons was measured during the irradiation. There are some limitations on this method, in particular, it is not possible to take into account unstable nuclei with very short half-life and those, whose half-life is too large, or even the stable nuclei. Also, many isotopes undergo a series of decay, and not every step of this chain might produce γ-rays, causing the necessity to use some phenomenological model to reconstruct the yields of unobservable products[ST73; Mos+89]. We would discuss this issue more in detail in chapter 5.

3.4.2 Particle spectra and multiplicities

The information on the outgoing particles in the references is often given in form of measured energy or momentum spectra of certain particles, but most of the publications are quite old, so it was necessary to digitize the plots and this was sometimes done in order to compare the spectral curves, but there is a substantial loss of precision and uncertainty information. Thus, we prefer analysing raw data if it was provided in the form of exact values, often with errors included. Such information is mostly particle multiplicity values, total cross section of channels or charge distributions. A table with available information is presented in Table 3.2.

Table 3.2: Outgoing particle data sources

Target	Reference	Beam ($\mathrm{MeV/c}$), (MeV)	Data type
^{28}Si	[McG+86b]	608, 197	π^+, p momentum spectra
^{12}C,^{238}U	[McG+86a]	608, 197	π^+, p momentum spectra, cross sections
$^{12}C - ^{238}U$	[Pol+95]	200, 21	$\pi^{\pm}, K^{\pm *}, p, n, D, T$ multiplicities, energy spectra
$^{6}Li - ^{232}Th$	[Sud+93]	300, 48	$p, D, T,^3He,^4He$ multiplicities, energy spectra
$^{6}Li - ^{232}Th$	[Bal+91]	300, 48	$p, D, T,^3He,^4He$ multiplicities, energy spectra
$^{12}C - ^{238}U$	[Mar+88]	200, 21	$p, D, T,^3He,^4He,^6He,^8He, Li$ multiplicities, energy spectra
^{12}C	[Gol+88]	1186, 750	$\pi^{\pm}, p$ angular distributions
^{12}C	[WL76]	200, 21	$\pi^{\pm}$ pion charge distribution
$C - Pb$	[Bug+73]	n/a	$\pi^{\pm}$ pion charge distribution
$^{14}N, D$	[Rie+89]	200, 21	$\pi^{\pm}, p$ energy spectra, pion charge distribution
$^{27}Al - ^{238}U$	[Egi+00]	1514, 1220	n energy spectra(+50°,-145°)
^{nat}Ta	[Miy+84]	4000, 3170	$\Lambda, \bar{\Lambda}, K^0$ production cross-sections

References

[Ada+92] A. Adamo et al. “First physics results from OBELIX”. In: *Sov. J. Nucl. Phys.* 55 (1992), pp. 1732–1742.

[Aff+93] S. Affatato et al. “The electromagnetic calorimeter for the OBELIX experiment”. In: *Nuclear Instruments and Methods in Physics Research Section A: Accelerators, Spectrometers, Detectors and Associated Equipment* 325.3 (1993), pp. 417–428. issn: 0168-9002. doi: https://doi.org/10.1016/0168-9002(93)90386-V.

[Agu+69] M. Aguilar-Benitez et al. “$K_1^0 K_1^0$ enhancements as observed in annihilations of slow antiprotons in hydrogen”. In: *Phys. Lett.* 29B (1969).

[Ahm+84a] S. Ahmad et al. “anti-p p ANNIHILATION AT REST FROM ATOMIC P STATES”. In: *7th European Symposium on Antiproton Interactions: From LEAR to the Collider and Beyond*. Sept. 1984.

[Ahm+84b] S. Ahmad et al. “p anti-p ANNIHILATIONS AT REST IN HYDROGEN GAS: REPORT ON PRELIMINARY RESULTS OF THE ASTERIX EXPERIMENT AT LEAR”. In: *International School of Physics of Exotic Atoms: Fundamental Interactions in Low-energy Systems*. July 1984.

[Ahm+85a] S. Ahmad et al. “anti-p p ANNIHILATION INTO NEUTRAL KAONS”. In: *3rd LEAR Workshop: Physics with Antiprotons at LEAR in the ACOL Era*. Apr. 1985.

[Ahm+85b] S. Ahmad et al. “First Observation of K X-rays From $p\bar{p}$ Atoms”. In: *Phys. Lett. B* 157 (1985), p. 333. doi: 10.1016/0370-2693(85)90676-8.

[Ahm+85c] S. Ahmad et al. “Search for Monochromatic Pion Emission in $\bar{p}p$ Annihilation From Atomic p States”. In: *Phys. Lett. B* 152 (1985), pp. 135–139. doi: 10.1016/0370-2693(85)91155-4.

[Ahm+90] S. Ahmad et al. “The Asterix Spectrometer at LEAR”. In: *Nucl. Instrum. Meth. A* 286 (1990), p. 76. doi: 10.1016/0168-9002(90)90210-W.

[Ake+91] E. Aker et al. “Observation of a 2^{++} resonance at 1515-MeV in proton anti-proton annihilations into 3 π^0”. In: *Phys. Lett. B* 260 (1991), pp. 249–258. doi: 10.1016/0370-2693(91)90999-7.

[Ake+92] E. Aker et al. “The Crystal Barrel spectrometer at LEAR”. In: *Nucl. Instrum. Meth. A* 321 (1992), pp. 69–108. doi: 10.1016/0168-9002(92)90379-I.

[Ams+89] Claude Amsler et al. “The Crystal Barrel at LEAR”. In: *BNL Workshop on Glueballs, Hybrids and Exotic Hadrons*. Apr. 1989, pp. 653–660. doi: 10.1063/1.38095.

[Ams+92a] Claude Amsler et al. “P-verus S-wave $\bar{p}p$-annihilation at rest in LH_2”. In: *Phys. Lett. B* 297 (1992), pp. 214–218. doi: 10.1016/0370-2693(92)91095-Q.

[Ams+92b] Claude Amsler et al. “Proton - anti-proton annihilation into eta eta pi: Observation of a scalar resonance decaying into eta eta”. In: *Phys. Lett. B* 291 (1992), pp. 347–354. doi: 10.1016/0370-2693(92)91057-G.

[Ams+92c] Claude Amsler et al. “Recent results from the Crystal Barrel experiment”. In: *Sov. J. Nucl. Phys.* 55 (1992). Ed. by Yu. S. Kalashnikova, L. A. Kondratyuk, and N. Ya. Smorodinskaya, pp. 767–777.

[Ams+92d] Claude Amsler et al. “The Pseudoscalar mixing angle theta(ps) from eta and eta-prime production in anti-p p annihilation at rest”. In: *Phys. Lett. B* 294 (1992), pp. 451–456. doi: 10.1016/0370-2693(92)91547-M.

[Ams+93] C. Amsler et al. “Anti-proton - proton annihilation at rest into omega pio pio”. In: *Phys. Lett. B* 311 (1993), pp. 362–370. doi: 10.1016/0370-2693(93)90583-4.

[Ams98] Claude Amsler. "Proton-antiproton annihilation and meson spectroscopy with the Crystal Barrel". In: *Reviews of Modern Physics* 70.4 (Oct. 1998), pp. 1293–1339. doi: 10.1103/revmodphys.70.1293.

[Ani+94] V. V. Anisovich et al. "Observation of two $J^{PC} = 0^{++}$ isoscalar resonances at 1365 and 1520 MeV". In: *Phys. Lett. B* 323 (1994), pp. 233–241. doi: 10.1016/0370-2693(94)90297-6.

[Ann+68] P. Anninos et al. "Production of three charged pions in $p\bar{n}$ annihilations at rest". In: *Phys. Rev. Lett.* 20 (1968).

[Arm+64a] R. Armenteros et al. "Evidence for a $(K\pi\pi)$ resonance with a mass of 1230 GeV/c^2". In: *Phys. Lett.* 9 (1964).

[Arm+64b] R. Armenteros et al. "Evidence for a $(K\bar{K})$ resonance with a mass of 1230 GeV/c^2". In: *Phys. Lett.* 9 (1964).

[Arm+65a] R. Armenteros et al. "Experimental results on the annihilation $p\bar{p} \to K^+K^-\pi^0$ at rest: non-K^* resonating events". In: *Phys. Lett.* 17 (1965).

[Arm+65b] R. Armenteros et al. "Experimental results on the annihilation production $p\bar{p} \to K^+K^-\pi^0$ at rest: K^*". In: *Phys. Lett.* 17 (1965).

[Arm+65c] R. Armenteros et al. "Experimental results on the annihilation production $\bar{p}p \to \bar{K}K\pi$ at rest: K^*". In: *Phys. Lett.* 17 (1965).

[Ast+67] A. Astier et al. "Further study of I = 1 $(K\bar{K})$ structure near threshold". In: *Phys. Lett.* 25B (1967).

[Ast+69] A. Astier et al. "Existence and properties of the C-meson as observed in $p\bar{p}$ annihilations at rest". In: *Nucl. Phys. B* 10 (1969).

[Aug+93] I. Augustin et al. "New states as observed by the Crystal Barrel experiment". In: *Nucl. Phys. A* 558 (1993). Ed. by C. Guaraldo, F. Iazzi, and A. Zenoni, pp. 3C–12C. doi: 10.1016/0375-9474(93)90378-B.

[Bai+67] P. Baillon et al. "Further study of the E-meson in antiproton annihilations at rest". In: *Nuovo Cimento* 50A (1967).

[Bal+65a] C. Baltay et al. "Annihilation of antiprotons in hydrogen at rest. II. Analysis of the annihilation into three pions". In: *Phys. Rev. B* 140 (1965).

[Bal+65b] C. Baltay et al. "Annihilation of antiprotons in hydrogen at rest. III. The reactions $\bar{p}p \to \omega\pi^+\pi^-$ and $\bar{p}p \to \omega\rho^0$". In: *Phys. Rev. B* 140 (1965).

[Bal+65c] C. Baltay et al. "Annihilations of antiprotons in hydrogen at rest into two mesons". In: *Phys. Rev. Lett.* 15 (1965).

[Bal+65d] C. Baltay et al. "Test of charge-conjugation invariance in $\bar{p}p$ annihilations at rest". In: *Phys. Rev. Lett.* 15 (1965).

[Bal+66] C. Baltay et al. "Annihilations of antiprotons at rest in hydrogen. V. Multipion annihilations". In: *Phys. Rev.* 145 (1966).

[Bal+67] C. Baltay et al. "Observation of the B meson in the reaction $\bar{p}p \to \omega\pi^+\pi^-$". In: *Phys. Rev. Lett.* 18 (1967).

[Bal+91] F. Balestra et al. "Strangeness production in antiproton annihilation at rest on 3He, 4He and 20Ne". In: *Nuclear Physics A* 526.3 (1991), pp. 415–452. issn: 0375-9474. doi: https://doi.org/10.1016/0375-9474(91)90428-9.

[Bar+65a] N. Barash et al. "Annihilation of antiprotons in hydrogen at rest. IV. $\bar{p}p \to \bar{K}K\pi\pi$". In: *Phys. Rev. B* 145 (1965).

[Bar+65b] N. Barash et al. "Annihilation of antiprotons in hydrogen at rest. IV. Kaonic final states". In: *Phys. Rev. B* 156 (1965).

[Bar+65c] N. Barash et al. “Antiproton annihilation in hydrogen at rest. I. Reaction $\bar{p}p \to \bar{K}K\pi$”. In: *Phys. Rev. B* 139 (1965).

[Bet+65] A. Bettini et al. “Spin and parity of the 1320 MeV η resonances”. In: *Nuovo Cimento* 38 (1965).

[Bet+66] A. Bettini et al. “Evidence for strong possible resonant scalar interactions”. In: *Nuovo Cimento* 42A (1966).

[Bet+67] A. Bettini et al. “Annihilation into pions of the $\bar{p}n$ system from antiprotons at rest in deuterium”. In: *Il Nuovo Cimento A (1965-1970)* 47.3 (1967), pp. 642–661. doi: 10.1007/BF02738758.

[Bet+69a] A. Bettini et al. “Annihilations of $p\bar{n}$ at rest into final states containing K-mesons”. In: *Nuovo Cimento* 62A (1969).

[Bet+69b] A. Bettini et al. “The annihilation at rest $\bar{N}N \to KK\bar{K}$”. In: *Nuovo Cimento* 63A (1969).

[Biz+69] R. Bizzarri et al. “Experimental results on the η and η' systems as observed in $p\bar{p}$ annihilations at rest: $p\bar{p} \to \eta + \eta^-$”. In: *Nucl. Phys. B* 14 (1969).

[Biz+70] R. Bizzarri et al. “Upper limit on the $\eta \to 2\pi$ decay rate from $p\bar{n}$ annihilations at rest”. In: *Phys. Rev. Lett.* 25 (1970).

[Biz+74a] R. Bizzarri et al. “Angular momentum states in antiproton-nucleon annihilations at rest in deuterium”. In: *Nucl. Phys. B* 69 (1974).

[Biz+74b] R. Bizzarri et al. “Comparison of the reaction $p\bar{p} \to K^0K\bar{K}^0$ at rest in hydrogen and deuterium: A test of S-state annihilation dominance”. In: *Nucl. Phys. B* 69 (1974).

[Biz+74c] R. Bizzarri et al. “Properties of the η meson as observed in $p\bar{n}$ annihilations at rest”. In: *Nuovo Cimento* 20A (1974).

[Biz68] R. Bizzarri. “On the comparison of the annihilations of antiprotons at rest in hydrogen and deuterium”. In: *Nuovo Cimento* 53A (1968).

[Bos64] A. Boserup. “An unsuccessful search for hyperstrange mesons with masses between 640 and 940 MeV”. In: *Physics Letters* 13.2 (1964), pp. 172–173. issn: 0031-9163. doi: https://doi.org/10.1016/0031-9163(64)90713-9.

[Bug+73] W. M. Bugg et al. “Evidence for a Neutron Halo in Heavy Nuclei from Antiproton Absorption”. In: *Phys. Rev. Lett.* 31 (7 Aug. 1973), pp. 475–478. doi: 10.1103/PhysRevLett.31.475.

[Cha+63a] G. Chadwick et al. “Study of the annihilation of stopped antiprotons in hydrogen: the reaction $p\bar{p} \to \pi^+\pi^-\pi^0$”. In: *Phys. Rev. Lett.* 10 (1963).

[Cha+63b] G. Chadwick et al. “Study of the annihilation of stopped antiprotons in hydrogen: the reaction $\bar{p}p \to \pi^+\pi^-\pi^0$”. In: *Phys. Rev. Lett.* 10 (1963).

[Chi+00] Masami Chiba et al. “Antiproton-nucleon Annihilation into π^0M and ηM with M=η, ω, ρ, and π in Antiproton-deuterium Annihilation at Rest”. In: *Journal of the Physical Society of Japan* 69 (5 May 2000), p. 1356. doi: 10.1143/JPSJ.69.1356.

[Chi+86] M. Chiba et al. “Search for narrow states by detection of monochromatic gamma rays in $\bar{p}p$ annihilation at rest”. In: *Physics Letters B* 177.2 (1986), pp. 217–222. issn: 0370-2693. doi: https://doi.org/10.1016/0370-2693(86)91060-9.

[Chi+88] M. Chiba et al. “Search for narrow peaks in inclusive π^0 spectra from $\bar{p}p$ annihilation at rest”. In: *Physics Letters B* 202.3 (1988), pp. 447–452. issn: 0370-2693. doi: https://doi.org/10.1016/0370-2693(88)90501-1.

[Con+67] B. Conforto et al. “Experimental results on the (KK) and $(K\bar{K})$ systems as observed in the annihilations $p\bar{p} \to K^+K^-\pi^0$ at rest”. In: *Nucl. Phys. B* 3 (1967).

[Dah+82] W. Dahme et al. "(q anti-q) SPECTROSCOPY AND SEARCH FOR GLUEBALLS, BARYONIA AND OTHER BOSON RESONANCES IN anti-p p ANNIHILATIONS AT REST WITH THE ASTERIX EXPERIMENT AT LEAR". In: *International School of Physics of Exotic Atoms: Workshop on Physics at Lear with Low-energy Cooled Antiprotons*. Nov. 1982, pp. 253–280.

[dAn+65] C. d'Andlau et al. "Evidence for a non-strange meson of mass 1290 MeV". In: *Phys. Lett.* 17 (1965).

[Dia+70] J. Diaz et al. "$p\bar{p}$ annihilations at rest into four pions". In: *Nucl. Phys. B* 16 (1970).

[Dos+88a] M. Doser et al. "$\bar{p}p$ Annihilation Into $\pi^+\pi^-$ and K^+K^- From Atomic p States". In: *Nucl. Phys. A* 486 (1988), pp. 493–511. doi: 10.1016/0375-9474(88)90159-5.

[Dos+88b] M. Doser et al. "$\bar{P}P$ Annihilation Into $K^0\bar{K}^0$ in Hydrogen Gas". In: *Phys. Lett. B* 215 (1988). Ed. by K. Kleinknecht and E. Klempt, pp. 792–798. doi: 10.1016/0370-2693(88)90063-9.

[Dos+98] M. Doser et al. "The crystal barrel Si-vertex detector". In: *Nuclear Instruments and Methods in Physics Research Section A: Accelerators, Spectrometers, Detectors and Associated Equipment* 412.1 (1998), pp. 70–79. issn: 0168-9002. doi: https://doi.org/10.1016/S0168-9002(98)00222-8.

[Duc+89a] K. D. Duch et al. "Observation and Analysis of e Mesons in $\bar{p}p$ Annihilation at Rest in ^{2}H Gas". In: *Z. Phys. C* 45 (1989), p. 223. doi: 10.1007/BF01674452.

[Duc+89b] K. D. Duch et al. "Study of the E (1420) in anti-p p annihilation at rest in H-2 gas". In: *Nucl. Phys. B Proc. Suppl.* 8 (1989). Ed. by K. Kleinknecht and E. Klempt, pp. 50–53. doi: 10.1016/0920-5632(89)90195-3.

[Egi+00] T. von Egidy et al. "Neutrons produced by 1.22 GeV antiproton interactions with nuclei". In: *The European Physical Journal A* 8.2 (July 2000), pp. 197–204. issn: 1434-601X. doi: 10.1007/s100500070106.

[Egi+90] T. von Egidy et al. "Yield of residual nuclei after antiproton annihilation in Ba". In: *Zeitschrift für Physik A Atomic Nuclei* 335.4 (Dec. 1990), pp. 451–457. issn: 0939-7922. doi: 10.1007/BF01290193.

[Fos+68a] M. Foster et al. "Experimental results on $p\bar{p} \to \pi^+\pi^-\pi^0$ and $p\bar{p} \to X^0\pi^+\pi^-$ for annihilations at rest". In: *Nucl. Phys. B* 8 (1968).

[Fos+68b] M. Foster et al. "Production of three pions in $p\bar{p}$ annihilation at rest". In: *Nucl. Phys. B* 6 (1968).

[Fow+68] F. C. Fowler et al. "Search for a K^* below $K\bar{K}$ threshold in $p\bar{p}$ annihilations at rest". In: *Phys. Rev. Lett.* 21 (1968).

[Gol+88] Ye.S. Golubeva et al. "Inelastic interactions of intermediate-energy antinucleons with nuclei". In: *Nuclear Physics A* 483.3 (1988), pp. 539–564. issn: 0375-9474. doi: https://doi.org/10.1016/0375-9474(88)90083-8.

[Hei+94] F. H. Heinsius et al. "eta decay branching ratios". In: *Phys. Atom. Nucl.* 57 (1994), pp. 1711–1715.

[Jam+68] F. James et al. "Experimental investigations of $\Delta S = \Delta Q$ rule in leptonic K^0 decays". In: *Nucl. Phys. B* 8 (1968).

[Jas+93] J. Jastrzębski et al. "Interaction of stopped antiprotons with copper". In: *Phys. Rev. C* 47 (1 Jan. 1993), pp. 216–224. doi: 10.1103/PhysRevC.47.216.

[KBR05] Eberhard Klempt, Chris Batty, and Jean-Marc Richard. "The antinucleon–nucleon interaction at low energy: Annihilation dynamics". In: *Physics Reports* 413.4-5 (July 2005), pp. 197–317. doi: 10.1016/j.physrep.2005.03.002.

[Kle+86] E. Klempt et al. “STATUS AND FUTURE OF THE ASTERIX EXPERIMENT”. In: *3rd LEAR Workshop: Physics with Antiprotons at LEAR in the ACOL Era*. 1986, pp. 347–352.

[Koc+87] H. Koch et al. “Meson spectroscopy and the Crystal Barrel detector at LEAR”. In: *International Symposium on Medium Energy Physics*. 1987, pp. 588–594.

[Lub+02] P. Lubiński et al. “Gold fragmentation induced by stopped antiprotons”. In: *Phys. Rev. C* 66 (4 Oct. 2002), p. 044616. doi: 10.1103/PhysRevC.66.044616.

[Mac+92] H. Machner et al. “Fission fragment distribution following antiproton absorption at rest on238U”. In: *Zeitschrift für Physik A Hadrons and Nuclei* 343.1 (Mar. 1992), pp. 73–77. issn: 0939-7922. doi: 10.1007/BF01291600.

[Mar+86] Glen M. Marshall et al. “Antiproton-proton annihilation into collinear charged pions and kaons”. In: *AIP Conf. Proc.* 150 (1986). Ed. by D. F. Geesaman, pp. 456–457. doi: 10.1063/1.36114.

[Mar+88] W. Markiel et al. “Emission of helium ions after antiproton annihilation in nuclei”. In: *Nuclear Physics A* 485.3 (1988), pp. 445–460. issn: 0375-9474. doi: https://doi.org/10.1016/0375-9474(88)90547-7.

[May+89] B. May et al. “Production of pi+ pi- pio in anti-p p annihilation at rest from atomic P state.” In: *Nucl. Phys. B Proc. Suppl.* 8 (1989). Ed. by K. Kleinknecht and E. Klempt, pp. 218–221. doi: 10.1016/0920-5632(89)90226-0.

[McG+86a] P. L. McGaughey et al. “Dynamics of Low-Energy Antiproton Annihilation in Nuclei as Inferred from Inclusive Proton and Pion Measurements”. In: *Phys. Rev. Lett.* 56 (20 May 1986), pp. 2156–2159. doi: 10.1103/PhysRevLett.56.2156.

[McG+86b] P.L. McGaughey et al. “Low energy antiproton-nucleus annihilation radius selection using an active silicon detector/target”. In: *Nuclear Instruments and Methods in Physics Research Section A: Accelerators, Spectrometers, Detectors and Associated Equipment* 249.2 (1986), pp. 361–365. issn: 0168-9002. doi: https://doi.org/10.1016/0168-9002(86)90689-3.

[Miy+84] K. Miyano et al. “Evaporation of Neutral Strange Particles in $\bar{p}$-Ta at 4 GeV/c”. In: *Phys. Rev. Lett.* 53 (18 Oct. 1984), pp. 1725–1727. doi: 10.1103/PhysRevLett.53.1725.

[Mos+89] E. F. Moser et al. “Residual nuclei after antiproton annihilation in Mo and Ho”. In: *Zeitschrift für Physik A Atomic Nuclei* 333.1 (Mar. 1989), pp. 89–105. issn: 0939-7922. doi: 10.1007/BF01290114.

[Ndi65] F. N. Ndili. “A study of two-prong events in $p\bar{p}$ annihilation at rest”. In: *Phys. Rev. B* 138 (1965).

[Pol+95] D. Polster et al. “Light particle emission induced by stopped antiprotons in nuclei: Energy dissipation and neutron-to-proton ratio”. In: *Phys. Rev. C* 51 (3 Mar. 1995), pp. 1167–1180. doi: 10.1103/PhysRevC.51.1167.

[Rie+89] J. Riedlberger et al. “Antiproton annihilation at rest in nitrogen and deuterium gas”. In: *Phys. Rev. C* 40 (6 Dec. 1989), pp. 2717–2731. doi: 10.1103/PhysRevC.40.2717.

[ST73] R. Silberberg and C. H. Tsao. “Partial Cross-Sections in High-Energy Nuclear Reactions, and Astrophysical Applications. I. Targets With z <= 28.” In: *Astrophys. J. Suppl.* 25 (1973), pp. 315–333. doi: 10.1086/190271.

[Sud+93] A.S. Sudov et al. “Production of light particles after antiproton-nucleus annihilation and their interpretation with statistical models”. In: *Nuclear Physics A* 554.2 (1993), pp. 223–245. issn: 0375-9474. doi: https://doi.org/10.1016/0375-9474(93)90340-4.

[Tru+85] Peter Truoel et al. “ANTI-PROTON ANNIHILATION AT REST IN NITROGEN AND ARGON”. In: 1985.

[WL76] M. Wade and V. G. Lind. “Ratio of antiproton annihilations on neutrons and protons in carbon for low-energy and stopped antiprotons”. In: *Phys. Rev. D* 14 (5 Sept. 1976), pp. 1182–1187. doi: 10.1103/PhysRevD.14.1182.

[Zie+88] M. Ziegler et al. “Measurement of the Strong Interaction Shift and Broadening of the Ground State of the $p\bar{p}$ Atom”. In: *Phys. Lett. B* 206 (1988), pp. 151–158. doi: 10.1016/0370-2693(88)91279-8.

4 | INCL: THE LIÈGE INTRANUCLEAR CASCADE MODEL

4.1 Introduction

The theoretical study of nuclear reactions started almost a hundred years ago and developed in two distinctive directions. On one hand, this was more or less the first time reactions between microscopic objects were studied, and theorists concentrated on the formal consideration of the reaction processes in general, inventing, for instance, the concept of the S-matrix (and also the R-matrix for the special cases of the resonant reactions). On the other hand, theorists designed a large number of specialized models corresponding partly to the many types of reactions showing apparently different facets. It is then not surprising that a theory allowing the ab initio calculation of a cross-section is still not really existing (except for very simple cases). This is partly due to the complexity of the nuclear forces, but also because of the fact that various types of reactions correspond mainly to differences in the number of involved degrees of freedom. The late developments present considerable progress along this line and allow for a clarification of the situation. Until the mid-1960s, nuclear reactions were primarily described by considering two distinct processes.

Firstly, the concept of a compound nucleus was introduced by Bohr[Boh36], suggesting that a collision between a projectile and a heavy target would result in the formation of a compound nucleus through a complex process involving all nucleons. This concept works efficiently when specific energy values are available, resulting in narrow resonances in the cross sections. These resonances correspond to quantum quasi-bound states of the compound nucleus, possessing quantum numbers similar to bound states, but also a resonance width representing a finite lifetime due to the Heisenberg uncertainty principle. Bohr concluded that the subsequent breakup of this intermediate system is unrelated to the initial collision stage, implying the independence of the production channel and compound nucleus evaporation. The time span of these reactions depends on the projectile's energy and can last from 10^{-15} s to 10^{-19} s. The independence hypothesis assumes that all outgoing channels compete and have their individual probabilities, and the compound nucleus state is reached when the residual nucleus attains statistical equilibrium.

Secondly, direct reactions involve an outgoing channel directly linked to the incoming channel, without the formation of any intermediate system. The time span for direct reactions is shorter than for compound nuclei, roughly corresponding to the projectile's transit time across the nucleus (about 10^{-22} s). The emitted particles follow a narrow forward-peaked angular distribution. Examples of direct reactions include inelastic scattering leading to low-lying states of the target or charge-exchange reactions where the emitted particle has the same mass as the projectile, resulting in a transfer of electric charge. In these reactions, the number of involved degrees of freedom is often limited to those of a single target nucleon.

The formation of a compound nucleus is ubiquitous at low energy and can coexist with direct reactions. As the incident energy increases, typically above 10 MeV, the resonances start to overlap, and the cross sections slowly vary with energy. Additionally, the energy spectra of the emitted particles become more complicated, no longer limited to the evaporation spectrum typical of compound nucleus reactions at very low energy or the high energy spectrum close to the projectile velocity, typical of direct reactions. Sometimes, particles are ejected after the direct reactions and before reaching statistical equilibrium. These reactions are explained as occurring through a series of nucleon-nucleon interactions, sometimes ejecting one of them, and progressively leading to a fully statistical excitation of the nucleus. They are referred to as pre-equilibrium emissions. The direct reactions describe the

high-energy part of the spectra, where the ejectile has nearly the same energy as the projectile. On the other hand, the compound nucleus is employed to describe the low-energy part of the spectra, wherein the residual nucleus has achieved statistical equilibrium, and the emitted particle barely has enough energy to surpass the Coulomb barrier. Between these two contributions, one can observe the increasing contribution of pre-equilibrium emission, which becomes more prominent with the energy of the projectile.

The intranuclear cascade, proposed by Serber in 1947[Ser47], conceptualizes the reaction induced by a high-energy particle as occurring in two stages. Firstly, there is a rapid intranuclear cascade (INC) involving a sequence of two-body collisions, progressively spreading the projectile's energy over an increasing number of nucleons. This stage is swift. Secondly, following the cascade, a slower stage takes place, during which the residual nucleus de-excites through the usual evaporation processes. The fundamental concept of this model is that when the energy of the projectile is sufficiently high for its de Broglie wavelength to be comparable to the size of the nucleons, the projectile interacts with the target nucleus not as a whole but rather triggers an intranuclear cascade of two-body reactions. This model explicitly considers the degrees of freedom of the nucleons, making it distinct from the compound nucleus approach.

4.2 Intra Nuclear Cascade Liege

Over the span of more than four decades, INCL has undergone multiple developmental stages. These stages can be categorized into three primary phases. The initial phase involved creating the code with the aim of investigating specific physical aspects such as heavy ion reactions and spallation[CMV81; CKV82; Cug87], incorporating various extensions tailored to each aspect. I will only cite here the works of Joseph Cugnon (he is also the founder of INCL) and others , which were related to antiprotons [CV87; CDV88; JCV88; CV89b; CV89a; CDV90; Cug92; CV92; Cug+95]. Its purpose as a modelling tool was not generalized during this phase. Subsequently, the code entered a second phase, during which it was restructured to serve broader applications and seamlessly integrate into transport codes for widespread use, these efforts were accomplished by the INCL group. The three articles [Bou+02; Bou+13; Man+14] include more detailed description and analysis of INCL features and may be addressed by the reader if a deeper understanding of the code is desired. The current and final phase is characterized by continuous efforts directed towards enhancing and expanding the capabilities of INCL, like the one made by my predecessor PhD student, who have added strange particles to INCL[Hir+18; Hir+20], the one made slightly earlier to add η and ω mesons[Dav+18], and other important improvements[Man+15; Rod+17]. One of the main goals of this thesis is to expand INCL capabilities to include handling of antiprotons.

Lets summarize the general hypothesis used within INCL, which are similar to those of Serber[Ser47].

$$\lambda/2\pi << d < \Lambda < R \tag{4.1}$$

where $\lambda/2\pi$ is the reduced de Broglie wavelength, d is the distance between two nucleons inside the target nucleus, Λ is the mean free path of the particle in the nucleus, R is the radius of the nucleus. The physical meanings of the sub-inequalities are:

- $\lambda/2\pi << d$: The size of the wave packet describing the particle is much lower than the internucleonic distance. Consequently, all nucleons appear distinct and well defined in momenta and positions for the incoming projectile. This allows a classical treatment of the particles propagation.
- $\lambda/2\pi < \Lambda$: The scattered wave reaches its asymptotic state before the next interaction and interactions can be treated in a classical approach.
- $d < \Lambda$: Interactions are independent from each other (assuming that the time between two collisions is larger than the interaction time scale). Interactions and transport can be treated independently.
- $\Lambda < R$: The possible interferences between the scattered waves cancel out due to the large number of interactions.

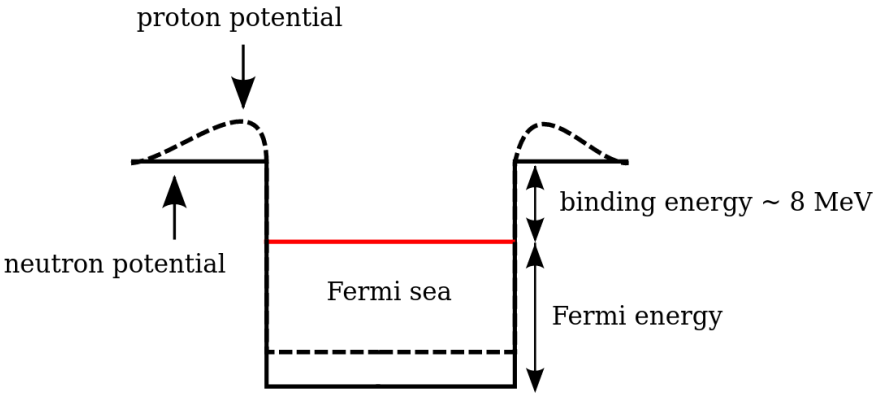

Figure 4.1: Potential well for neutrons and protons in a heavy nucleus showing the Fermi level. Protons should additionally feel the Coulomb potential.

These conditions define the limits of the validity of INCL. The low energy limit is practically eliminated as what actually happens is that the projectile particle is absorbed or reflected by the nucleus as a whole without causing any secondary interactions. However, INCL is not valid above certain energies where the quark and gluon degrees of freedom come into play. In reality the upper limit is even lower due to the available elementary cross-section data, which in the current case of $\bar{p}$ is 10 GeV of the projectile incident energy.

4.2.1 Initialization

First, we initialize the projectile particle. Basically, an impact parameter is assigned at random, which then undergoes adjustments due to the Coulomb force acting between the projectile and the target. As the projectile penetrates the target nucleus, its energy is recalibrated based on the nuclear potential.

Second, the nucleus is initialized. Here I have to mention the r-p (position-momentum) correlation, which works like that: we start with sampling momentum for each nucleon, which is uniformly distributed with a maximum defined as:

$$p_F = \left(\frac{9\pi}{8}\right)^{1/3} \frac{\hbar}{r_0} \tag{4.2}$$

This momentum corresponds to the Fermi energy $E_F = p_F^2/2M$, where M is the nucleon mass. All together nucleons form the so-called Fermi sea (Fig.4.1). After that, each nucleon of a target nucleus is assigned its position, which is also sampled in a Monte-Carlo way, but may not be larger (in its distance from the center of the nucleus) than the kinematically allowed for the momentum chosen previously. Depending on the mass number of the target, the position is distributed according to the Woods-Saxon, the modified-harmonic-oscillator, or the Gaussian density distributions, respectively:

$$\rho = \begin{cases} \dfrac{\rho_0}{1+\exp\left(\frac{r-R_0}{a}\right)}, & A > 19 \\ \rho_0 \dfrac{1+\alpha\left(\frac{r^2}{a^2}\right)}{\exp\left(\frac{r^2}{a^2}\right)}, & 6 < A \leq 19 \\ \dfrac{\rho_0}{\exp\left(\frac{r^2}{a^2}\right)}, & A \leq 6 \end{cases} \tag{4.3}$$

where a, α and ρ_0 are defined separately for neutrons and protons in each nucleus and $R_0 = r_0 A^{1/3}$, with $r_0 \approx 1.25fm$. We also limit the computation volume with $R_{max} = R_0 + 8a$ and the density beyond R_{max} is zero. In most cases there are more neutrons than protons in the nucleus, so the neutronic density pops out beyond the protonic one and a "neutron skin" naturally appears.

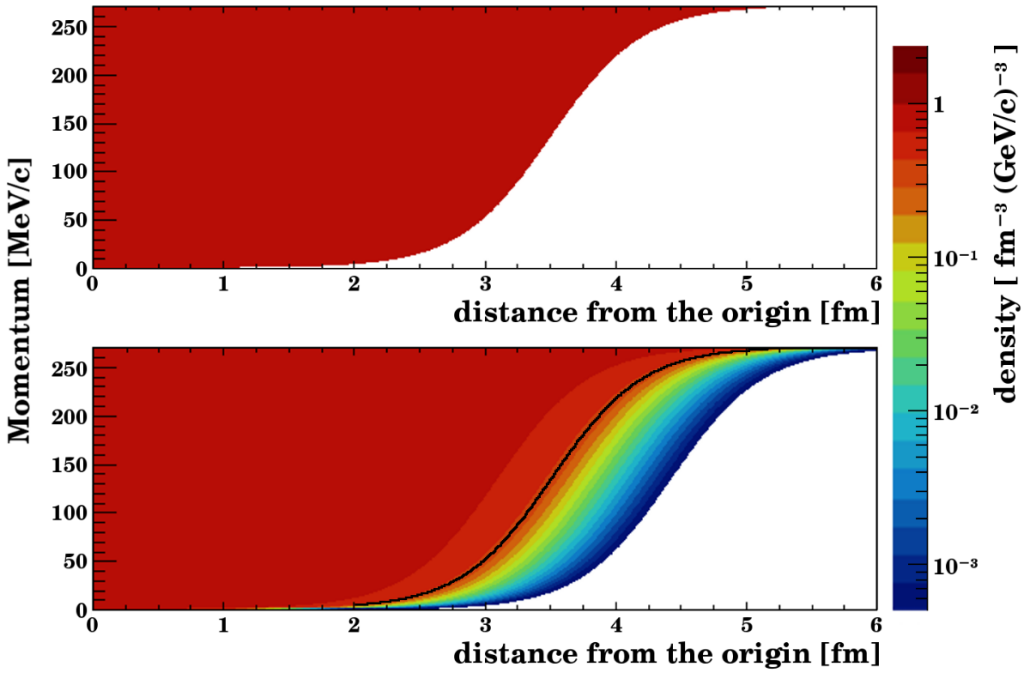

Figure 4.2: Phase space distribution of protons in a nucleus of Al^{27}. Upper panel: proton distribution in the classic approach. Lower panel: proton distribution in the quantum approach of [Man+15]. The black line in the lower panel is the classical phase space limit of the proton distribution seen in the top panel.

Recently, the correlation r-p has been made less strict, allowing low-nucleons to go a little farther than the classical picture authorizes. Doing so, the quantum nature of the position of nucleons is accounted for, which led to better simulate the one-nucleon reactions for example. Fig.4.2 shows the difference of energy content on the nucleus within the two pictures, expecially at the border (more details in [Man+15]).

4.2.2 General workflow

Within the nucleus, particles experience a nuclear potential resembling a square well. As a result, the kinetic energy of particles transitioning in or out of the nucleus changes as they pass through its surface. Once inside the nucleus, particles move freely in straight lines.

4.2.2.1 Participants and Spectators

With classical interpretation of nucleon interactions within INCL, there are potential unphysical occurrences. For instance, without any external projectile influence, nucleons in the target might interact and exchange energy. This can lead to some nucleons gaining momentum beyond the Fermi level, causing them to leave even a stable nucleus, a phenomenon termed "spontaneous Fermi sea boiling."

To counteract this, INCL introduces the notion of "spectator" and "participant" nucleons. Initially, all nucleons inside the target are spectators, while those in the projectile are participants. Spectator nucleons are restricted from interacting with each other, limiting interactions only between participant-participant and spectator-participant nucleons. As interactions occur, a spectator nucleon that interacts with a participant becomes a participant itself, along with any new particles formed.

Furthermore, if a participant nucleon's energy drops below a certain threshold, it reverts to being a spectator. This approach not only prevents unphysical scenarios but also reduces computation time. However, the chosen energy limit for this transition is arbitrary, lacking a physical basis. In INCL, the threshold to revert a participant nucleon to spectator status is set at 7 MeV for neutrons and for protons, it's the emission threshold added to two-thirds of the Coulomb barrier.

4.2.2.2 Binary cascade

The intranuclear cascade (see Fig. 4.3) encompasses a three-step cycle. Initially, particles within the nucleus are advanced until a pair collides. In INCL, multi-particle interactions (three or more) aren't accommodated, except for the Pauli blocking. This decision stems from the inequality $d < \Lambda$ i.e. the scattered wave reaches its asymptotic state before the next collision and so, can be treated in the classical approach. Practically, INCL determines the site and timing of potential collisions, surface interactions, or decays—collectively known as avatars. Subsequently, the list of avatars is updated for any particle newly formed, altered, or annihilated in preceding collisions. In the INCL framework, a collision is recognized when the inter-particle distance drops below the minimum approach distance derived from their total interaction cross-sections, defined as $d_{min} = \sqrt{\sigma_{tot}/\pi}$. Concluding this step, the next avatar poised for subsequent processing is identified. The second step, primarily addressing binary collisions, ascertains the kind of the impending binary collision by randomly selecting based on pertinent reaction cross-sections, such as, for example, the reaction $\bar{N}N \to \bar{N}N\pi$. The final step creates the phase space and the charge distribution of particles in the avatar's end state. For binary collisions, this creation is either anchored on differential cross sections or phase space generators. Post this step, tests like Pauli blocking are executed. Should any test reject the end state, steps two and three are nullified, and the related avatar is excised from the processing list. This cycle persists till the end of the cascade. Notably, INCL integrates a unique constraint to sidestep reactions perennially obstructed by the Pauli principle, specifically those of minimal energy nucleon-nucleon interactions. In scenarios where paired nucleons possess a center-of-mass energy under 1910 MeV, we don't treat them, because they will be in all likelihood Pauli blocked, except if it is the first collision, in order to get the right reaction cross section.

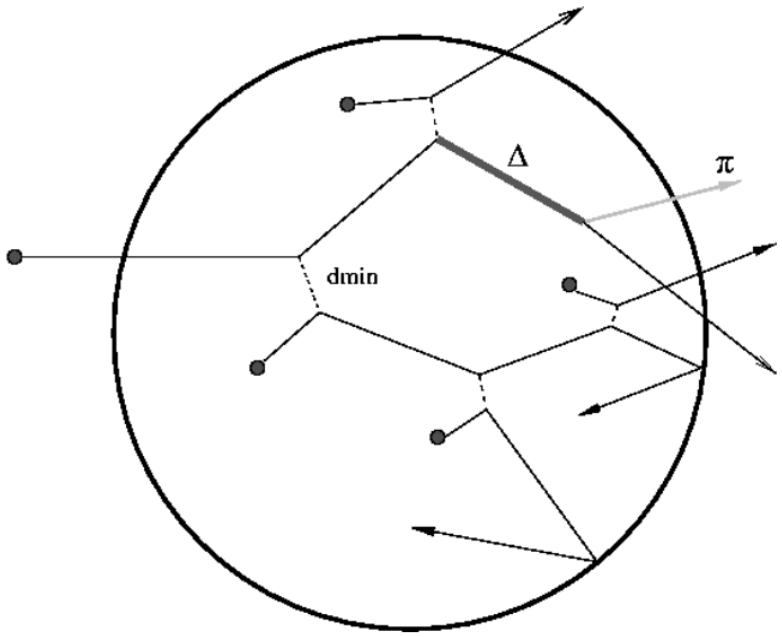

Figure 4.3: Representation of an intranuclear cascade.

4.2.2.3 Pauli blocking

Another shortcoming of the classical approach in INCL can lead to the generation of states that aren't physically possible. In particular, states prohibited by the Pauli principle must not be produced. INCL addresses this through two Pauli-blocking tests on collisions.

The first test applies to all interactions except the initial one. This test monitors the existence of similar nucleons in the final state of an interaction within a defined phase space (with Δr = 3.185 fm and Δp = 200 MeV/c). Depending on the number of particles identified in this space, the state might be blocked with a certain probability. Essentially, the acceptance probability of the collision decreases

by 21% for each similarly typed nucleon in the predetermined phase space. For the initial collision, the applied test strictly prevents the production of nucleons beneath the Fermi momentum.

The second test, applicable to all collisions, checks for vacancies in the Fermi sea that could cause the nucleus to have negative excitation energy. Both tests should be negative in order for the interaction to occur.

4.2.2.4 Particle decay

In the INCL model, particles with a half-life smaller than $10^{-20}s$ are considered for in-flight decay during the cascade. Specifically, the Δ particle with its mass chosen based on its nominal mass, width, and available energy in the collision. For other particles, like the meson ω and the Σ^0, their nominal masses are used due to their relatively small widths compared to their respective masses. The default threshold of $10^{-20}s$ is chosen rather arbitrary, so that in-flight decays of the meson ω and the Σ^0 are possible, but not for the meson η. However, the threshold value can be changed when INCL is launched.

4.2.2.5 Reflection, transmission, and cluster formation

Aside from binary collisions and particle decay during flight, interactions at the nuclear surface are treated during the cascade. When a particle approaches the nucleus's surface, it might be reflected or transmitted. The decision hinges on the transmission probability. If the nuclear potential experienced by the particle is repulsive, the particle is automatically transmitted with a transmission probability of 1. Otherwise, the transmission probability, Pt, is calculated as:

$$Pt = \frac{4 \times p_{in} \times p_{out}}{(p_{in} + p_{out})^2} e^{-2G} \tag{4.4}$$

where: p_{in} is the particle's momentum inside the nucleus, p_{out} represents the anticipated momentum outside the nucleus, accounting for the nuclear potential and binding energy adjustments, G is the Gamow factor, which is zero for neutral or negatively charged particles.

By default, particle refraction isn't considered, implying that transmitted particles retain their initial direction. But, with the INCL's input options, refraction can be computed. For particles like protons, neutrons, or Λ particles, INCL evaluates surrounding particles in phase space proximity. Potentials clusters including the primary particle are deemed formed and subsequently ejected. Default maximum cluster dimensions are $A_{max} = 12$ (default $A_{max} = 8$), $Z_{max} = 8$, and $|S|_{max} = 3$ – representing baryonic number, electric charge, and absolute strange charge respectively. The best cluster candidate is chosen based on its binding energy. Tests are then conducted to determine the cluster's viability for formation. A cluster is emitted if it surpasses the emission energy threshold, clears the Coulomb barrier, and its trajectory isn't too tangential (with $cos(\theta) \leq 0.7$). If these conditions aren't met, only the initial particle is transmitted. Despite multiple efforts to discover bound states which would include antiprotons and some other nucleons and the natural expectation for them to exist due to the presence of attractive potentials, there are yet no confirmation of their existence, so there is no clustering for antiprotons.

4.2.2.6 Cascade stopping

At certain point of the cascade all energetic particles are emitted and only those with low momenta are still wandering around reflecting from the surface, and so we set certain value of time period after which we pass our nucleus to a deexitation model:

$$t_{stop} = 29.8 \times A_T^{0.16} \tag{4.5}$$

where A signifies the initial baryonic number of the target. The cascade also halts if no nucleus-contained particle exceeds the Fermi energy by at least 10 MeV, optimizing computation time without altering the final outcome. Once the cascade ends, post-cascade processes act on the remnant's interior particles. For instance, pions get absorbed, converting their energy into nuclear excitation energy. Particles that escaped during the cascade and possess a half-life below a specified threshold are mandated to decay. Subsequently, INCL validates conservation principles, ensuring preservation

of key quantum numbers: the baryonic number, electric charge, and strange charge. While these quantum numbers are consistently conserved, the energy-momentum four-vector conservation is then checked. This evaluation aids in deducing the remnant's momentum. Ultimately, the remnant's intrinsic angular momentum gets determined by adhering to the angular momentum conservation principle.

4.2.3 Deexcitation

As the cascade time is over or terminated due to the absence of any particles with substantial energy, the remnant is still often highly excited. This is why INCL needs to be coupled to a deexcitation model, like ABLA, which was used in our case. This will ensure the fulfillment of the low energy parts of the emitted particle spectra and will produce a proper nuclear remnant in its ground state. The nucleus has several potential deexcitation pathways. Specifically, it can emit light particles such as γ-rays, nucleons, hyperons, or α-particles. Heavier clusters, known as intermediate mass fragments, can also be emitted. Another deexcitation mechanism is nuclear fission. All these processes compete, and the remnant might utilize multiple deexcitation channels either sequentially or concurrently. Ultimately, if the energy of the remnant is sufficiently high, a multi-fragmentation process might happen.

After the remnant has discarded all its surplus energy and achieved a bound state, the deexcitation and, consequently, the cascade simulation is finished. It's worth noting that the final nucleus resides in its ground state and is stable, but it can be very radioactive. When residual nuclei yields are studied, the outcomes from the INCL-ABLA model should be assessed considering radioactive decay chains, which will be addressed in chapter 5 (page 66) in more detail.

4.3 Antiprotons in GEANT4

It is important to mention that there is current interest among the people of GEANT4 collaboration to introduce new models for $\bar{p}$ interactions modelling, as there are many experiments mentioned above which may require simulations with transport codes, while there is currently only two models available in GEANT4 which is Fritiof (FTF) and Parton String model.

FTF is utilized in GEANT4 for simulating hadron-nucleus, nucleus-nucleus, $\bar{N}$-nucleus, and antinucleus-nucleus interactions. The model's validity is capped at 1000 GeV/c per hadron or nucleon. It assumes the production of unstable objects, termed quark-gluon strings, in elementary interactions. These objects can interact with other nucleons and can generate additional objects in hadron-nucleus and nucleus-nucleus collisions. In the FTF model, hadron-nucleon interactions are simulated, encompassing elastic scattering, diffractive events, non-diffractive events, and annihilation in antibaryon-nucleon interactions. The LUND string fragmentation model simulates the decay of these unstable objects. The model also uses a simplified Glauber model for multiplicity sampling and integrates the reggeon theory inspired model (RTIM) for secondary particle cascading. More information on FTF could be found in the GEANT4 physics reference manual and in publications[Uzh10; Uzh11]. We would include the results of FTF into some comparisons in chapters 5 and 6.

The Parton String model has a recommended projectile energy of more than 5 GeV. Two approaches, based on diffractive excitation or soft scattering with diffractive admixture according to cross-section, are considered. Hadron-nucleus collisions in the both approaches (diffractive and parton exchange) are considered as a set of the independent hadron-nucleon collisions. However, the string excitation procedures in these approaches are rather different [Cap+94; BCG12].

References

[BCG12] Baznat, M.I., Chigrinov, S.E., and Gudima, K.K. "QGSM development for spallation reactions modeling". In: *EPJ Web of Conferences* 38 (2012), p. 17003. doi: 10.1051/epjconf/20123817003.

[Boh36] Niels Bohr. "Neutron Capture and Nuclear Constitution". In: *Nature* 137.3461 (Feb. 1936), pp. 344–348. issn: 1476-4687. doi: 10.1038/137344a0.

[Bou+02] A. Boudard et al. “Intranuclear cascade model for a comprehensive description of spallation reaction data”. In: *Phys. Rev. C* 66 (4 Oct. 2002), p. 044615. doi: 10.1103/PhysRevC.66.044615.

[Bou+13] A. Boudard et al. “New potentialities of the Liège intranuclear cascade model for reactions induced by nucleons and light charged particles”. In: *Phys. Rev. C* 87 (1 Jan. 2013), p. 014606. doi: 10.1103/PhysRevC.87.014606.

[Cap+94] A. Capella et al. “Dual parton model”. In: *Phys. Rept.* 236 (1994), pp. 225–329. doi: 10.1016/0370-1573(94)90064-7.

[CDV88] J. Cugnon, P. Deneye, and J. Vandermeulen. “Charge distribution and charge correlation in the annihilation of antiprotons on nuclei”. In: *Phys. Rev. C* 38 (2 Aug. 1988), pp. 795–799. doi: 10.1103/PhysRevC.38.795.

[CDV90] J. Cugnon, P. Deneye, and J. Vandermeulen. “Strangeness production in antiproton annihilation on nuclei”. In: *Phys. Rev. C* 41 (4 Apr. 1990), pp. 1701–1718. doi: 10.1103/PhysRevC.41.1701.

[CKV82] J. Cugnon, D. Kinet, and J. Vandermeulen. “Pion production in central high energy nuclear collisions”. In: *Nuclear Physics A* 379.3 (1982), pp. 553–567. issn: 0375-9474. doi: https://doi.org/10.1016/0375-9474(82)90014-8.

[CMV81] J. Cugnon, T. Mizutani, and J. Vandermeulen. “Equilibration in relativistic nuclear collisions. A Monte Carlo calculation”. In: *Nuclear Physics A* 352.3 (1981), pp. 505–534. issn: 0375-9474. doi: https://doi.org/10.1016/0375-9474(81)90427-9.

[Cug+95] J Cugnon et al. “Double strangeness production in low-energy antiproton-nucleus annihilation”. In: *Nuclear Physics A* 587.4 (1995), pp. 596–608. issn: 0375-9474. doi: https://doi.org/10.1016/0375-9474(95)00006-M.

[Cug87] J. Cugnon. “Proton-nucleus interaction at high energy”. In: *Nuclear Physics A* 462.4 (1987), pp. 751–780. issn: 0375-9474. doi: https://doi.org/10.1016/0375-9474(87)90575-6.

[Cug92] J. Cugnon. “Antideuteron annihilation on nuclei”. In: *Nuclear Physics A* 542.4 (1992), pp. 559–578. issn: 0375-9474. doi: https://doi.org/10.1016/0375-9474(92)90257-K.

[CV87] J. Cugnon and J. Vandermeulen. “Two-body exit channels in $\bar{p}$-p and $\bar{p}$-nucleus annihilations”. In: *Phys. Rev. C* 36 (6 Dec. 1987), pp. 2726–2728. doi: 10.1103/PhysRevC.36.2726.

[CV89a] J. Cugnon and C. Volant. “Multifragmentation in the intranuclear cascade — percolation approach”. In: *Zeitschrift für Physik A Atomic Nuclei* 334.4 (Dec. 1989), pp. 435–442. issn: 0939-7922. doi: 10.1007/BF01294750.

[CV89b] Cugnon, J. and Vandermeulen, J. “Antiproton-nucleus interaction”. In: *Ann. Phys. Fr.* 14.1 (1989), pp. 49–87. doi: 10.1051/anphys:0198900140104900.

[CV92] J. Cugnon and J. Vandermeulen. “Medium effects in antiproton annihilation on nuclei. A phase space approach”. In: *Physics Letters B* 279.1 (1992), pp. 5–9. issn: 0370-2693. doi: https://doi.org/10.1016/0370-2693(92)91830-3.

[Dav+18] J.-C. David et al. “η and ω mesons as new degrees of freedom in the intranuclear cascade model INCL”. In: *The European Physical Journal Plus* 133.7 (July 2018), p. 253. issn: 2190-5444. doi: 10.1140/epjp/i2018-12079-9.

[Hir+18] J. Hirtz et al. “Parametrization of cross sections for elementary hadronic collisions involving strange particles”. In: *The European Physical Journal Plus* 133.10 (Oct. 2018). doi: 10.1140/epjp/i2018-12312-7.

[Hir+20] J. Hirtz et al. “Strangeness production in the new version of the Liège intranuclear cascade model”. In: *Physical Review C* 101.1 (Jan. 2020). doi: 10.1103/physrevc.101.014608.

[JCV88] P. Jasselette, J. Cugnon, and J. Vandermeulen. “Residual mass distribution following $\bar{p}$-nucleus annihilation”. In: *Nuclear Physics A* 484.3 (1988), pp. 542–556. issn: 0375-9474. doi: https://doi.org/10.1016/0375-9474(88)90309-0.

[Man+14] Davide Mancusi et al. “Extension of the Liège intranuclear-cascade model to reactions induced by light nuclei”. In: *Phys. Rev. C* 90 (5 Nov. 2014), p. 054602. doi: 10.1103/PhysRevC.90.054602.

[Man+15] Davide Mancusi et al. “Improving the description of proton-induced one-nucleon removal in intranuclear-cascade models”. In: *Phys. Rev. C* 91 (3 Mar. 2015), p. 034602. doi: 10.1103/PhysRevC.91.034602.

[Rod+17] Jose Luis Rodríguez-Sánchez et al. “Improvement of one-nucleon removal and total reaction cross sections in the Liège intranuclear-cascade model using Hartree-Fock-Bogoliubov calculations”. In: *Phys. Rev. C* 96 (5 Nov. 2017), p. 054602. doi: 10.1103/PhysRevC.96.054602.

[Ser47] R. Serber. “Nuclear Reactions at High Energies”. In: *Phys. Rev.* 72 (11 Dec. 1947), pp. 1114–1115. doi: 10.1103/PhysRev.72.1114.

[Uzh10] Vladimir Uzhinsky. “Development of the Fritiof model in Geant4”. In: Proceedings of SNA + MC2010: Joint international conference on supercomputing in nuclear applications + Monte Carlo 2010 Tokyo. PHYSICS OF ELEMENTARY PARTICLES AND FIELDS. Japan, 2010, p. 1630.

[Uzh11] V. Uzhinsky. *Tuning of the GEANT4 FRITIOF (FTF) Model Using NA61/SHINE Experimental Data*. 2011.

5 Antiproton at rest annihilation

5.1 General hypothesis and workflow

As a heavy charged particle, antiproton loses its energy rapidly via electromagnetic interaction as it passes through the matter. At some point its energy becomes low enough, so that it can be captured into a high atomic orbit of an atom, after which it will cascade down towards the nucleus. During capture and early stages of electronic shell cascade, the electrons are expelled. The problem is that from the theoretical point of view, it is not forbidden for antiproton to interact directly with the nucleus even at very low momentum, so it is not trivial to define the threshold value of energy, at which antiproton annihilation would proceed through atomic shell capture and cascade, rather than direct particle-nucleus collision.

One possible way to define such an arbitrary threshold is the value of momentum, at which the lightest meson production, without annihilation becomes kinematically possible. Namely, the π^0 production at 775 MeV/c or ≈278 MeV of kinetic energy of the antiproton (see Fig.5.1). This could be justified with the reason, that such production channel, if available, would significantly change the spectrum of outgoing pions, while the elastic scattering or charge-exchange reaction (i.e. $p\bar{p} \rightarrow n\bar{n}$), will not change the destiny of a $\bar{p}$ significantly - annihilation may happen in a neighbour nucleus, but it is still inevitable. The case of direct (i.e. in-flight) interaction of antiproton with the nucleus will be considered in the next chapter. As it follows from the INC formulation by Serber[Ser47] the wave function is too large at low energy to interact via binary collision with nuclei. Also, the cross section parametrizations might diverge from the reality due to the lack of data points in low energy region.

One might pose a question about the cross-section of the capture of an antiproton in order to compare it with the nuclear cross sections. While certain efforts have been made to study this problem, experimental measurements of a process like this are difficult to conduct as it requires precise observation of Auger-electrons and the γ-rays simultaneously. Moreover, from my personal communication with Slawomir Wycech experimentalists have noticed the difference in capture behaviour and even in the annihilation orbit for targets made of bulk metal and of glued powdered metal for certain isotope, however, this problem was too complex to be thoroughly studied at the time. Nevertheless, attempts have been made to understand the capture process of heavy negative particles via the fermion-molecular-dynamics method[Coh97; Coh00; Coh04], which found that capture process can be greatly enhanced by multiple ionization and molecular rotational-vibrational excitations as well as increase the maximum energy of capture, with the latter leading to a significant dependence on the projectile mass and target isotope. We won't deal here with this atomic conundrum, as we believe that electronic orbitals occupy much more volume in the matter, than the nucleus, and thus we expect the antiproton to annihilate via the Coulombic cascade at low energies. This chapter is fully devoted to the simulation of such scenario (from now on referred to as at rest annihilation), specifically the final part, when antiproton approaches the nucleus close enough to annihilate.

The way we model at rest is quite similar to a normal INCL workflow, but with a different initialization procedure. Instead of shooting a particle with randomized impact parameter, we place the products of $\bar{p}p$ or $\bar{p}n$ annihilation at a certain distance from the center of the nucleus. Here is another assumption: we do not consider the so called Pontecorvo reactions, which might involve a deuteron instead of a nucleon in the annihilation step. We use experimental data to determine the final state particles produced in annihilation, and we use the embedded phase-space model of INCL to determine their energies and momenta in a Monte-Carlo fashion. INCL uses this phase-space model for binary collisions, when more than two particles are produced and momenta of outgoing particles have to be defined.

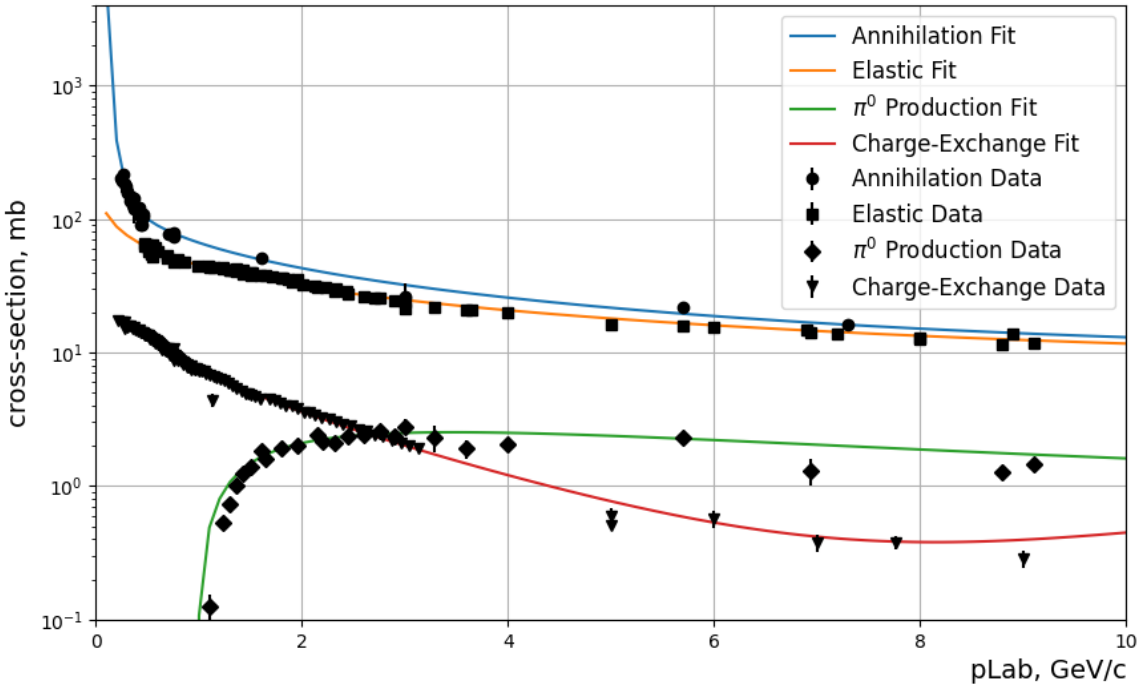

Figure 5.1: Elementary cross-sections for $p\bar{p}$. 0.775 GeV/c is the threshold of pion production. Cross section data is taken from Ref. [Bal+87]. Fits are done with $f(x) = a + b \cdot x^c + d \cdot \ln(x) + e \cdot \ln(x)^2$ recommended in the same reference.

We do not take into account the additional possible Fermi energy which the nucleon could have owned before, nor the deductible energy which antiproton have emitted in form of γ-rays and Auger-electrons prior to annihilation The total energy of the final state particles is assumed to be equal to the sum of masses of annihilated baryons ($\bar{p}p$ or $\bar{p}n$). Also, we initialize nucleus from the very beginning as it was lacking either a proton or a neutron (depending on which is chosen to be annihilated). For example, if antiproton annihilates at rest on a ^{197}Au target, the nucleus would be initialized as ^{196}Au or ^{196}Hg.

After assigning energy and momentum to each of the final state particles (meson star) and computing their position in relation to the nucleus (nucleus is assumed to be spherically symmetrical, so the 3D vector of the meson star position reduces to distance from the center of the nucleus). After all mesons and nucleons are initialized the intra-nuclear cascade proceeds as usual.

5.2 Model ingredients

Hereafter we will discuss the constituents of our model approach, namely the rules of defining the distance from the center of the nucleus, the choice between proton or neutron to annihilate, the choice of the final state mesons and the formula used for the reaction cross section.

5.2.1 Annihilation distance

The illustration in Fig.5.2 may visually represent the at rest annihilation process in INCL. From this picture one might see that as the annihilation point is closer to the center, there will be more secondary interactions, thus the amount of nucleons emitted will increase, as they can be kicked away by primary mesons. For the amount of emitted pions it is not so obvious, because a pion can be absorbed by a nucleus, but may also be produced in binary collisions of the cascade. By interacting with the nucleus primary mesons will "thermalize", thus changing the emitted particle spectra.

The distance of annihilation in INCL is sampled in a distribution which is the overlap of antiprotonic radial density with the nuclear densities (for protons and neutrons) of the target nucleus (see Fig.5.3).

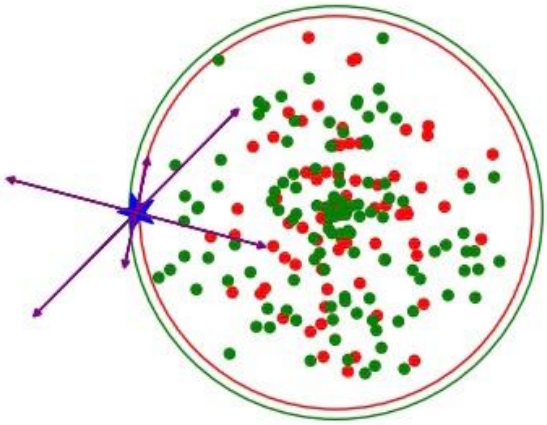

Figure 5.2: Illustration of a meson star production in the vicinity of the nucleus. Arrows are the primary mesons, some of which escape immediately with so secondary interaction, while some will cause secondary binary collisions.

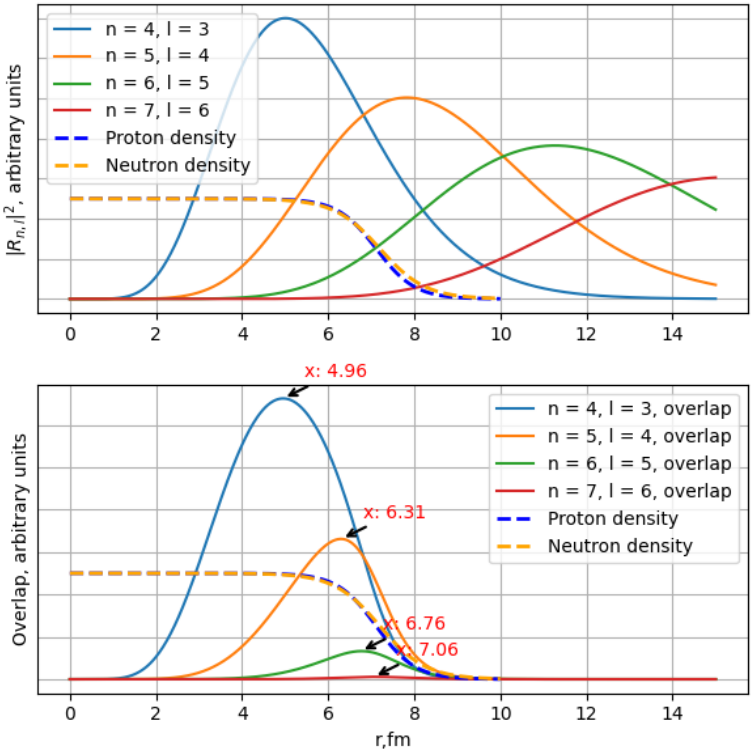

Figure 5.3: Top plot: proton and neutron Wood-Saxon distributions are drawn for Au^{197} nucleus together with antiproton atomic density probability distributions $|R_{n,l}|^2$ for different orbits and angular momentum. Normalization is not completed, so the y axis is arbitrary units.
Bottom plot: Overlap of antiproton atomic densities with proton density distributions. Antiproton orbit at n=7, l=6 has practically zero overlap with the nucleus. Mean annihilation distance is denoted in red for each orbit.

The overlap is computed as:

$$P_{neutronic}(r) = N_{nl} \times \rho_n \times r^2 \times |R_{n,l}|^2 \tag{5.1}$$

$$P_{protonic}(r) = N_{nl} \times \rho_p \times r^2 \times |R_{n,l}|^2 \tag{5.2}$$

where N_{nl} is the normalization constant, ρ_n, ρ_p are the nuclear densities for neutrons and protons, r is the distance from the nuclear center and $|R_{n,l}|$ is the radial component of the $\bar{p}$ atomic wave function. For clarity, the exact formulas taken from a quantum mechanics textbook used for $|R_{n,l=n-1}|$ and N_{nl} are provided:

$$|R_{n,l=n-1}| = ((2n)!)^{\frac{1}{2}} \left(\frac{2}{na}\right)^{\frac{3}{2}} \left(\frac{2r}{na}\right)^{(n-1)} \exp\left(\frac{-r}{na}\right)$$

$$N_{nl} = \frac{2}{n^2}\sqrt{\frac{(n-l-1)!}{((n+l)!)^3}} \quad \text{(a is the Bohr radius)}$$

first, we choose the type of nucleon (proton or neutron, see section 5.2.2) to annihilate with, then we compute the overlap function $P(r)$ for a known orbit of annihilation and chosen type of nucleon, and finally, we place the final state particles with randomized momenta at the distance sampled randomly from the overlap function $P(r)$. Henceforth, the detailed discussion about each component of this computation is presented in the following subsections.

5.2.1.1 Orbit of annihilation

We know from the γ-spectroscopy experiments[Pot84; Wyc+93] that as the antiproton cascades through the atomic shell down the nucleus, radiative transitions are only visible, till certain principal quantum number is reached, at which the width of annihilation becomes substantially higher that the width of subsequent radiative transition to a lower orbit. This value of n is called the last observed annihilation orbit, meaning that the annihilation does not occur at lower orbits, but it still can occur at the n values precedent to last observed n. In fact, processes of radiative transition, Auger-electron emission and annihilation compete with each other, so annihilations may happen prior to reaching the last observed n value. Experimentally it is seen as the reduction in intensity of radiative γ-transitions before the last observed n.

In certain exotic cases, nuclear excitation modes (e.g. the E2-resonance) may couple to $\bar{p}$-atomic state energy and lead to nuclear-resonance effect in antiprotonic atoms, first observed with Molybdenum isotopes in experiment PS186 at LEAR[Kan+86]. The possibility of such effect lies in the proximity of the $\bar{p}$-atomic transition energy to the excitation energy of the nucleus, which greatly enhances the transition probability (see Fig.5.4). Effectively, it means that isotope ^{100}Mo would annihilate the $\bar{p}$ at a lower orbit, than the others. Such effect is highly pronounced for ^{100}Mo, but was also observed in other nuclei[Wyc+93], whenever certain $\bar{p}$-atomic transition energy is close to nuclear excitation levels.

In the previous paragraphs I tried to outline the peculiarities of the annihilation orbit determination, which drastically complicate their ab initio estimation for an arbitrary isotope of arbitrary element. Hence, the phenomenological approach was chosen instead, and the last observed annihilation orbit from γ-spectroscopy experiments was taken for those elements, which have been studied experimentally. Based on these measurements, for the sake of simplicity, a cubic fit was done over the existing data in order to define the annihilation orbit for any possible target, which could be used in INCL, data, the fit and fitted elements are displayed in Fig.5.5. As we will see in the sensitivity analysis section, such approximation changes the observable statistics negligibly.

5.2.2 $\bar{p}p/\bar{p}n$ annihilation ratio

In our model, antiproton is able to annihilate at rest with either proton or neutron, Pontecorvo reactions (i.e $\bar{p}d$) are not considered. The probabilities of selecting one of these two nucleons depend on several factors. These factors include the quantity of these nucleons in the target nucleus, the Coulombic attraction towards protons, the radii and diffuseness parameters of the corresponding density distributions, and the composition of the outer nuclear shell. For example, some heavy nuclei with the excess of neutrons might possess an outer neutron skin (could be seen in the case of

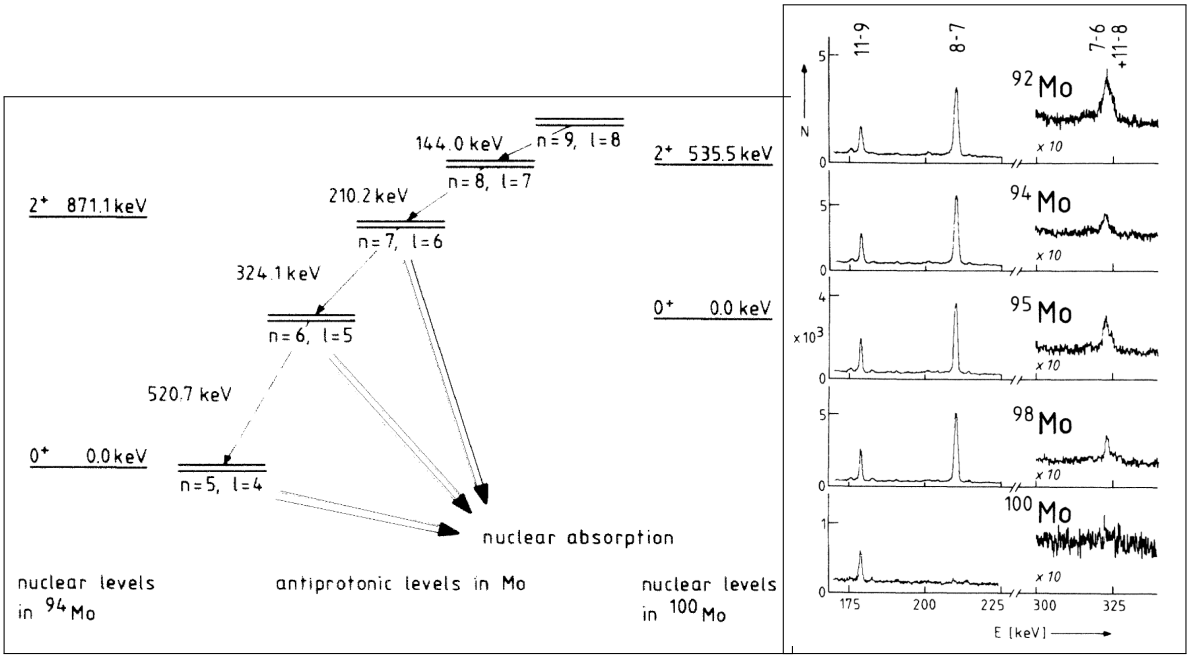

Figure 5.4: Left part: Scheme of nuclear and $\bar{p}$-atomic levels in Mo^{94} and Mo^{100} relevant to the E2-resonance effect[Kan+86]. Right part: Parts of the antiprotonic x-ray spectra for Molybdenum isotopes. Normally, for molybdenum the last observed transition is 7->6, after which it surely annihilates, but in case of Mo^{100} the transition energy from (n=8,l=7) to (n=6,l=5) is very close to E2-excitation energy, so that the transitions 8->7 and 7->6 are strongly attenuated[Kan+86].

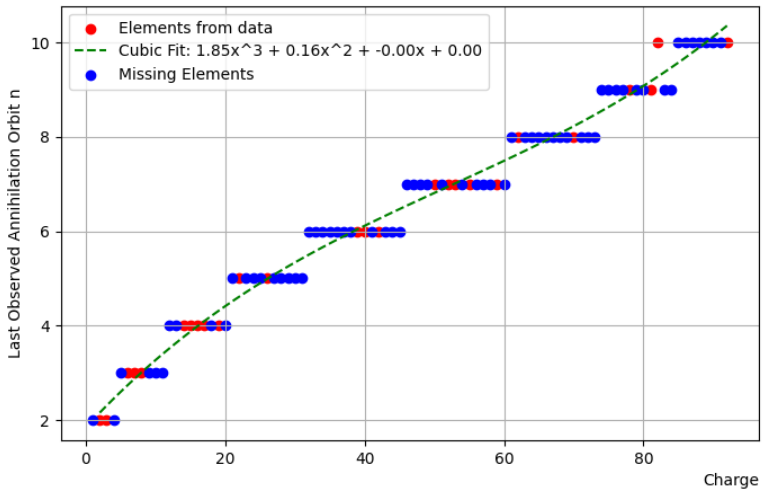

Figure 5.5: Principal quantum number n distribution for wave functions used to compute the annihilation distance in INCL. The red points are taken from γ-spectroscopy data[Pot84; Wyc+93], lightest element from data for each value of n is labelled. These data points are fitted with a curve, and for all other elements annihilation orbit n is defined with the fit.

^{197}Au nucleon distributions in Fig.5.3), also known in some articles as neutron halo[Chr+22; Bug+73; Wyc+96].

Taking all of these factors into account is a non-trivial task, thus we assumed that the probabilities would be same as for a deuterium target taken from [KBR05a] weighted with the corresponding quantities of protons and neutrons:

$$S_p/S_n(Z,A) = S_p/S_n(D_2)\frac{Z}{A-Z} \tag{5.3}$$

where $S_p/S_n(D_2) = 1.331 \pm 0.019$ [Biz68] S_p/S_n here is the ratio of probabilities for proton and neutron to be chosen. The validity of this simplification will be examined for a range of target nuclei in the sensitivity analysis section5.4. For now we just want to mention that there exist slightly different experimental values of this parameters obtained by other groups in Table 5.1.

Table 5.1: Table Caption

Group	S_p/S_n
Rome-Syracuse[Bar+64]	1.31 ± 0.03
Berkeley[CK66]	1.33 ± 0.07
Padova-Pisa[Bet+67]	1.45 ± 0.07

Moreover, in a later study [Biz+74] proton and neutron annihilation cross-section measurements have been done for antiproton-deuterium annihilations at different incident $\bar{p}$ momentum ranging from 333 MeV/c up to 591 MeV/c which corresponds to energies roughly between 57 and 170 MeV. The results for the value $S_n/S_p = \frac{1}{S_p/S_n} = \sigma_{ann,n}/\sigma_{ann,p}$ were scattered non-linearly between 0.730 and 0.882, which corresponds to the range of S_p/S_n between 1.113 and 1.369. Deuterium is a specific target which has very low stopping power, in this case it might be incorrect to assume the annihilation via the capture process, so we see the energy dependence of the S_p/S_n ratio, while if for the annihilation from atomic orbits, we believe that this ratio should remain constant for a given $\bar{p}$ orbit

5.2.3 Final states

All types of mesons which have their mass less than the mass of a proton could be possibly produced as a final state particles of annihilation, but most of them decay rapidly. In INCL we only consider pions, kaons, ω and η, so if data contains particles like $\rho^{\pm}$ or ρ^0, for example, they are converted into their decay products according to know probabilities. Tables of final states for $\bar{p}p$ $\bar{p}n$ annihilations with their frequencies (in %) were taken from the compilations[KBR05a; Gol+92]. Most frequencies are results of direct experimental observations, some were derived by using the isotopic relations. From the experimental values the probabilities for those channels that have the same configuration but different particle charges were added. Finally, for the remaining intermediate channels allowed by the energy conservation, the predictions based on the SU(3) symmetry law were fulfilled. The tables could be accessed via the INCL code or from the publications[KBR05a; Gol+92].

Final states containing kaons are placed in a separate table and kaonic final states have overall 5% probability to occur in average. This was done to be able to test the sensitivity of this parameter later, and also due to the peculiarities of neutral kaon detection by different experiments. Neutral kaons are famous for their ability to decay as Kshort (even number of decay products) or Klong (odd number of decay products) while they propagate as K^0 and $\bar{K}^0$. In our final states tables we are required to input the propagation state of neutral kaon, for example, the $\bar{p}p$ annihilation may result in $K^0K^-\pi^+$ or $\bar{K}^0K^0\pi^+\pi^-$ meson star. Experiments instead can measure the decay states K_short or K_long, and the probability of, say K^0 to decay like K_s or K_l depend on the detector materials (see neutral kaon regeneration effect), detector geometry and kaon momenta (see neutral kaon oscillation effect). Thus, the detector data has to be reinterpreted to infer the initial final state composition, not to mention the difficulties of measuring the decay products of K_l, which not all detectors are able to reconstruct reliably. A demonstrative example of neutral kaon decay intricacy was given in Ref. [Adl+97], where the ratio K_sK_s/K_lK_l of the detected pairs of neutral kaons is found to be dependent on the hydrogen pressure in the annihilation chamber.

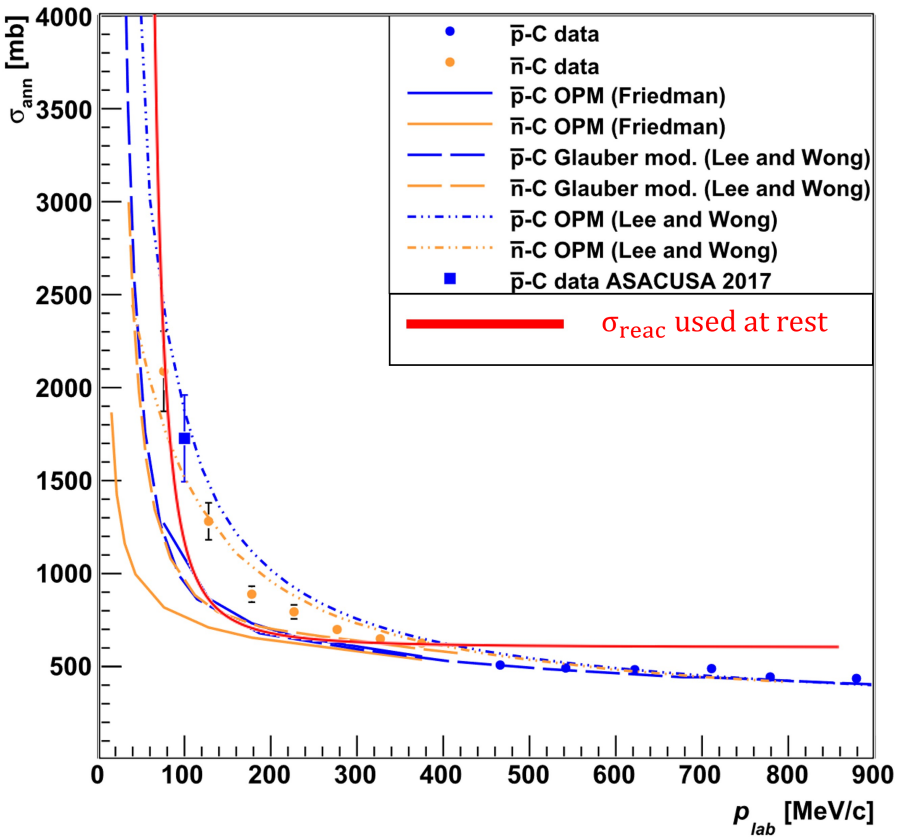

Figure 5.6: Antinucleon σ_{reac} at low energies on carbon. In orange the antineutron values, in blue those for antiproton. The points are the experimental data. The continuous lines represent the calculations with the optical potential model. The dashed lines are from the calculations with the extended Glauber model. The dotted-dashed lines are preliminary calculations obtained by means of a phenomenological optical model whose parameters are tuned to reproduce the N-nucleus annihilation data. Red line is the formula used in INCL from Ref.[Bia+11]. The original plot is taken from Ref.[Agh+18].

From the Ref.[AF69] the total yield of strange particle production was found to be $(6.82 \pm 0.25)\%$, while estimation of Batusov et al. was $(4.74 \pm 0.22)\%$ [Bat+88]. The recommended value from Ref.[KBR05b] was:

$$BR(\bar{p}p \rightarrow kaons + anything) = (5.4 \pm 1.7)\% \tag{5.4}$$

which is why we inserted the 5% probability as a default value in our model, we will discuss the influence of this parameter in the sensitivity analysis section later.

5.2.4 Reaction cross-section

In at rest annihilation we use frequencies instead of cross sections, and INCL outputs emitted particle and residual nucleus data after completion of cascade and de-excitation, the total reaction cross section is given with a post-process. In experiments researchers often provide data in form of cross-sections. For this reason one requires a normalization value, also known as the reaction cross section, to convert particle yields into barns. This is why we searched for a simple formula, which would work for all possible target isotopes, finally the one from Ref.[Bia+11] has been chosen:

$$\sigma_{reac} = \pi R^2 \left(1 + \frac{Ze^2(m_{\bar{p}} + M_{target})}{4\pi\epsilon_0 E_{kin} R M_{target}}\right) \tag{5.5}$$

where $R = R_0 \cdot A^{1/3}$, ϵ_0 is the vacuum permittivity and e is the elementary charge. One can see in Fig. 5.6 how it compares with experimental data and other approaches to compute the reaction cross section. This formula is only used for normalization in INCL, but not in Geant4, as the Geant4 has its own embedded procedure to normalize cross-sections. Still, this factor would introduce some additional uncertainty in case INCL is used as standalone version.

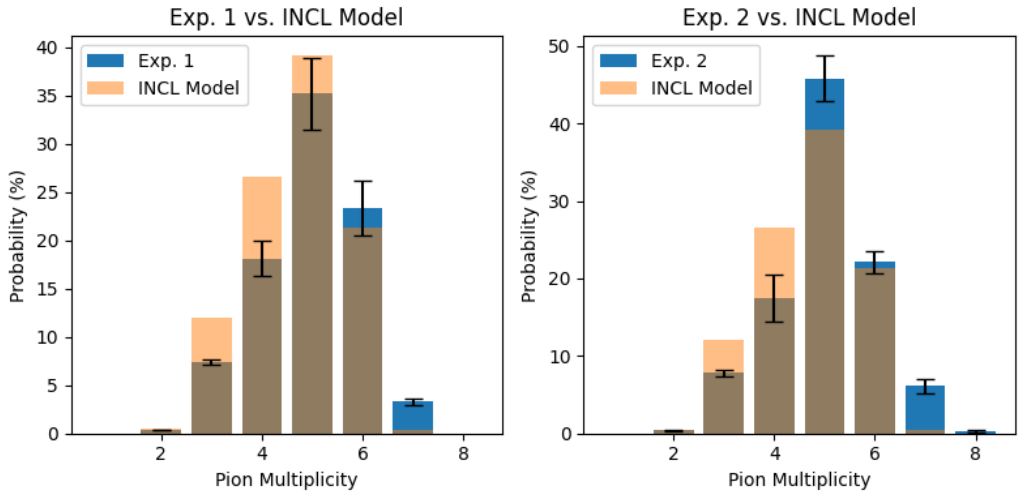

Figure 5.7: Pionic multiplicity distributions from [Ams+03](exp. 1) and [Ghe74](exp. 2) vs INCL $p\bar{p}$

5.3 Comparison to the experimental data

The main outputs of our model are the multiplicities and spectra of emitted particles and characteristics of residual nuclei. In this section we will compare the results of INCL with the results of certain experiments.

5.3.1 Multiplicities

Let's first discuss the multiplicity of pions in elementary $p\bar{p}$ at rest annihilations. In fact, such parameter may be considered as verification of the model, because elementary $p\bar{p}$ collisions are not typically modelled with intra-nuclear cascades, but may occur when our model will be used within Geant4. First, lets have a look at the pion multiplicity distributions of INCL compared with two sets of data: one deduced by the Crystal Barrel [Ams+03] and another by CERN-College de France collaboration [Ghe74], both presented in the table 5.2 along with INCL and plotted in Fig. 5.7.

Table 5.2: Comparison of Experimental Pionic multiplicity distributions with INCL Model

Number of Pions	Ref. [Ams+03] (%)	Ref. [Ghe74] (%)	INCL (%)
2	0.38 ± 0.03	0.38 ± 0.03	0.48
3	7.4 ± 0.3	7.8 ± 0.4	12.01
4	18.1 ± 1.8	17.5 ± 3.0	26.55
5	35.2 ± 3.7	45.8 ± 3.0	39.16
6	23.3 ± 2.8	22.1 ± 1.5	21.37
7	3.3 ± 0.3	6.1 ± 1.0	0.43
8	-	0.3 ± 0.1	0.00

As we can see from both comparisons, INCL produces pions in lower amounts averagely. As we said earlier, we only implement those final states, for which we found the exclusive channel probability, like $p\bar{p} \to 3\pi^+ 3\pi^- 2\pi^0$ for example, and such channels might be harder to measure experimentally, as one needs to detect all particles simultaneously, to get the full final state composition. This is different from average pionic multiplicity measurements, where one just estimates the count quantity. Also, the more final state particles are produced, the higher is the probability for certain simultaneous pions with vicinal momentum vectors to be detected as one, so the systematic underestimation might occur. In case of INCL we populate final states, which among pions contain ω, η-mesons and kaons. All mesons we decomposed into their decay products using the corresponding branching ratios, except for kaons, which might also reduce the pion multiplicity in INCL. Here are the average multiplicity

values deduced from Crystal Barrel data:

$$\begin{aligned} N(\pi) &= 4.98 \pm 0.35, \\ N(\pi^{\pm}) &= 3.14 \pm 0.28, \\ N(\pi^{0}) &= 1.83 \pm 0.21 \end{aligned} \tag{5.6}$$

while in INCL we have for $p\bar{p}$:

$$\begin{aligned} N(\pi) &= 4.904, \\ N(\pi^{\pm}) &= 3.1, \\ N(\pi^{0}) &= 1.804 \end{aligned} \tag{5.7}$$

and for $n\bar{p}$:

$$\begin{aligned} N(\pi) &= 4.911, \\ N(\pi^{\pm}) &= 3.195, \\ N(\pi^{0}) &= 1.717. \end{aligned} \tag{5.8}$$

For some other mesons, such as the η-meson, the average multiplicity reported in reference [Chi+89] is 0.0698 $\pm$ 0.0079, whereas INCL predicts a value of 0.906. Still, the experimental multiplicity numbers are different among sources and a compilation of such measurements and estimations can be found in at rest annihilation physics review by Klempt et al. [KBR05b].

After we got a brief idea of how our inputs work in comparison to $p\bar{p}$ annihilations, which is related to verification step of the model, we now may switch to validation by comparing INCL outputs to experimental multiplicities collected with heavier targets. For instance, one may test whether the equation 5.3 (S_p/S_n) is an acceptable assumption. In experiment we may not directly measure the ratio between proton and neutron annihilations, but there are still some observables to shed light on it. This ratio may be inferred from the ratio of emitted pions π^+/π^-. Such measurements were done in Ref. [McG+86a] from where we have total inclusive cross section values of $\bar{p} + (A, Z) \rightarrow \pi^{\pm} + X$ for ^{12}C, ^{89}Y and ^{238}U targets at 197 MeV incident antiproton energy, the information is summarized in Table. 5.3. Ratio π^+/π^- for ^{12}C at $E_{kin}(\bar{p})$ = 21 MeV(200 MeV/c) was estimated in Ref. [Bug+73; WL76] to be 0.780$\pm$0.012 and 0.784$\pm$0.015 correspondingly, while for ^{14}N target the result was 0.800$\pm$0.080 from Ref. [Rie+89] (INCL gives 0.77368 for ^{14}N).

Table 5.3: Total pion-production cross sections and their ratio from Ref. [McG+86a] compared with INCL. $E_{kin}(\bar{p})$ = 180 MeV (608 MeV/c).

Target	σ_{π^+} **(mb)**	σ_{π^-} **(mb)**	π^+/π^- **exp.**	π^+/π^- **INCL**
^{12}C	488 ± 31	631 ± 41	0.773 ± 0.070	0.764
^{89}Y	1240 ± 80	1760 ± 110	0.705 ± 0.063	0.698
^{238}U	2000 ± 130	3000 ± 190	0.667 ± 0.061	0.656

The ratios are taken for the measured cross sections of data and for the yields of INCL, thus the normalization factor is excluded. Also, it should be noted that the incident momentum was 608 MeV/c, at which antiproton has a chance to annihilate via in-flight scenario. We will consider this energy domain more in detail in the next chapter. For now, we might reproduce some phenomenological analysis done in Ref. [WP23], which considers pionization as a method to study the nuclear surface. As we know, in the free space, the total charge carried by mesons in $p\bar{p}$ annihilation is Q = 0. The rate of this process can be normalized in nucleus to be 1 and refer other rates relative to this:

$$P_{ini}(Q = 0) = 1. \tag{5.9}$$

With this normalization the rate of initial $n\bar{p}$ annihilations is defined as:

$$P_{ini}(Q = -1) = \frac{A - Z}{Z} R_{n/p} f_{halo}, \tag{5.10}$$

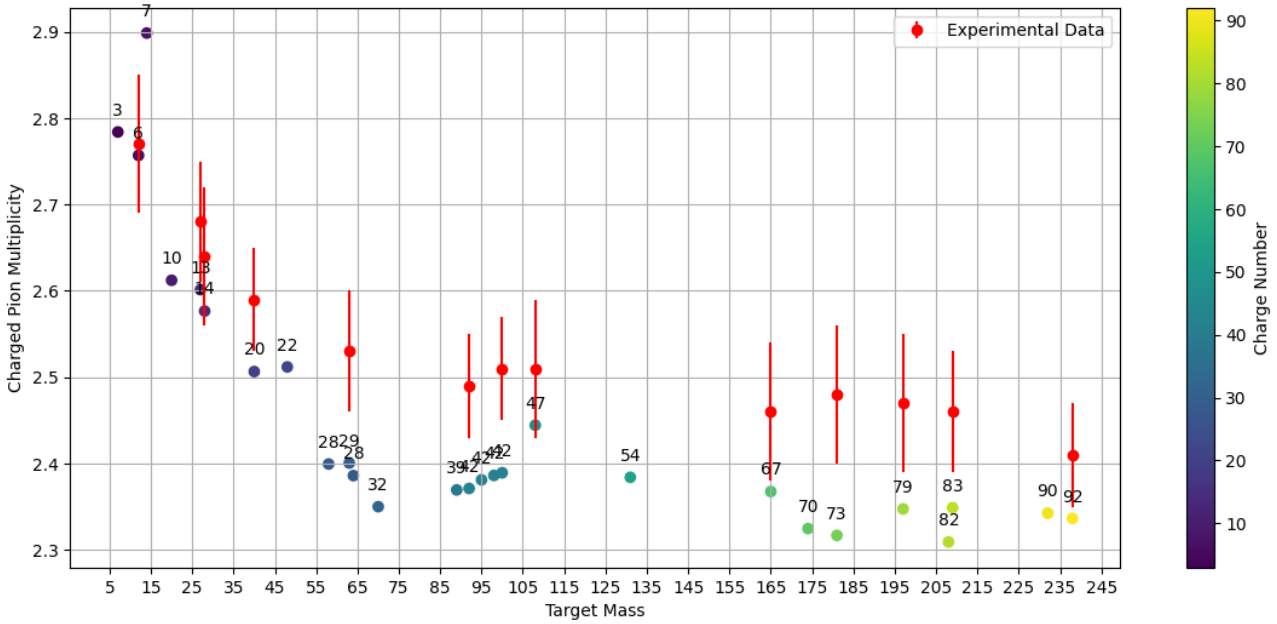

Figure 5.8: Charged pion multiplicities for a group of target nuclei from INCL, experimental values with errors are taken from [Pol+95]. No nuclei with the same mass number are present on this plot; the charge numbers are color-coded.

The halo factor f_{halo} was introduced by Bugg et al. [Bug+73] to represent an additional excess of neutrons over protons in the capture region. Note, that this definition of halo has no universal value because it depends on the initial atomic capture state as well as on the experimental method chosen to detect the final products: residuals, mesons, or atomic x-rays. Also, the term halo is defined differently in certain nuclear models[RBD09] and the factor f_{halo} which we will be using hereafter has no meaning in this context.

The "real" rate of mesons also depends on absorption rate of the nucleus and the rate of charge-exchange reactions, which converts charged pions into neutral, e.g. $\pi^+ n \to \pi^0 p$ or $\pi^- p \to \pi^0 n$. Even nuclei with Z = A-Z have different absorption and conversion rates for pions of different charge. There is also a reverse conversion of neutral pions into charged ones, which should be taken into account. By isospin symmetry the direct and the inverse reactions offer the same transition amplitudes but do not balance each other in most nuclei.The interplay of these processes is one of the crucial and difficult problems of the pionization experiments to infer the information about the nuclear structure. Well-tuned INC models might help to simulate such processes, for example, we have plotted the value of charged pion yields for a bunch of isotopes in Fig. 5.8, where we generally tend to follow the experimental pattern with more apparent underproduction towards heavier targets. Cross sections for processes involving pions and nucleons are well tuned in INCL as they were implemented much earlier and tested more extensively with many benchmarks [Int10], so the reason of underproduction might be again the annihilation distance. If we annihilate too far, the pions might be less multiplied, while if we annihilate to close, more pions might be absorbed. It would be interesting to see the effect of annihilation distance on the pionic multiplicities, this will be done in the sensitivity analysis section of this chapter.

We might also observe a correlation between the ratio of charged pions in Fig. 5.9 and the probability of annihilation with proton, which we are able to extract directly from INCL (Fig. 5.10). While this trend is obvious for INCL, which is also to expect as we use a linear formula, it might be different in reality and more data is certainly desired for conclusions.

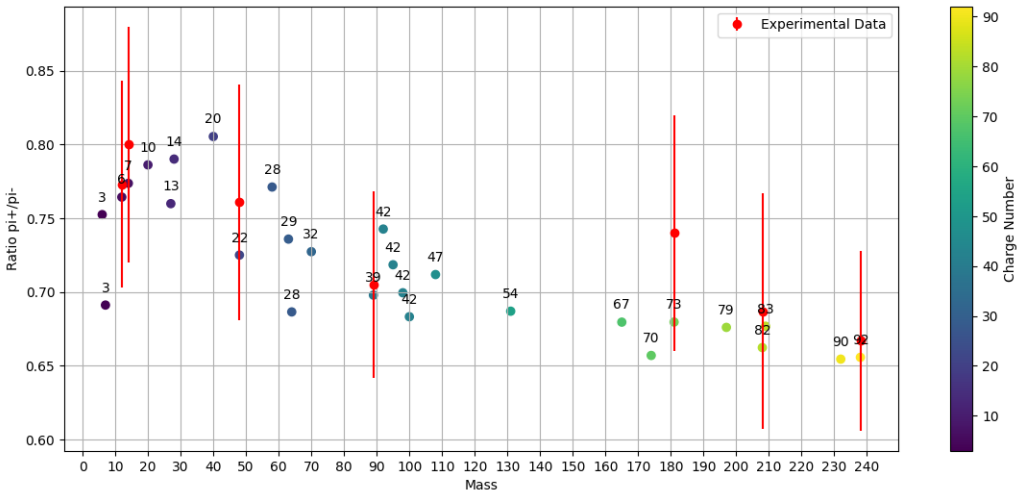

Figure 5.9: Ratio π^+/π^- for a group of target nuclei from INCL, experimental points are taken from [Bug+73; McG+86a; Rie+89; WL76]. No nuclei with the same mass number are present on this plot; the charge numbers are color-coded. Note, that incident beam energy was slightly different in the references, but in all cases assumed to annihilate through the capture. Also, sometimes materials of natural isotope composition were used as targets, in these cases the mass value was taken as for most abundant isotope.

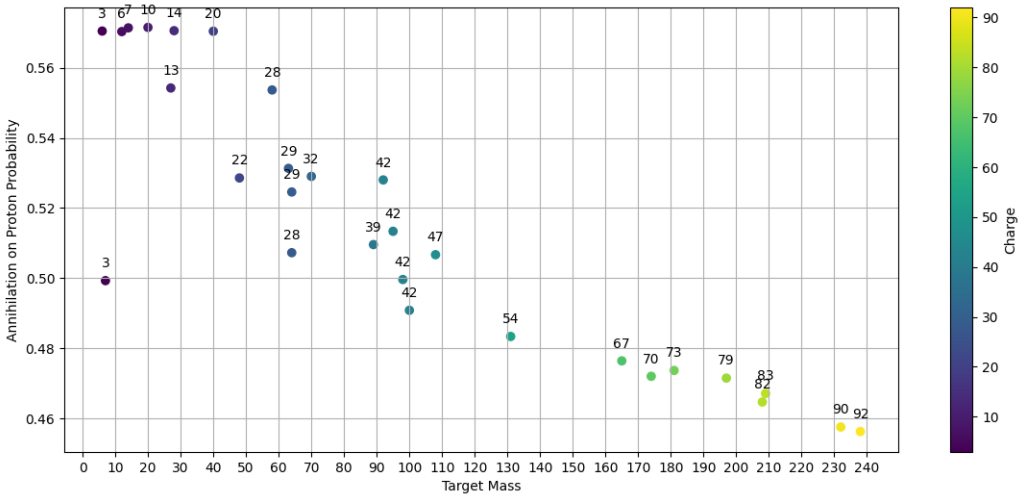

Figure 5.10: Probability for a nuclear target to annihilate with a proton in INCL. No nuclei with the same mass number are present on this plot; the charge numbers are color-coded.

Thanks to an exceptionally detailed work of Polster et al. [Pol+95], we are able to compare the yields for charged hadrons like protons, deuterons and tritons for multiple target nuclei in Fig. 5.11. Of course one should take into account that these multiplicities were taken in specific energy ranges due to a detector limitations, but still one is able to observe slight underproduction of protons for light targets and a simultaneous overproduction of deuterons. Within the INCL deuterons are produced when a proton and a neutron meet at the border of the nucleus and their momenta are correlated, alternatively a deuteron might be emitted by ABLA during the de-excitation stage. Tritons are generally underproduced, except for ^{20}Ne target, and it is rather strange, as such a p-n symmetric nucleus is expected to behave similar to carbon or nitrogen. The lack of triton production may be also explained by the existence of correlated pn-pairs population inside of the nucleus, which would increase the probability for three particles to meet at the right conditions.

Another reference [Mar+88] provides some multiplicity values for various hadronic emissions for a set of targets at 200 MeV/c antiproton energy, summarized in Table 5.4. INCL estimations are given for each type of emitted particle. Also, results of FLUKA [Fas+03] transport code and FTF [Uzh10] were computed for calcium and carbon targets. While the energy range is significantly different from that of Polster, it seems like here we are overestimating proton multiplicities up till ^{98}Mo, for which the INCL value is almost two times lower than for ^{92}Mo - quite a drastic change with just 6 neutrons of difference. In previous plots we observed a change but it was almost linear, this time is might be de-excitation part, which decides to emit these low-energy protons after the cascade. An energy spectra will be compared in the next section to check if this is the issue.

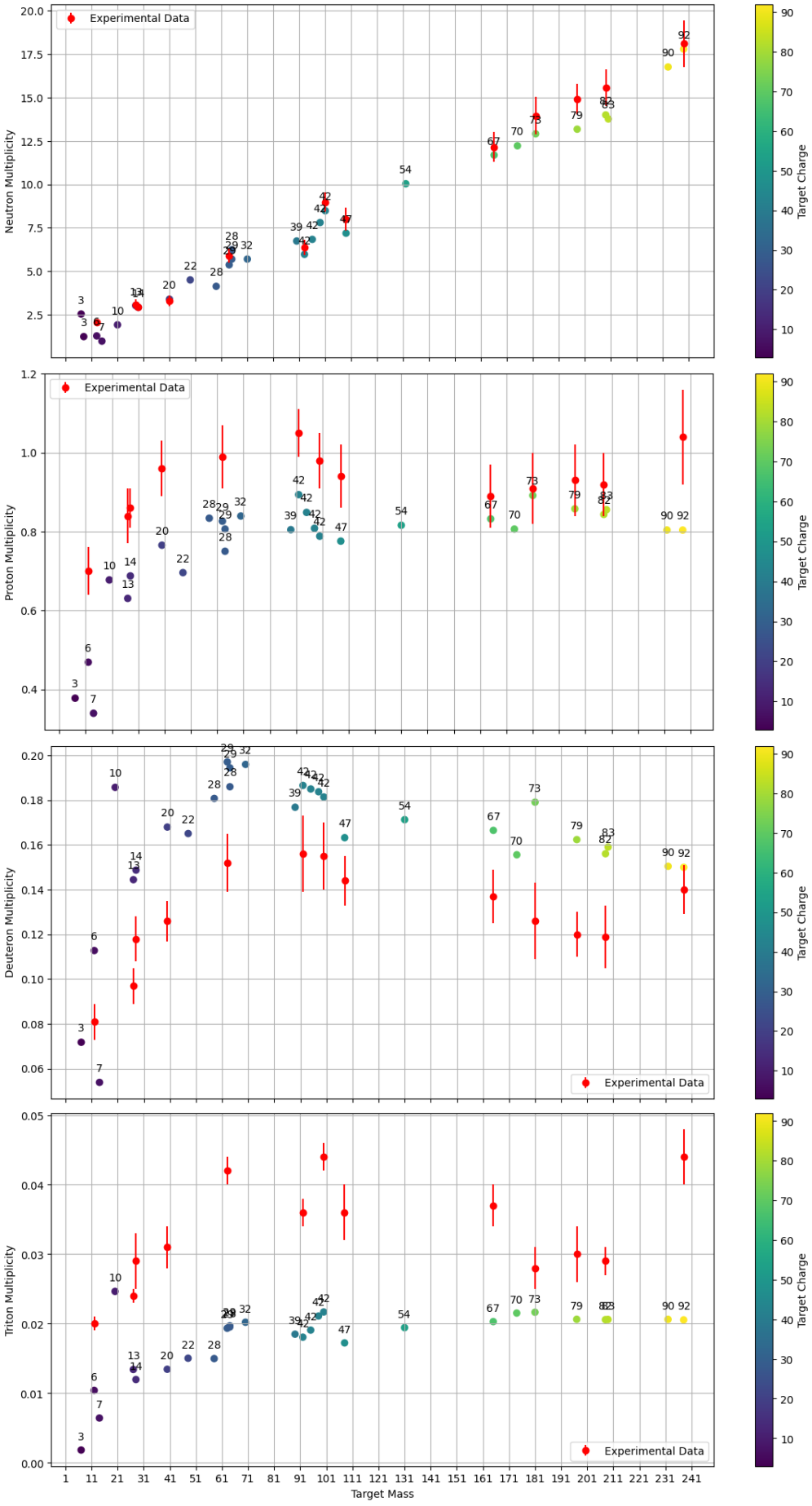

Figure 5.11: Total neutron/proton/deuteron/triton multiplicities per 100 $\bar{p}$ for kinetic energy range (0-300)/(35-200)/(50-160)/(60-150) MeV for a group of target nuclei, experimental values with errors are taken from [Pol+95]. No nuclei with the same mass number are present on this plot; the charge numbers are color-coded.

Table 5.4: Particle multiplicities for a given energy range after antiproton annihilation. The top value in each cell is taken from [Mar+88], statistical error in superscript, while systematic is subscript, error values are given with respect to the last digit (e.g. $74.2^{\pm 3}_{\pm 38} \equiv 74.2^{\pm 0.3}_{\pm 3.8}$). The second value is the INCL, the red is FTF and the blue is FLUKA. The FLUKA and FTF results were kindly provided by Angela Gligorova (Stefan Meyer Institute).

range(MeV)	C12	Ca40	Cu63	Mo92	Mo98	U238
p (6-18)	$23.3^{\pm 2}_{\pm 18}$ 21.2 3.0 18.3	$74.2^{\pm 3}_{\pm 38}$ 122.2 6.7 30.2	$94.5^{\pm 4}_{\pm 78}$ 115.3	$127.2^{\pm 4}_{\pm 58}$ 155.6	$124.3^{\pm 3}_{\pm 64}$ 98.5	$76.6^{\pm 3}_{\pm 240}$ 34.9
d (8-24)	$9.3^{\pm 1}_{\pm 7}$ 19.9 0.0 13.1	$18.1^{\pm 2}_{\pm 9}$ 25.6 0.0 19.1	$28.0^{\pm 2}_{\pm 23}$ 31.0	$29.0^{\pm 2}_{\pm 13}$ 34.1	$30.4^{\pm 2}_{\pm 15}$ 29.9	$31.3^{\pm 2}_{\pm 99}$ 14.9
t (11-29)	$4.5^{\pm 1}_{\pm 3}$ 5.4 0.0 5.0	$5.7^{\pm 1}_{\pm 3}$ 5.0 0.0 8.1	$9.9^{\pm 1}_{\pm 8}$ 8.4	$11.8^{\pm 1}_{\pm 5}$ 8.7	$12.7^{\pm 1}_{\pm 7}$ 10.6	$18.8^{\pm 2}_{\pm 59}$ 12.1
^{3}He (30-70)	$1.72^{\pm 4}_{\pm 13}$ 1.74 0.0 2.0	$2.22^{\pm 5}_{\pm 12}$ 1.59 0.1 0.2	$2.60^{\pm 6}_{\pm 21}$ 1.62	$2.33^{\pm 5}_{\pm 11}$ 1.58	$2.06^{\pm 4}_{\pm 10}$ 1.25	$2.66^{\pm 6}_{\pm 84}$ 1.03
^{4}He (30-70)	$1.14^{\pm 3}_{\pm 9}$ 1.32 12.0 2.5	$2.18^{\pm 5}_{\pm 11}$ 2.67 4.0 1.6	$3.25^{\pm 7}_{\pm 26}$ 4.04	$3.78^{\pm 6}_{\pm 17}$ 4.69	$3.69^{\pm 6}_{\pm 17}$ 4.57	$5.94^{\pm 9}_{\pm 190}$ 7.66
^{6}He (39-89)	$0.025^{\pm 5}_{\pm 2}$ 0.022	$0.045^{\pm 7}_{\pm 3}$ 0.046	$0.048^{\pm 8}_{\pm 4}$ 0.083	$0.061^{\pm 8}_{\pm 3}$ 0.077	$0.060^{\pm 8}_{\pm 3}$ 0.111	$0.150^{\pm 20}_{\pm 50}$ 0.194
^{8}He (44-90)	$0.0041^{\pm 18}_{\pm 3}$ 0.0	$0.014^{\pm 4}_{\pm 1}$ 0.004	$0.0094^{\pm 36}_{\pm 8}$ 0.017	$0.011^{\pm 3}_{\pm 1}$ 0.021	$0.013^{\pm 4}_{\pm 1}$ 0.036	$0.041^{\pm 8}_{\pm 13}$ 0.088
Li (61-96)	$0.017^{\pm 4}_{\pm 2}$ 0.003	$0.075^{\pm 9}_{\pm 4}$ 0.022	$0.058^{\pm 9}_{\pm 5}$ 0.051	$0.086^{\pm 9}_{\pm 4}$ 0.054	$0.083^{\pm 9}_{\pm 4}$ 0.067	$0.180^{\pm 16}_{\pm 60}$ 0.120

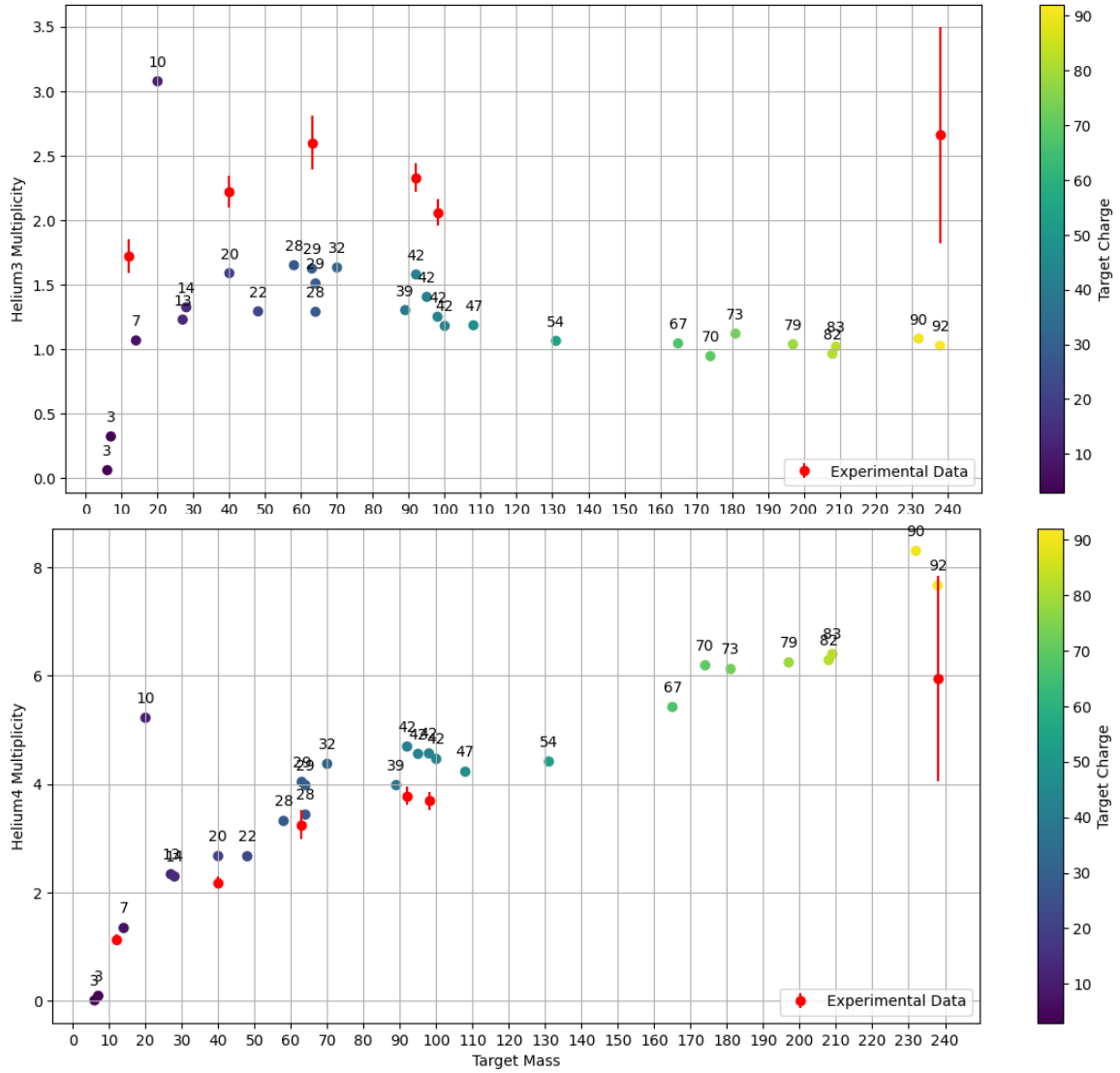

Figure 5.12: Total ^3He and ^4He multiplicities per 100 $\bar{p}$ for kinetic energy range 30-70 MeV for a group of target nuclei, experimental values with errors are taken from [Mar+88]. No nuclei with the same mass number are present on this plot; the charge numbers are color-coded.

The role of de-excitation model in this energy range becomes more apparent if we plot the yields of helium ions versus the target mass using the same dataset as in the table (see Fig. 5.12). Apparently, the probability of four nucleons with vicinal momentum vectors should be lower that that of three nucleons, but for the de-excitation model α-particle emission might often be a more favorable channel.

Multiplicities of charged pions could be used to probe the existence of neutron haloes in neutron excess nuclei, which was done in recent Ref. [WP23] where all the data from historical "pionization" experiments [Agn+60; Bug+73; WL76; Rie+89] was analyzed with the help of modern knowledge of $\bar{p}$-nucleus potential and pion-nucleus interactions. Authors analyse the S_p/S_n parameter corrected by the halo factor and the influence of the angular momentum number of the dominant capture orbit by fitting the charge distribution of the emitted pions.

$$S_p/S_n = \frac{Im(a_n)}{Im(a_p)} = \frac{N(\bar{p},n)Z}{N(\bar{p},p)(A-Z)} f_{halo} \tag{5.11}$$

Where $Im(a_n), Im(a_p)$ are the amplitudes to annihilate with the neutron or the proton, authors in Ref. [WP23] have used Paris potential[El-+09] for the amplitude estimations as an additional way to extract the halo factors, alternatively $S_p/S_n \cdot f_{halo}$ values were taken from other experiments. They have applied phenomenological model to extract probabilities of pion absorption or charge conversion for various nuclei, alternatively they could have used INCL model to fit these charge distributions, like it is done in Fig. 5.13. Unfortunately, neither in their study, nor in INCL we are not able to calculate the

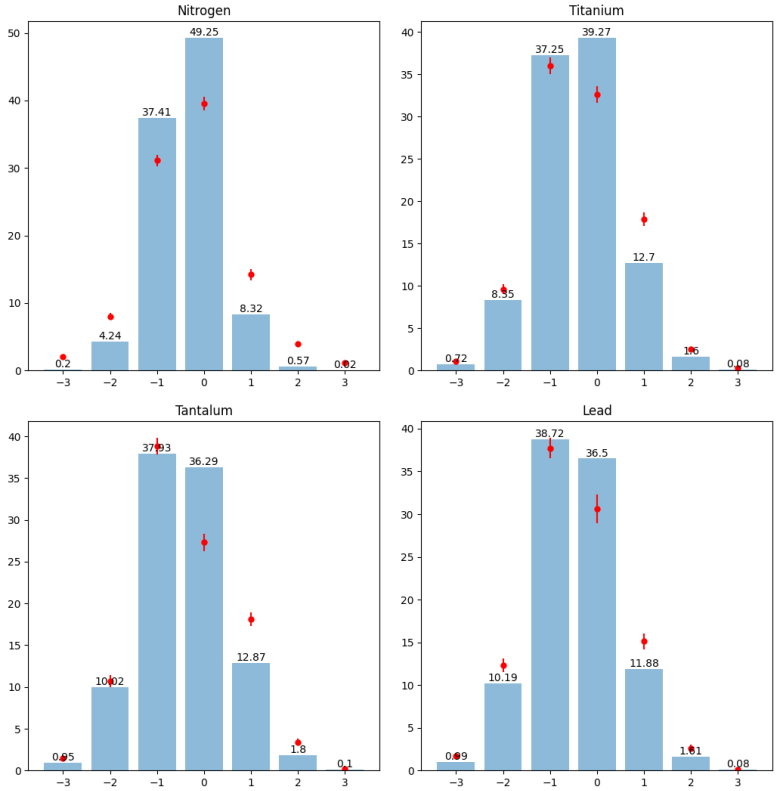

Figure 5.13: Charge distribution of pions obtained with INCL compared to experimental data (red points) for nitrogen[Rie+89], titanium, tantalum and lead[Bug+73]. All targets had natural isotope distribution, the numbers are given per 100 annihilations. Errors for the experimental data are taken from the review[BK94]

uncertainty of our results, error propagation in such complicated models is not at all straightforward, hopefully this option should be introduced in INCL in the nearest future (project ANR NURBS (NUclear Reaction model improvement with Bayesian Statistics); 2024-2027). Pionization might be a more clear method to model the effects influenced by the outer region of the nucleus in comparison to residual nuclei study, as it is less influenced by the physics of residual nucleus, which is different from the target, this method might be applied to study neutron (or proton) haloes in radioactive nuclei in the context of the oncoming PUMA experiment [Aum+19].

5.3.2 Inclusive particle spectra

First, we have to verify that we reproduce as close as possible the pion spectrum of elementary $p\bar{p}$ at rest annihilation. After the final state is randomly chosen, we use embedded phase-space model to distribute the available energy among final state particles and assign a momentum value to each of them. Spectra of charged and neutral pions from our phase-space model are compared with the experimental results from Crystal Barrel in Fig. 5.14.

There are two principal differences. First, the experiment does not produce low-energy pions, while kinematically it should be possible. The explanation here is the same as with exclusive frequency measurements of final states with >5 particles - it is just practically difficult to measure pions with low momentum. INCL does not have this problem and is able to fulfill the low momentum part of the spectrum. Second, there are straight lines in the INCL spectra, which are responsible for two-particle final states like $p\bar{p} \to \pi^+\rho^-$ or $p\bar{p} \to \pi^0\omega$. In reality, these lines would be spread in the detector and barely visible. The experimental distributions reveal no significant structure, except for $\pi\rho$ production which identifies itself as a peak at 773 MeV/c in the neutral pion momentum distribution. The ρ^0 signal seems much more pronounced, this is an artefact of the experimental resolution which is better for the recoiling π^0 than for $\pi^\pm$ mesons.

In Ref. [Pol+95] the only target, for which all n, p, d and t spectra was plotted was the ^{238}U, our comparison to these spectra is presented in Fig. 5.15, additionally there were kinetic energy spectra of protons and neutrons for ^{197}Au, ^{nat}Cu and ^{12}C targets. All this information was digitized manually,

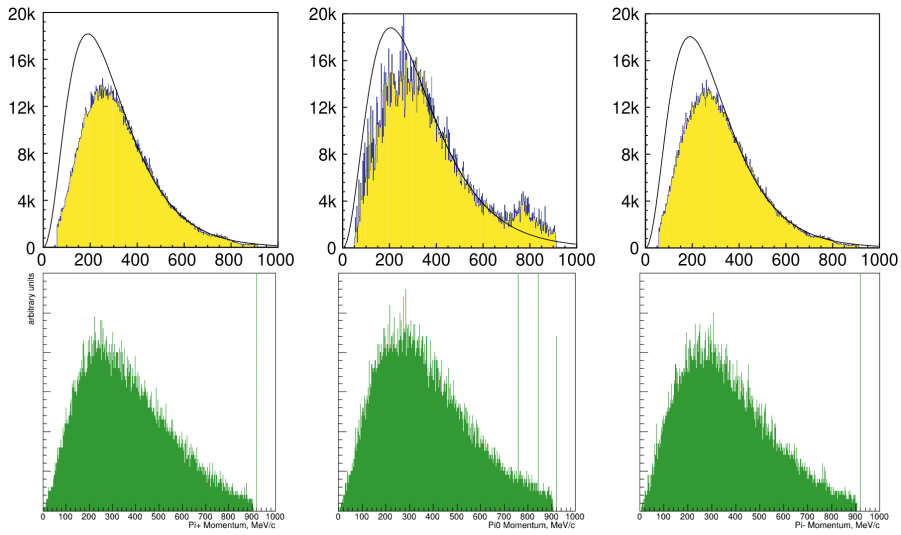

Figure 5.14: The top row are experimental spectra of π^+ (right), π^0 (middle) and π^- (left) from the $\bar{p}p$ reaction in yellow, taken from [KBR05b], while INCL results are below in green.

so there might be an additional uncertainty. There are also fitted n, p, d and t spectra for all targets compared to INCL, which one might find in Appendix A (page 111). Concerning neutron and proton, INCL calculation results match well the experimental data, except maybe a slight underestimation of the decrease of the yields with energy. The larger difference between neutron and proton yields in experimental data compared to INCL could be due to, for example, the S_p/S_n ratio or the place where the annihilation occurs. Section 5.4 is dedicated to this type of sentivity analysis. For deuteron and triton the results are less good with a clear overestimation. INCL is known to overestimate the high-energy tail of light clusters, but in that case we should study whether that's the only reason.

The production of pions seems to be on par with the data for 608 MeV/c momentum, and from Fig. 5.16, we can see that the curve on INCL at rest annihilation is more in agreement with reality in terms of the form. This suggests that at this energy and below, antiprotons should highly likely annihilate through the capture process, as we assumed.

The substantial underproduction of protons in all three cases, which increases towards heavier targets, is also apparent. If it might be the normalization which is to blame (again, the curve is better for at rest scenario, which means that the physics at rest is more appropriate), then there must be an overestimation of pion production, because the normalization coefficient is the same for both spectra. Moreover, from Fig. 5.6 we can see that for ^{12}C the formula used in INCL gives a reaction cross section roughly 20-30% to high, what would result in better results for pions here, but worst for protons.

Underestimation of the distance at which a meson star is created might be another reason due to which mesons interact less with the nucleus and thus kick out fewer protons, while more pions are able to escape absorption. At Fig. 5.17, we have yields instead of cross sections, thus we can see that proton production is even overestimated at 200 MeV/c of incident momentum. For INCL at rest implementation incident momentum value is only used for normalization, which means that yields of particles would be the same for 200 MeV/c and 608 MeV/c. Neutron production is in quite good agreement with the data, especially towards heavier targets. Still, we generally overproduce fast neutrons on heavier targets. These comparisons clearly show that the question of the reaction cross section is important and must be taken into account in the analysis, and that the shape is more appropriate for testing the physics included in INCL.

In the Fig. 5.18 one may see the same data as in Fig. 5.17, but with additional results of FTF+Precompound model currently available in Geant4. Although, FTF is often coupled with lower energy cascade models like Binary cascade model, Bertini or INCL. Also, the philosophy of FTF model is better suited for higher energies.

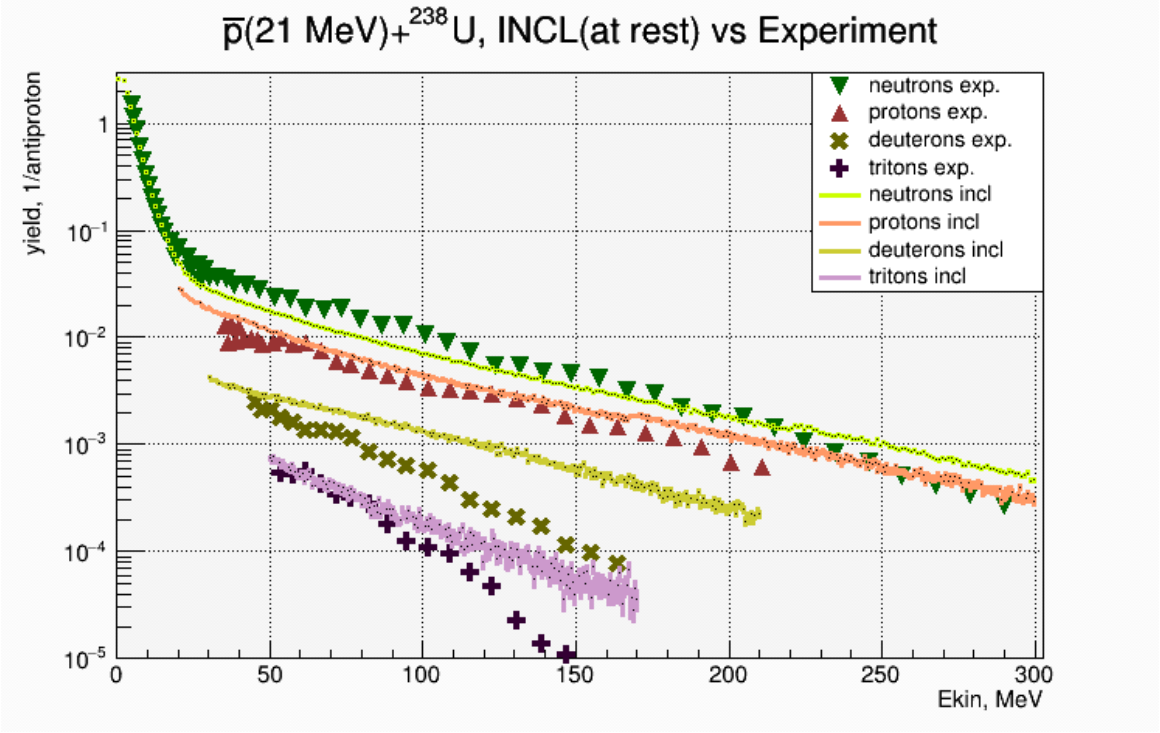

Figure 5.15: Emitted particle spectra from Ref. [Pol+95] compared to INCL, the data points were manually digitized.

5.3.3 Residual nuclei production

Historically, The idea to study nuclear residuals formed after $\bar{p}$ annihilation on nuclei was elaborated by the Munich-Warsaw collaboration [Trz+01] as an alternative for x-ray measurements of antiprotonic atoms. By radiochemical methods final (Z - 1, A) and (Z, A - 1) nuclei were detected, which made it possible to study the relative rates of $\bar{p}n$ and $\bar{p}p$ annihilations. As a result the number of neutrons relative to the number of protons in the capture region was extracted. Neutron haloes were detected in a large number of nuclides [Lub+98; Har+01].

In order to estimate the fidelity of INCL+ABLA results regarding the production of residual nuclei we might will compare our model with the results of $\bar{p}$-nucleus fragmentation experiments, starting from molybdenum isotopes ^{92}Mo, ^{95}Mo and ^{98}Mo from Ref. [Mos+86; Mos+89]. Their first activity measurement started about ten minutes after the end of the irradiation. The duration of the measurements spanned from five minutes up to several days. The γ-ray lines were fitted and used to identify the residual nuclei. This method only allows one to identify residual nuclei with half-lives between 15 minutes and about 100 days and emitting γ-rays during the decay. Therefore, all stable and also some radioactive nuclei cannot be detected with this method. Tables with calculated yields were taken directly from the articles. Yields were estimated from γ-ray intensities taking decay chains into account (see section 5.3.3.1 for more details). Sometimes the isomeric states were observed, while the ground one was not, in this case we discard these data points, as there is no isomer production in ABLA. Our results with molybdenum isotopes are presented in Fig. 5.19, 5.20 and 5.21. It is particularly notable from INCL results, how the probability of the remnant to conserve its initial charge (e.g. $^{n}Mo(\bar{p},x)^{n-\Delta n}Mo$) increases towards heavier isotopes: we have 5, 8 and 11 INCL data points for such reactions in cases of ^{92}Mo, ^{95}Mo and ^{98}Mo targets correspondingly. Similar effect is apparent for those residual nuclei, which are next to molybdenum (e.g $^{n}Mo(\bar{p},x)^{n-\Delta n}Nb$, $^{n}Mo(\bar{p},x)^{n-\Delta n}Zr$). We also did same comparisons for ^{197}Au and ^{165}Ho targets and natural Ba target, which can be found in Appendix A (page 111).

In such comparisons models are usually considered as good when they fit the experimental data within a few tens percent up to a factor 2. This is what we obtained here. This proves that the excited remnant nuclei produced at the end of the INCL cascade have the right characteristics (mass, charge, excitation energy) and that the code ABLA treats well the de-excitation phase. It must be stressed that this observable is difficult to simulate properly because first it is the final product of all the processes and second the values are spread over several orders of magnitude.

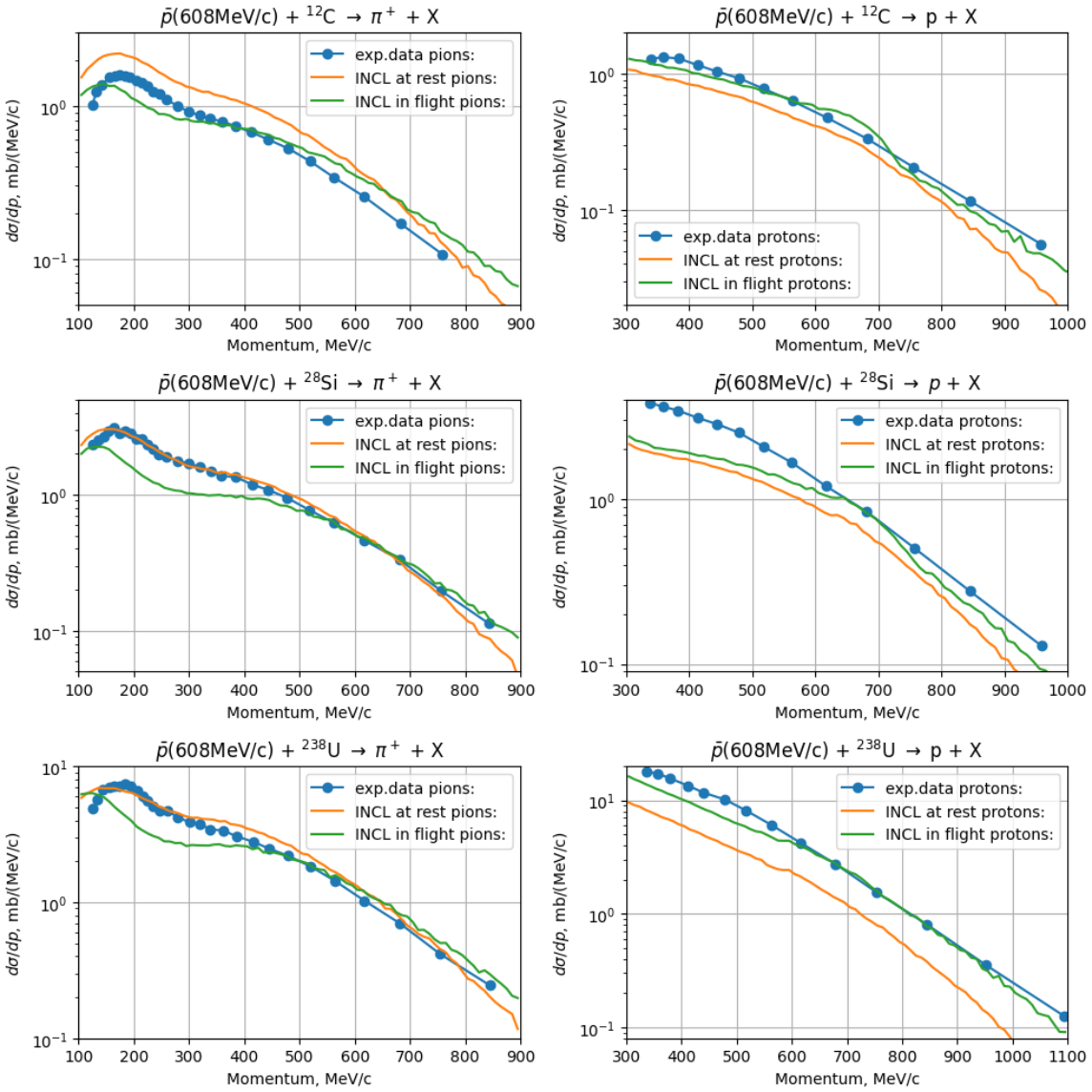

Figure 5.16: π^+ and proton spectra at P_{lab} = 608MeV/c ≈ 180 MeV $\bar{p}$ incident energy. Data are taken from Ref. [McG+86a] and Ref. [McG+86b], the ^{28}Si data was manually digitized.

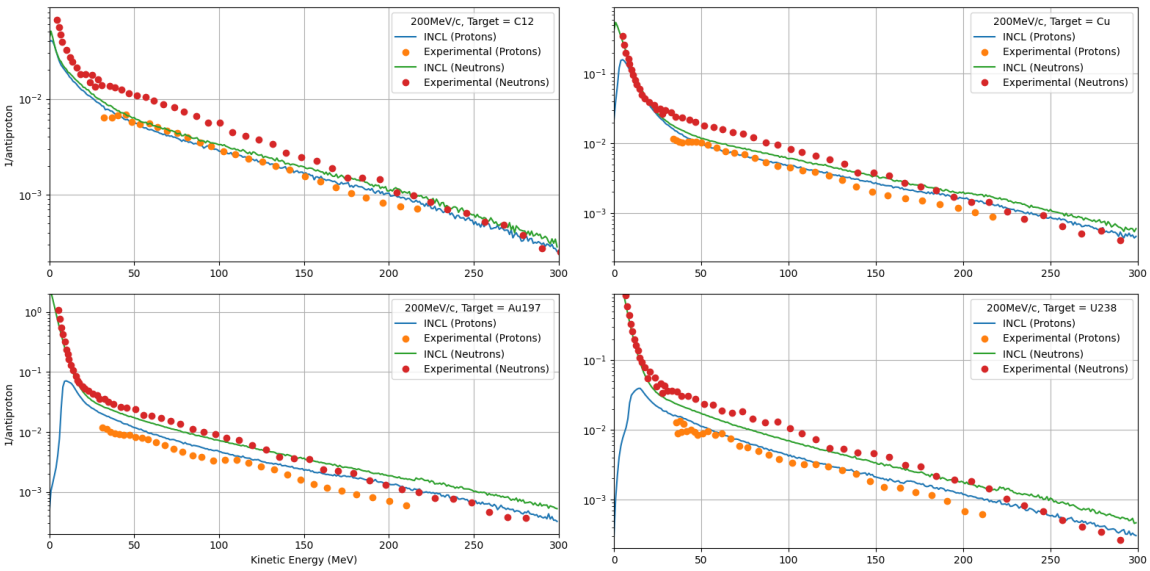

Figure 5.17: At rest annihilation of stopped antiprotons in INCL vs the experimental data, taken from Ref. [Pol+95] for ^{12}C, ^{natural}Cu, ^{197}Au and ^{238}U targets. Data was manually digitized.

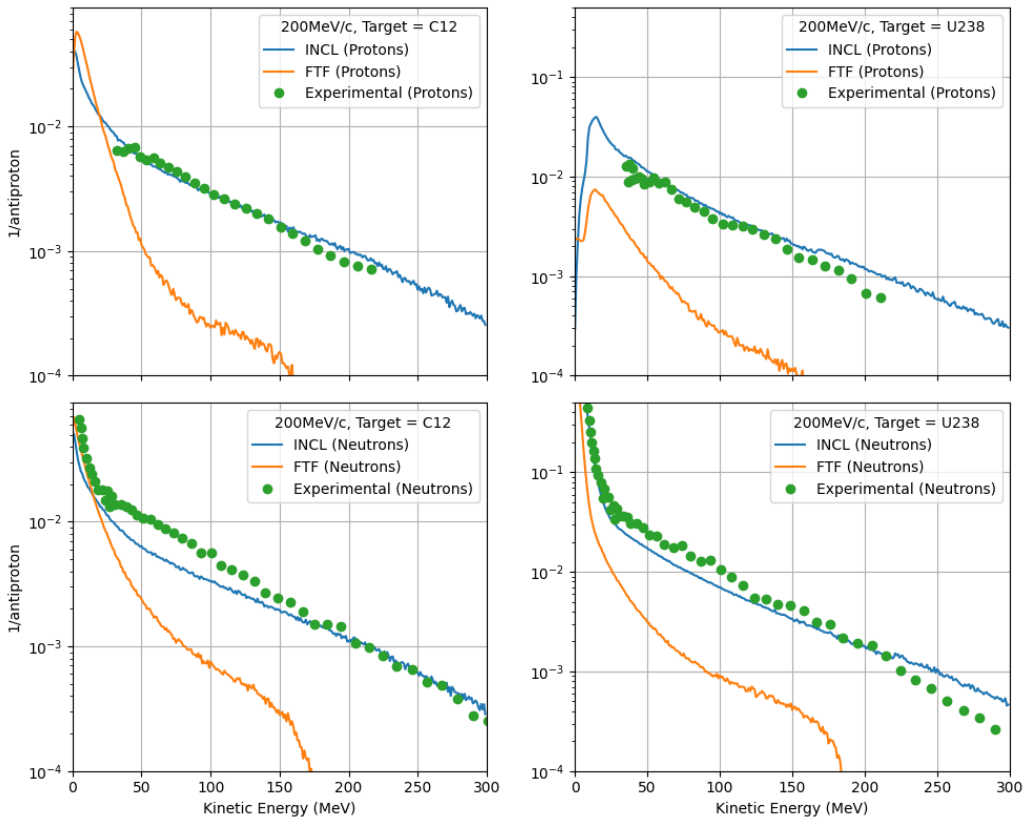

Figure 5.18: FTF and INCL versus digitized data from Ref. [Pol+95].

Next, we will compare the same type of data in case of natural copper target [Jas+93]. This time authors divided their experimentally measured isotope yields into individual and cumulative, so also did we with independent nuclides in Fig. 5.22 and cumulative ones in Fig. 5.23. In case of independent isotopes, one might expect less of an uncertainty, as the cumulative yield calculation procedure includes its own uncertainties. The ^{238}U target was analyzed similarly, with our comparisons for independent yields on Fig. 5.24, while cumulative ones are on Fig. 5.25.

Concerning Copper, The results are rather good for the independent case and of the level of reliability as the usual ones for proton-induced reactions. For the cumulative case, the results are a little less good, but still correct in value and shape. The Uranium target is interesting, because the comparisons is made with fission products. The results are less good than with Copper, with a constant overall underestimation in both cases, independent and cumulative. Another characteristics of the remnant nucleus is involved for the fission products: the angular momentum. We assumed in our model that the annihilation gives no angular momentum. This is questionable. If this angular momentum is not zero, then we can expect a higher angular momentum for the excited remnant nuclei and the fission barrier will be then reduced, with a higher production of fission products. This should be studied more quantitatively. It must be noted that some experimental data seems inconsistent, especially the points for Z=43 and Z=45, which seem to be too high compared to the other charges.

In order to get a sense of how the discrepancies of INCL+ABLA are far from the measured data, and how far the measured data is from reality, it makes sense to compare our results with the well-studied case of proton projectile at energies of about few GeV. The residual nuclei is determined by sequential operations of intra-nuclear cascade and de-excitation code. When the nucleus is "passed" from INCL to ABLA, there are in fact just few input parameters which ABLA receives, such as kinetic energy (momentum) of the remnant, remnant excitation energy, remnant angular momentum, and nucleon constitution (mass, charge, strangeness). This set of parameters remains the same, regardless of the projectile type, thus it may be interesting to compare these parameters in case of antiproton at rest annihilation and of a proton projectile with kinetic energy close to that of a double proton mass ($E_{kin} \approx 1876 MeV$). Such comparison is done at Fig. 5.26, and while there are certain differences, it is hard to expect a substantially different final distributions of residual nuclei between these two cases. Similar fission isotope distribution results from GSI [Ber+03; Taï+03; Ric+06], but for the 1 GeV/nucleon

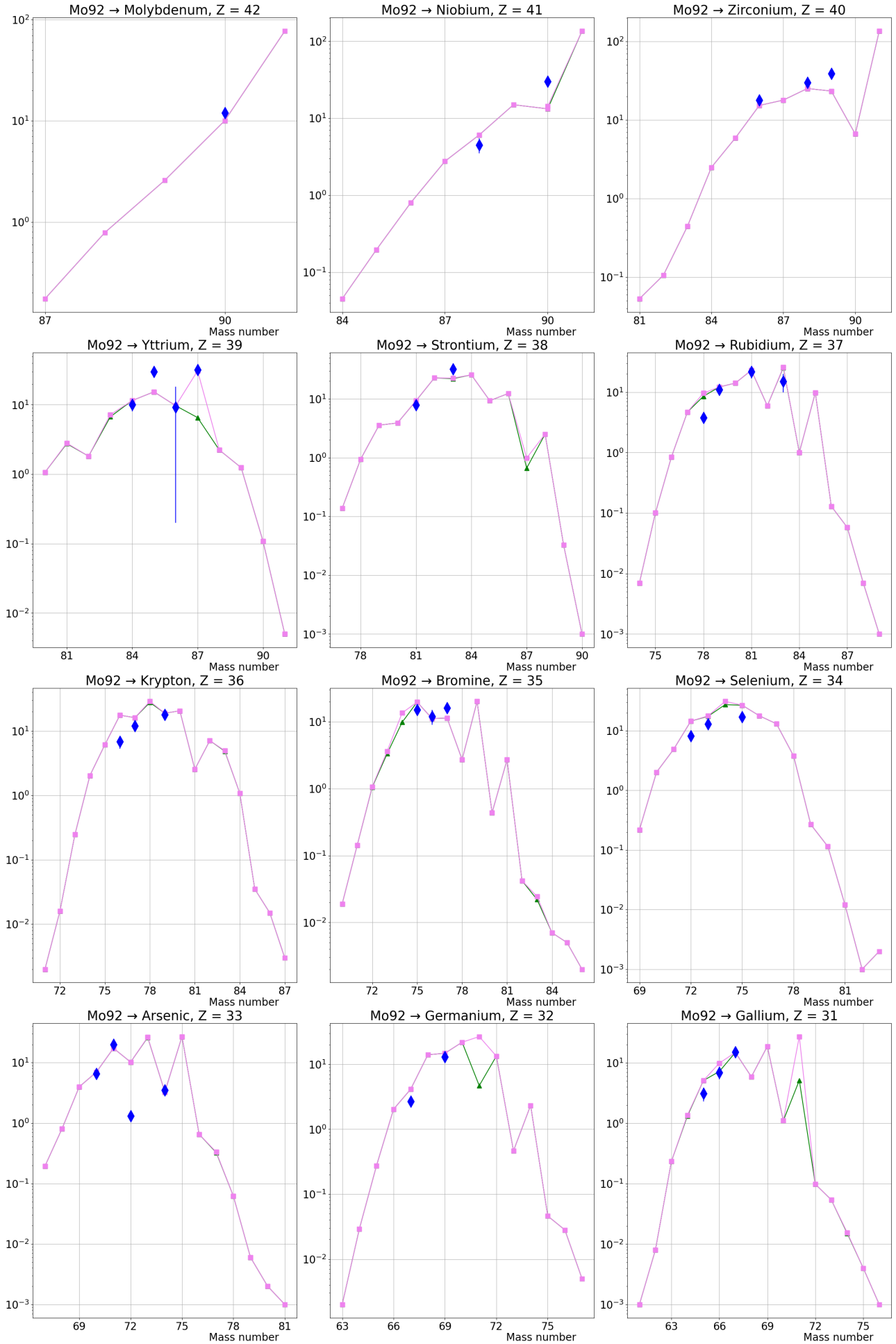

Figure 5.19: Cumulative isotopic distributions from the reaction $\bar{p}+^{92}Mo$. Calculated results are in violet (option $\frac{\lambda_D}{\lambda_P} = 0.1$), and in green (option $\frac{\lambda_D}{\lambda_P} = 0.5$). Definition of $\frac{\lambda_D}{\lambda_P}$ in section 5.3.3.1. Data are from [Mos+89].

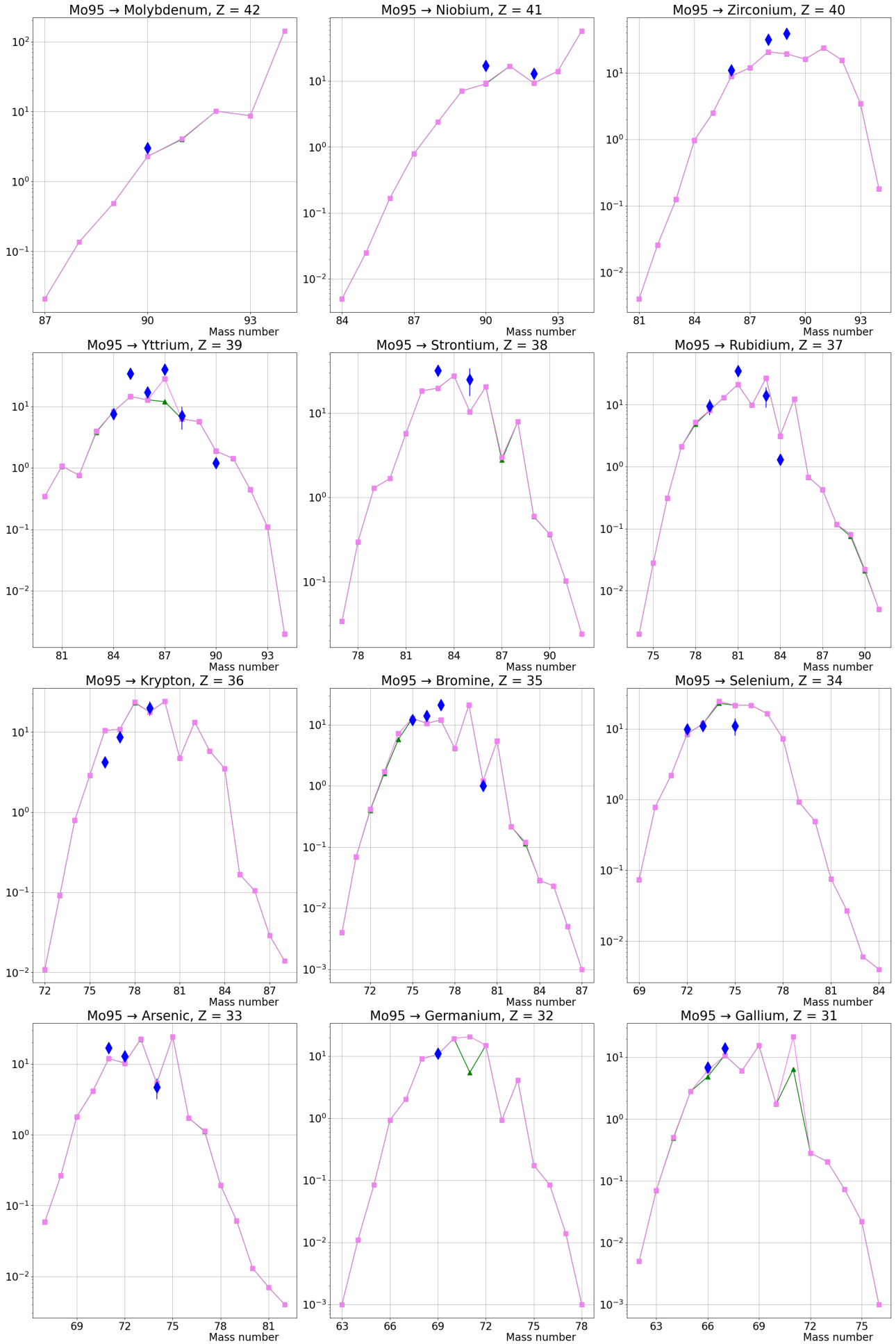

Figure 5.20: Cumulative isotopic distributions from the reaction $\bar{p}+^{95}Mo$. Calculated results are in violet (option $\frac{\lambda_D}{\lambda_P} = 0.1$), and in green (option $\frac{\lambda_D}{\lambda_P} = 0.5$). Definition of $\frac{\lambda_D}{\lambda_P}$ in section 5.3.3.1. Data are from [Mos+89].

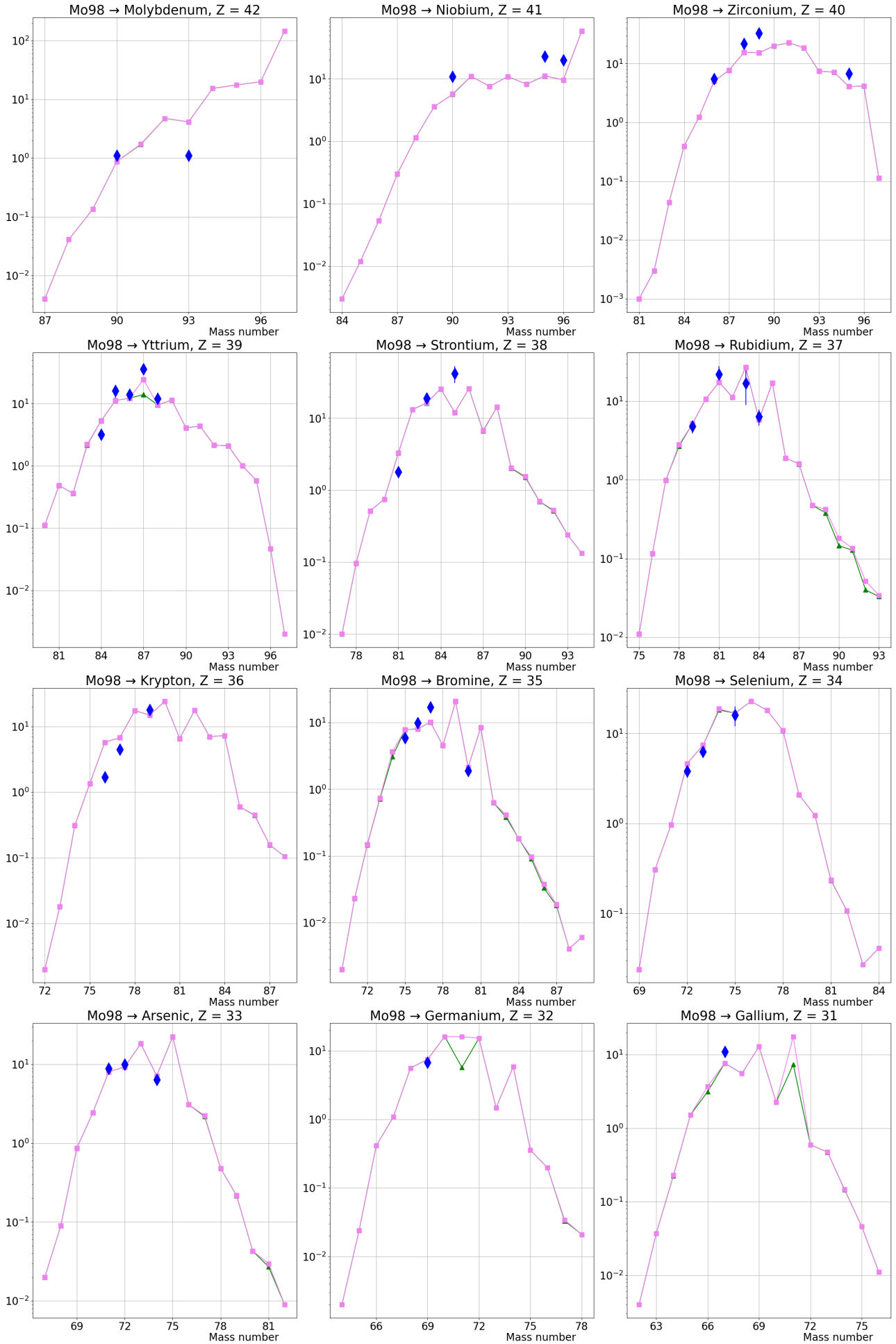

Figure 5.21: Cumulative isotopic distributions from the reaction $\bar{p}+^{98}Mo$. Calculated results are in violet (option $\frac{\lambda_D}{\lambda_P} = 0.1$), and in green (option $\frac{\lambda_D}{\lambda_P} = 0.5$). Definition of $\frac{\lambda_D}{\lambda_P}$ in section 5.3.3.1. Data are from [Mos+89].

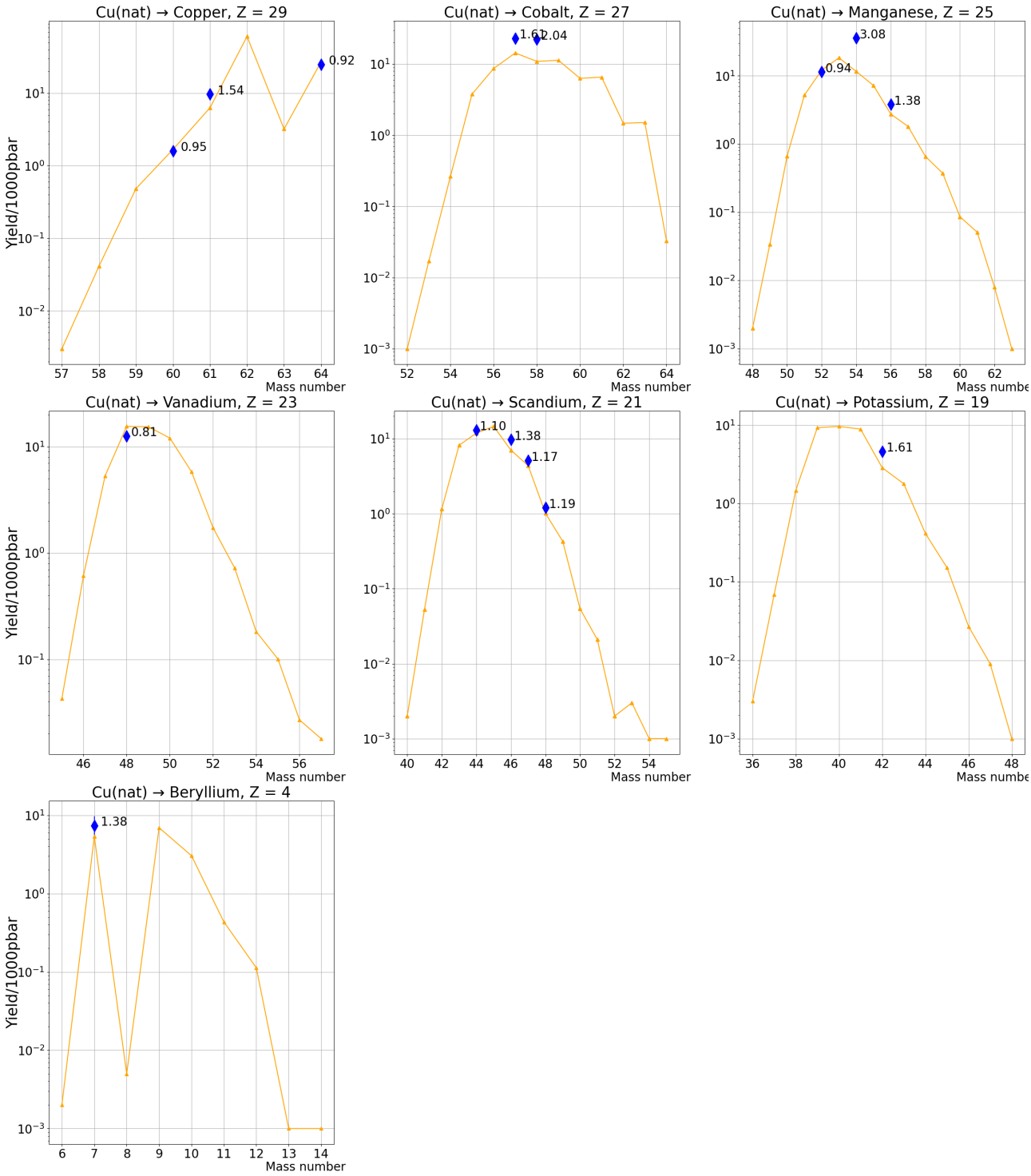

Figure 5.22: Independent isotopic distributions from the reaction $\bar{p} +^{nat} Cu$. Calculated results are in orange. Data are from [Jas+93].

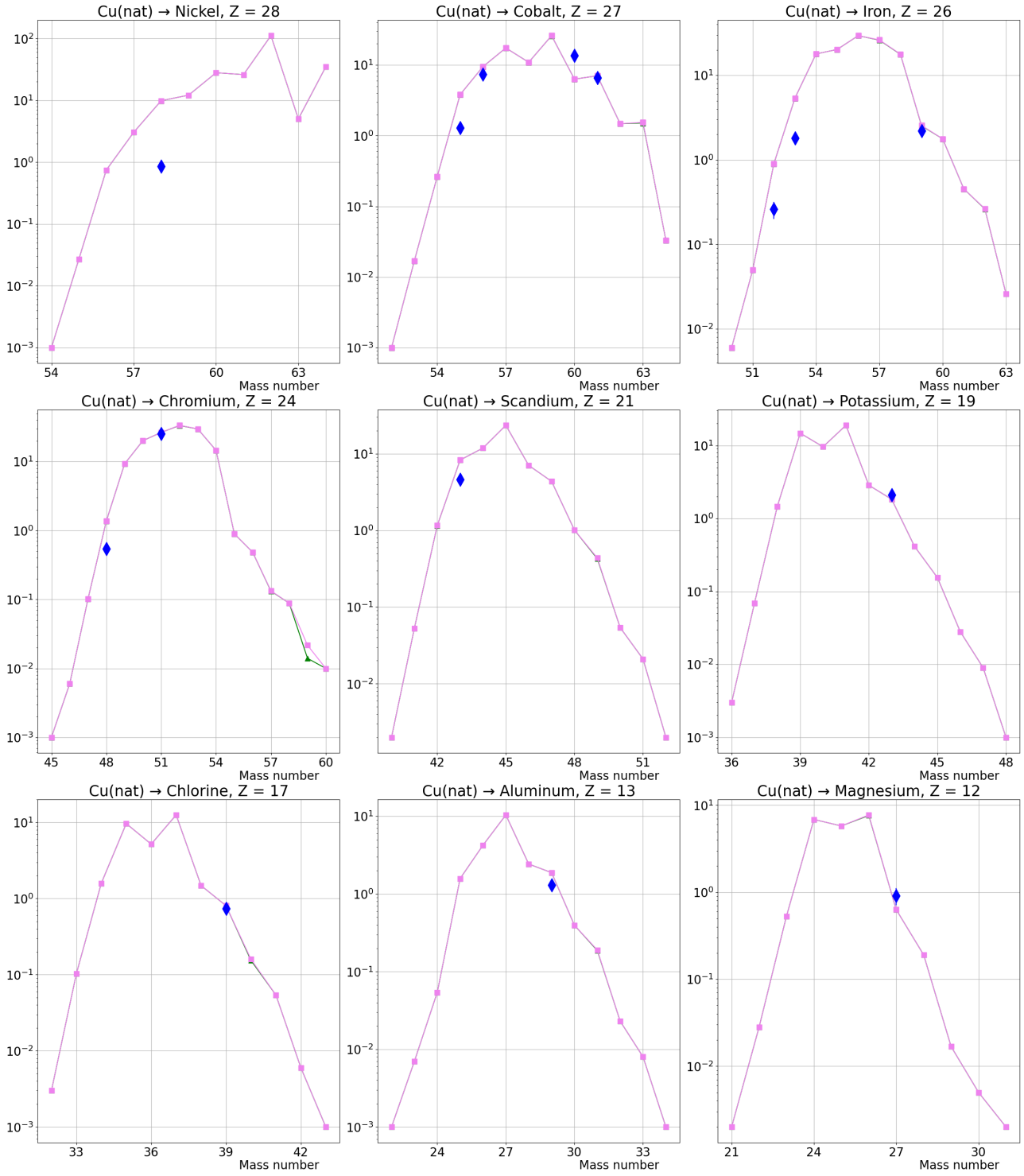

Figure 5.23: Cumulative isotopic distributions from the reaction $\bar{p}+^{nat}Cu$. Calculated results are in violet (option $\frac{\lambda_D}{\lambda_P} = 0.1$), and in green (option $\frac{\lambda_D}{\lambda_P} = 0.5$). Definition of $\frac{\lambda_D}{\lambda_P}$ in section 5.3.3.1. Data are from [Jas+93].

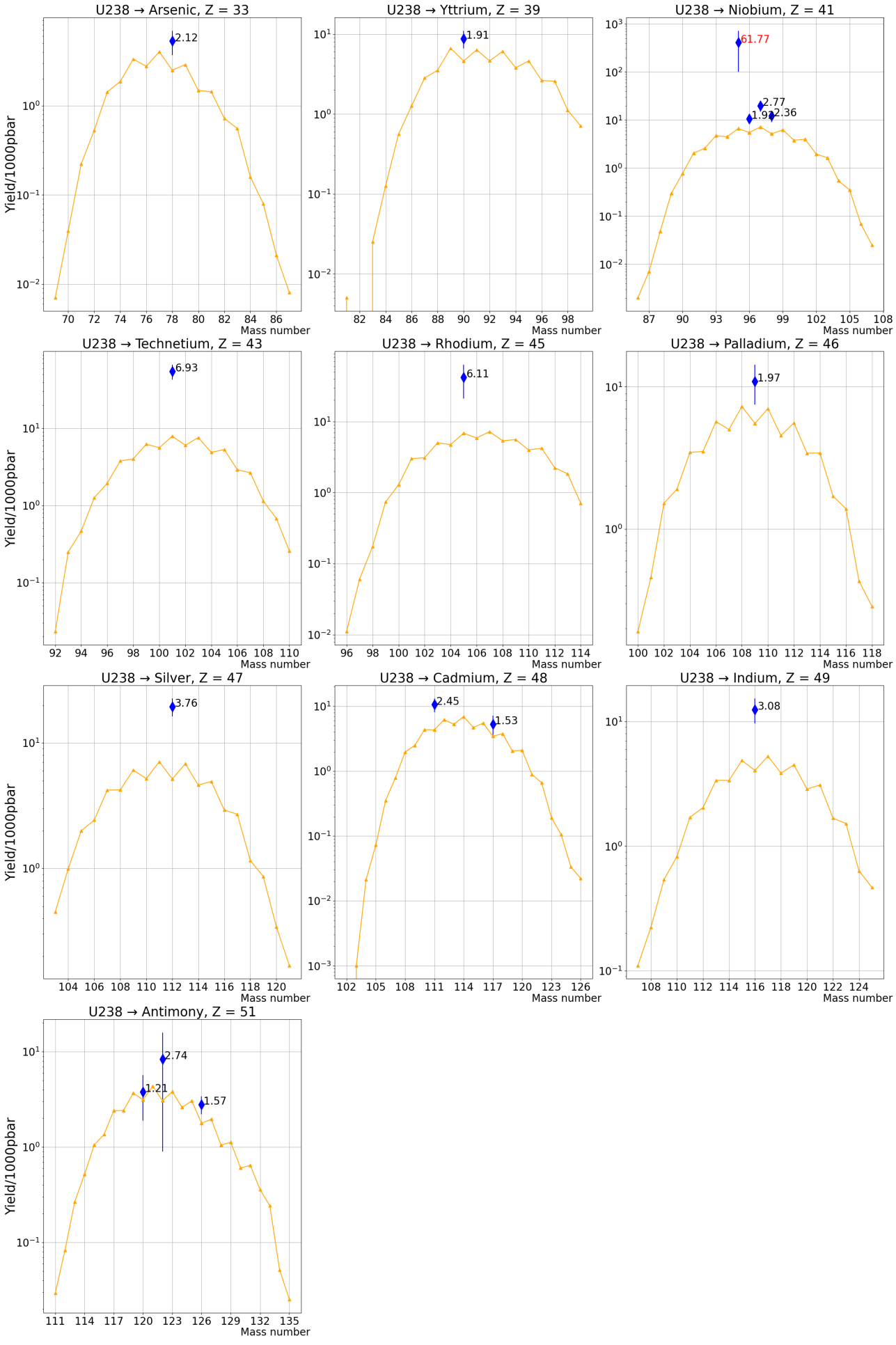

Figure 5.24: Independent isotopic distributions from the reaction $\bar{p} +^{238} U$. Calculated results are in orange. Data are from [Mac+92].

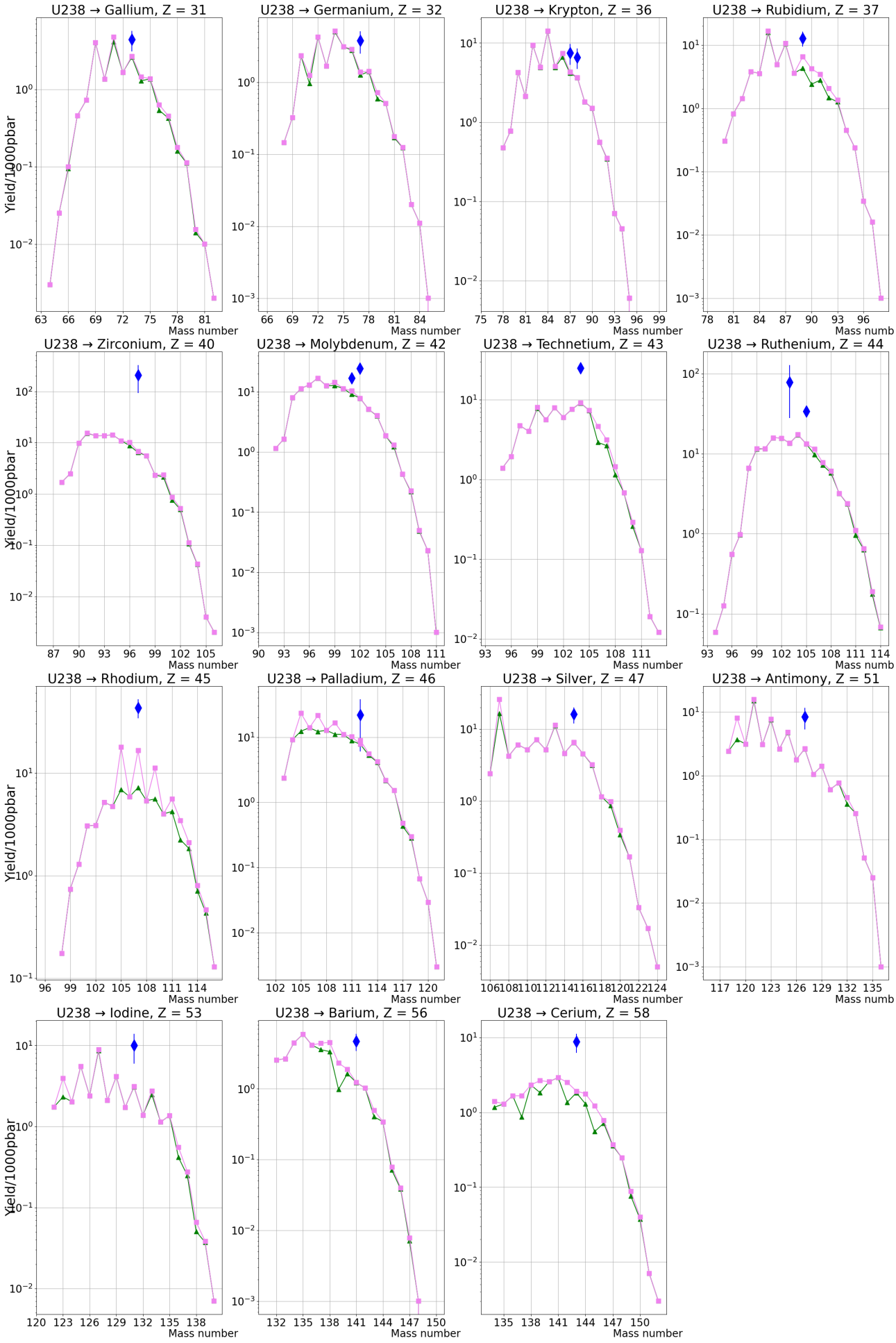

Figure 5.25: Cumulative isotopic distributions from the reaction $\bar{p}+^{238}U$. Calculated results are in violet (option $\frac{\lambda_D}{\lambda_P} = 0.1$), and in green (option $\frac{\lambda_D}{\lambda_P} = 0.5$). Definition of $\frac{\lambda_D}{\lambda_P}$ in section 5.3.3.1. Data are from [Mac+92].

accelerated ^{238}U ions on hydrogen target vs INCL estimations [Int10] are given in Appendix A (page 111). Fission residue detection in inverse kinematics experiments is direct (time of flight spectrometry) and does not rely on γ-ray emission from the fragments, which makes it possible to acquire much more data. Inverse kinematics experiments with an antiproton target and various radioactive nuclei beams is the goal of the PUMA [Aum+22] project.

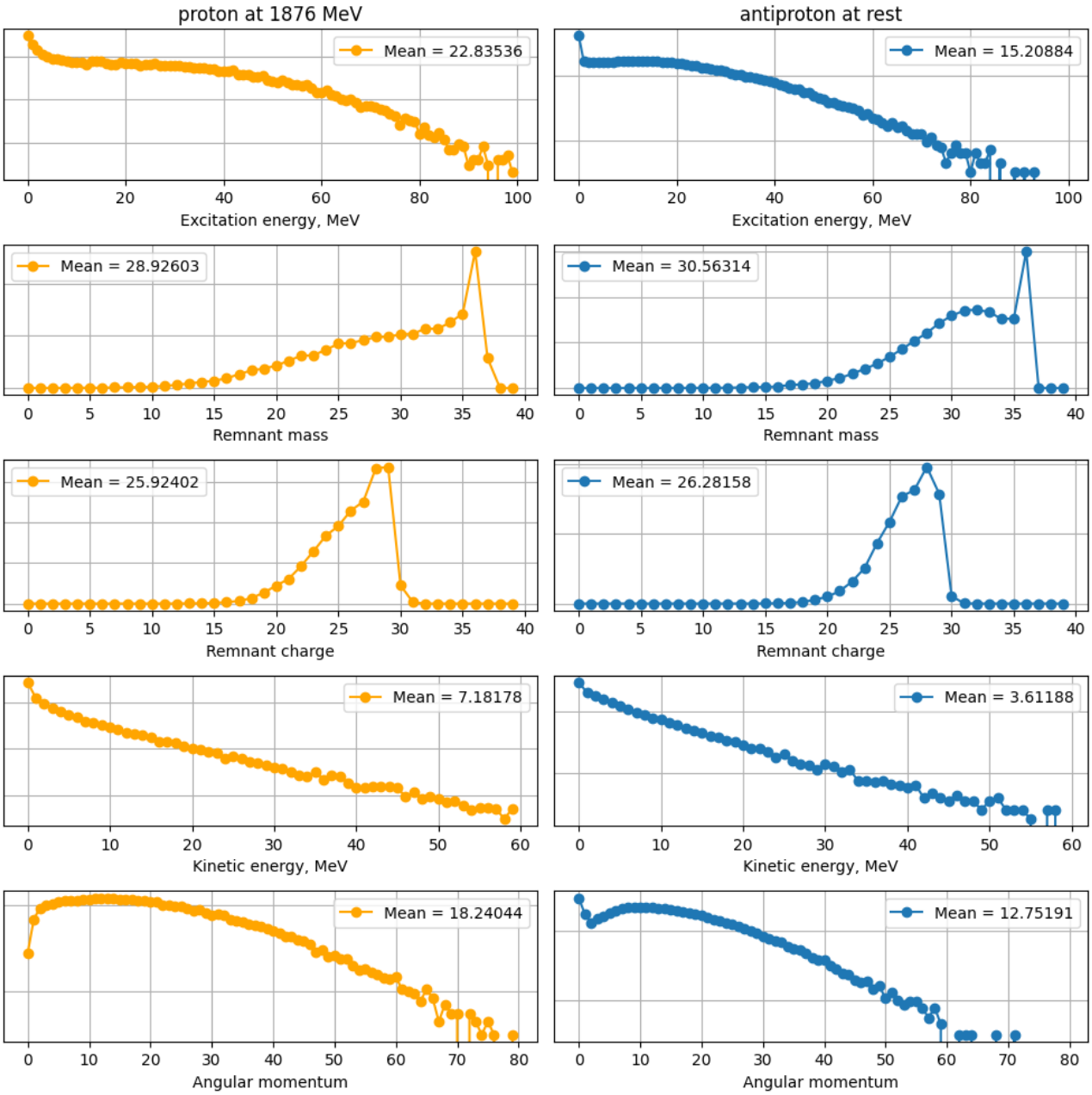

Figure 5.26: Main parameters passed to ABLA after cascade termination. Proton at $E_{kin} = 1876MeV$ is on the left (orange), while antiproton is on the right (blue). In both cases ^{197}Au was used as a target. 1 GeV/nucleon accelerated ^{238}U ions on hydrogen target vs INCL estimations[Int10] are given in Appendix A (page 111).

5.3.3.1 Residual yield estimation

There have been quite substantial effort at LEAR facility towards investigating radioactive residual nuclei produced as a result of $\bar{p}$ annihilation at rest. It is important to consider the peculiarities of isotope yield computation prior to diving into data analysis. The cross-sections for isotope production as a function of the incident projectile energy (primarily protons) come in two types: independent cross-sections and cumulative cross-sections. The independent cross-sections correspond to the direct production of a specific isotope, while the cumulative cross-sections take into account the precursor isotopes that may have decayed into the target isotope before measurement. Thus, results obtained from calculations can be directly compared to independent cross-sections, but for cumulative cross-sections, a certain summation needs to be performed. If we consider the simple case of an isotope with a parent isotope, then the measured activity of that isotope can be expressed as follows:

$$A(t) = N_t\Phi\left[\left(\sigma_D + \sigma_P\frac{\lambda_P}{\lambda_P-\lambda_D}\right)(1-e^{-\lambda_D t_{irr}})e^{(-\lambda_F t)}\right] - N_t\Phi\left[\sigma_P\frac{\lambda_P}{\lambda_P-\lambda_D}(1-e^{-\lambda_D t_{irr}})e^{(-\lambda_D t)})\right], \tag{5.12}$$

Where N_t is the number of target nuclei, Φ is the projectile flux, t_{irr} is the irradiation time, t is the time elapsed between the start of irradiation and measurement, σ are the direct production cross-sections, λ are the decay constants, and the indices D and P refer to Daughter and Parent isotopes.

If we define the cumulative cross-section as the cross-section that appears in the formula giving the activity of the isotope assumed without a parent, then the activity should be described as follows:

$$A(t) = N_t\Phi\left[\sigma_D^{cum}\left(1-e^{(-\lambda_D t_{irr})}\right)e^{(-\lambda_D t)}\right], \tag{5.13}$$

This is equivalent to defining the cumulative cross-section as:

$$\sigma_D^{cum} = \sigma_D + \sigma_P\frac{\lambda_P}{\lambda_P-\lambda_D}, \tag{5.14}$$

Note, that we may substitute cross-sections with yields, if we divide both sides by the total reaction cross section. This is only possible in cases where the decay period of the daughter is much greater than that of the parent ($\frac{\lambda_D}{\lambda_P} \ll 1$). This condition affects the decay chains that need to be considered since Equation (5.14) is iterative. Three libraries were used for three values of the $\frac{\lambda_D}{\lambda_P}$ ratio (0.1, 0.3 and 0.5), as well as a library where no condition was imposed, but where the cumulative section then takes the simple form of a sum of direct sections. The last method of simple summation was not used as it provided yields, which were obviously overestimated. Also, I have decided to only include values computed for $\frac{\lambda_D}{\lambda_P}$ ratio 0.1 and 0.5, as to make the value span visible in the figures, in most cases ratio 0.1 is optimal as can be observed in the INCL+ABLA vs data comparisons.

5.4 Sensitivity analysis

It is important to see the influence of certain input parameters, many of which are introduced to INCL with assumptions and simplifications. One of such parameters is the $S_n/S_p = \frac{1}{S_p/S_n}$ ratio, which in reality is dependent on the absorptive parts of the $\bar{p}$-nucleon potentials $S_n/S_p = \frac{Im(a_n)}{Im(a_p)}$. We know from experiments, that this ratio is different for deuterium and helium-4 targets and is explained by the binding energy of the nucleons on the nuclear surface. $\frac{Im(a_n)}{Im(a_p)} = 0.751(\pm 0.011)$ and $\frac{Im(a_n)}{Im(a_p)} = 0.47(\pm 0.04)$ were deduced from experiments on the emission of charged particles after antiproton annihilation with deuterons [Biz68] and helium nuclei [Bal+91], respectively.

Another input parameter to be tested is the annihilation orbit. In INCL we assign fixed value of annihilation orbit number for each element, for instance n=3 for carbon, which we know from atomic x-ray spectroscopy experiments [Pot84], but we also know that almost half of annihilations occur from n = 4, which is not taken into account. So, It might be useful to understand the sensitivity of particular observables to this parameter. Finally, we will address the problem of kaon production in $\bar{p}$ annihilations, and its implementation in INCL.

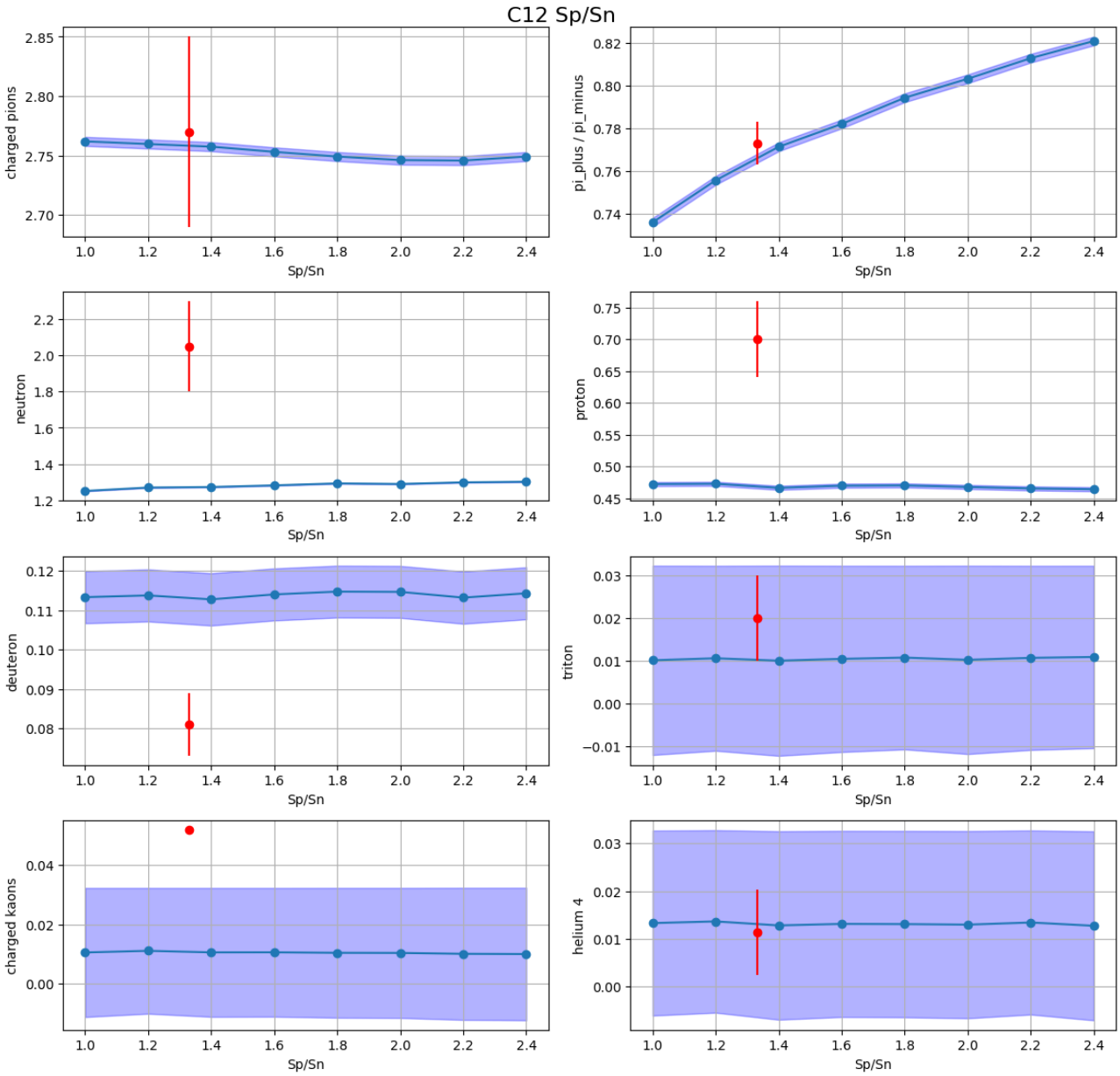

Figure 5.27: Parameter sensitivity to the value of proton to neutron annihilation probability ratio S_p/S_n for ^{12}C target.

5.4.1 Sp/Sn ratio

Below we will test the dependence of our INCL results on the value of S_p/S_n constant of the equation 5.3, which we use to determine the relative probability to annihilate with protons or neutrons. We will focus on ^{12}C and ^{238}U targets, assuming that the effect would be similar for other nuclei. For each multiplicity value or particle spectrum we always run one million cascades in order to reduce statistical uncertainties making them almost negligible in most cases, but in these cases we did only 200 thousands runs for each value of S_p/S_n to reduce the computation time, so we add statistical error of INCL as a belt for our plots 5.27 for carbon and 5.28 for uranium. All experimental points were placed at x = 1.331 just to mark the S_p/S_n value which was used in INCL by default.

We may observe that the most influenced value is the π^+/π^- which is to be expected. The decrease in the overall charged pion production is explained in the charged pion multiplicity values of elementary $n\bar{p}$ (eq. 5.8) and $p\bar{p}$ (eq. 5.7) final states, which is a bit higher for $n\bar{p}$. The neutron yield slightly increases with higher S_p/S_n which might be explained by the fact that if we annihilate a neutron, there is simply less neutrons to knock out after that, but the increase is more pronouncd for uranium which implies the presence of some additional mechanism. Such mechanism is even more apparent if we compare proton yield behaviour, which is different for carbon and uranium. One possible way to explain the excess of neutron, proton and deuteron yields for Uranium is the asymmetry

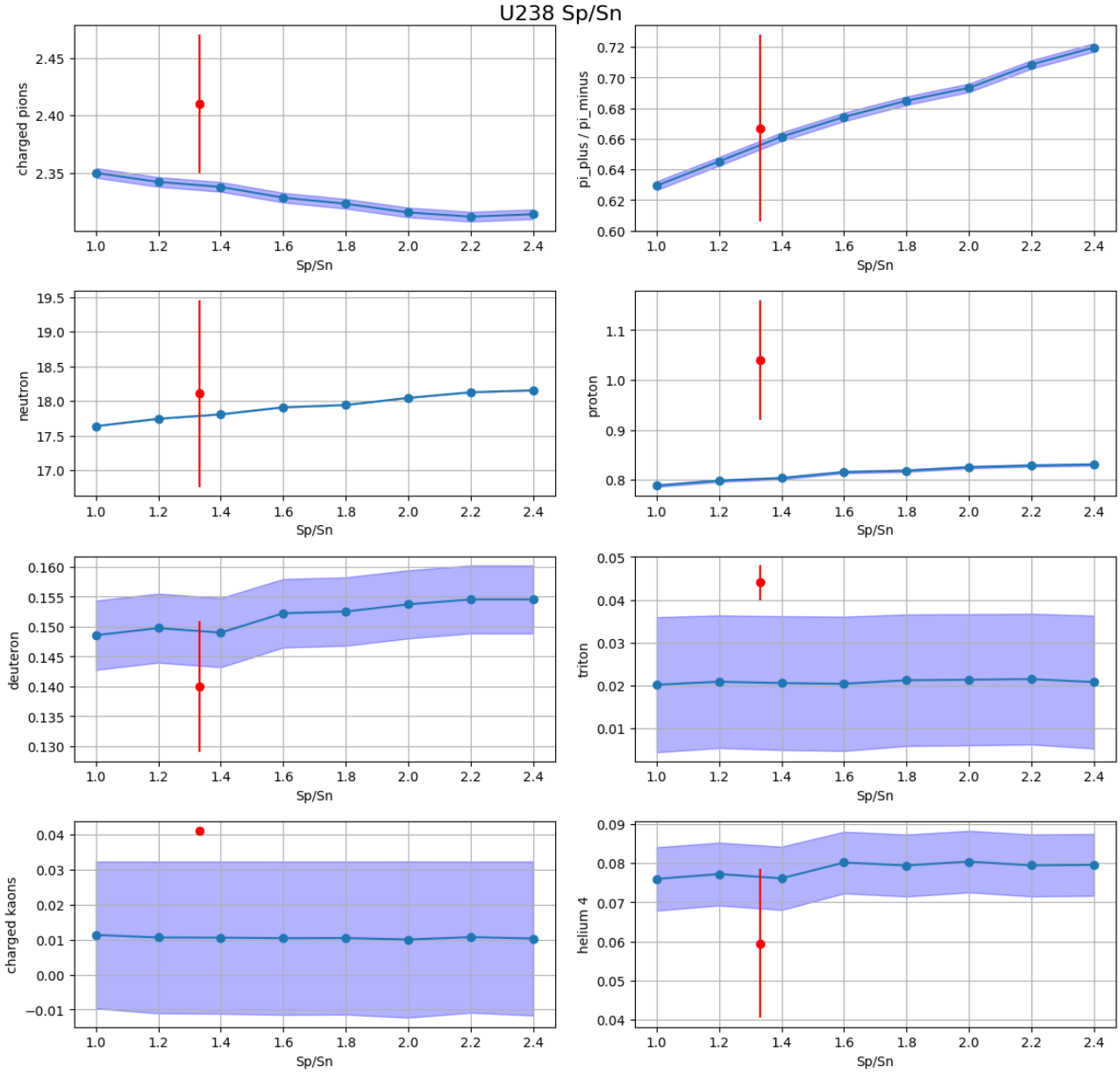

Figure 5.28: Parameter sensitivity to the value of proton to neutron annihilation probability ratio S_p/S_n for ^{238}U target.

of absorption cross sections for pions.

5.4.2 Annihilation orbit

One of the assumptions of INCL is the annihilation orbit principal quantum number n, which we fit from several data points known from x-ray spectroscopy of the antiprotonic atoms (see Fig. 5.5). Hereafter, we will explore the effect of annihilation orbit in the case of ^{12}C, ^{92}Mo, ^{181}Ta, and ^{238}U targets, for which we normally use the values of n equal to 3, 6, 8, and 10, respectively. In Fig. 5.29, 5.30, 5.31 and Fig. 5.32 we present the values of certain multiplicities and π^+/π^- parameter for several annihilation orbits. For each annihilation orbit we compute the mean distance of the overlap with the protonic density in order to see the influence of orbit number on the mean distance of pion star from the center of the nucleus. Proton and neutron density distributions are drawn in all plots to illustrate the influence of the different spatial onset of density increase for protons and neutrons. Note, that the ^{12}C case, there is proton skin instead of typical neutron skin in INCL, because its R_p parameter of the Wood-Saxon distribution is larger.

Experimental data values are taken from Ref. [Mar+88] for α-particles (helium 4), π^+/π^- ratio was taken from Ref. [McG+86a], while all other experimental values are from Ref. [Pol+95], the value for charged kaon multiplicity was digitized and has no error value. Multiplicities are integrated for kinetic energy range of 35-200 MeV for protons, 50-160 MeV for deuterons, 60-150 MeV for tritons, 60-200 MeV for charged kaons and 36-70 MeV for α-particles as it was done in the publications.

The effect which we see for proton, neutron, deuteron, triton, α-particles and the multiplicity of charged pions is pronounced and obvious: the closer we annihilate (Δn is negative) the more energy is transferred from pions to the nucleus, thus we observe less pions and more baryons. However, for the ratio of π^+/π^- the behaviour is different for heavy targets like tantalum and uranium, which exhibits a U-shaped pattern. The explanation might be found in higher neutron amount, which means that the charge-exchange reaction probability for π^+ will be higher closer to the center, while in the outer region it is the equality restoration of the proton and neutron densities which gives slight rise of the charged pion ratio. In other words, this bump is the effect of neutron skin which is more prominent at heavier targets.

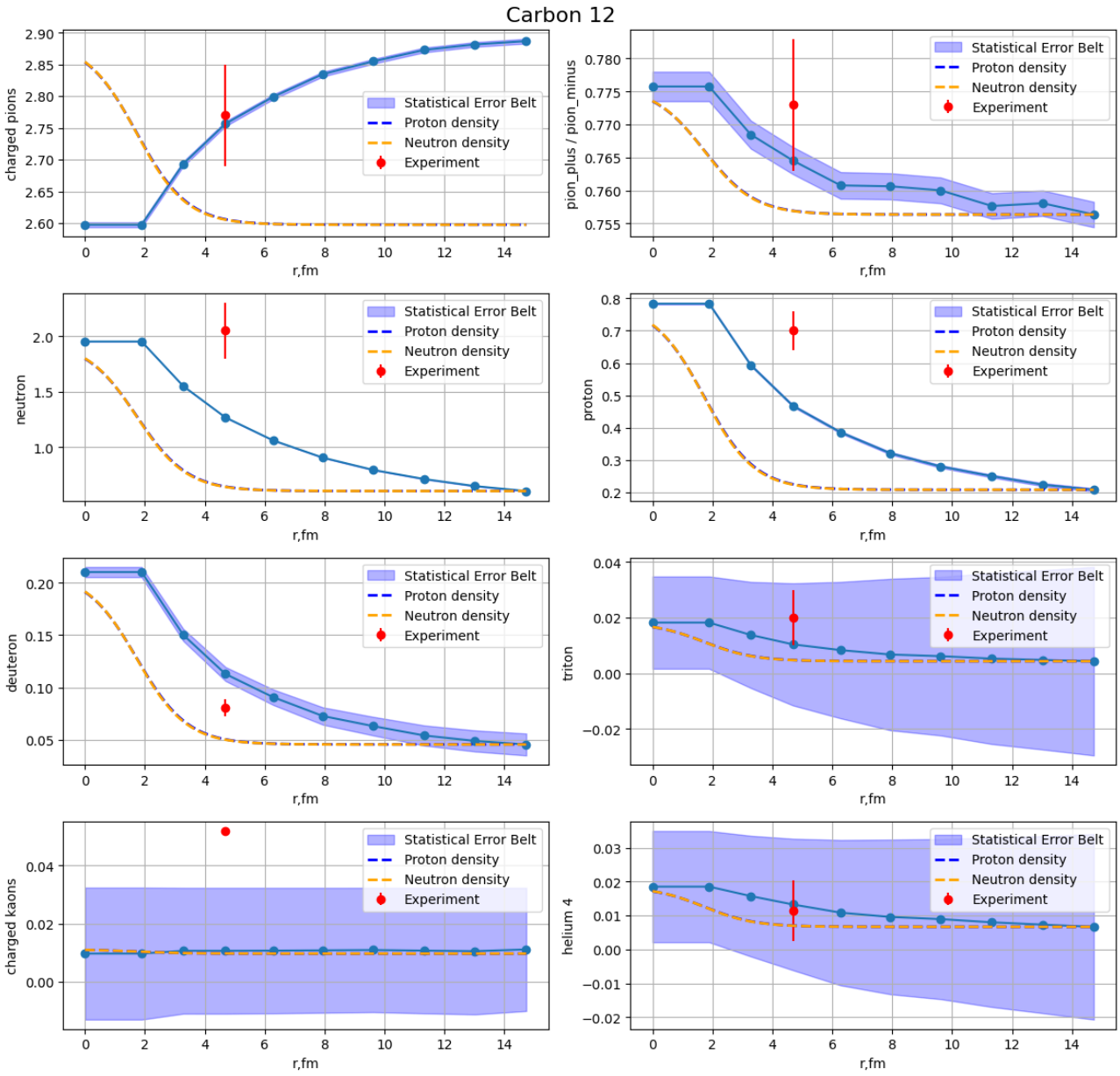

Figure 5.29: Parameter sensitivity to the value of annihilation orbit for ^{12}C target. Note, that first two points of INCL give the same result, because orbit number can't be zero or negative. Points are given for annihilation orbits from 1 to 9.

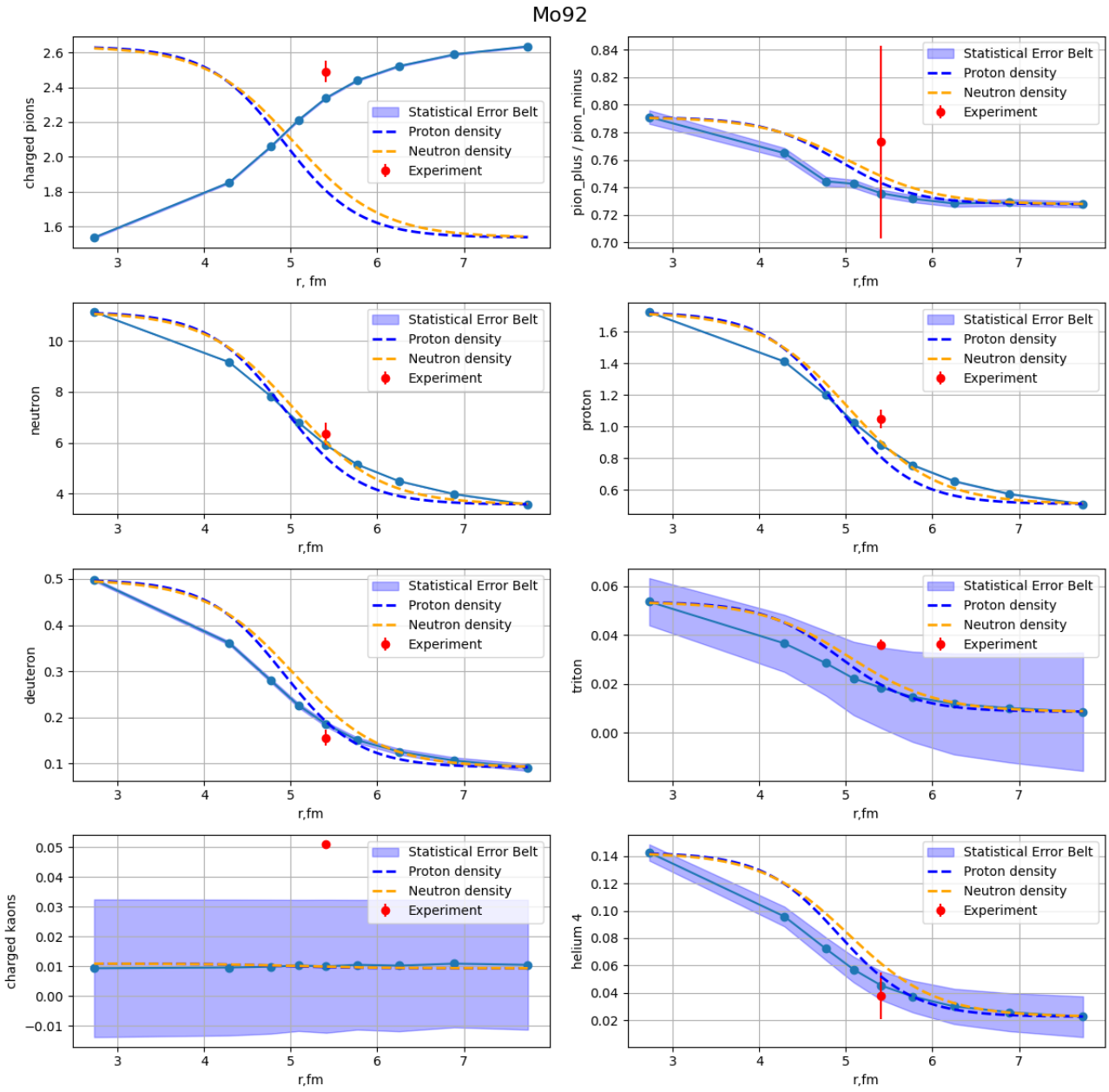

Figure 5.30: Parameter sensitivity to the value of annihilation orbit for ^{92}Mo target. Points are given for annihilation orbits from 2 to 10.

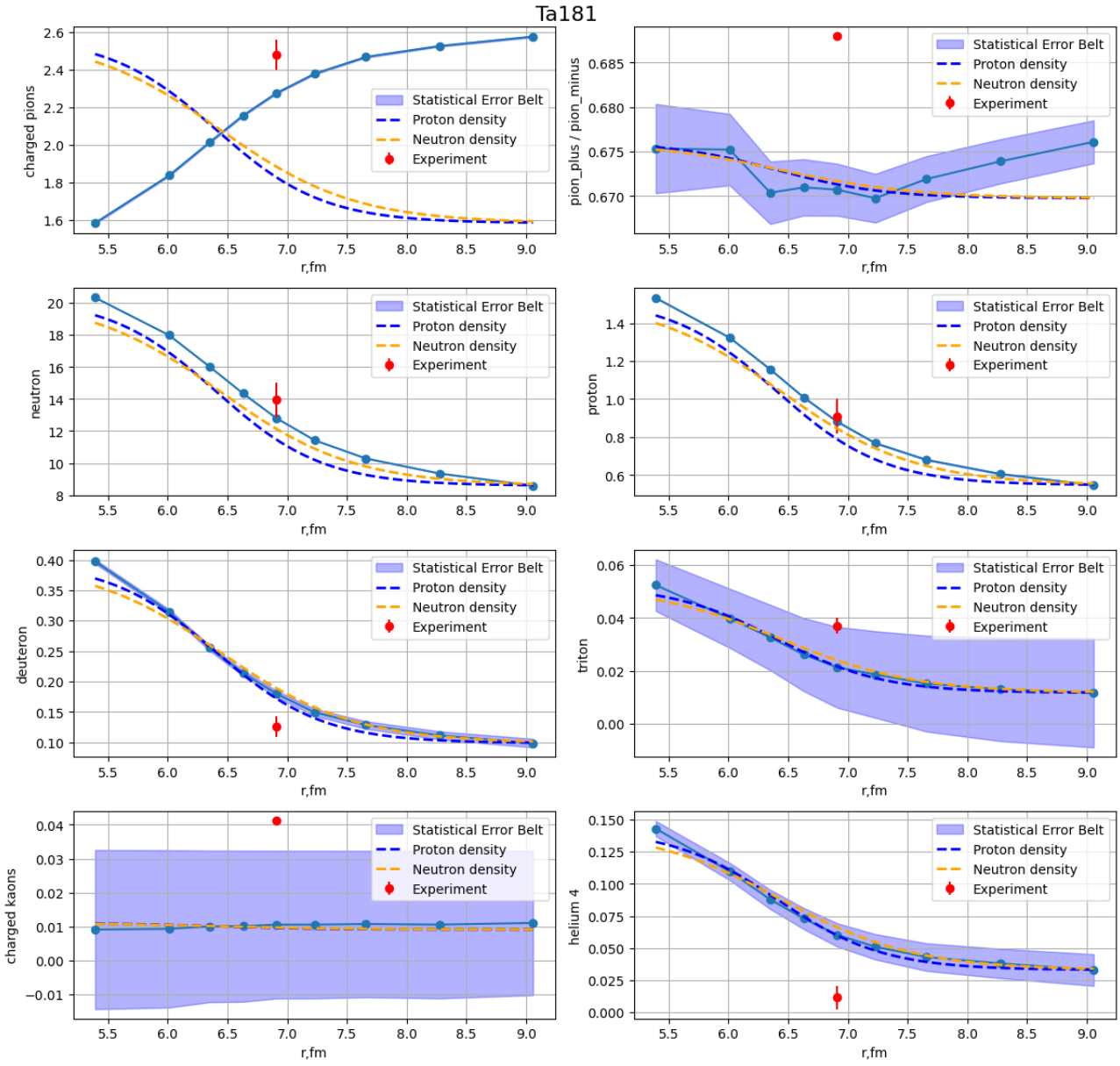

Figure 5.31: Parameter sensitivity to the value of annihilation orbit for ^{181}Ta target. Points are given for annihilation orbits from 4 to 12.

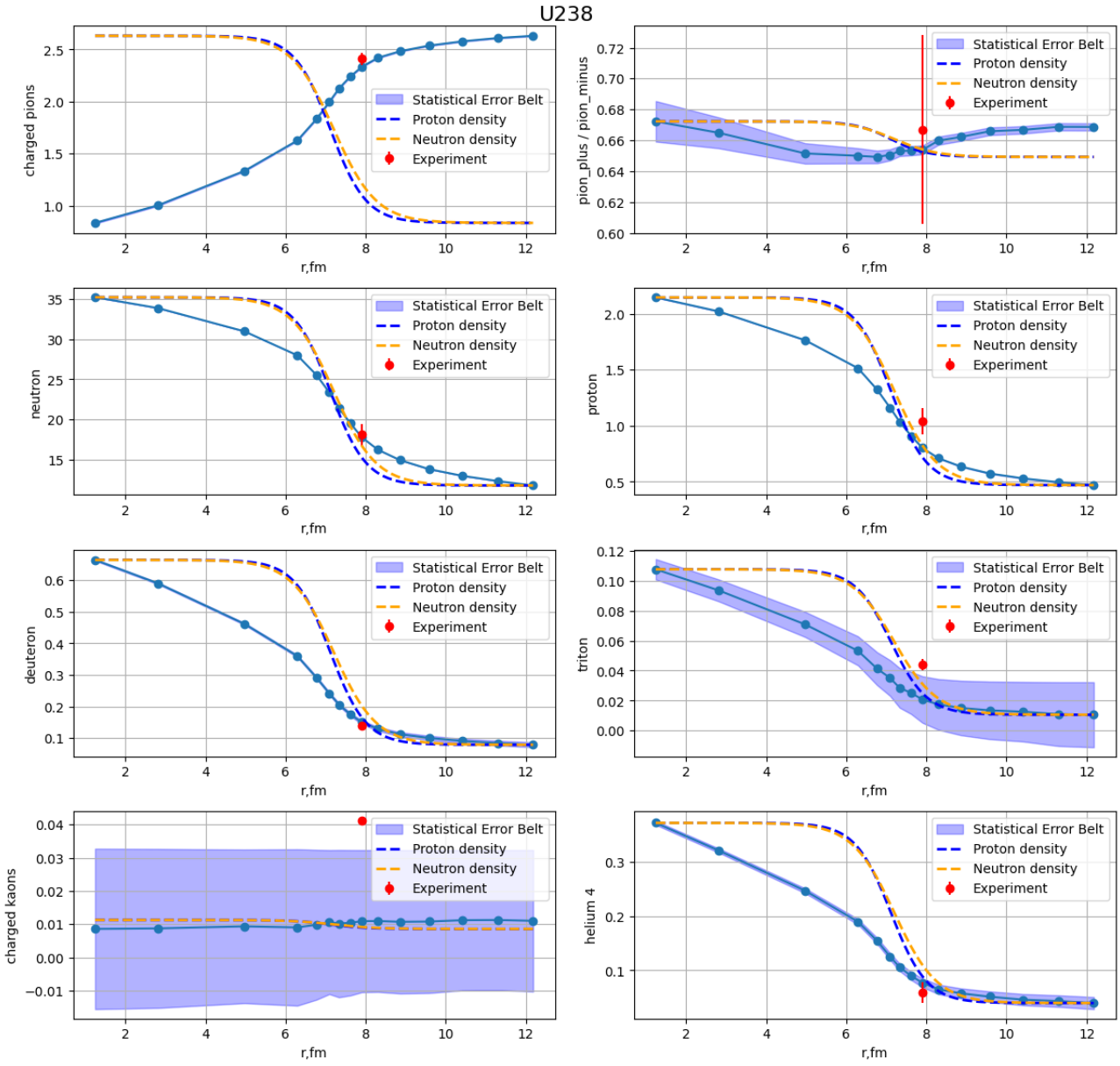

Figure 5.32: Parameter sensitivity to the value of proton to neutron annihilation orbit for ^{238}U target. Points are given for annihilation orbits from 2 to 16.

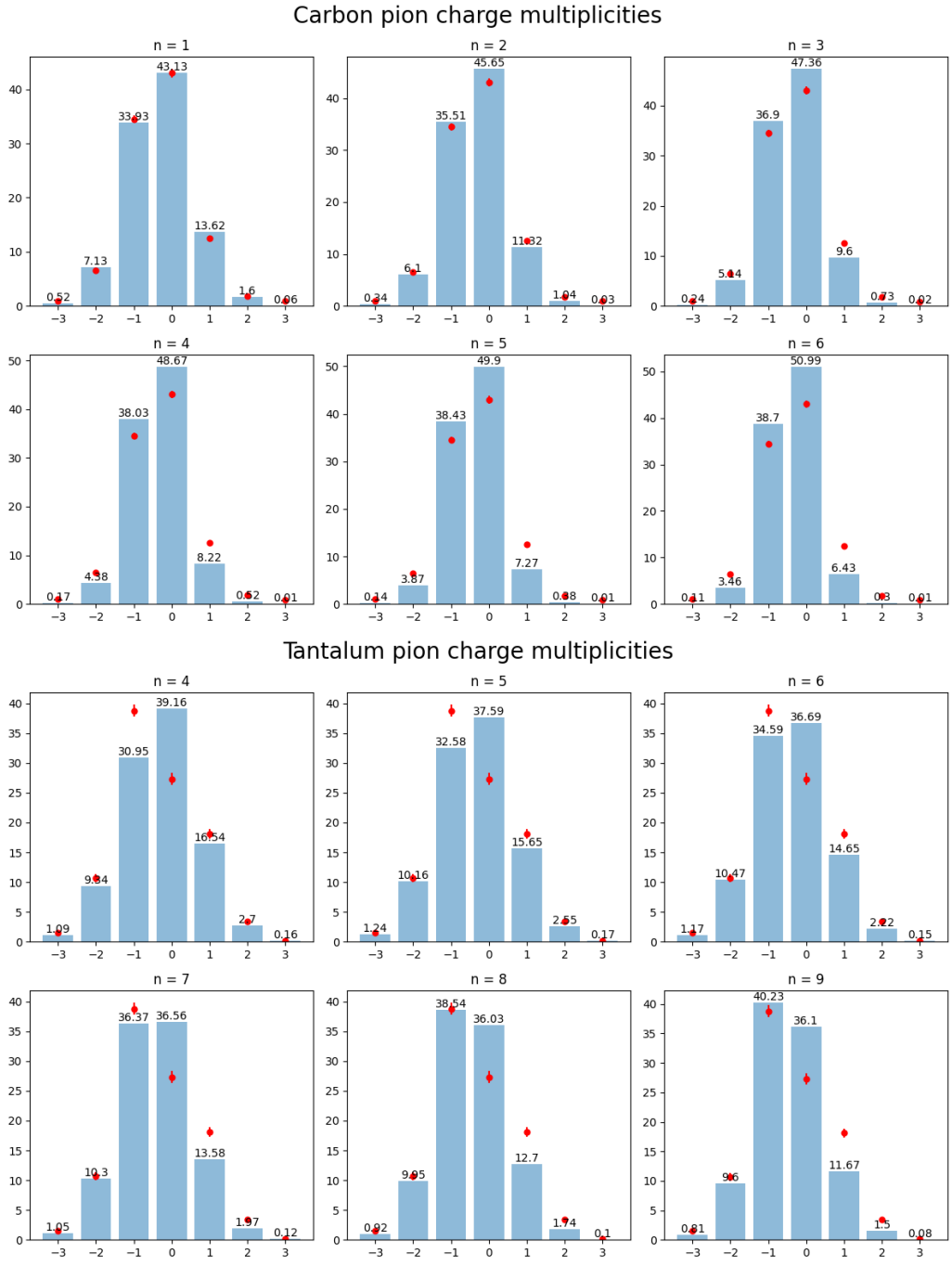

Figure 5.33: Parameter sensitivity to the value of annihilation orbit for ^{nat}C and ^{nat}Ta targets for pion charge multiplicities. n is the orbit number. Carbon: Data from Ref. [WL76], while the tantalum points are from Ref. [Bug+73] with errors from review [BK94]. More elements could be found in Appendix A (page 111).

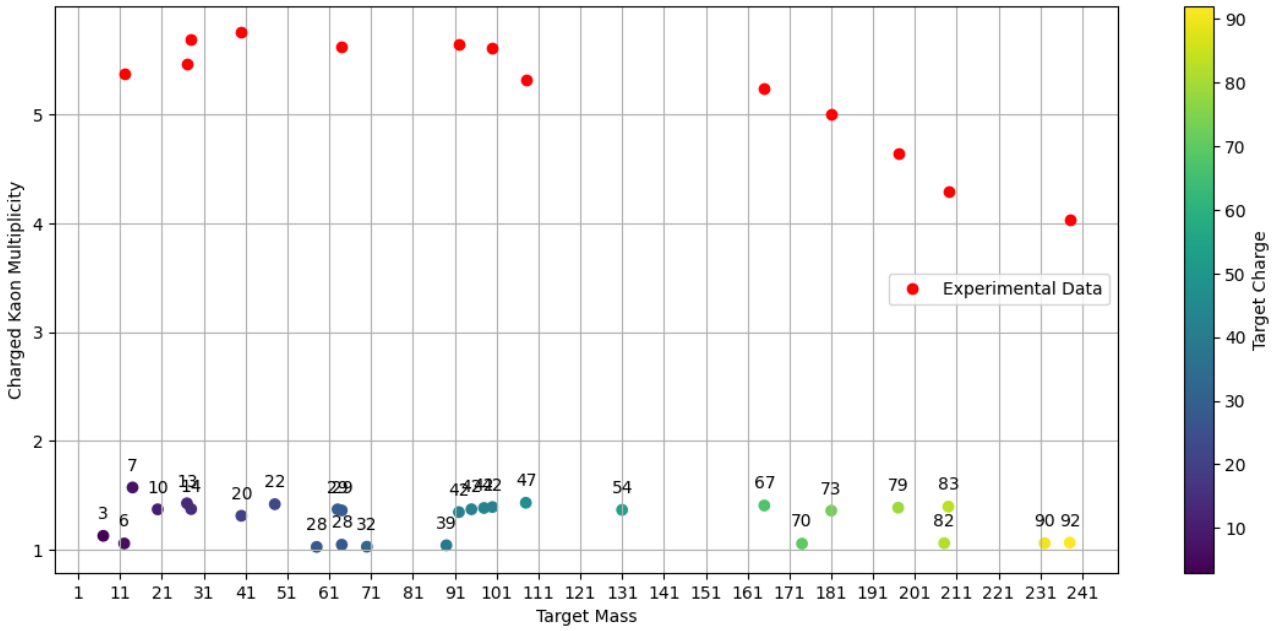

Figure 5.34: Charged kaon multiplicity in the kinetic energy range 60-200 MeV for targets from ^{12}C to ^{238}U. Values were digitized manually from Ref. [Pol+95].

Additionally, we will explore the influence of annihilation orbit on the charge distributions of pions for carbon and tantalum, which we will compare with the data from Ref. [WL76] and from Ref. [Bug+73] respectively in Fig. 5.33, we have to notice that there was a problem of hydrogen contamination (see Ref.[WP23]) in carbon target in Ref. [Bug+73], so in the Fig. 5.33(a) we compared our INCL to Ref. [WL76] measurements which were taken in a freon atmosphere. Such sensitivity test could be used to tune the parameter of the annihilation orbit together with the S_n/S_p ratio, for instance we know that the value for carbon is $S_n/S_p = \frac{Im(a_n)}{Im(a_p)} = 0.63(\pm 0.06)$ which is different from 0.751 ± 0.011 for deuteron which we use in INCL. What we see in response is that for orbit with n = 1 INCL is closer to the data (lowest root mean square error(RMSE) and Chi-squared) than in the case n = 3 or n = 4 known from atomic x-rays. For Tantalum the reported S_n/S_p was equal to 0.889 [Bug+73], which is larger than the INCL input. Here the orbit with n = 6 gives the lowest Chi-squared, while orbit with n = 8 has lowest RMSE and largest R-squared value which is the observed orbit for Tantalum [Pot84].

5.4.3 Kaonic final state probability

In Ref. [KBR05b] the total frequencies of annihilation final states (FS) containing kaons was estimated to be around 5% for hydrogen and deuterium. The exact FS with frequencies were also taken from the same reference, the sum of these frequencies was set to be 5% both for proton and neutron cases (kaonic FS probability), and while we are quite limited on data for strangeness production in at rest annihilations, INCL apparently underestimates kaon multiplicities compared to given in Ref. [Pol+95](see Fig. 5.34).

These values were digitized, so it makes sense probably to share the original plot in Fig. 5.35. On this figure the experimental values of multiplicities are taken in the range 60-200 MeV and the fit over the spectra is done to infer the overall multiplicity, which from the Fig. 5.35 seem to be almost two times higher that the measured one, meaning that roughly half of charged kaons are with the range. In case of INCL we only have third part of our charged kaons within this energy range, which could be possibly explained by too high relative probability of FS with high amount of particles (e.g. $\bar{p}p \rightarrow K^+K^-\pi^+\pi^-\pi^0$), while also the two-body kaonic FS (see Fig. 5.36). Perhaps the presence of the nucleus can affect the probability to create kaonic FS or, at least to produce more charged kaons, then the neutral ones as in the hydrogen case.

Kaons are the "white crow" particles in INCL, meaning that increasing the kaonic FS probability by several times (up to 15%) does not significantly impact the spectra and multiplicities of other particles. In other words, we can adjust this parameter to match the data without observable consequences for other outputs.

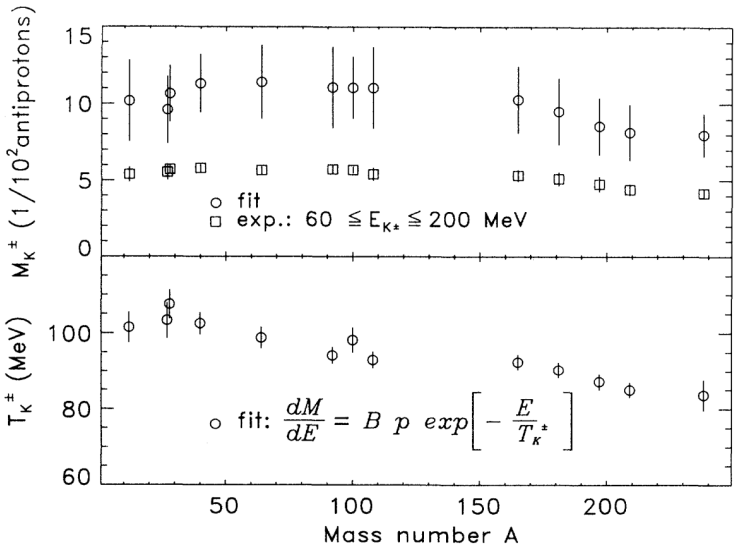

Figure 5.35: Multiplicities of charged kaons (upper panel), deduced from integration of the experimental spectrum over the given and the whole energy range, respectively (based on a fit to the spectra), and the "temperature" parameters of these spectra (lower panel) as function of the target mass. Taken from Ref. [Pol+95].

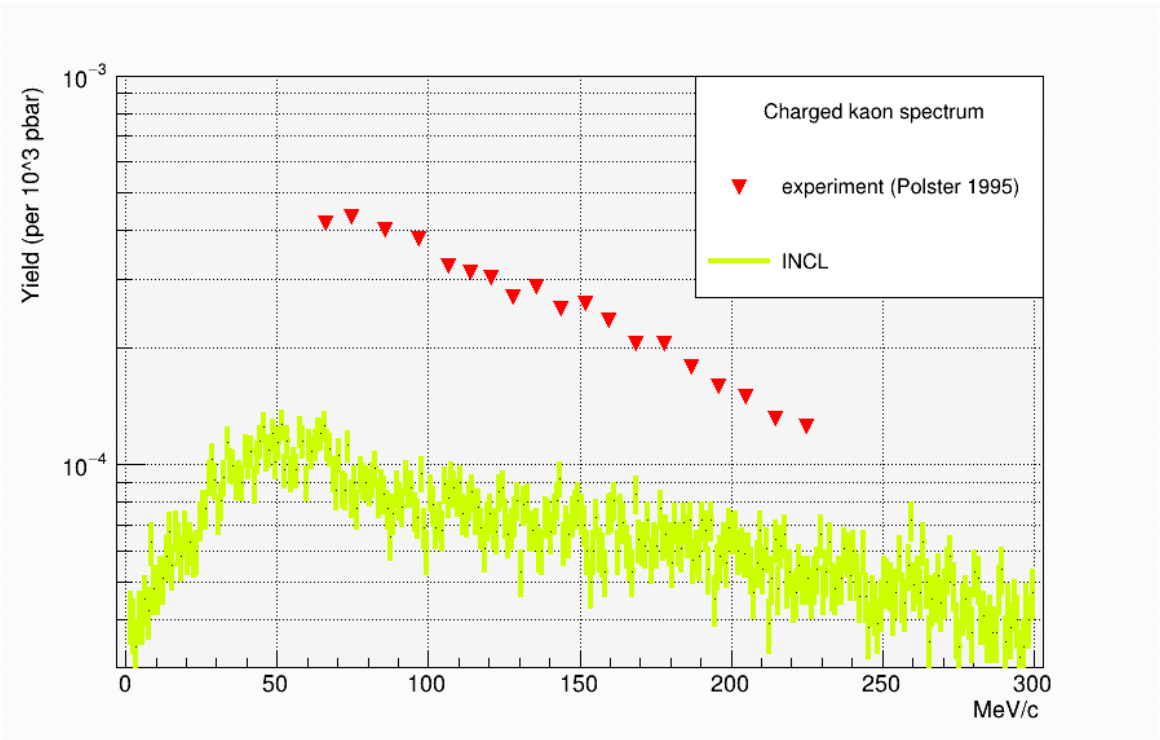

Figure 5.36: Spectrum of charged kaons emitted from ^{238}U target with $\bar{p}$ stopped from 200 MeV/c. Data points is digitized manually.

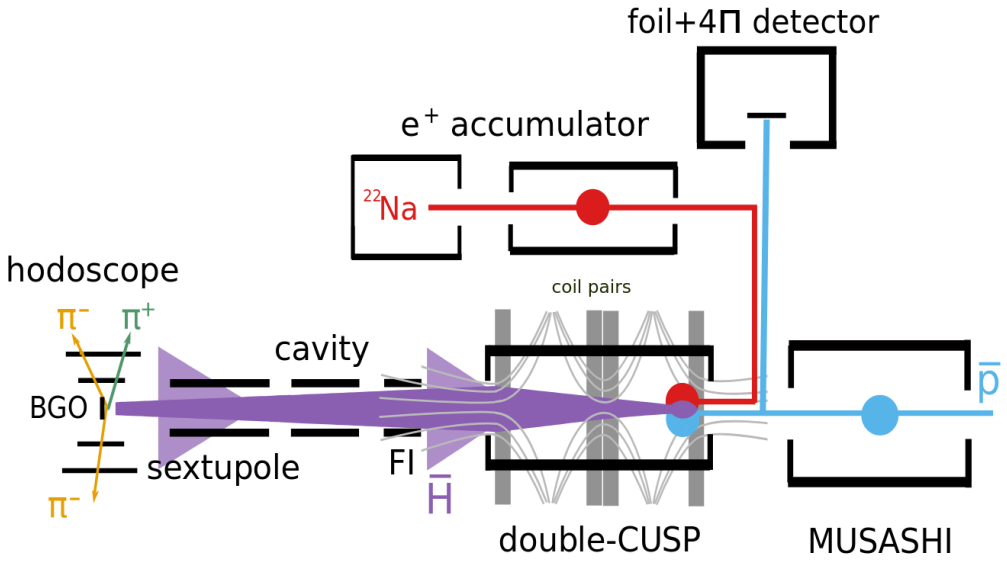

Figure 5.37: A scheme showing the path of the two experimenters operating at the ASACUSA facility, one of which is about to study antiproton annihilation at rest (the 4π detector).

5.5 Future experiments

There is high interest for the proper simulation tool for antiprotons not only regarding the aforementioned PUMA collaboration, but also for the ASACUSA (Atomic Spectroscopy And Collision Using Slow Antiprotons) group at the CERN AD.

The ASACUSA apparatus (see Fig. 5.37) measures antihydrogen's ground state hyperfine structure using Rabi spectroscopy in a field-free region. Antihydrogen is created by mixing antiprotons and positrons in the CUSP trap. A microwave cavity excites hyperfine transitions, changing low-field-seeking states to high-field seekers. These are defocused by a sextupole magnet. The transition frequency is determined by detecting remaining antihydrogen atoms. Another branch of ASACUSA is the 4π sr solid angle detector around the annihilation foil (target), which will:

- Detect both pions and heavy fragments ($p, d, t,^3$ He,^{4} He,^{6} He, etc.) and count the prong multiplicity of single pA annihilation events;
- Measure the deposited energy and the angular distribution of the different prongs;
- Measure the direction and the specific ionization ($\frac{dE}{dx}$) for pions, allowing for a 3D reconstruction of the annihilation vertex;

New studies have started to emerge in the past few years, investigating the annihilation of ~ 100 keV antiprotons in various targets and the results of these studies showed that the measured data are not well reproduced by the different existing models of Geant4. For example, the average multiplicity number of the charged pions, or minimum ionizing particles (MIPs), depending on the target nucleus, differs from the data from a factor 0.25 to ~ 2, whereas the multiplicity of the heavier fragments, or heavily ionizing particles (HIPs), is off by a factor 0.1 to 4. FLUKA describes the measured data with somewhat better precision, but even there the predictions are off by e.g. a factor ~ 0.3 (see Table 5.4). INCL could help to fulfill this gap in the simulation tools available for low-energy antiproton interactions, and we are currently in contact with the ASACUSA group to apply INCL for their needs.

References

[Adl+97] R. Adler et al. "Experimental measurement of the K(S) K(S) / K(S) K(L) ratio in anti-proton annihilations at rest in gaseous hydrogen at 15-bar and 27-bar". In: *Phys. Lett. B* 403 (1997), pp. 383–389. doi: 10.1016/S0370-2693(97)00489-9.

[AF69] R Armenteros and B French. “ANTINUCLEON–NUCLEON INTERACTIONS.” In: *pp 237-417 of High Energy Physics. Vol. IV. Burhop, E. H. S. (ed.). New York, Academic Press, 1969.* (Oct. 1969).

[Agh+18] H. Aghai-Khozani et al. “Measurement of the antiproton–nucleus annihilation cross-section at low energy”. In: *Nuclear Physics A* 970 (2018), pp. 366–378. issn: 0375-9474. doi: https://doi.org/10.1016/j.nuclphysa.2018.01.001.

[Agn+60] Lewis E. Agnew et al. “Antiproton Interactions in Hydrogen and Carbon below 200 Mev”. In: *Phys. Rev.* 118 (5 June 1960), pp. 1371–1391. doi: 10.1103/PhysRev.118.1371.

[Ams+03] C. Amsler et al. “Annihilation at rest of antiprotons and protons into neutral particles”. In: *Nucl. Phys. A* 720 (2003), pp. 357–367. doi: 10.1016/S0375-9474(03)00912-6.

[Aum+19] T Aumann et al. *PUMA: antiprotons and radioactive nuclei*. Tech. rep. Geneva: CERN, 2019.

[Aum+22] T. Aumann et al. “PUMA, antiProton unstable matter annihilation”. In: *The European Physical Journal A* 58.5 (2022), p. 88. issn: 1434-601X. doi: 10.1140/epja/s10050-022-00713-x.

[Bal+87] A. Baldini et al. *Total Cross-Sections for Reactions of High Energy Particles (Including Elastic, Topological, Inclusive and Exclusive Reactions) / Totale Wirkungsquerschnitte fur Reaktionen hochenergetischer Teilchen (einschliesslich elastischer,topologischer, inklusiver u*. Landolt-Börnstein: Numerical Data and Functional Relationships in Science and Technology - New Series. Springer Berlin Heidelberg, 1987. isbn: 9783540183860.

[Bal+91] F. Balestra et al. “Strangeness production in antiproton annihilation at rest on 3He, 4He and 20Ne”. In: *Nuclear Physics A* 526.3 (1991), pp. 415–452. issn: 0375-9474. doi: https://doi.org/10.1016/0375-9474(91)90428-9.

[Bar+64] V. Barnes et al. “Proceedings of the XII International Conference on High Energy Physics”. In: *Dubna, 1964*. Vol. 1. 1964, p. 731.

[Bat+88] Yu. A. Batusov et al. “PRODUCTION OF NEUTRAL STRANGE PARTICLES IN ANTI-P HE-4 ANNIHILATION AT 600-MEV/C. (IN RUSSIAN)”. In: (1988).

[Ber+03] M. Bernas et al. “Fission-residues produced in the spallation reaction 238U + p at 1AGeV”. In: *Nuclear Physics A* 725 (2003), pp. 213–253. issn: 0375-9474. doi: https://doi.org/10.1016/S0375-9474(03)01576-8.

[Bet+67] A. Bettini et al. “Annihilation into pions of the $\bar{p}n$ system from antiprotons at rest in deuterium”. In: *Il Nuovo Cimento A (1965-1970)* 47.3 (1967), pp. 642–661. doi: 10.1007/BF02738758.

[Bia+11] A. Bianconi et al. “Measurement of the antiproton–nucleus annihilation cross section at 5.3 MeV”. In: *Physics Letters B* 704.5 (2011), pp. 461–466. issn: 0370-2693. doi: https://doi.org/10.1016/j.physletb.2011.09.069.

[Biz+74] R. Bizzarri et al. “Antiproton-deuteron low-energy cross-sections”. In: *Il Nuovo Cimento A (1965-1970)* 22.2 (1974), pp. 225–250. issn: 1826-9869. doi: 10.1007/BF02813436.

[Biz68] R. Bizzarri. “On the comparison of the annihilation of antiprotons at rest in hydrogen and deuterim”. In: *Il Nuovo Cimento A (1965-1970)* 53.4 (Feb. 1968), pp. 956–968. issn: 1826-9869. doi: 10.1007/BF02758737.

[BK94] G. Bendiscioli and D. Kharzeev. “Antinucleon-nucleon and antinucleon-nucleus interaction. A review of experimental data”. In: *La Rivista del Nuovo Cimento (1978-1999)* 17.6 (1994), pp. 1–142. issn: 1826-9850. doi: 10.1007/BF02724447.

[Bug+73] W. M. Bugg et al. “Evidence for a Neutron Halo in Heavy Nuclei from Antiproton Absorption”. In: *Phys. Rev. Lett.* 31 (7 Aug. 1973), pp. 475–478. doi: 10.1103/PhysRevLett.31.475.

[Chi+89] M. Chiba et al. “η and η' production in $\overline{p}p$ annihilation at rest”. In: *Phys. Rev. D* 39 (11 June 1989), pp. 3227–3238. doi: 10.1103/PhysRevD.39.3227.

[Chr+22] Christiansen, Martin et al. “Exploring the neutron skin by hyperon-antihyperon production in antiproton-nucleus interactions”. In: *EPJ Web Conf.* 271 (2022), p. 02011. doi: 10.1051/epjconf/202227102011.

[CK66] W. Chinowsky and G. Kojoian. “Antiproton annihilation at rest in deuterium”. In: *Il Nuovo Cimento A (1965-1970)* 43.3 (1966), pp. 684–700. doi: 10.1007/BF02756689.

[Coh00] James S. Cohen. “Antiproton capture by simple atoms and molecules”. In: *AIP Conference Proceedings* 500.1 (Feb. 2000), pp. 540–550. issn: 0094-243X. doi: 10.1063/1.1302685.

[Coh04] James S. Cohen. “Capture of antiprotons by some radioactive atoms and ions”. In: *Phys. Rev. A* 69 (2 Feb. 2004), p. 022501. doi: 10.1103/PhysRevA.69.022501.

[Coh97] James S. Cohen. “Molecular effects on antiproton capture by H_2 and the states of $\overline{p}p$ formed”. In: *Phys. Rev. A* 56 (5 Nov. 1997), pp. 3583–3596. doi: 10.1103/PhysRevA.56.3583.

[El-+09] B. El-Bennich et al. “Paris $N\overline{N}$ potential constrained by recent antiprotonic-atom data and $\overline{n}p$ total cross sections”. In: *Phys. Rev. C* 79 (5 May 2009), p. 054001. doi: 10.1103/PhysRevC.79.054001.

[Fas+03] A. Fasso’ et al. *The physics models of FLUKA: status and recent development*. 2003.

[Ghe74] Claude Ghesquiere. “An inclusive view on $\overline{p}p \to n\pi$ at rest”. In: (1974). doi: 10.5170/CERN-1974-018.436.

[Gol+92] E.S. Golubeva et al. “Effects of mesonic resonance production in annihilation of stopped antiprotons on nuclei”. In: *Nuclear Physics A* 537.3 (1992), pp. 393–417. issn: 0375-9474. doi: https://doi.org/10.1016/0375-9474(92)90362-N.

[Har+01] F. J. Hartmann et al. “Study of the nuclear periphery with Antiprotons”. In: *Acta Physica Hungarica* 13.1 (Mar. 2001), pp. 51–60. issn: 1588-2675. doi: 10.1556/APH.13.2001.1-3.7.

[Int10] International Atomic Energy Agency. *IAEA Benchmark of Spallation Models - Experimental Data*. 2010. url: https://www-nds.iaea.org/spallations/cal/iso/p_UU238_1000_isodst_ic45a07_tbbr06a_cmp.pdf (visited on 2010).

[Jas+93] J. Jastrzębski et al. “Interaction of stopped antiprotons with copper”. In: *Phys. Rev. C* 47 (1 Jan. 1993), pp. 216–224. doi: 10.1103/PhysRevC.47.216.

[Kan+86] W Kanert et al. “First observation of the E-italic2 nuclear-resonance effect in antiprotonic atoms”. In: *Phys. Rev. Lett.; (United States)* (June 1986). doi: 10.1103/PhysRevLett.56.2368.

[KBR05a] Eberhard Klempt, Chris Batty, and Jean-Marc Richard. “The antinucleon-nucleon interaction at low energy: Annihilation dynamics”. In: *Physics Reports* 413 (Jan. 2005). doi: 10.1016/j.physrep.2005.03.002.

[KBR05b] Eberhard Klempt, Chris Batty, and Jean-Marc Richard. “The antinucleon–nucleon interaction at low energy: Annihilation dynamics”. In: *Physics Reports* 413.4-5 (July 2005), pp. 197–317. doi: 10.1016/j.physrep.2005.03.002.

[Lub+98] P. Lubinski et al. “Composition of the nuclear periphery from antiproton absorption”. In: *Phys. Rev. C* 57 (6 June 1998), pp. 2962–2973. doi: 10.1103/PhysRevC.57.2962.

[Mac+92] H. Machner et al. “Fission fragment distribution following antiproton absorption at rest on238U”. In: *Zeitschrift für Physik A Hadrons and Nuclei* 343.1 (Mar. 1992), pp. 73–77. issn: 0939-7922. doi: 10.1007/BF01291600.

[Mar+88] W. Markiel et al. “Emission of helium ions after antiproton annihilation in nuclei”. In: *Nuclear Physics A* 485.3 (1988), pp. 445–460. issn: 0375-9474. doi: https://doi.org/10.1016/0375-9474(88)90547-7.

[McG+86a] P. L. McGaughey et al. “Dynamics of Low-Energy Antiproton Annihilation in Nuclei as Inferred from Inclusive Proton and Pion Measurements”. In: *Phys. Rev. Lett.* 56 (20 May 1986), pp. 2156–2159. doi: 10.1103/PhysRevLett.56.2156.

[McG+86b] P.L. McGaughey et al. “Low energy antiproton-nucleus annihilation radius selection using an active silicon detector/target”. In: *Nuclear Instruments and Methods in Physics Research Section A: Accelerators, Spectrometers, Detectors and Associated Equipment* 249.2 (1986), pp. 361–365. issn: 0168-9002. doi: https://doi.org/10.1016/0168-9002(86)90689-3.

[Mos+86] E.F. Moser et al. “Yields of residual nuclei after antiproton annihilation in 95Mo and 98Mo”. In: *Physics Letters B* 179.1 (1986), pp. 25–29. issn: 0370-2693. doi: https://doi.org/10.1016/0370-2693(86)90429-6.

[Mos+89] E. F. Moser et al. “Residual nuclei after antiproton annihilation in Mo and Ho”. In: *Zeitschrift für Physik A Atomic Nuclei* 333.1 (Mar. 1989), pp. 89–105. issn: 0939-7922. doi: 10.1007/BF01290114.

[Pol+95] D. Polster et al. “Light particle emission induced by stopped antiprotons in nuclei: Energy dissipation and neutron-to-proton ratio”. In: *Phys. Rev. C* 51 (3 Mar. 1995), pp. 1167–1180. doi: 10.1103/PhysRevC.51.1167.

[Pot84] H. Poth. “Physics with Antiprotonic Atoms”. In: *Physics at LEAR with Low-Energy Cooled Antiprotons*. Ed. by Ugo Gastaldi and Robert Klapisch. Boston, MA: Springer New York, 1984, pp. 567–588. isbn: 978-1-4684-8727-5. doi: 10.1007/978-1-4684-8727-5_54.

[RBD09] V. Rotival, K. Bennaceur, and T. Duguet. “Halo phenomenon in finite many-fermion systems: Atom-positron complexes and large-scale study of atomic nuclei”. In: *Phys. Rev. C* 79 (5 May 2009), p. 054309. doi: 10.1103/PhysRevC.79.054309.

[Ric+06] M. V. Ricciardi et al. “Light nuclides produced in the proton-induced spallation of ^{238}U at 1 GeV”. In: *Phys. Rev. C* 73 (1 Jan. 2006), p. 014607. doi: 10.1103/PhysRevC.73.014607.

[Rie+89] J. Riedlberger et al. “Antiproton annihilation at rest in nitrogen and deuterium gas”. In: *Phys. Rev. C* 40 (6 Dec. 1989), pp. 2717–2731. doi: 10.1103/PhysRevC.40.2717.

[Ser47] R. Serber. “Nuclear Reactions at High Energies”. In: *Phys. Rev.* 72 (11 Dec. 1947), pp. 1114–1115. doi: 10.1103/PhysRev.72.1114.

[Taï+03] J. Taïeb et al. “Evaporation residues produced in the spallation reaction 238U+p at 1AGeV”. In: *Nuclear Physics A* 724.3 (2003), pp. 413–430. issn: 0375-9474. doi: https://doi.org/10.1016/S0375-9474(03)01517-3.

[Trz+01] A. Trzcinska et al. “Information on antiprotonic atoms and the nuclear periphery from the PS209 experiment”. In: *Nuclear Physics A* 692.1 (2001). Sixth Biennial Conference on Low-Energy Antiproton Physics, pp. 176–181. issn: 0375-9474. doi: https://doi.org/10.1016/S0375-9474(01)01176-9.

[Uzh10] Vladimir Uzhinsky. “Development of the Fritiof model in Geant4”. In: Proceedings of SNA + MC2010: Joint international conference on supercomputing in nuclear applications + Monte Carlo 2010 Tokyo. PHYSICS OF ELEMENTARY PARTICLES AND FIELDS. Japan, 2010, p. 1630.

[WL76] M. Wade and V. G. Lind. “Ratio of antiproton annihilations on neutrons and protons in carbon for low-energy and stopped antiprotons”. In: *Phys. Rev. D* 14 (5 Sept. 1976), pp. 1182–1187. doi: 10.1103/PhysRevD.14.1182.

[WP23] S. Wycech and K. Piscichia. “Pionization: A method to study the nuclear surface”. In: *Phys. Rev. C* 108 (1 July 2023), p. 014313. doi: 10.1103/PhysRevC.108.014313.

[Wyc+93] S. Wycech et al. “Antiprotonic atoms with heavy nuclei”. In: *Nuclear Physics A* 561.4 (1993), pp. 607–627. issn: 0375-9474. doi: https://doi.org/10.1016/0375-9474(93)90068-9.

[Wyc+96] S. Wycech et al. “Antiprotonic studies of nuclear neutron halos”. In: *Phys. Rev. C* 54 (4 Oct. 1996), pp. 1832–1842. doi: 10.1103/PhysRevC.54.1832.

6 | In-flight $\bar{p} - A$ interaction

6.1 General hypotheses and workflow

The philosophy of the $\bar{p}$-nucleus in-flight interaction scenario modelling is the same as for any other particle already existing in the INCL. We set the antiproton kinetic energy and the target nucleus charge and mass, after which we plant protons and neutrons in the correspondent quantities, we cast some random impact parameter (which will be affected by the Coulomb distortion in case of charged projectile) and let the cascade begin. All principal hypotheses were described in the INCL related section 4.2.

One may already note certain peculiarity of the initialization step for the in-flight scenario: we initialize the target nucleus as it was set by the user, while in at rest scenario we initialized a nucleus with one nucleon less considering it as an already annihilated one. In particular, this implements the possibility for the target nucleus to conserve its mass and charge due to the elastic scattering for example, whose cross section grows towards lower projectile momenta, or due to a more exotic scenario, through the charge exchange of antiproton into antineutron ($\bar{p}p \rightarrow \bar{n}n$) with subsequent charged pion emission in a collision with another nucleon ($nn \rightarrow pn\pi^-$ or $np \rightarrow pp\pi^-$), if the antineutron is also emitted.

Another issue of the in-flight scenario implementation is that it is based on the experimental data of exclusive channels' cross sections rather than frequencies like it was at rest. The inevitability of annihilation at rest makes it much more simple to normalize the frequencies (the probability is one), while in-flight we have to require the sum of our exclusive channels to be consistent with the total cross section and certain inclusive cross sections (e.g. the annihilation).

We have to introduce certain assumptions in our implementation due to the necessity of handling not only the particles which have been already introduced to INCL, but also new antibaryons, like $\bar{n}$, $\bar{\Lambda}$, $\bar{\Sigma}$ and even $\bar{\Xi}$. There is very little or no experimental data about these particles and their reactions with the nucleons. For instance, we assume the $n\bar{p}$ cross sections to be exactly same as for the $p\bar{n}$[1], but for the case of $n\bar{n}$ it is slightly different, from where the information must be taken, and we assume the similarity of the inclusive channels with the $p\bar{p}$ (thought, with corrections to be discussed below). Finally, we have to acknowledge the current inability to properly treat secondary reactions for exotic specimen like the $\bar{\Lambda}$, $\bar{\Sigma^+}$, $\bar{\Sigma^0}$, $\bar{\Sigma^-}$, and $\bar{\Xi}$, these particles would simply leave the nucleus if produced, although the overall production rate of these particles is quite low (i.e. their production cross sections almost never exceed 1% of the total).

6.2 Model ingredients

If we consider the in-flight collision of antiproton with the nucleus, it turns out, that there is only three types of parameters which must be introduced to this particular scenario:

1. Exclusive cross-sections
2. Nuclear potentials
3. Energy thresholds (min and max)

and the most significant ones here are the cross-sections. The energy thresholds are not used explicitly, but rather define the range of energies where our model is consistent and recommended

[1] $n\bar{p}$ and $p\bar{n}$ states are CPT-symmetrical initial states

for applications. We already discussed this issue in Section 5.1 for the minimal energy to apply INCL in-flight, and an additional sense of this threshold could be perceived from Fig. 6.3. In fact, there is a range of energies (roughly between 100 and 300 MeV) where both scenarios should give adequate results. Meanwhile, the maximal (recommended) energy was chosen to be 9 GeV (10 GeV/c). Nuclear potentials (which are implemented as simple square well) have the effect on the model outputs, which resembles simple addition of incident energy (sensitivity test is done in Fig. B.1 in Appendix B), thus hereafter we would principally discuss the means and methods to fulfill cross section data into our model. Also, as we will show later, certain information is borrowed from the at rest annihilation, due to the lack of data.

6.2.1 Cross section

The key components of elementary total cross sections are depicted in Figure 6.1. It is evident that both in the $p\bar{p}$ and $n\bar{p}$ cases, INCL begins to underestimate the total sum by up to 10% as the momentum approaches 10 GeV/c. This underestimation is likely attributable to the omission of certain resonance production channels. Additionally, we identified specific points in the $p\bar{p}$ chart of Figure 6.1 for which both inelastic and annihilation cross sections were measured. By deducing the production cross section ($\sigma_{prod} = \sigma_{inelastic} - \sigma_{ann}$) from these points, we observed that our model's deviation from the data is nearly identical to the deviation of all-inclusive channel sum from the experimental total cross section, implying that it is the production channels which are missing. Still, it is also clear from Fig. 6.1 that the errors in data are frequently underestimated.

All selected channels were parametrized with the five parameter formula provided in the same reference: $f(x) = a + b \cdot x^c + d \cdot \ln(x) + e \cdot \ln(x)^2$. Note, that this fit might not possess any physical sense, and was rather used for the sake of consistency. Despite the wealth of data available, there were few additional challenges that needed to be addressed. Firstly, there was a significant asymmetry in the availability of data for $p\bar{p}$ and $n\bar{p}$ cross sections. This disparity can be expected due to the absence of a pure neutron target to collect experimental data. Typically, measurements in this context were conducted using deuterium gas, which introduced additional complexity, as the outgoing particles were often contaminated with $p\bar{p}$ reaction products. Secondly, there was an issue related to the lack of data at incident antiproton momentum higher than 10 GeV/c.

6.2.1.1 Channel selection

The successful implementation of antiprotons in the INCL model owes a great deal to the exhaustive data compilation carried out by Baldini, Flaminio, Moorhead, and Morrison in their seminal work [Bal+87]. Their work provides information for many channels, but many of them are internally inclusive. For example, let us consider channel $p\bar{p} \to 2\pi^+\pi^0 2\pi^-$ which was present in the aforementioned reference, this channel was given twice: first time without any notice and second time with a "non-resonant" mark implying this final state was produced via the creation of three primary mesons (e.g. $2\rho^0\pi^0$ or $\rho^+\rho^0\pi^-$) instead of two-meson doorway (e.g. $\omega\rho^0$ or $\phi\rho^0$). Adding these data points into the same data set prior to fitting would result in completely inconsistent curve. Introducing separate fits is impossible because there are often two or three measured points in the non-resonant case, and spanning the fit over 10 GeV/c range introduces too much uncertainty.

Moreover, sometimes the channel $p\bar{p} \to \omega\rho^0$ would be also provided, and now there is an additional problem to avoid double counting. Same problem was not only in annihilation channels, but also in production, for example there was a channel with delta-resonances $p\bar{p} \to \Delta^{++}_{1232}\bar{\Delta}^{--}_{1232}$ which was not included, because we had also channel $p\bar{p} \to p\pi^+\pi^-\bar{p}$, which should include the resonance production. Finally, a set of rules was established to select channels for annihilation and production cross sections:

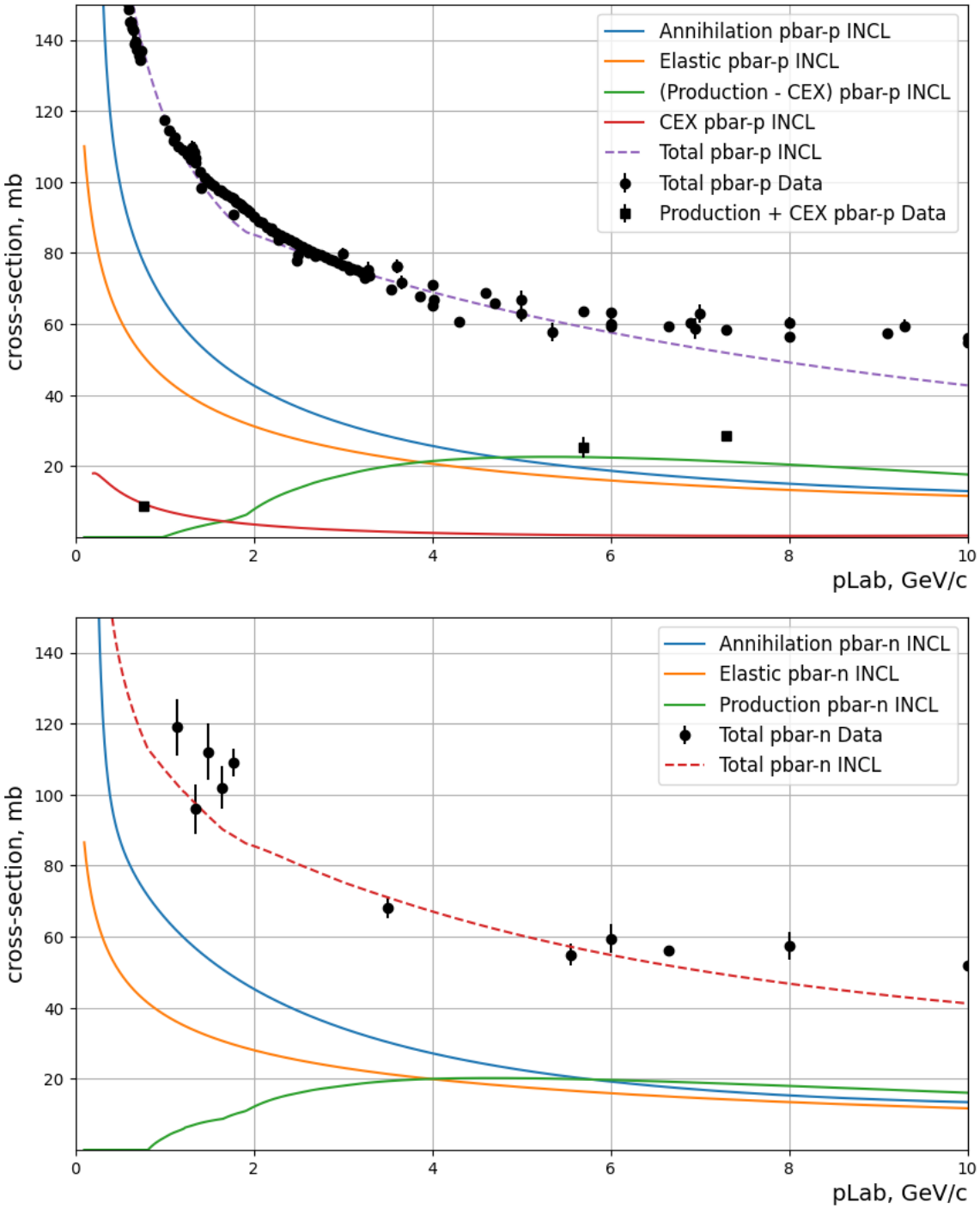

Figure 6.1: Cross-sections for $p\bar{p}$ and $n\bar{p}$. Cross section data is taken from Ref. [Bal+87]. Production cross section is the difference of inelastic and annihilation (antibaryon survives). Fits of exclusive channel data are done with $f(x) = a + b \cdot x^c + d \cdot \ln(x) + e \cdot \ln(x)^2$ recommended in the same reference.

1. At least three data points
2. At least 1% of the inclusive σ_{ann} or σ_{prod}
3. No overlap with other final states

In the first rule even three points was not enough, if they were all in the same energy region. This was the case for the inclusive σ_{ann} for $n\bar{p}$, so we had to renormalize it with the known $p\bar{p}$ cross section (see next section). The second rule was sometimes ignored when we wanted to include some channels of interest e.g. the antihyperon production ($\bar{\Lambda}, \bar{\Sigma}, \bar{\Xi}$). Meanwhile, the third rule implies exclusion of channels which contain particles like ϕ-meson for example as it may decay into K^+K^- at $48.9\% \pm 0.5\%$, $K^0_S K^0_L$ at $34.2\% \pm 0.4\%$, and various indistinguishable combinations of ρ's and pions at $15.3\% \pm 0.3\%$ [NP10], which would overlap with other implemented channels. Following these rules, a set of channels was chosen for implementation in INCL, the exact values of cross section parameters could be found in Appendix B.

Another special case is the antineutron which can be produced during the cascade and for which the experimental data is vanishingly rare. In INCL we treat antineutrons with same $\sigma_{elastic}$ as in case of $\bar{p}n$ (for both $\bar{n}n$ and $\bar{n}p$ cases) and same production cross sections as for $\bar{p}p$ or $\bar{p}n$ for $\bar{n}n$ and $\bar{n}p$ respectively, taking into account different total charge of $\bar{n}p$ initial state and slightly lower energy thresholds. When in comes to annihilation the inclusive cross section values for $\bar{n}n$ and $\bar{n}p$ were taken as for $\bar{p}n$, like for the elastic. Such choice should account for the absence of Coulombic attraction for antineutron case this effect only slightly reduces the σ_{ann} and $\sigma_{elastic}$ at lower momenta. As a side note, it have been observed[Bia+14] that the antineutron reaction cross section rise is too steep towards lower incident momenta if attributed solely to the strong interaction. This increase has prompted speculations about whether it might be the induced electric dipole moment of the antineutron in nuclear matter which causes this effect.

6.2.1.2 Annihilation channels

It became clear quite soon, that the sum of all exclusive channel data we had is not enough to be consistent with the information we had about the inclusive annihilation cross sections. For instance, in $p\bar{p}$ case we hardly had the half of the required cross section to fulfill the σ_{ann}, while for $n\bar{p}$ the situation is even worse. For this, we have taken the final state frequencies used in the at rest scenario (Ref. [KBR05; Gol+92]) and modified them by excluding every final state for which we had data (these were the most frequent final states with highest cross sections), after which we renormalized these remaining frequencies. Now, if our antiproton decides to annihilate in-flight, this could happen via one of the exclusive channels from Ref. [Bal+87], or one of the "missing" annihilation channels. For instance, such situation is probable for final states with a pair of neutral kaons, because the information from Ref. [Bal+87] sometimes contained only the K_s related channels, but it does not provide the necessary information to deduce the K_0 and $\bar{K}_0$ production rates.

We also had to resolve another problem related to the annihilation channel: there was a lack of data for inclusive annihilation cross section for the $n\bar{p}$ (see the bottom plot in Fig. 6.2), so it was not possible to make a decent fit up to 10 GeV/c of momentum. The solution we used was based on the observation, that both $p\bar{p}$ and $n\bar{p}$ have similar total cross sections at more than ≈ 4 GeV/c, and same was true for some other channels, like the elastic scattering (see Fig. 6.1), so we assumed that the difference in the low energy region is due to the Coulombic interaction and thus, we considered the annihilation cross-section for the $n\bar{p}$ to be expressed as:

$$\sigma^{n\bar{p}}_{annihilation} = \sigma^{p\bar{p}}_{annihilation} \frac{\sigma^{n\bar{p}}_{total}}{\sigma^{p\bar{p}}_{total}} \tag{6.1}$$

Having the inclusive values for $p\bar{p}$ and $n\bar{p}$ we deduced every exclusive channel on which we had data, and the resulting function was a channel which led to the at rest like annihilation, but with renormalized final states and frequencies. For $p\bar{n}$ the final states were the same as for $n\bar{p}$ but with the charge sign inversed, while for $n\bar{n}$ only the total energy of the meson star was slightly increased in comparison with $p\bar{p}$.

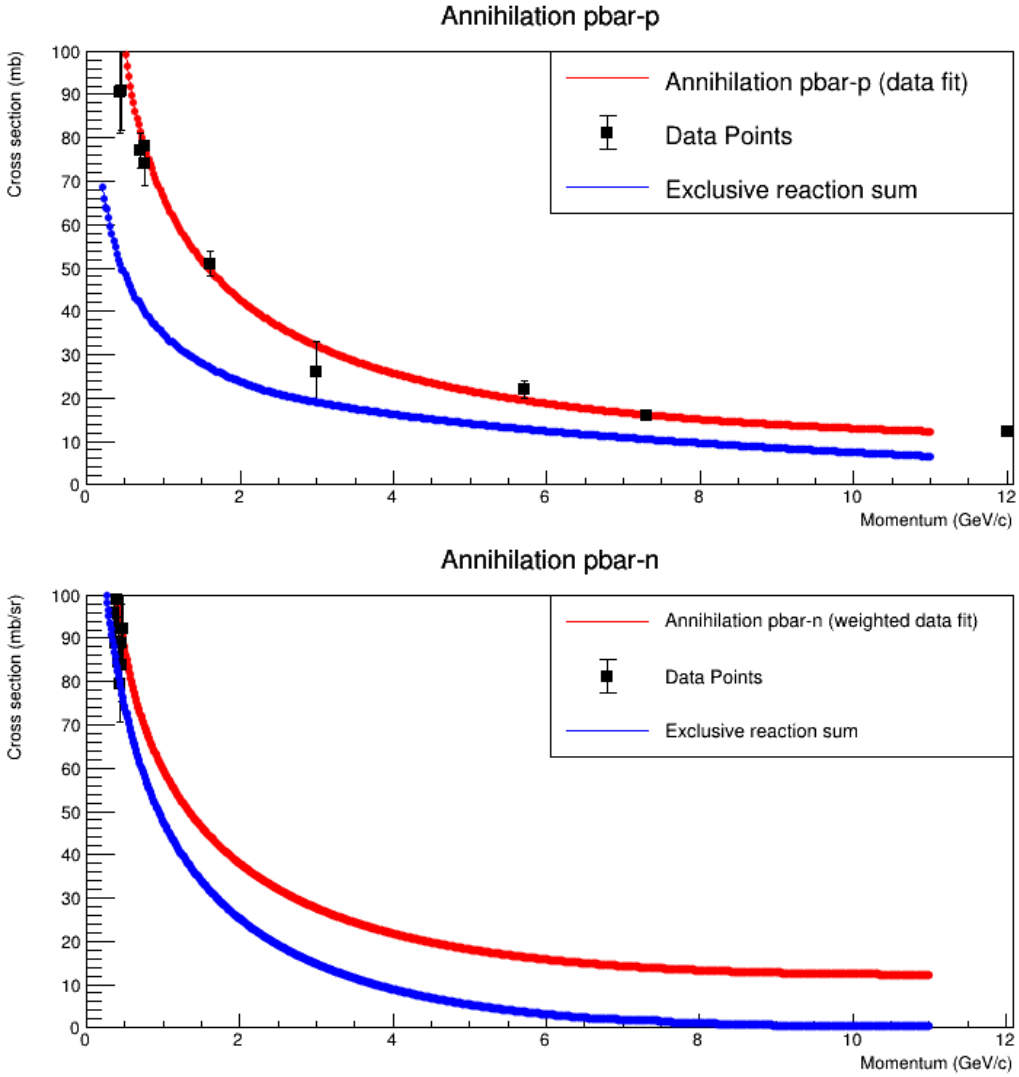

Figure 6.2: Annihilation cross-sections and the available sum of the exclusive annihilation channels for $p\bar{p}$ and $n\bar{p}$. Cross section data is taken from Ref. [Bal+87]. The data fit for $n\bar{p}$ is the same as for $p\bar{p}$, but weighted with the relation of $p\bar{p}$ and $n\bar{p}$ total cross sections due to the lack of data.

6.2.1.3 Production channels

The most significant contribution to the production inclusive cross section, which includes channels of the type $\bar{N}N \to \bar{N}N + X$, arises from the inelastic production of pions. To put this into perspective, consider the next largest non-pionic exclusive production channel, $\bar{p}p \to \bar{\Lambda}\Lambda$, which never exceeds 0.2 mb, its maximum is measured at around 2 GeV/c of incident momentum after which the cross section slowly decreases up to 7 GeV/c and no data is available for higher momenta. In contrast, the inclusive production cross section can reach as high as 20 mb. This striking difference underscores the dominance of inelastic pion production in these processes.

Initial state → Final state ↓	$p\bar{p}$	$n\bar{p}$
$p\bar{p}$	$\boldsymbol{\pi^0}$ $\boldsymbol{\pi^+\pi^-}$ $\boldsymbol{\pi^+\pi^-\pi^0}$	$\boldsymbol{\pi^-}$ $\boldsymbol{\pi^-\pi^0}$ $\pi^-\pi^-\pi^+$
$p\bar{n}$	$\boldsymbol{\pi^-}$ $\pi^-\pi^0$ $\boldsymbol{\pi^-\pi^-\pi^+}$	impossible $\boldsymbol{\pi^-\pi^-}$ $\pi^-\pi^-\pi^0$
$n\bar{p}$	$\boldsymbol{\pi^+}$ $\pi^0\pi^+$ $\boldsymbol{\pi^-\pi^+\pi^+}$	$\boldsymbol{\pi^0}$ $\boldsymbol{\pi^+\pi^-}$ $\pi^+\pi^-\pi^0$
$n\bar{n}$	π^0 $\boldsymbol{\pi^-\pi^+}$ $\boldsymbol{\pi^+\pi^-\pi^0}$	π^- $\pi^-\pi^0$ $\pi^-\pi^-\pi^+$

Table 6.1: Data fulfillment table for exclusive 1, 2 or 3 pions production channels. The column headers represent the initial state of nucleon-antinucleon pairs, while the row headers are the final state pair with the various pionic contributions to the final states given in the cells. Entries in bold are the channels with experimentally measured cross sections taken from Ref. [Bal+87]. The rest were fulfilled with the use of symmetry properties.

The data available for exclusive production cross sections is limited. For instance, measurements exist for inelastic production channels where up to three pions are produced. However, simply adding these channels would neither be consistent nor sufficient to match the total cross section. To illustrate this, if we had information for a process like $\bar{p}p \to \bar{p}p + \pi^+\pi^-\pi^0$, it implies that the channel $\bar{p}n \to \bar{p}n + \pi^+\pi^-\pi^0$ should also be implemented. In our analysis, we assume that the cross sections for these channels are equal, a reasonable assumption given the observed equality in many different exclusive cross sections of a similar final states. To introduce one example of such observations: we have data for both $\bar{p}p \to \bar{p}p + \pi^0$ and $\bar{p}n \to \bar{p}n + \pi^0$, and in each case their cross section values are similar within the errors.

6.2.2 Nuclear potentials

The question of which nuclear potential to utilize for each particle in INCL presents a considerable challenge, as we cannot directly measure these values without relying on nuclear models. One such model-based set of potentials was derived in Ref. [LGM12], which can be seen in Table 6.2. Among the presented values there are some contradictions about the attractiveness of Σ-baryons for example, while for Λ, kaons and antiprotons they are consistent as we know from the Ref. [Lar+09] for antiprotons and from the Ref. [FG07] for strange particles. Currently, we employ a 100 MeV attractive potential for both antiprotons ($\bar{p}$) and antineutrons ($\bar{n}$). It's worth noting that the Coulombic interaction is treated differently, primarily influencing the trajectory of the projectile and impacting the impact parameter.

i	Λ	Σ	Ξ	N	$\bar{\Lambda}$	$\bar{\Sigma}$	$\bar{\Xi}$	K	$\bar{K}$
U_i	-38	-39	-22	-150	-449	-449	-227	-18	-224

Table 6.2: The Schrödinger equivalent potentials of different particles at zero kinetic energy in nuclear matter at central density (in MeV, negative value means attractive) used in GiBUU model [LGM12].

However, for other antiparticles, we do not assign a potential. This decision stems from the fact that introducing a potential in the absence of cross-section data for these particles would effectively confine them within the nucleus until they undergo decay. In the case of certain particles, such as $\bar{\Lambda}$, the decay time is sufficiently long that it raises the possibility of creating a nucleus with positive strangeness (ABLA de-excitation code currently does not treat such exotic nuclei). Although INCL is capable of generating hypernuclei (with a 30 MeV potential for Λ), the choice was made to release these exotic antiparticles instead.

6.3 Comparison to the experimental data

In the previous sections we discussed all the ingredients, which are mostly the elementary $N\bar{N}$ channels and their cross sections. It would make sense now to check if our total reaction cross-section ($\bar{p}A$) is consistent with the measurements with nuclei at various momenta. Also, we might compare our reaction cross section formula (Eq. 5.5) which we used at rest for normalization purposes, such comparison is presented on Fig. 6.3 together with the data from Ref. [Gar+84; Nak+84; Bal+91]. One might see the close coincidence of at rest and in-flight region, which might indicate another possible momentum value to switch between at rest and in-flight INCL scenarios and this value would be target dependent. Also, it seems that INCL in-flight σ_{tot} fits the data slightly better with lighter target nuclei, which could be explained by a higher neutron content of heavier nuclides for which we underestimate the corresponding $n\bar{p}$ elementary cross sections more, than in the $p\bar{p}$ case.

Ideally, for the antiproton in-flight scenario validation one would require experimental measurements of outgoing particles taken at various incident $\bar{p}$ momenta. There were not many experiments like that, still, one of the examples we have is data from Ref.[Bal+91] with the negative pions and charged prongs measured at 193, 306 and 608 MeV/c (20, 49 and 180 MeV) $\bar{p}$ on a gaseous Neon target. These energies are still quite low, and by default should be considered at rest. Still, we tried to compare the in-flight version with the results of this work, together with at rest, because the at rest scenario is not sensitive to the energy of antiproton beam, it would only change the normalization constant (given by eq. 5.5) effectively scaling the resulting distributions.

Charged prong distributions for all three beam energies are given in Fig. 6.4 and one might notice that discrepancy with the data arises towards lower energies, this is why we decided to additionally plot the INCL at rest at 20 MeV $\bar{p}$ energy, which nevertheless have produced very similar results. Still, the odd prong multiplicities have slightly higher production rate for the at rest case which stems from the fact that annihilation with protons has higher relative probability for this scenario implying the production of even number of charged mesons to make up zero total charge. The data is well reproduced for 180 MeV case with even the peak positioned at the value of nine, but the presence of such a peak is cumbersome to explain. Additionally, we plotted the normalized numbers of negative pion multiplicities at various energies in Fig. 6.5, but this particular observable does not show any significant change with the energy, especially taking the uncertainty into account.

Hereafter, we present a comparative analysis (as illustrated in Fig. 6.6) of the neutron spectra obtained through our model, Fritiof model and the experimental measurements from Ref. [Egi+00] involving 1.22 GeV antiprotons interacting with different target nuclei, namely ^{27}Al, $^{natural}Cu$, ^{181}Ta, and ^{238}U. The neutron spectra considered were measured at two distinct angular positions, specifically at 50° and 145° relative to the incident antiproton beam direction. This experimental setup enabled the investigation of the forward-backward asymmetry in relation to the momentum of the incident antiproton projectile.

In general, INCL is overall in agreement with the data and demonstrates a better correspondence than the other option which Geant4 currently possess for antiproton-nucleus simulations (option FTF+Preco in Ref. [GRU19], the other option FTF+Binary cascade model was not readily available for the Geant4 end user, and requires a non-trivial junction of two codes). Still, one may observe a slight

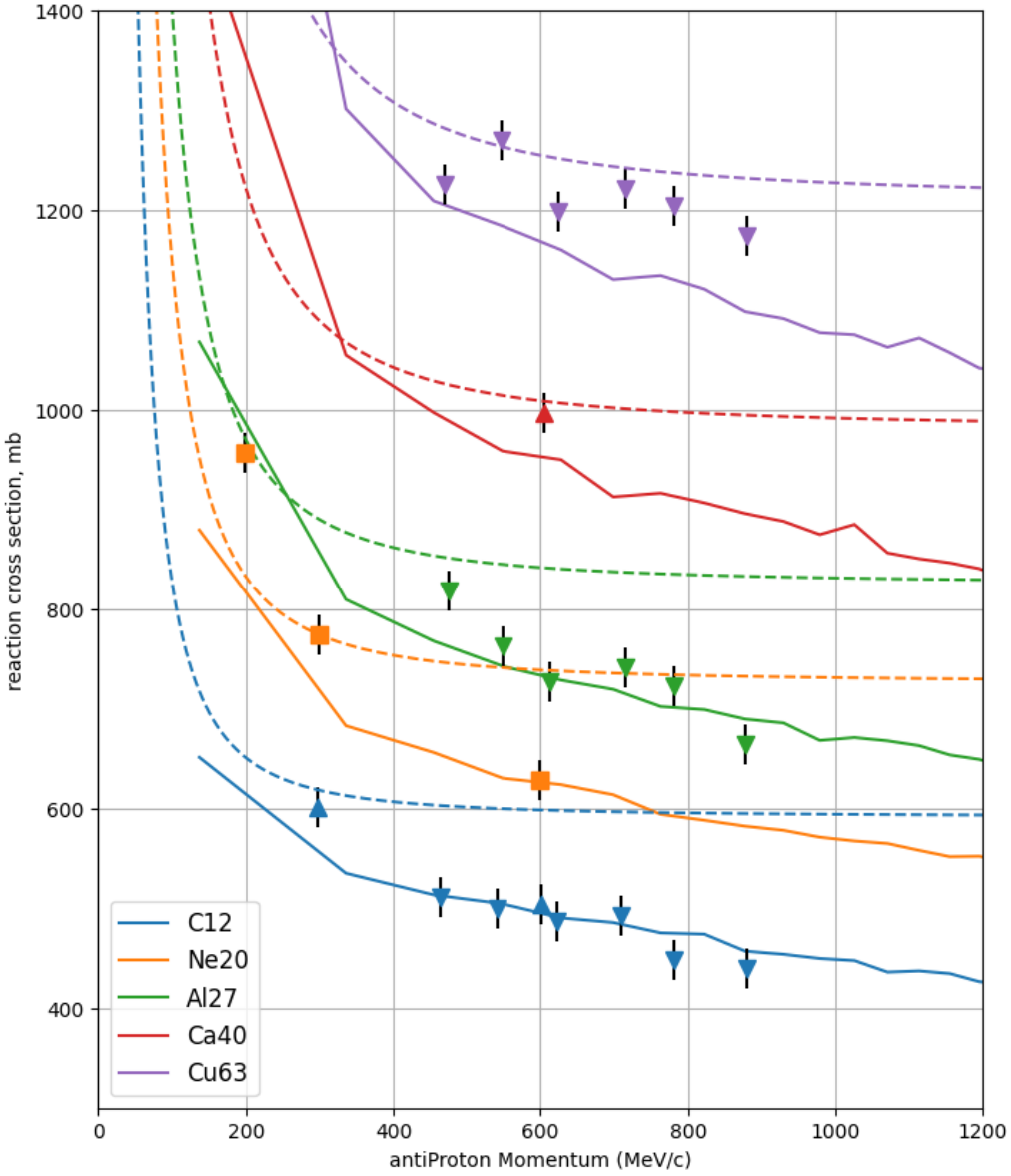

Figure 6.3: Reaction cross-sections for in-flight $\bar{p}$-nucleus interaction. Triangle data points are from Ref. [Gar+84] (^{12}C,^{40}Ca), inverted triangles are from Ref. [Nak+84] (^{12}C,^{27}Al,^{63}Cu), square points are from Ref. [Bal+91] (^{20}Ne). Dashed lines are for at rest (Eq. 5.5), while solid lines are for in-flight.

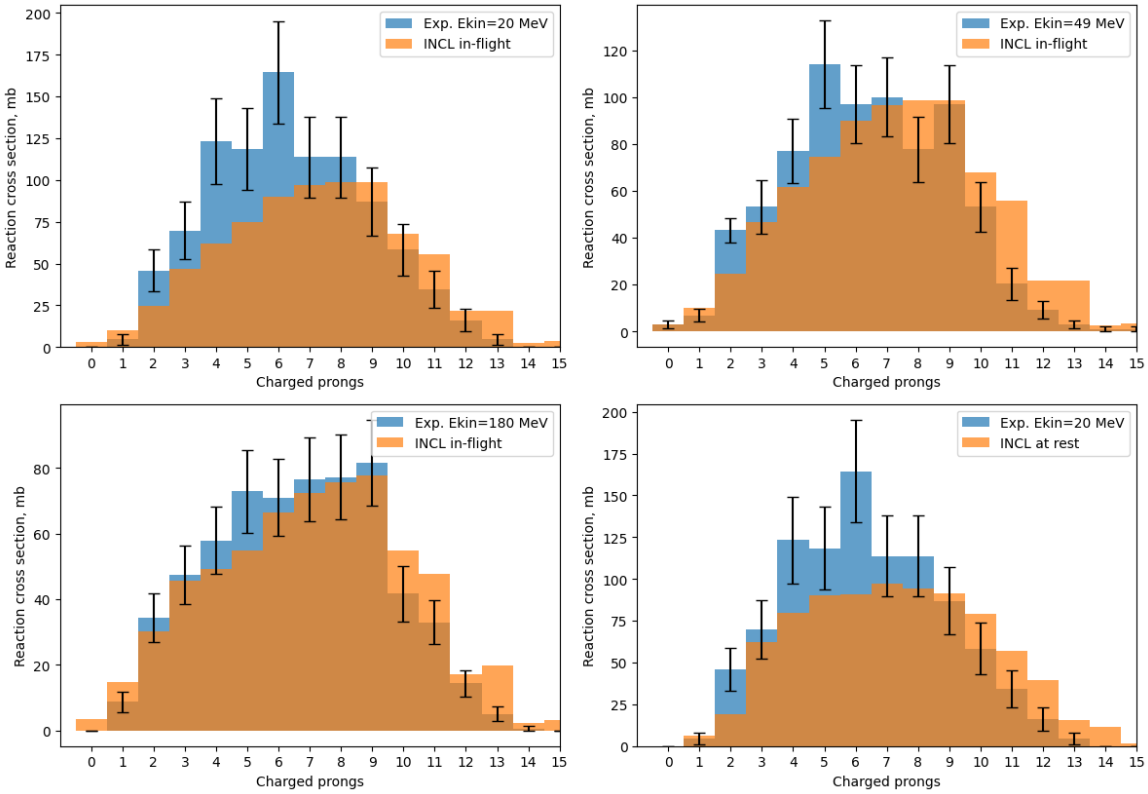

Figure 6.4: Charged prong multiplicity distributions for E_{kin} = 20, 49 and 180 MeV, the corresponding numbers of observed events are 956±47, 771±28 and 623±21. The systematic error is added directly to the statistical one, and was claimed to be 7% by the authors in Ref. [Bal+91].

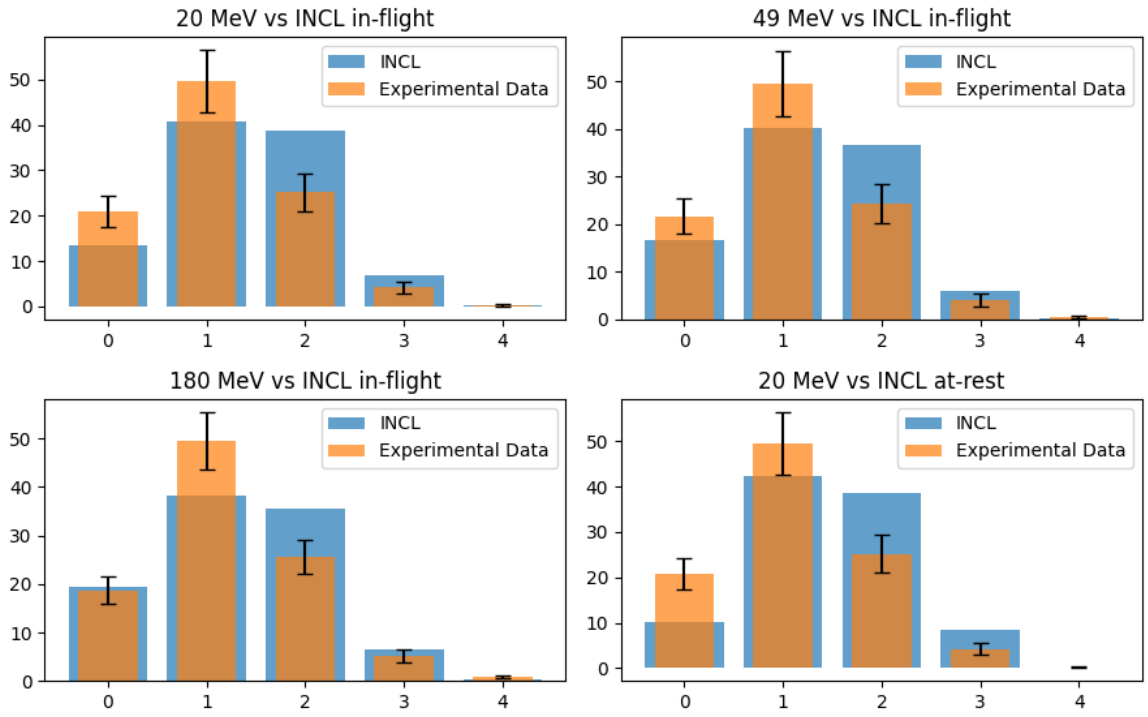

Figure 6.5: π^- multiplicity distributions for E_{kin} = 20, 49 and 180 MeV, the corresponding numbers of observed events are 956±47, 771±28 and 623±21. The systematic error is added directly to the statistical one, and was claimed to be 7% by the authors in Ref. [Bal+91].

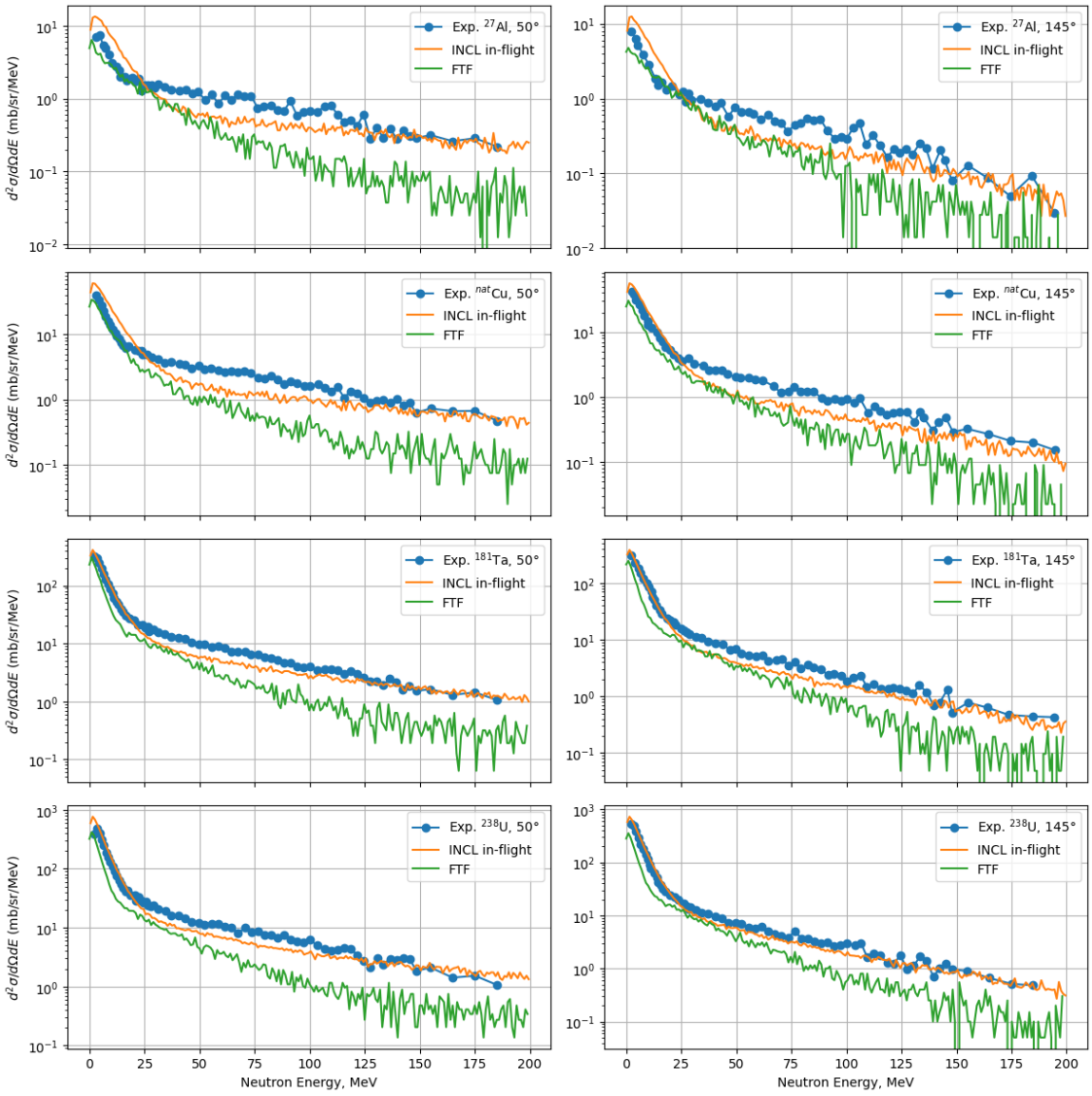

Figure 6.6: Neutron energy spectra from $\bar{p}$-A collisions at 1.22 GeV. Data taken from Ref. [Egi+00]. The FTF calculation is made with FTF+Precompound option (FTFP) with Geant4.

underproduction in the intermediate energy part of the spectrum with a bit of an excess at lower energies. In Ref. [Pol+95] authors divide neutron spectra into three parts: evaporative part (emitted during the de-excitation stage), intermediate preequilibrium and direct (kicked out within the first binary interactions) neutron source. Perhaps, it is the intermediate neutrons, which are not emitted and are later converted into evaporative thermal neutrons.

It is noteworthy that the forward-backward asymmetry is evident in both the experimental data and the results generated by INCL. However, an observation is the relatively more pronounced underestimation in the case of the 50° angle measurements when comparing our model's predictions to the experimental data. Moreover, across both angles, INCL appears to provide a more accurate representation of particles scattered in the more backward direction, suggesting that the nucleus is too absorbing in our model. Another trend is the systematic reduction in the level of discrepancy with the experimental data as we transition from lighter to heavier target nuclei. This trend is indicative of an increased number of collisions occurring in heavier nuclei, consequently leading to a greater fraction of available energy being transferred to neutrons owing to the increased frequency of binary collisions. Another observation emerges with the size of the target nucleus; there is a discernible shift in the thermal portion of the neutron spectra. This shift transforms the initial INCL overestimation into a more concordant agreement with the experimental data.

Finally, we would like to validate our in-flight scenario for the strangeness production property. For this purpose the data from Ref. [Miy+84] was used for comparison. Charged prongs multiplicity distributions were provided for all events, events including K_s^0 and events including Λ hyperon, the

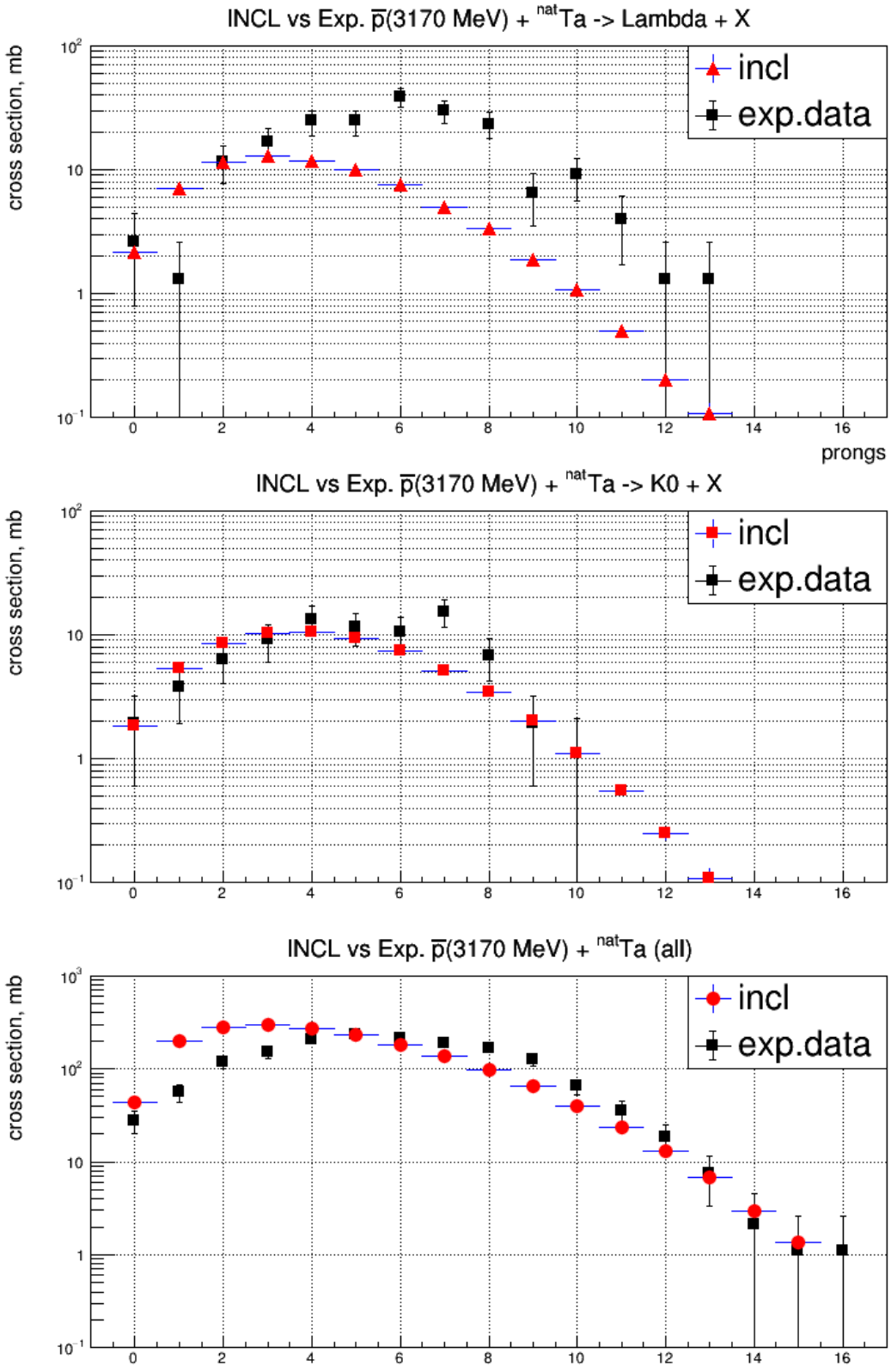

Figure 6.7: Topological cross sections in the $\bar{p}Ta$ reaction at 4 GeV/c for all events, events with a K_s^0 and events with Λ.

comparisons with INCL are presented in Fig. 6.7. This experiment was done at 4 GeV/c (3170 MeV) $\bar{p}$ incident momentum, and there were a lot of limitations regarding the detector acceptance and particle identification. Only limited channels were seen, for instance, the decay of Λ was only detected if its decay channel was $\pi^- p$, and not $\pi^0 n$, while neutral kaons were only seen in their "short" two-pion decay mode, while the overall probability of a kaon to decay as K_s^0 is generally detector and momentum dependent (see Ref. [Adl+97]). INCL is predominantly consistent with these experimental findings, except for the Lambda production case. One possible source of such divergence may be explained by the absence of the $\eta N \to K\Lambda$ channel implemented, though this factor alone might not be enough to fulfill this lack. Interestingly, a production ratio of $\bar{\Lambda}/\Lambda$ was obtained to be $\approx 2.0 \pm 1.0\%$ while in INCL this value was 7%. This $\bar{\Lambda}$ production overestimation is presumably the consequence of absence of the annihilation channels for strange antiparticles. Such problem will be addressed in the future by introducing statistical model for strange antiparticle pionisation, but was not yet implemented for the sake of consistency as we are now implementing mostly the information on exclusive channels with sometimes the help of SU(3) symmetry. Additional reason of this effect may also be the absence of potential for $\bar{\Lambda}$ which is predicted to be strongly attractive by the authors in Ref. [LGM12].

References

[Adl+97] R. Adler et al. "Experimental measurement of the K(S) K(S) / K(S) K(L) ratio in anti-proton annihilations at rest in gaseous hydrogen at 15-bar and 27-bar". In: *Phys. Lett. B* 403 (1997), pp. 383–389. doi: 10.1016/S0370-2693(97)00489-9.

[Bal+87] A. Baldini et al. *Total Cross-Sections for Reactions of High Energy Particles (Including Elastic, Topological, Inclusive and Exclusive Reactions) / Totale Wirkungsquerschnitte fur Reaktionen hochenergetischer Teilchen (einschliesslich elastischer,topologischer, inklusiver u*. Landolt-Börnstein: Numerical Data and Functional Relationships in Science and Technology - New Series. Springer Berlin Heidelberg, 1987. isbn: 9783540183860.

[Bal+91] F. Balestra et al. "Strangeness production in antiproton annihilation at rest on 3He, 4He and 20Ne". In: *Nuclear Physics A* 526.3 (1991), pp. 415–452. issn: 0375-9474. doi: https://doi.org/10.1016/0375-9474(91)90428-9.

[Bia+14] A. Bianconi et al. "Enhancement of annihilation cross sections by electric interactions between the antineutron and the field of a large nucleus". In: *The European Physical Journal A* 50.12 (Dec. 2014). doi: 10.1140/epja/i2014-14182-x.

[Egi+00] T. von Egidy et al. "Neutrons produced by 1.22 GeV antiproton interactions with nuclei". In: *The European Physical Journal A* 8.2 (July 2000), pp. 197–204. issn: 1434-601X. doi: 10.1007/s100500070106.

[FG07] E. Friedman and A. Gal. "In-medium nuclear interactions of low-energy hadrons". In: *Physics Reports* 452.4 (2007), pp. 89–153. issn: 0370-1573. doi: https://doi.org/10.1016/j.physrep.2007.08.002.

[Gar+84] D. Garreta et al. "Elastic scattering of antiprotons from carbon, calcium, and lead at 180 MeV". In: *Physics Letters B* 149.1 (1984), pp. 64–68. issn: 0370-2693. doi: https://doi.org/10.1016/0370-2693(84)91552-1.

[Gol+92] E.S. Golubeva et al. "Effects of mesonic resonance production in annihilation of stopped antiprotons on nuclei". In: *Nuclear Physics A* 537.3 (1992), pp. 393–417. issn: 0375-9474. doi: https://doi.org/10.1016/0375-9474(92)90362-N.

[GRU19] Aida Galoyan, Alberto Ribon, and Vladimir Uzhinsky. "Simulation of neutron production in hadron-nucleus and nucleus-nucleus interactions in Geant4". In: *EPJ Web of Conferences* 204 (2019). Ed. by S. Bondarenko, V. Burov, and A. Malakhov, p. 03004. doi: 10.1051/epjconf/201920403004.

[KBR05] Eberhard Klempt, Chris Batty, and Jean-Marc Richard. "The antinucleon-nucleon interaction at low energy: Annihilation dynamics". In: *Physics Reports* 413 (Jan. 2005). doi: 10.1016/j.physrep.2005.03.002.

[Lar+09] A. B. Larionov et al. "Antiproton-nucleus collisions simulation within a kinetic approach with relativistic mean fields". In: *Phys. Rev. C* 80 (2 Aug. 2009), p. 021601. doi: 10.1103/PhysRevC.80.021601.

[LGM12] A. B. Larionov, T. Gaitanos, and U. Mosel. "Kaon and hyperon production in antiproton-induced reactions on nuclei". In: *Phys. Rev. C* 85 (2 Feb. 2012), p. 024614. doi: 10.1103/PhysRevC.85.024614.

[Miy+84] K. Miyano et al. "Evaporation of Neutral Strange Particles in $\bar{p}$-Ta at 4 GeV/c". In: *Phys. Rev. Lett.* 53 (18 Oct. 1984), pp. 1725–1727. doi: 10.1103/PhysRevLett.53.1725.

[Nak+84] K. Nakamura et al. "Absorption and Forward Scattering of Antiprotons by C, Al, and Cu Nuclei in the Region 470-880 MeV/c". In: *Phys. Rev. Lett.* 52 (9 Feb. 1984), pp. 731–734. doi: 10.1103/PhysRevLett.52.731.

[NP10] K. Nakamura and et al. (Particle Data Group). "Review of Particle Physics". In: *Journal of Physics G: Nuclear and Particle Physics* 37 (2010), p. 075021.

[Pol+95] D. Polster et al. "Light particle emission induced by stopped antiprotons in nuclei: Energy dissipation and neutron-to-proton ratio". In: *Phys. Rev. C* 51 (3 Mar. 1995), pp. 1167–1180. doi: 10.1103/PhysRevC.51.1167.

7 | Conclusion

The principal mission of this thesis was extending the Liège intranuclear cascade model INCL to include the relevant physics for simulating the antiproton-nucleus interactions in the range from the lowest energies up to several GeV. The results are able to resemble closely most part of the experimental data, with the additional benefit of the capability to run on a desktop machine and still accumulate good statistics.

Moreover, it was crucial to integrate this new capability into the Geant4 - one of the most widely adopted simulation toolkits for particle-matter simulations. As we have demonstrated in both last chapters, the previously available options do not always provide sufficiently adequate predictions in the aforementioned energy region, while at rest the results were so far, that the team working on ASACUSA experiment have explicitly notified us about their interest for a better modelling tool. It is now possible to say that in Geant4 INCL can be used for stopped antiproton (E_{kin} = 0), while other cases are on the last stages of integration and will be available for the end user in the nearest future.

For the validation of INCL, different outgoing particle spectra were compared at various incident antiproton momenta ranging from few MeV/c (which we consider as "stopped") up to 4 GeV/c. Various targets ranging from ^{12}C to ^{238}U were considered. For most of the studied cases there is a good agreement between experimental data and INCL predictions. Notably, the results of both INCL scenarios sometimes even coincide in certain energy ranges (though this range varies for different targets), which demonstrates that the core physics has been successfully implemented. Nevertheless, slight discrepancies still exist. In some cases experimental data might be overestimated, which we suspect to be the case for charged kaon multiplicities in Ref. [Pol+95].

There are of course many nuances to improve in the INCL code in general and in the antiproton scenarios implementation in particular. For instance, it might be beneficial to introduce additional channel for the Λ-hyperon production (e.g. $\eta N \rightarrow K\Lambda$) and improve the phase space coalescence process to remove the excess of the deuterons and tritons from the intermediate part of the spectra. While on the antiproton part, one could have added the antiproton production channels such as the $NN \rightarrow \bar{N}NNN$, the exact channel which is utilised to generate antiproton beams in labs and a large part of cosmic antiprotons. Many possible channels were not added for the antiproton in-flight scenario due to the absence of data, but their cross sections might still be evaluated with the help of SU(3) symmetry (e.g. $\bar{p}p \rightarrow \bar{n}n\pi^0$ or $\bar{p}p \rightarrow \bar{p}p2\pi^0$) also known as the Bystricky procedure, decribed in Ref. [Bys+87]. The procedure, which is based on the isospin decomposition of systems, was used previously in INCL[PC11] to find missing cross sections in channels involving multiple pion production in INCL. The procedure was applied up to the production of four pions and the determined cross sections were then implemented in INCL earlier versions. Similar approach could be exploited to obtain more anti-hyperon production channels (e.g. the $\bar{p}p \rightarrow \bar{\Xi}^0\Xi^0$) which might be of interest nowadays in the scope of the oncoming PANDA project[Gia15] at FAIR. This project could additionally contribute to the information on the nuclear potentials for certain exotic antibaryons which we are currently missing in INCL.

Considering the at rest scenario, one possible way to make it more realistic is to introduce an additional uncertainty to the annihilation orbit of the antiproton. This might be done in a context of a more broad parametric study, similar to the one in the section 5.4 but embracing the full parameter space of at least the S_p/S_n ratio and the annihilation orbit. The problem is that these parameters might be optimized separately for each nuclide and thus such study would require not only a lot of computational time (which grows exponentially with the number of parameters), but also the experimental information of pionic spectra for the target. According to the Ref. [WP23] the "pionisation" experiments at low energy might be the most sensitive type of measurement when we talk about the antiproton-nucleus optical potential model validation and study of nuclear surface.

Another part of the future improvement plan is the integration of antineutron as projectile, which might seem to be straightforward, but is non-trivial to treat properly especially at lower energies. It might seem trivial as there is no atomic repercussions like with the antiproton, but the difficulty lies in the proper handling of cross sections at low energies. They already come with large errors and rare availability for this energy range, in the case of antiproton we normally don't mind about such problem as we proceed with completely different scenario, but for the $\bar{n}$ this issue is much more severe. Additional uncertainty is introduced when annihilating in-flight at low energies due to the Fermi energy of nucleons which can reach up to 38 MeV for some nucleons. The total cross section and thus the minimal distance of binary collision might greatly vary due to this addition. The implementation of heavier antiparticles like antideuteron and even larger would be the consecutive steps after both antiproton and antineutron will be validated.

A | Appendix A

Inclusive particle spectra

In the Ref. [Pol+95] in order to reduce the large amount of data of 4 or 6 particle species from 13 targets and to facilitate comparison with theoretical models, authors have fitted each measured spectrum with Maxwellian distributions:

$$\frac{dM}{dE} = \sum_{i}^{n} \left(\frac{\langle M_i \rangle}{\pi^{1/2} T_i^{3/2}} \right) \sqrt{E} exp\left(-\frac{E}{T_i} \right), \quad n = 1, 2, 3 \tag{A.1}$$

with $\langle M_i \rangle$ and T_i being the multiplicity and slope parameters. For targets ^{12}C to ^{108}Ag neutron spectra were parametrized as the high direct and low evaporative parts, while for targets ^{165}Ho to ^{238}U there was also intermediate preequilibrium component. For p, d and t only one Maxwellian slope was given substituting E with $E - V_c$, where $V_c = 1.44 Z_p (Z_{target} - Z_p - 1)/(r_0 A^{1/3})$ with ($p = \{p, d, t\}, r_0 = 1.2 fm$) to account for the Coulombic barrier. The comparisons of INCL to these spectral fits is presented in Fig. A.1.

Sensitivity analysis

Parameter sensitivity analysis for the S_p/S_n ratio and for the annihilation orbit is presented in Fig. A.2a and Fig. A.2b for the ^{nat}Ti target.

Residual nuclei production

Here are isotopic distributions of residual nuclei from targets: ^{165}Ho (Fig. A.3), ^{nat}Ba (Fig. A.4) and ^{197}Au (Fig. A.5, A.6 for independent and A.7, A.8 for cumulative). Figures A.9, A.10, A.11, A.12 contain fission isotope distributions from GSI [Ber+03; Taï+03; Ric+06] for the 1 GeV/nucleon accelerated ^{238}U ions on hydrogen target vs INCL [Int10].

References

[Bal+87] A. Baldini et al. *Total Cross-Sections for Reactions of High Energy Particles (Including Elastic, Topological, Inclusive and Exclusive Reactions) / Totale Wirkungsquerschnitte fur Reaktionen hochenergetischer Teilchen (einschliesslich elastischer,topologischer, inklusiver u*. Landolt-Börnstein: Numerical Data and Functional Relationships in Science and Technology - New Series. Springer Berlin Heidelberg, 1987. isbn: 9783540183860.

[Ber+03] M. Bernas et al. "Fission-residues produced in the spallation reaction 238U + p at 1AGeV". In: *Nuclear Physics A* 725 (2003), pp. 213–253. issn: 0375-9474. doi: https://doi.org/10.1016/S0375-9474(03)01576-8.

[Biz68] R. Bizzarri. "On the comparison of the annihilation of antiprotons at rest in hydrogen and deuterim". In: *Il Nuovo Cimento A (1965-1970)* 53.4 (Feb. 1968), pp. 956–968. issn: 1826-9869. doi: 10.1007/BF02758737.

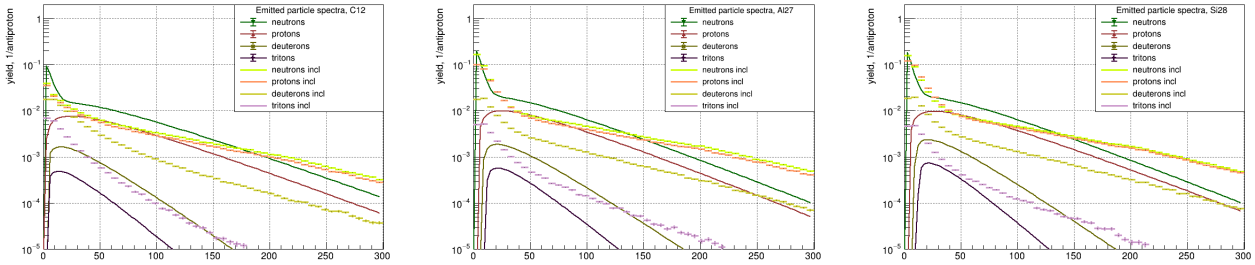

(a) C12 **(b)** Al27 **(c)** Si28

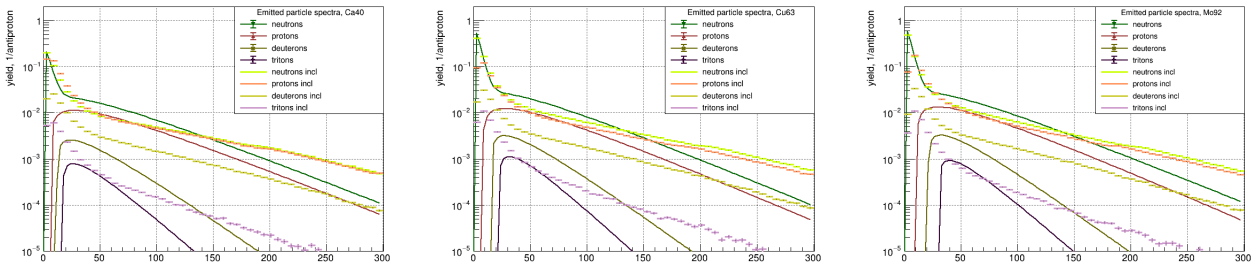

(d) Ca40 **(e)** Cu63 **(f)** Mo92

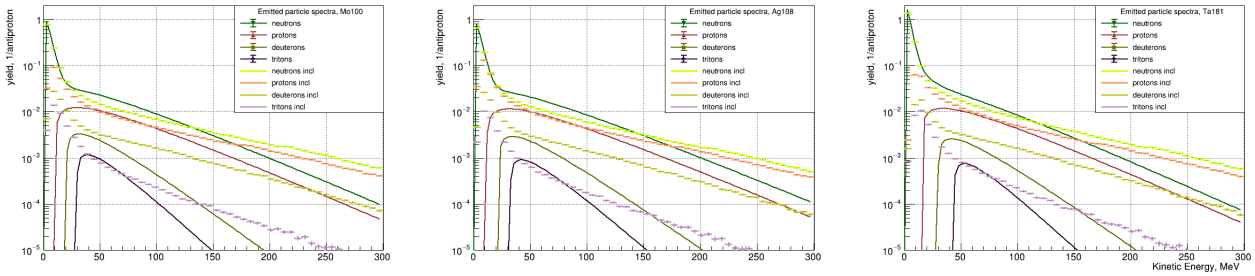

(g) Mo100 **(h)** Ag108 **(i)** Ta181

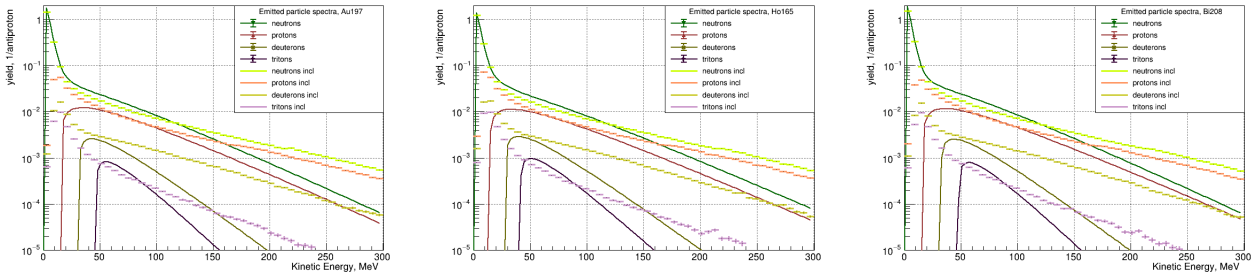

(j) Au197 **(k)** Ho165 **(l)** Bi209

Figure A.1: Parametrized n, p, d and t spectra from Ref. [Pol+95] compared to INCL.

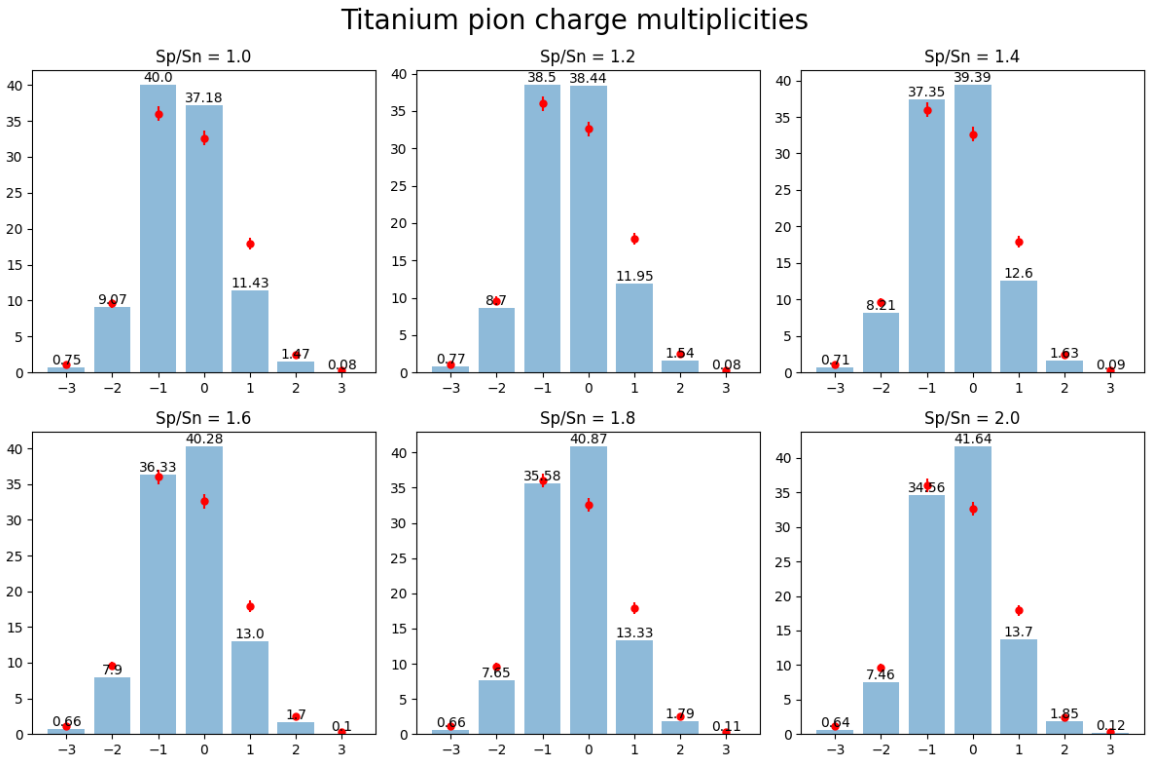

(a) S_p/S_n ratio sensitivity for the ^{nat}Ti target for pion charge multiplicities. Titanium: points are from Ref. [Bug+73] with errors from review [BK94]. For $S_p/S_n = 1.4$ INCL has lowest Chi-squared, while the root mean square error and R-squared are best for $S_p/S_n = 1.4$. The INCL default value is 1.331 from Ref. [Biz68].

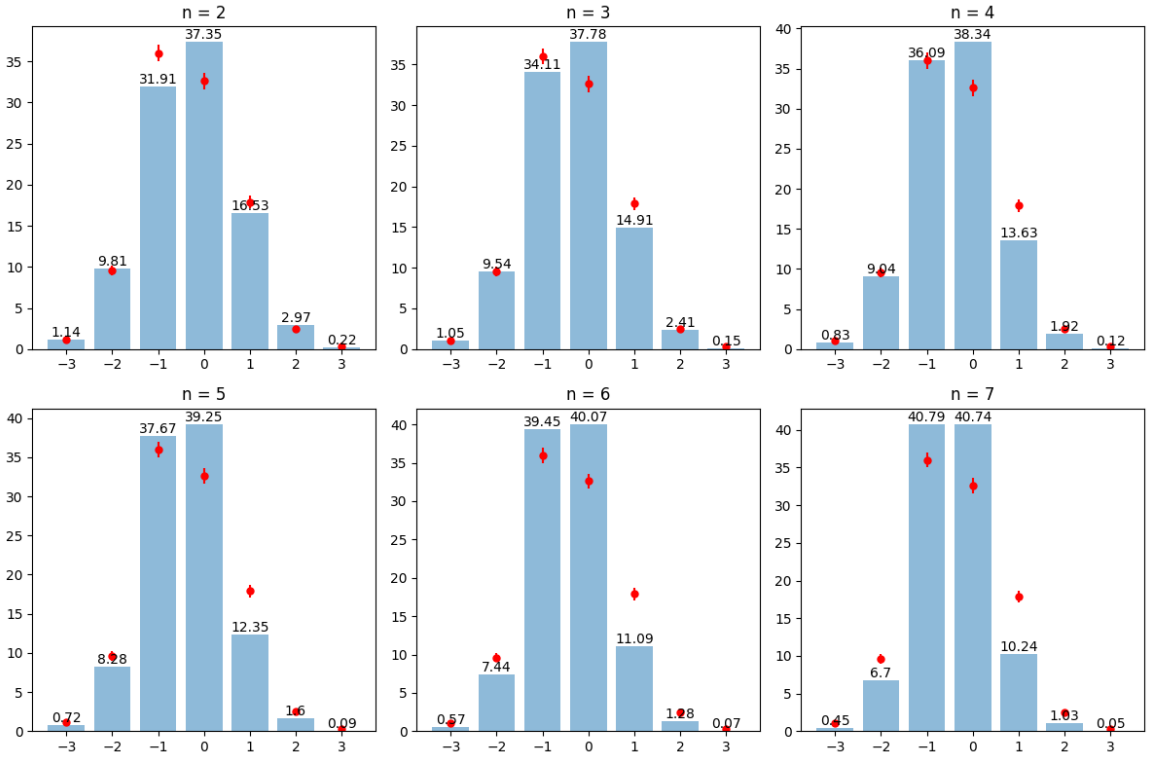

(b) annihilation orbit sensitivity for the ^{nat}Ti target for pion charge multiplicities. n is the orbit number. Titanium: points are from Ref. [Bug+73] with errors from review [BK94]. For orbit with n = 2 INCL has lowest Chi-squared, while the RMSE and R-squared are best for n = 3. The last observed n is 5 from [Pot84].

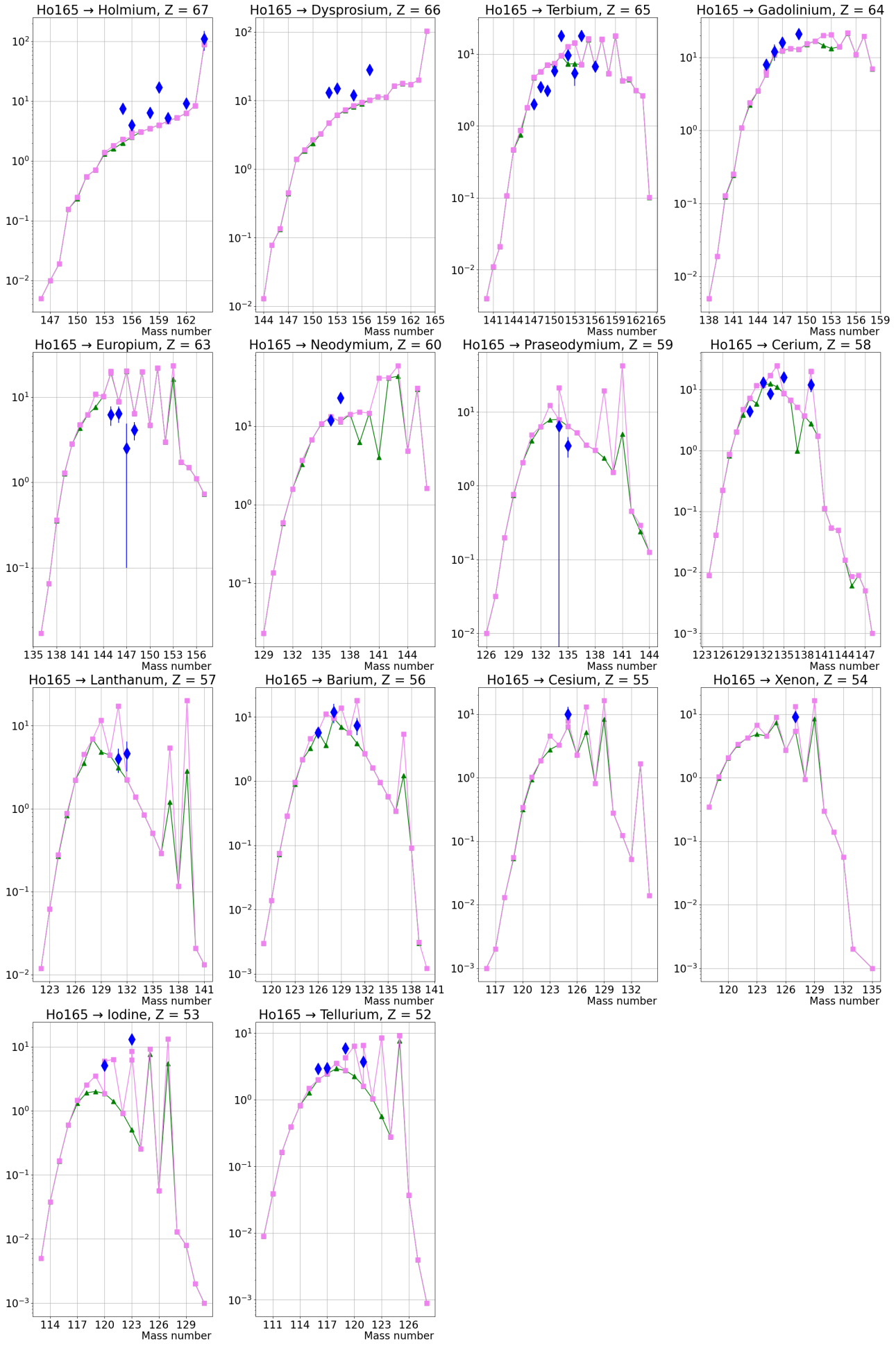

Figure A.3: Cumulative isotopic distributions from the reaction $\bar{p}+^{165}Ho$. Calculated results are in violet (option $\frac{\lambda_D}{\lambda_P} = 0.1$), and in green (option $\frac{\lambda_D}{\lambda_P} = 0.5$). Definition of $\frac{\lambda_D}{\lambda_P}$ in section 5.3.3.1. Data are from [Mos+89].

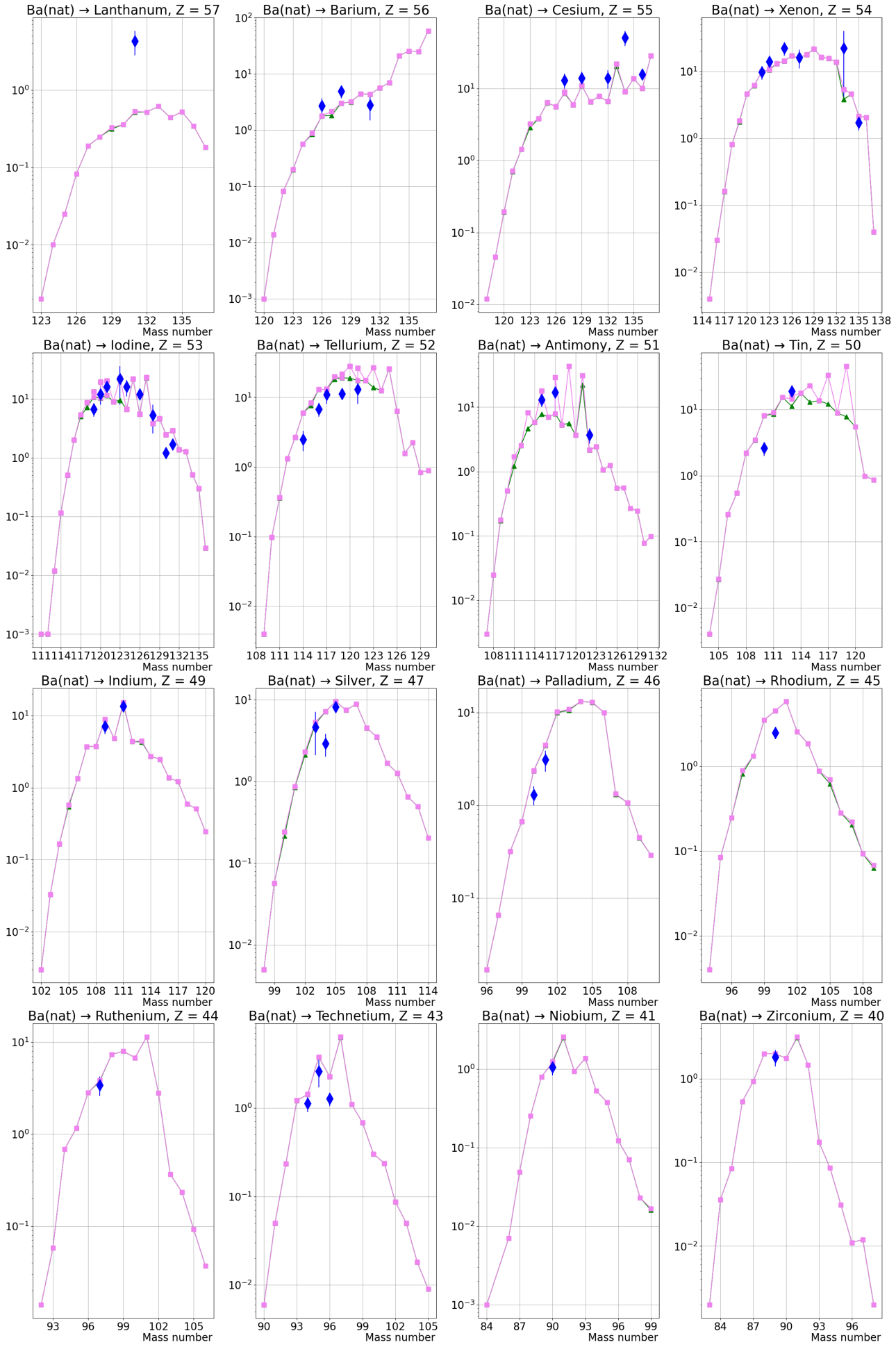

Figure A.4: Cumulative isotopic distributions from the reaction $\bar{p}+^{nat}Ba$. Calculated results are in violet (option $\frac{\lambda_D}{\lambda_P} = 0.1$), and in green (option $\frac{\lambda_D}{\lambda_P} = 0.5$). Definition of $\frac{\lambda_D}{\lambda_P}$ in section 5.3.3.1. Data are from [Egi+90].

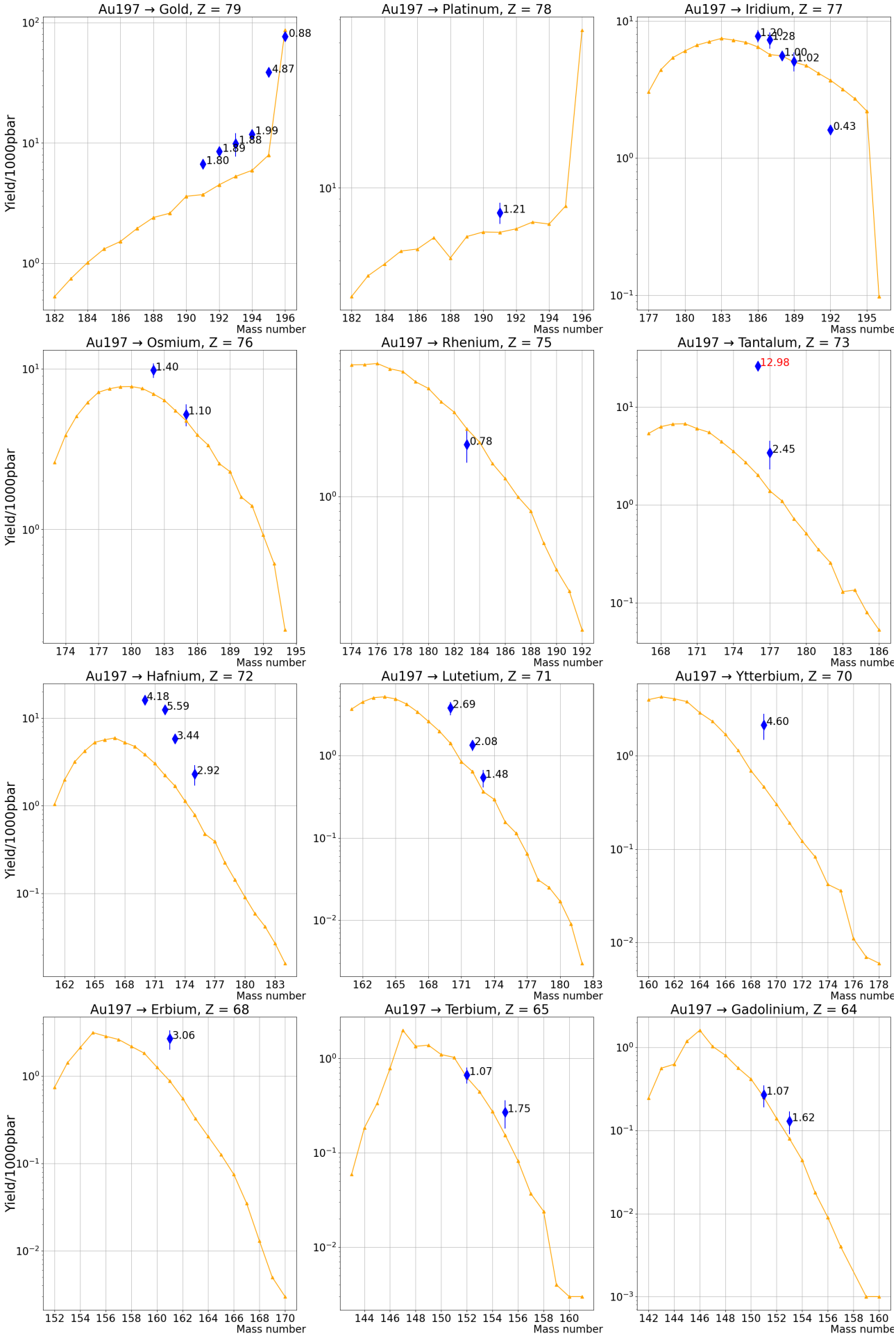

Figure A.5: Independent isotopic distributions from the reaction $\bar{p} + ^{197}Au$. Calculated results are in orange. Data are from [Lub+02].

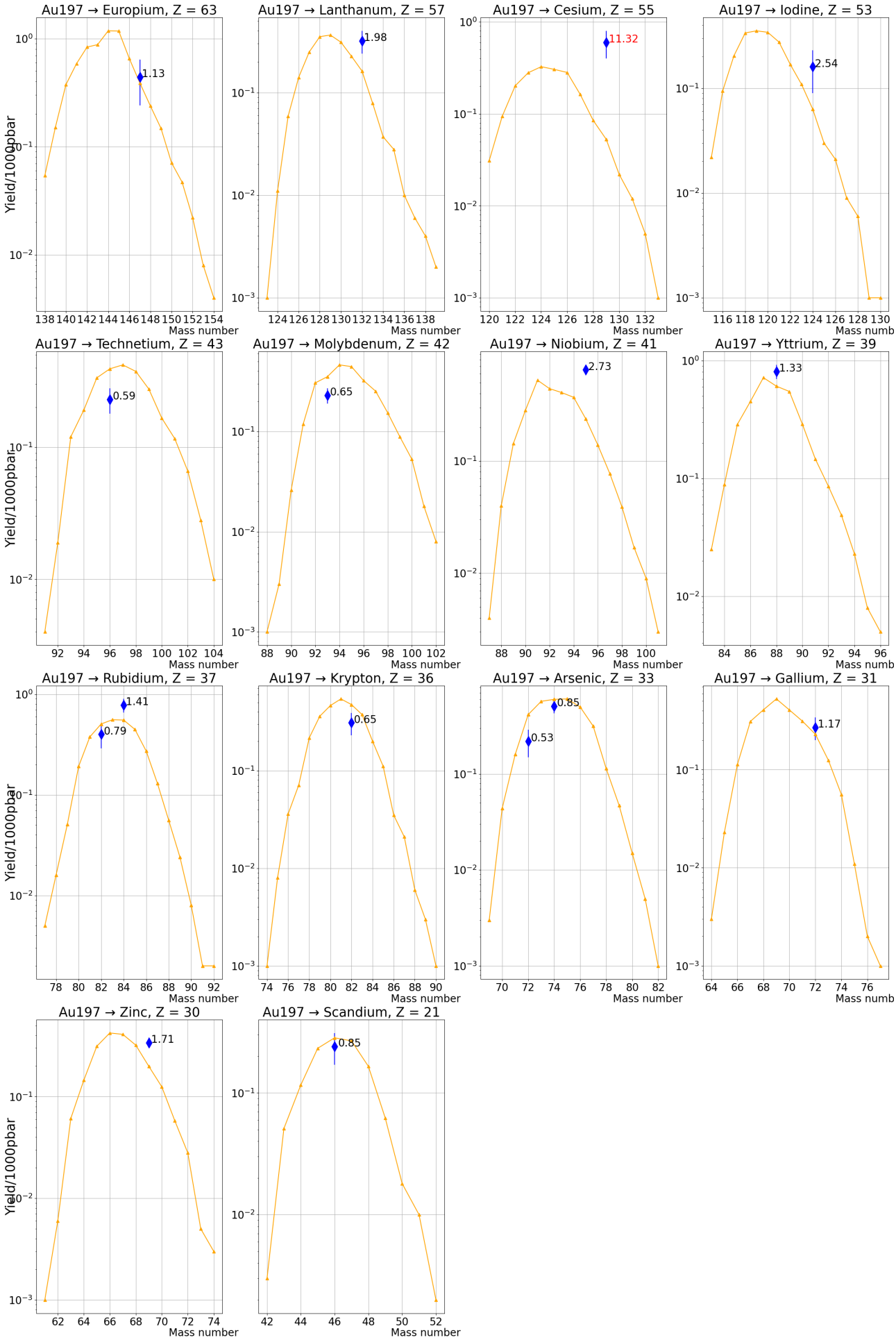

Figure A.6: Independent isotopic distributions from the reaction $\bar{p} + ^{197}Au$. Calculated results are in orange. Data are from [Lub+02].

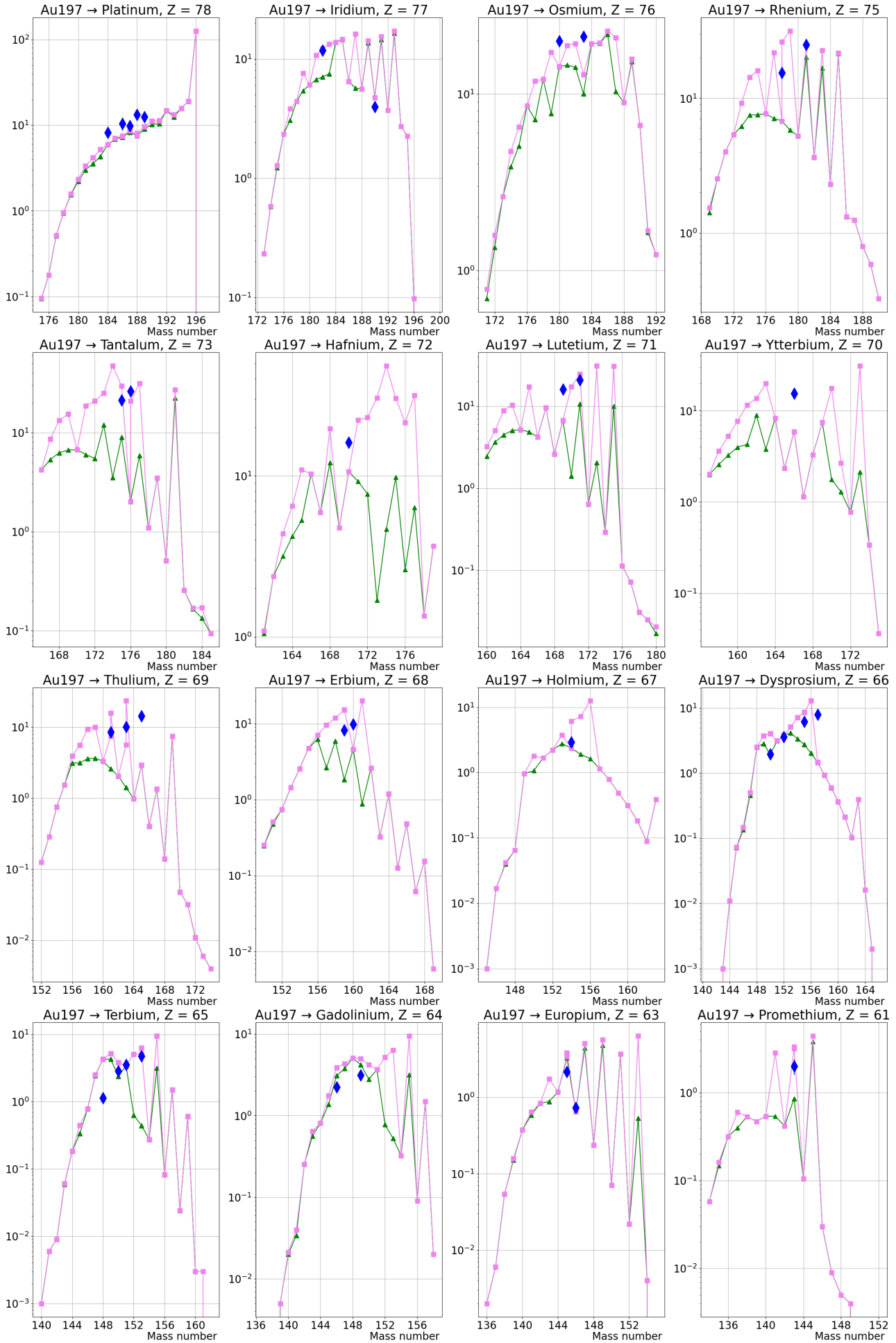

Figure A.7: Cumulative isotopic distributions from the reaction $\bar{p}+^{197}Au$. Calculated results are in violet (option $\frac{\lambda_D}{\lambda_P} = 0.1$), and in green (option $\frac{\lambda_D}{\lambda_P} = 0.5$). Definition of $\frac{\lambda_D}{\lambda_P}$ in section 5.3.3.1. Data are from [Lub+02].

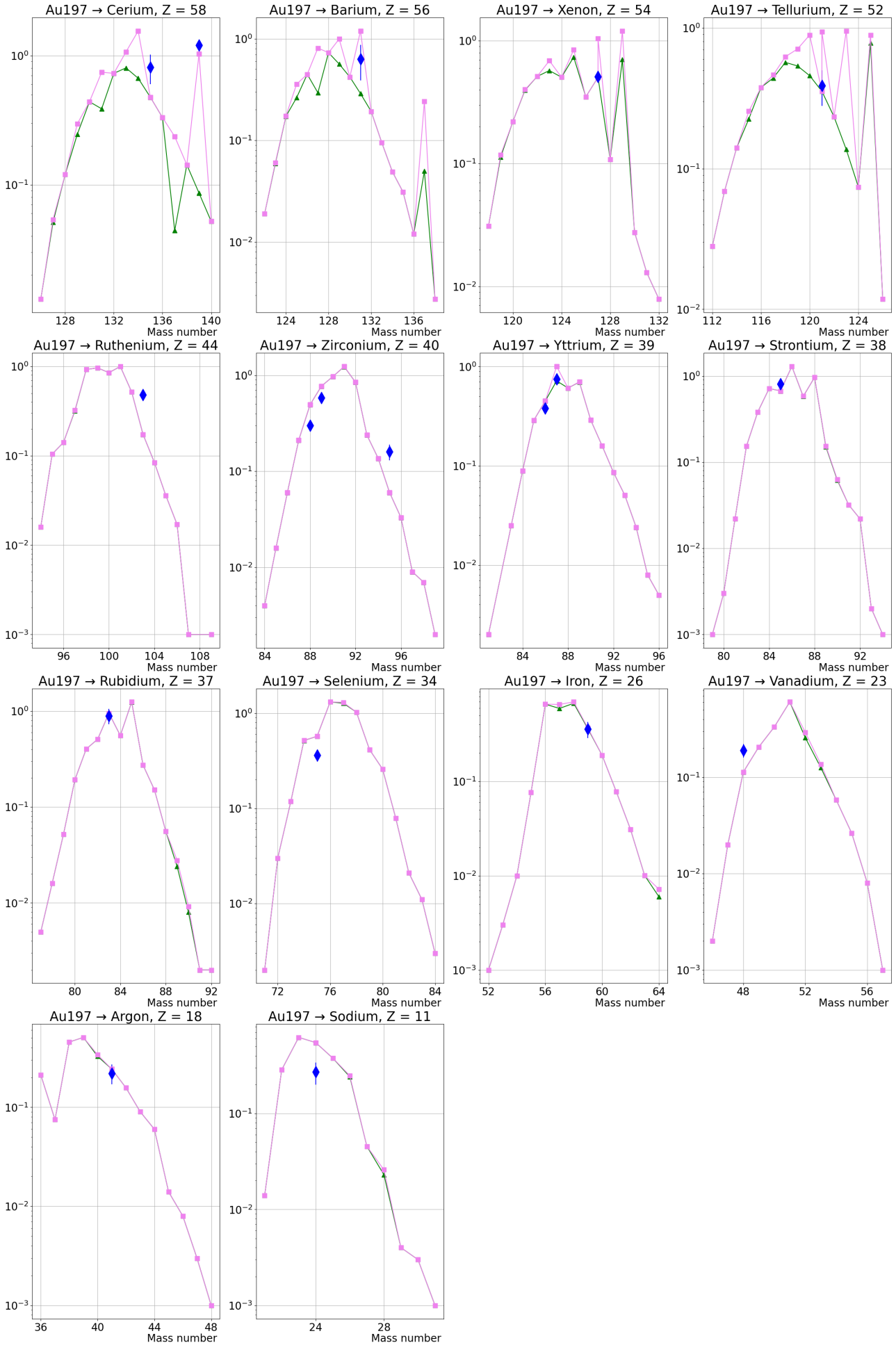

Figure A.8: Cumulative isotopic distributions from the reaction $\bar{p}+^{197}Au$. Calculated results are in violet (option $\frac{\lambda_D}{\lambda_P} = 0.1$), and in green (option $\frac{\lambda_D}{\lambda_P} = 0.5$). Definition of $\frac{\lambda_D}{\lambda_P}$ in section 5.3.3.1. Data are from [Lub+02].

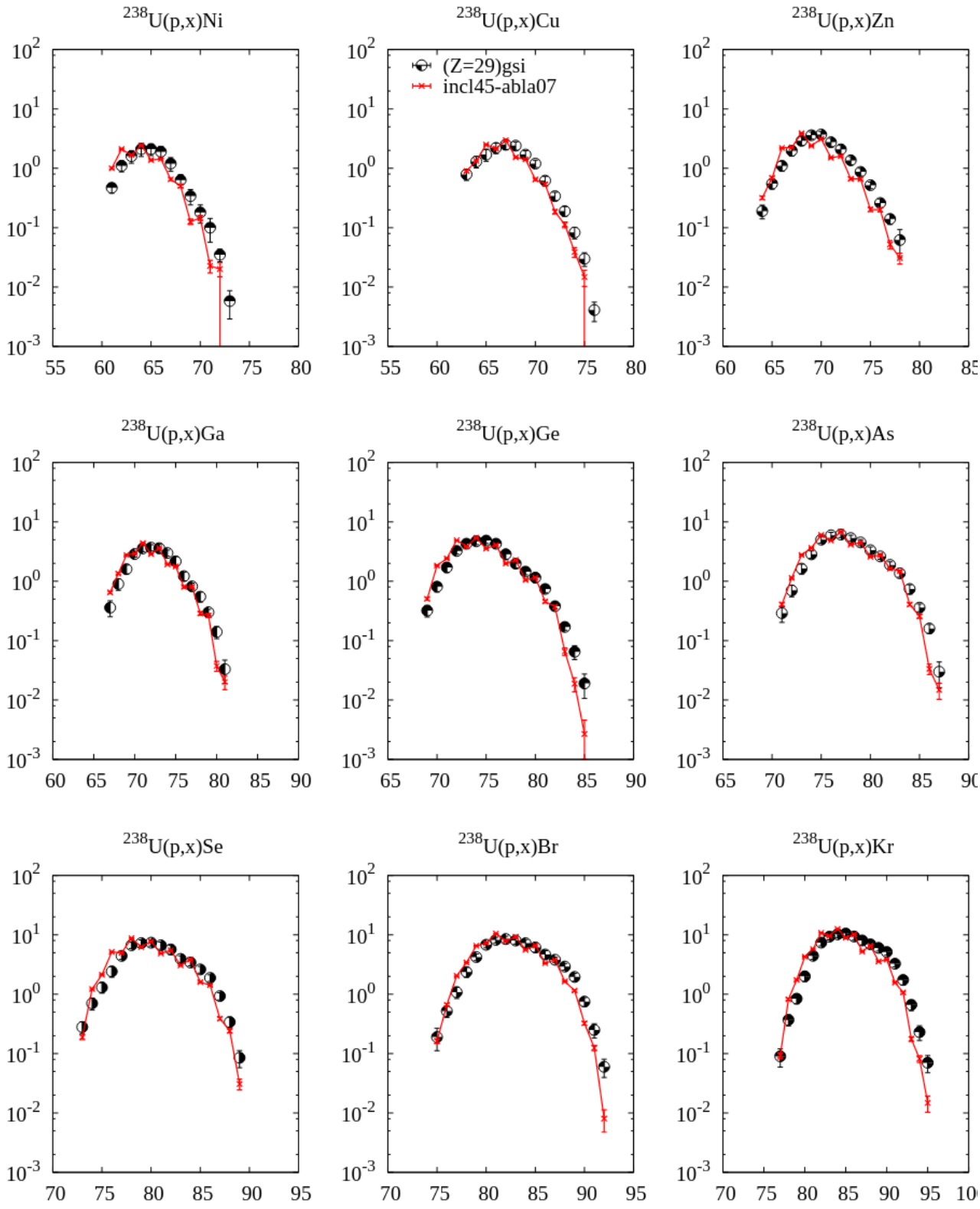

Figure A.9: INCL benchmarks [Int10] versus the data of 1 GeV/nucleon accelerated ^{238}U ions on hydrogen target from GSI experiments [Ber+03; Taï+03; Ric+06].

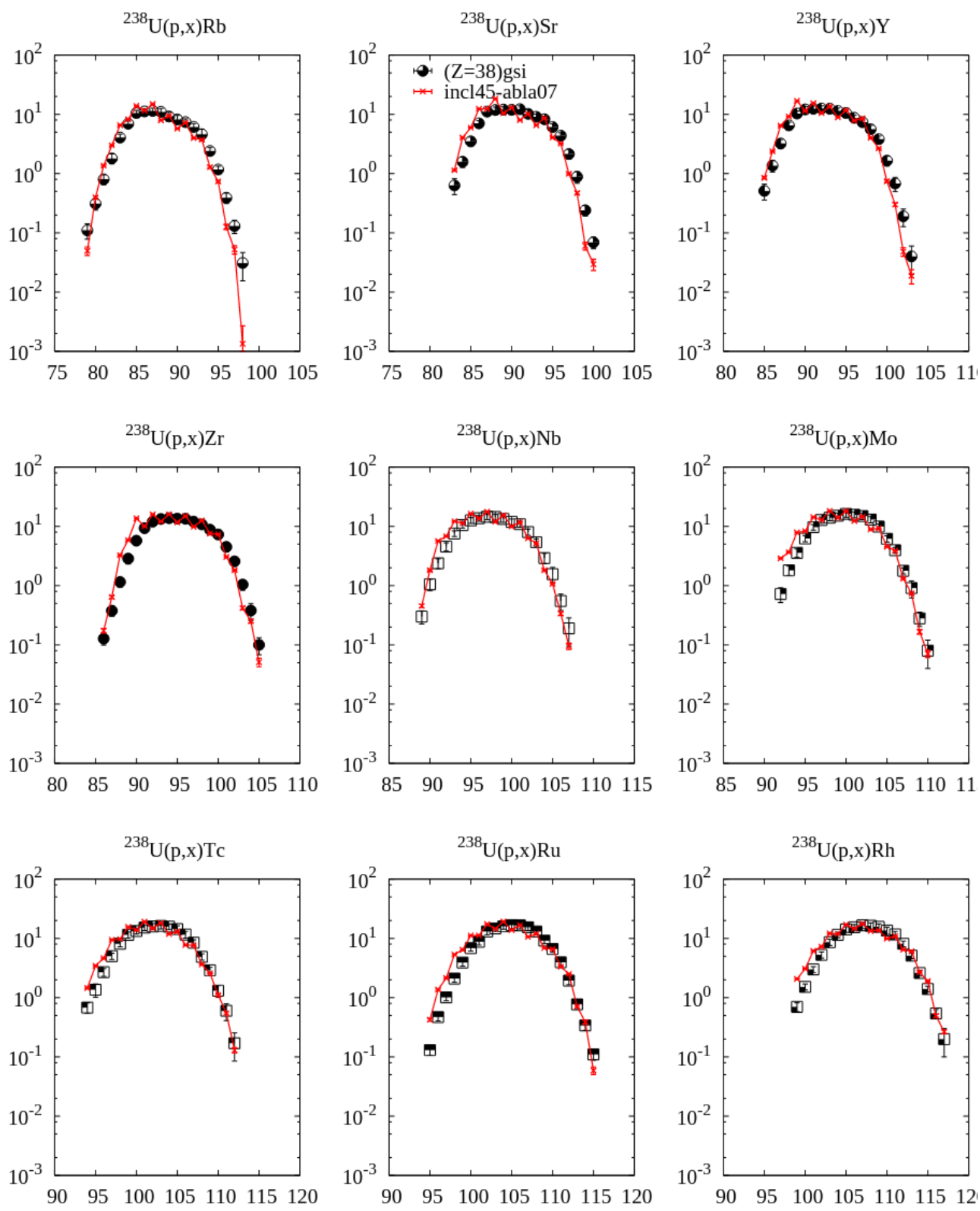

Figure A.10: INCL benchmarks [Int10] versus the data of 1 GeV/nucleon accelerated ^{238}U ions on hydrogen target from GSI experiments [Ber+03; Taï+03; Ric+06].

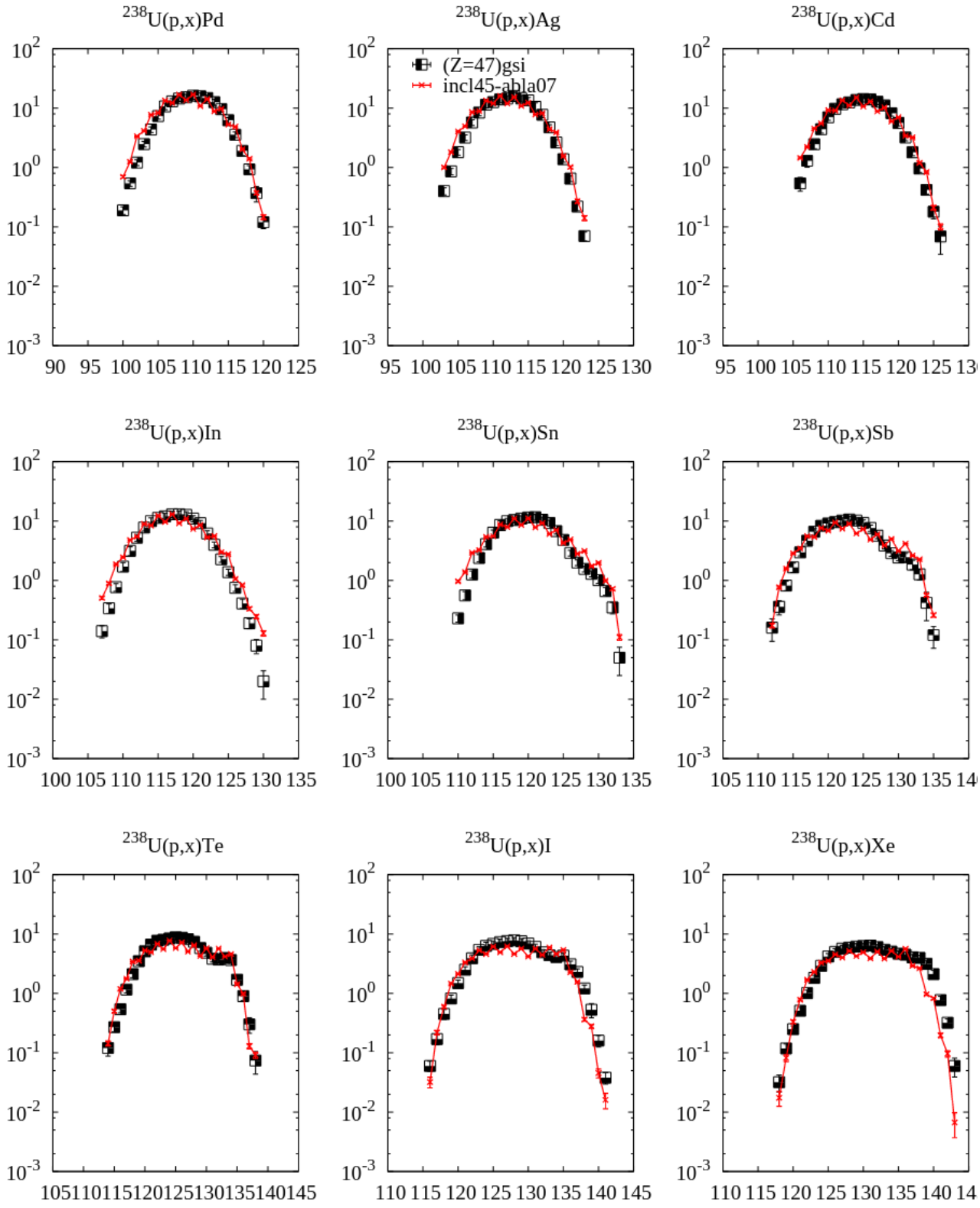

Figure A.11: INCL benchmarks [Int10] versus the data of 1 GeV/nucleon accelerated ^{238}U ions on hydrogen target from GSI experiments [Ber+03; Taï+03; Ric+06].

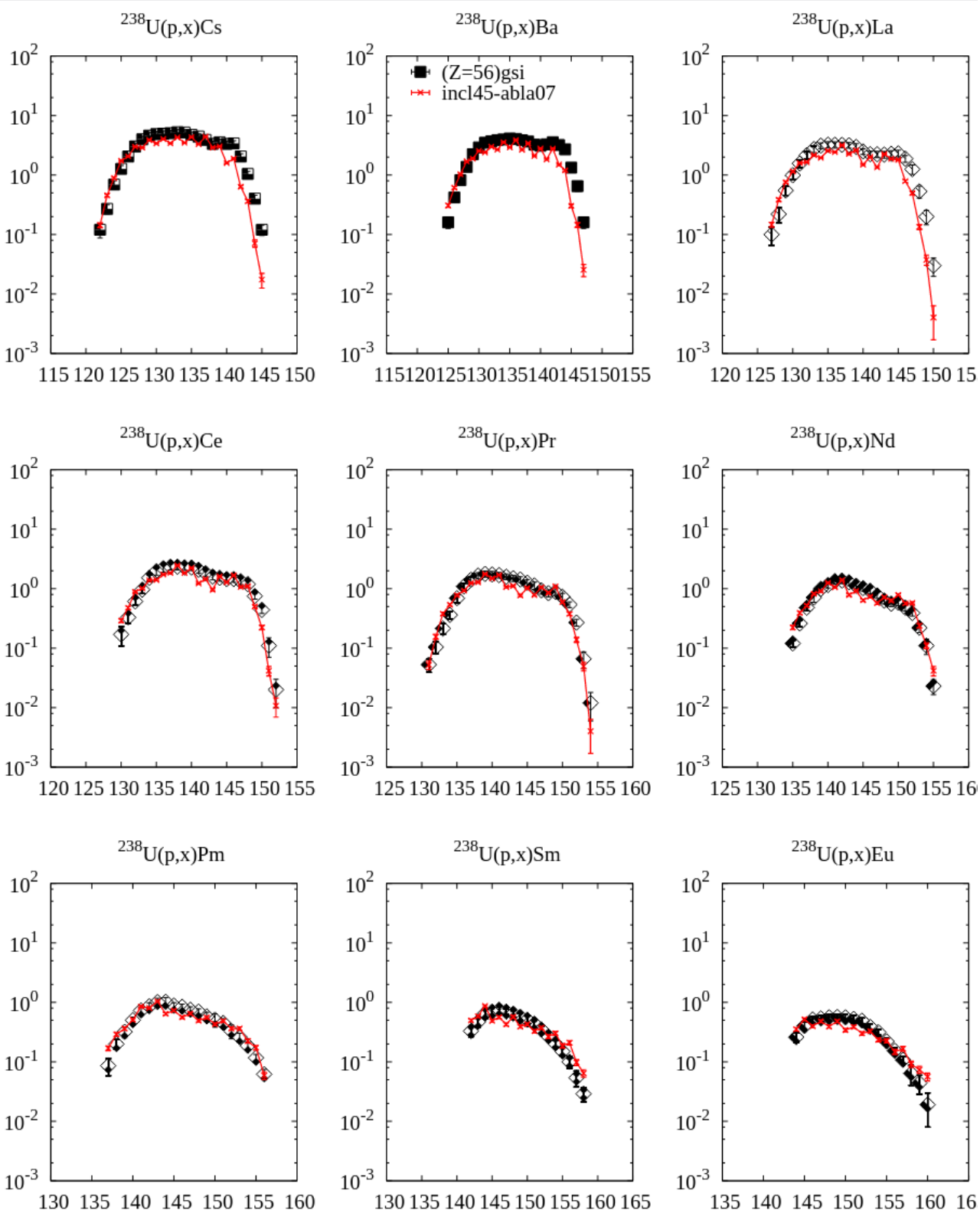

Figure A.12: INCL benchmarks [Int10] versus the data of 1 GeV/nucleon accelerated ^{238}U ions on hydrogen target from GSI experiments [Ber+03; Taï+03; Ric+06].

[BK94] G. Bendiscioli and D. Kharzeev. "Antinucleon-nucleon and antinucleon-nucleus interaction. A review of experimental data". In: *La Rivista del Nuovo Cimento (1978-1999)* 17.6 (1994), pp. 1–142. issn: 1826-9850. doi: 10.1007/BF02724447.

[Bug+73] W. M. Bugg et al. "Evidence for a Neutron Halo in Heavy Nuclei from Antiproton Absorption". In: *Phys. Rev. Lett.* 31 (7 Aug. 1973), pp. 475–478. doi: 10.1103/PhysRevLett.31.475.

[Egi+90] T. von Egidy et al. "Yield of residual nuclei after antiproton annihilation in Ba". In: *Zeitschrift für Physik A Atomic Nuclei* 335.4 (Dec. 1990), pp. 451–457. issn: 0939-7922. doi: 10.1007/BF01290193.

[Gol+92] E.S. Golubeva et al. "Effects of mesonic resonance production in annihilation of stopped antiprotons on nuclei". In: *Nuclear Physics A* 537.3 (1992), pp. 393–417. issn: 0375-9474. doi: https://doi.org/10.1016/0375-9474(92)90362-N.

[Int10] International Atomic Energy Agency. *IAEA Benchmark of Spallation Models - Experimental Data*. 2010. url: https://www-nds.iaea.org/spallations/cal/iso/p_UU238_1000_isodst_ic45a07_tbbr06a_cmp.pdf (visited on 2010).

[KBR05] Eberhard Klempt, Chris Batty, and Jean-Marc Richard. "The antinucleon-nucleon interaction at low energy: Annihilation dynamics". In: *Physics Reports* 413 (Jan. 2005). doi: 10.1016/j.physrep.2005.03.002.

[Lub+02] P. Lubiński et al. "Gold fragmentation induced by stopped antiprotons". In: *Phys. Rev. C* 66 (4 Oct. 2002), p. 044616. doi: 10.1103/PhysRevC.66.044616.

[McG+86] P. L. McGaughey et al. "Dynamics of Low-Energy Antiproton Annihilation in Nuclei as Inferred from Inclusive Proton and Pion Measurements". In: *Phys. Rev. Lett.* 56 (20 May 1986), pp. 2156–2159. doi: 10.1103/PhysRevLett.56.2156.

[Mos+89] E. F. Moser et al. "Residual nuclei after antiproton annihilation in Mo and Ho". In: *Zeitschrift für Physik A Atomic Nuclei* 333.1 (Mar. 1989), pp. 89–105. issn: 0939-7922. doi: 10.1007/BF01290114.

[Pol+95] D. Polster et al. "Light particle emission induced by stopped antiprotons in nuclei: Energy dissipation and neutron-to-proton ratio". In: *Phys. Rev. C* 51 (3 Mar. 1995), pp. 1167–1180. doi: 10.1103/PhysRevC.51.1167.

[Pot84] H. Poth. "Physics with Antiprotonic Atoms". In: *Physics at LEAR with Low-Energy Cooled Antiprotons*. Ed. by Ugo Gastaldi and Robert Klapisch. Boston, MA: Springer New York, 1984, pp. 567–588. isbn: 978-1-4684-8727-5. doi: 10.1007/978-1-4684-8727-5_54.

[Ric+06] M. V. Ricciardi et al. "Light nuclides produced in the proton-induced spallation of ^{238}U at 1 GeV". In: *Phys. Rev. C* 73 (1 Jan. 2006), p. 014607. doi: 10.1103/PhysRevC.73.014607.

[Taï+03] J. Taïeb et al. "Evaporation residues produced in the spallation reaction 238U+p at 1AGeV". In: *Nuclear Physics A* 724.3 (2003), pp. 413–430. issn: 0375-9474. doi: https://doi.org/10.1016/S0375-9474(03)01517-3.

B | Appendix B

In-flight cross sections

Cross-sections in INCL are computed for two types of possible binary collisions: $\bar{p}p$ and $\bar{p}n$, the collisions with other particles are forbidden. In both cases our total cross section is:

$$\sigma^{\bar{N}N}_{total} = \sigma^{\bar{N}N}_{elastic} + \sigma^{\bar{N}N}_{inelastic} \tag{B.1}$$

$$\sigma^{\bar{N}N}_{inelastic} = \sigma^{\bar{N}N}_{anninilation} + \sigma^{\bar{N}N}_{production} \tag{B.2}$$

INCL normally includes only exclusive channels, but in this case we were not able to fulfill the total, because of the lack of data about annihilation channels, for $\bar{p}n$ even the inclusive annihilation sum was not properly defined so $\sigma^{\bar{p}n}_{anninilation}$ was assumed to be equal to $\sigma^{\bar{p}p}_{anninilation} \frac{\sigma^{\bar{p}n}_{total}}{\sigma^{\bar{p}p}_{total}}$. All of these inclusive and elastic channels are given in Table B.1. Production channel cross sections can be found in Tables B.2 and B.3 for $\bar{p}p$ and $\bar{p}n$ respectively. The situation with annihilation is bit trickier as the exclusive channels were definitely not enough to reach the value of $\sigma_{annihilation}$ so a combined approach was used, when random number is first cast to choose between annihilation into one of the known n exclusive channels or into "missing" channels with cross section $\sigma_{missing} = \sigma_{annihilation} - \sum_{k=1}^{n} \sigma_{k,exclusive}$. Annihilating via the "missing" channel is similar to at rest annihilation - the final state is chosen from the final state probability tables: non-strange (95% probability) or kaonic (5%). These complementary tables are made up from at rest annihilation final state tables (from Ref. [Gol+92; KBR05]) by removing the lines for which we have data for in-flight and renormalizing the remaining probabilities. In-flight exclusive channel cross sections from Ref. [Bal+87] are given in Tables B.4 and B.5 for $\bar{p}p$ and $\bar{p}n$ correspondingly, while complementary information for missing channels with non-strange and strange final states is collected in Tables B.6 and B.8 for $\bar{p}p$ and B.7 and B.9 for $\bar{p}n$.

Sensitivity analysis

References

[Bal+87] A. Baldini et al. *Total Cross-Sections for Reactions of High Energy Particles (Including Elastic, Topological, Inclusive and Exclusive Reactions) / Totale Wirkungsquerschnitte fur Reaktionen hochenergetischer Teilchen (einschliesslich elastischer,topologischer, inklusiver u*. Landolt-Börnstein: Numerical Data and Functional Relationships in

Channel	a	b	c	d	e
$\sigma^{\bar{p}p}_{elastic}$	110.496	-65.605	-0.198	-34.813	4.317
$\sigma^{\bar{p}n}_{elastic}$	14.625	23.413	-0.288	-9.002	1.084
$\sigma^{\bar{p}p}_{anninilation}$	66.098	0.153	-4.576	-38.319	6.625
$\sigma^{\bar{p}p}_{total}$	119.066	6.251	-0.006	-60.046	11.958
$\sigma^{\bar{p}n}_{total}$	108.104	15.708	0.832	-54.632	-6.958

Table B.1: $\bar{N}N$ elastic and inclusive channel cross section parameters of the equation $f(x) = a + b \cdot x^c + d \cdot \ln(x) + e \cdot \ln(x)^2$, where x is the incident momentum (based on data from Ref. [Bal+87]). Total cross sections are only used to get the $\sigma^{\bar{p}n}_{anninilation}$.

Final state	a	b	c	d	e	threshold (GeV/c)
$\bar{n}n$	7.549	-0.041	-2.959	-6.835	1.629	0.114
$\bar{p}p\pi^0$	-0.734	0.841	0.905	3.415	-2.316	0.775
$\bar{n}p\pi^-$	-0.442	0.501	0.002	3.434	-1.201	0.798
$\bar{p}n\pi^+$	-2.025	2.055	-2.355	6.064	-2.004	0.798
$\bar{p}p\pi^+\pi^-$	-6.885	0.476	1.206	13.857	-5.728	1.220
$\bar{n}p\pi^-\pi^0$	1.857	-21.213	-3.448	0.827	-0.390	1.231
$\bar{p}n\pi^+\pi^0$	-3.594	0.811	0.306	5.108	-1.625	1.201
$\bar{n}n\pi^+\pi^-$	-3.594	0.811	0.306	5.108	-1.625	1.201
$\bar{p}p\pi^+\pi^-\pi^0$	-6.434	1.351	-5.185	7.754	-1.692	1.604
$\bar{n}p\pi^+2\pi^-$	3.696	-5.356	-0.053	1.941	-0.432	1.624
$\bar{p}n2\pi^+\pi^-$	-1.070	-0.636	-0.009	2.335	-0.499	1.624
$\bar{n}n\pi^+\pi^-\pi^0$	1.857	-21.213	-3.448	0.827	-0.390	1.616
$\bar{\Lambda}\Lambda$	2.379	-2.738	-1.260	-1.915	0.430	1.437
$\bar{\Lambda}\Lambda\pi^0$	-0.105	0.000	-5.099	0.188	-0.050	1.820
$\bar{\Lambda}\Lambda$	0.142	-0.291	-1.702	-0.058	0.001	1.851
$\bar{\Sigma}^+\Sigma^+$	1.855	-2.238	-1.002	-1.279	0.252	1.896
$\bar{\Sigma}^-\Sigma^-$	1.749	-2.506	-1.222	-1.262	0.274	2.042
$\bar{\Lambda}\Sigma^+\pi^-$ + B.C.C.	1.037	-1.437	-1.155	-0.709	0.138	2.065
$\bar{\Lambda}\Sigma^-\pi^+$ + B.C.C.	0.652	-1.006	-1.805	-0.537	0.121	1.653
$\bar{\Sigma}^0\Sigma^0$	0.008	0.0	0.0	0.0	0.0	2.000
$\bar{\Xi}^-\Xi^-$	0.002	0.0	0.0	0.0	0.0	2.800

Table B.2: $\bar{p}p$ exclusive production channel cross section parameters of the equation $f(x) = a + b \cdot x^c + d \cdot \ln(x) + e \cdot \ln(x)^2$, where x is the incident momentum. B.C.C. stands for baryon charge conjugated, antihyperon denoted as $\bar{\Sigma}^+$ has negative charge. Last two channels were implemented with constant cross sections, due to the lack of data (see Ref. [Bal+87]).

Final state	a	b	c	d	e	threshold (GeV/c)
$\bar{p}p\pi^-$	24.125	-20.669	-1.534	-19.573	4.493	0.787
$\bar{n}n\pi^-$	-0.442	0.501	0.002	3.434	-1.201	0.798
$\bar{p}n\pi^0$	-0.650	-0.140	-0.058	5.166	-1.705	0.777
$\bar{p}p\pi^-\pi^0$	21.688	-38.709	-2.062	-17.783	3.895	1.221
$\bar{n}p2\pi^-$	-5.443	7.254	-2.936	8.441	-2.588	1.221
$\bar{n}n\pi^-\pi^0$	-3.594	0.811	0.306	5.108	-1.625	1.201
$\bar{p}n\pi^+\pi^-$	-3.594	0.811	0.306	5.108	-1.625	1.201
$\bar{p}p\pi^+2\pi^-$	3.696	-5.356	-0.053	1.941	-0.432	1.624
$\bar{n}p\pi^02\pi^-$	3.696	-5.356	-0.053	1.941	-0.432	1.624
$\bar{n}n\pi^+2\pi^-$	-6.434	1.351	-5.185	7.754	-1.692	1.604
$\bar{p}n\pi^+\pi^-\pi^0$	1.857	-21.213	-3.448	0.827	-0.390	1.616
$\bar{\Lambda}\Lambda\pi^-$	0.048	0.0	0.0	0.0	0.0	2.100
$\bar{\Lambda}\Sigma^-$ + B.C.C.	0.139	0.0	0.0	0.0	0.0	2.000

Table B.3: $\bar{p}n$ exclusive production channel cross section parameters of the equation $f(x) = a + b \cdot x^c + d \cdot \ln(x) + e \cdot \ln(x)^2$, where x is the incident momentum. B.C.C. stands for baryon charge conjugated, antihyperon denoted as $\bar{\Sigma}^+$ has negative charge. Last two channels were implemented with constant cross sections, due to the lack of data (see Ref. [Bal+87]).

Final state particles	a	b	c	d	e
$\pi^+\pi^-$	0.637	-0.340	-0.003	-0.439	0.144
$\pi^+\pi^-\pi^0$	-2.065	4.893	-1.130	1.231	-0.212
$\pi^+\pi^-\omega$	3.020	0.425	-0.029	-3.420	0.867
$\pi^+\pi^-K^+K^-$	-1.295	1.897	-0.001	-0.365	0.044
$\pi^+\pi^-\pi^0K^+K^-$	-12.220	12.509	-0.351	4.682	-0.777
$2\pi^+2\pi^-$	3.547	0.095	0.957	-3.444	0.685
$2\pi^+2\pi^-\pi^0$	13.044	1.449	0.695	-12.313	1.627
$2\pi^+2\pi^-3\pi^0$	6.398	0.199	-1.103	-1.271	-0.380
$3\pi^+3\pi^-$	1.490	0.240	0.002	-1.012	0.134
$3\pi^+3\pi^-\pi^0$	0.286	1.634	-1.369	3.099	-1.294
$3\pi^+3\pi^-2\pi^0$	-11.370	12.503	-0.680	10.059	-2.501
$3\pi^+3\pi^-3\pi^0$	-14.732	12.338	-0.724	11.342	-2.224
$4\pi^+4\pi^-$	-1.574	1.607	-0.864	1.253	-0.276
$4\pi^+4\pi^-\pi^0$	-1.096	0.977	-0.995	1.007	-0.171

Table B.4: $\bar{p}p$ exclusive annihilation channel cross section parameters of the equation $f(x) = a + b \cdot x^c + d \cdot \ln(x) + e \cdot \ln(x)^2$, where x is the incident momentum (based on data from Ref. [Bal+87]).

Final state particles	a	b	c	d	e	upper limit (GeV/c)
$\pi^+2\pi^-$	-12.116	14.485	-0.094	-1.632	0.882	5.000
$\pi^+2\pi^-2\pi^0$	8.276	5.057	0.483	-15.864	2.552	7.000
$\pi^+2\pi^-3\pi^0$	-1.500	9.574	0.528	-11.633	-0.615	7.000
$\pi^+2\pi^-\pi^0$	7.999	4.135	0.608	-14.136	1.590	7.000
$\pi^+\pi^-\pi^0K^-\bar{K^0}$	0.083	0.091	-1.709	0.284	-0.107	-
$\pi^+\pi^-K^-K^0$	0.003	0.297	-0.001	-0.143	0.052	-
$2\pi^+3\pi^-\pi^0$	-14.701	22.258	-0.001	-3.094	-0.190	-
$2\pi^+3\pi^-$	-0.616	4.575	-0.002	-1.921	-0.153	-

Table B.5: Cross-section values for exclusive $n\bar{p}$ annihilation final states. The cross section above the upper limit is zero.

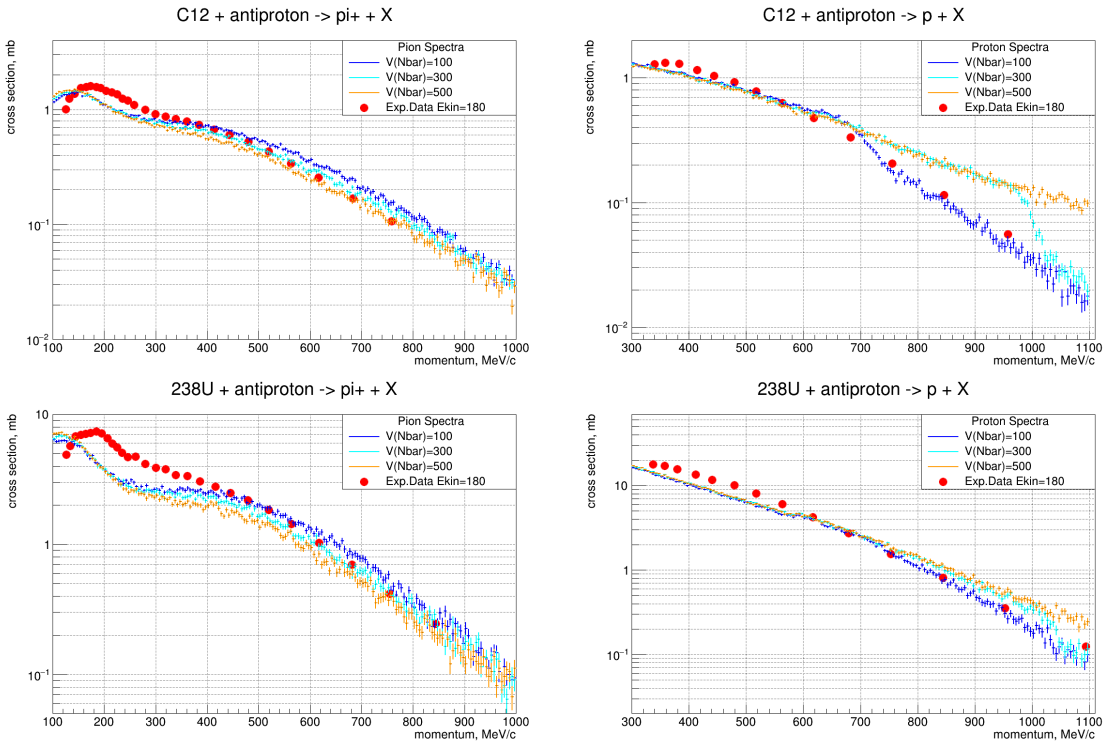

Figure B.1: INCL in-flight outgoing proton and π^+ spectra comparison with data from Ref. [McG+86] at various attractive potential values: 100(default), 300 and 500 MeV. Note, that this is done in-flight, while at rest scenario is more suitable for this energy (see Fig. 5.16).

Science and Technology - New Series. Springer Berlin Heidelberg, 1987. isbn: 9783540183860.

[Ber+03] M. Bernas et al. "Fission-residues produced in the spallation reaction 238U + p at 1AGeV". In: *Nuclear Physics A* 725 (2003), pp. 213–253. issn: 0375-9474. doi: https://doi.org/10.1016/S0375-9474(03)01576-8.

[Biz68] R. Bizzarri. "On the comparison of the annihilation of antiprotons at rest in hydrogen and deuterim". In: *Il Nuovo Cimento A (1965-1970)* 53.4 (Feb. 1968), pp. 956–968. issn: 1826-9869. doi: 10.1007/BF02758737.

[BK94] G. Bendiscioli and D. Kharzeev. "Antinucleon-nucleon and antinucleon-nucleus interaction. A review of experimental data". In: *La Rivista del Nuovo Cimento (1978-1999)* 17.6 (1994), pp. 1–142. issn: 1826-9850. doi: 10.1007/BF02724447.

[Bug+73] W. M. Bugg et al. "Evidence for a Neutron Halo in Heavy Nuclei from Antiproton Absorption". In: *Phys. Rev. Lett.* 31 (7 Aug. 1973), pp. 475–478. doi: 10.1103/PhysRevLett.31.475.

[Egi+90] T. von Egidy et al. "Yield of residual nuclei after antiproton annihilation in Ba". In: *Zeitschrift für Physik A Atomic Nuclei* 335.4 (Dec. 1990), pp. 451–457. issn: 0939-7922. doi: 10.1007/BF01290193.

[Gol+92] E.S. Golubeva et al. "Effects of mesonic resonance production in annihilation of stopped antiprotons on nuclei". In: *Nuclear Physics A* 537.3 (1992), pp. 393–417. issn: 0375-9474. doi: https://doi.org/10.1016/0375-9474(92)90362-N.

[Int10] International Atomic Energy Agency. *IAEA Benchmark of Spallation Models - Experimental Data*. 2010. url: https://www-nds.iaea.org/spallations/cal/iso/p_UU238_1000_isodst_ic45a07_tbbr06a_cmp.pdf (visited on 2010).

[KBR05] Eberhard Klempt, Chris Batty, and Jean-Marc Richard. "The antinucleon-nucleon interaction at low energy: Annihilation dynamics". In: *Physics Reports* 413 (Jan. 2005). doi: 10.1016/j.physrep.2005.03.002.

[Lub+02] P. Lubiński et al. “Gold fragmentation induced by stopped antiprotons”. In: *Phys. Rev. C* 66 (4 Oct. 2002), p. 044616. doi: 10.1103/PhysRevC.66.044616.

[McG+86] P. L. McGaughey et al. “Dynamics of Low-Energy Antiproton Annihilation in Nuclei as Inferred from Inclusive Proton and Pion Measurements”. In: *Phys. Rev. Lett.* 56 (20 May 1986), pp. 2156–2159. doi: 10.1103/PhysRevLett.56.2156.

[Mos+89] E. F. Moser et al. “Residual nuclei after antiproton annihilation in Mo and Ho”. In: *Zeitschrift für Physik A Atomic Nuclei* 333.1 (Mar. 1989), pp. 89–105. issn: 0939-7922. doi: 10.1007/BF01290114.

[Pol+95] D. Polster et al. “Light particle emission induced by stopped antiprotons in nuclei: Energy dissipation and neutron-to-proton ratio”. In: *Phys. Rev. C* 51 (3 Mar. 1995), pp. 1167–1180. doi: 10.1103/PhysRevC.51.1167.

[Pot84] H. Poth. “Physics with Antiprotonic Atoms”. In: *Physics at LEAR with Low-Energy Cooled Antiprotons*. Ed. by Ugo Gastaldi and Robert Klapisch. Boston, MA: Springer New York, 1984, pp. 567–588. isbn: 978-1-4684-8727-5. doi: 10.1007/978-1-4684-8727-5_54.

[Ric+06] M. V. Ricciardi et al. “Light nuclides produced in the proton-induced spallation of $^{238}\mathrm{U}$ at 1 GeV”. In: *Phys. Rev. C* 73 (1 Jan. 2006), p. 014607. doi: 10.1103/PhysRevC.73.014607.

[Taï+03] J. Taïeb et al. “Evaporation residues produced in the spallation reaction 238U+p at 1AGeV”. In: *Nuclear Physics A* 724.3 (2003), pp. 413–430. issn: 0375-9474. doi: https://doi.org/10.1016/S0375-9474(03)01517-3.

Probability (%)	Final State Particles
0.03	$\pi^+\pi^-\pi^0\pi^0\pi^0\pi^0\pi^0$
16.18	$\pi^+\pi^+\pi^-\pi^-\pi^0\pi^0$
0.16	$\pi^+\pi^+\pi^-\pi^-\pi^0\omega$
0.49	$\pi^+\pi^+\pi^-\pi^-\pi^0\eta$
4.39	$\pi^+\pi^-\pi^0\pi^0\pi^0\pi^0$
0.10	$\pi^+\pi^-\pi^0\pi^0\pi^0\omega$
0.27	$\pi^+\pi^-\pi^0\pi^0\pi^0\eta$
0.11	$\pi^0\pi^0\pi^0\pi^0\pi^0\pi^0$
0.02	$\pi^0\pi^0\pi^0\pi^0\pi^0\eta$
2.85	$\pi^+\pi^+\pi^-\pi^-\omega$
0.27	$\pi^+\pi^+\pi^-\pi^-\eta$
21.36	$\pi^+\pi^-\pi^0\pi^0\pi^0$
4.09	$\pi^+\pi^-\pi^0\pi^0\omega$
0.57	$\pi^+\pi^-\pi^0\pi^0\eta$
0.11	$\pi^0\pi^0\pi^0\pi^0\pi^0$
0.16	$\pi^0\pi^0\pi^0\pi^0\omega$
0.02	$\pi^0\pi^0\pi^0\pi^0\eta$
19.52	$\pi^+\pi^-\pi^0\pi^0$
8.90	$\pi^+\pi^-\pi^0\omega$
5.30	$\pi^+\pi^-\pi^0\eta$
0.06	$\pi^+\pi^-\omega\eta$
0.11	$\pi^+\pi^-\eta\eta$
0.33	$\pi^0\pi^0\pi^0\pi^0$
0.63	$\pi^0\pi^0\pi^0\omega$
0.27	$\pi^0\pi^0\pi^0\eta$
0.02	$\pi^0\pi^0\omega\eta$
0.03	$\pi^0\pi^0\eta\eta$
3.81	$\pi^+\pi^-\eta$
1.78	$\pi^0\pi^0\pi^0$
1.25	$\pi^0\pi^0\omega$
1.49	$\pi^0\pi^0\eta$
0.59	$\pi^0\omega\omega$
0.48	$\pi^0\omega\eta$
0.17	$\pi^0\eta\eta$
0.03	$\pi^0\pi^0$
0.92	$\pi^0\omega$
0.10	$\pi^0\eta$
2.49	$\omega\omega$
0.54	$\omega\eta$
0.02	$\eta\eta$

Table B.6: Final state complementary table for $\bar{p}p$ annihilation.

Probability (%)	Final State Particles
0.04	$\pi^+\pi^+\pi^+\pi^-\pi^-\pi^-\pi^-$
0.37	$\pi^+\pi^+\pi^-\pi^-\pi^-\pi^0\pi^0$
0.12	$\pi^+\pi^-\pi^-\pi^0\pi^0\pi^0\pi^0$
0.10	$\pi^+\pi^+\pi^-\pi^-\pi^-\omega$
0.29	$\pi^+\pi^+\pi^-\pi^-\pi^-\eta$
0.19	$\pi^+\pi^-\pi^-\pi^0\pi^0\omega$
0.62	$\pi^+\pi^-\pi^-\pi^0\pi^0\eta$
1.18	$\pi^-\pi^0\pi^0\pi^0\pi^0\pi^0$
0.02	$\pi^-\pi^0\pi^0\pi^0\pi^0\omega$
0.10	$\pi^-\pi^0\pi^0\pi^0\pi^0\eta$
0.83	$\pi^+\pi^-\pi^-\pi^0\omega$
1.16	$\pi^+\pi^-\pi^-\pi^0\eta$
1.28	$\pi^-\pi^0\pi^0\pi^0\pi^0$
0.19	$\pi^-\pi^0\pi^0\pi^0\omega$
0.23	$\pi^-\pi^0\pi^0\pi^0\eta$
23.93	$\pi^+\pi^-\pi^-\omega$
3.69	$\pi^+\pi^-\pi^-\eta$
10.13	$\pi^-\pi^0\pi^0\pi^0$
16.66	$\pi^-\pi^0\pi^0\omega$
3.00	$\pi^-\pi^0\pi^0\eta$
0.06	$\pi^-\pi^0\omega\eta$
0.12	$\pi^-\pi^0\eta\eta$
4.91	$\pi^-\pi^0\pi^0$
17.74	$\pi^-\pi^0\omega$
7.25	$\pi^-\pi^0\eta$
1.47	$\pi^-\omega\omega$
1.24	$\pi^-\omega\eta$
0.44	$\pi^-\eta\eta$
1.02	$\pi^-\pi^0$
0.99	$\pi^-\omega$
0.60	$\pi^-\eta$

Table B.7: Final state complementary table for $\bar{p}n$ annihilation.

Probability (%)	Final State Particles
21.87	K^-K^+
18.41	$\bar{K}^0\bar{K}^0$
5.08	$\bar{K}^0\bar{K}^0\pi^0$
4.85	$\bar{K}^0K^-\pi^+$
4.85	$K^+\bar{K}^0\pi^-$
14.03	$\bar{K}^0\bar{K}^0\pi^+\pi^-$
10.68	$K^+\bar{K}^0\pi^-\pi^0$
10.68	$\bar{K}^0K^-\pi^+\pi^0$
7.92	$K^+\bar{K}^0\pi^-\pi^0\pi^+$
0.81	$K^-\bar{K}^0\pi^-\pi^+\pi^+$
0.81	$\bar{K}^0K^+\pi^-\pi^-\pi^+$

Table B.8: Kaonic final state complementary table for $\bar{p}p$ annihilation.

Probability (%)	Final State Particles
4.80	$\bar{K}^0 K^-$
16.53	$\bar{K}^0 \bar{K}^0 \pi^-$
11.76	$\bar{K}^0 K^- \pi^0$
19.60	$K^+ K^- \pi^-$
8.10	$\bar{K}^0 K^+ \pi^- \pi^-$
24.80	$\bar{K}^0 \bar{K}^0 \pi^- \pi^0$
11.43	$\bar{K}^0 K^- \omega$
2.45	$\bar{K}^0 \bar{K}^0 \pi^+ \pi^- \pi^-$
0.52	$\bar{K}^0 K^+ \pi^- \pi^- \pi^0$

Table B.9: Kaonic final state complementary table for $\bar{p}n$ annihilation.